



Sara Pena Barros

OFDM for Data Distribution in Phased Array Antennas

”Waar een wil is, is een weg.”

— Unknown



Sara Pena Barros

OFDM para Distribuição de Dados de Controlo em Phased Array Antenas

OFDM for Data Distribution in Phased Array Antennas

Dissertação apresentada à Universidade de Aveiro para cumprimento dos requisitos necessários à obtenção do grau de Mestre em Engenharia Electrónica e Telecomunicações, realizada sob a orientação científica do Doutor Manuel Violas, Professor Auxiliar do Departamento de Electrónica, Telecomunicações e Informática da Universidade de Aveiro e co-orientação do Doutor Reza Mahmoudi, Professor do Departamento de Electrónica da Universidade Técnica de Eindhoven e do Doutor Wim de Heij, Manager do grupo de Advanced Development da Thales Netherlands; colaboração do Engenheiro Richard Vinke, Senior Development Engineer na Thales Netherlands

Project funded by

THALES

© THALES NEDERLAND B.V.

THIS INFORMATION CARRIER CONTAINS PROPRIETARY INFORMATION WHICH SHALL NOT BE USED, REPRODUCED OR DISCLOSED TO THIRD PARTIES WITHOUT PRIOR WRITTEN AUTHORIZATION BY THALES NEDERLAND B.V.

The jury

President

Prof. Doutor Eng. José Carlos da Silva Neves
Professor Catedrático da Universidade de Aveiro

Examiners committee

Prof. Doutor Eng. Manuel Violas
Professor Auxiliar da Universidade de Aveiro (orientador)

Doutor Eng. Wim de Heij
Manager of the Advanced Development group at Thales Nederlands (co-orientador)

Prof. Doutor Eng. Domine Leenaerts
Full Professor at Technische Universiteit Eindhoven and Senior Principal Scientist at NXP Semiconductors, Eindhoven

Key words

OFDM, Phased Array RADARs, RF

Acknowledgements

First of all, I would like to thank Reza Mahmoudi, the person who made all of it possible. Without his persistence and belief, I would have never had this amazing opportunity at Thales-NL and my thesis work and path would have been completely else. Having the chance to stay in The Netherlands and do my final project research in a (top) company environment is something I will always be grateful for and will never forget. Meeting the right person, be at the right place: these are the small details that greatly impact our life when we least expect.

For taking care of all the arrangements at the University of Aveiro, I would like to thank Manuel Violas and, specially, Carlos Bastos. Carlos Bastos was the one responsible for coordinating my internship at Thales-NL and my Erasmus period at the University of Eindhoven, and am perfectly aware of how much I may have sometimes tested his patience and understanding. Thank you for keeping the balls in the air while I pushed deadlines to the limit.

I would also like to express my sincere gratitude to Wim de Heij, my main supervisor at Thales-NL, who was a constant presence throughout my research. I would like to thank him for his guidance, support and all the valuable discussions and extra hours spent reviewing my work. I do not think it is too much to say that the outcome of this thesis would not be the same without him.

Although less involved in the end, I would like to leave a special thank you to Richard Vinke, my second supervisor at Thales-NL. I would like to thank him for his pertinent and always in time contributions and for all his help on putting together a functioning test setup for my final results. The assistance provided by Marco van Zuilekom and Corne Stoffels on the test setup build up is also greatly appreciated.

To my colleagues at Thales-NL, thank you for the warm reception. You made the transition from an academic into a company world easier. I knew I could count on each of you for any problem or doubt I might had, and there is nothing more important when you are out of your comfort zone than to know you are not alone.

Last but not least, there is my family. I know how hard it has been since I left, two years ago. I would like to thank them for their strength and for keeping me going, in spite of the hole my absence creates in their hearts. I loved the whole experience and it helped me to grow both personally and as an engineer, but not a day went by that I did not miss my family and friends, my country, my home. And to the one that has always been there, from my first year to the last, it is not yet time to say goodbye. I am (happily) afraid we will see each other plenty in this next chapter of ours.

Approval Graduation Project

This report (both the printed and digital version) was read and commented on by the Thales Nederland B.V. supervisor. During this the supervisor, besides reviewing technical content, has paid careful attention to private information such as schematics, floor plans, confidential information or organization charts that include names.

Reports are categorized in one the following categories. This report is filed under the following category:

- Reports and/or summaries thereof, that for security or commercial reasons must remain within Thales. The report may never leave the Thales archive. In the event that the educational institute wishes to review the report, they may send a representative to view it at Thales. This is done on the condition that the representative signs a non-disclosure agreement.
- Reports and/or summaries thereof that may be published within the educational institute and/or the student's related academy, but not within two years after the date of submission.
- Reports and/or summaries thereof that may be published publically. This includes publication on the internet.

Due to the nature of certain assignments/internships, it may be required to create a modified report for the educational institute.

* Thales supervisor decides in which category the report is filed. The report is signed by both the supervisor and a representative of the Thales Human Resources department.

Signatures for approval:

(Supervisor at Thales)

(Internship Agency Thales)

(Educational Institute)

Location and Date

Resumo

Actualmente, toda a informação de controlo por detrás dos módulos T/R (Transmit/Receive) em radares com phased arrays é transmitida digital e simultaneamente através de fibra óptica, resultando numa rede de distribuição massiva. Para que se possa reduzir o custo de produção e limitações no design, é fundamental a exploração de alternativas para a transmissão destes dados. Uma ideia intuitiva e que não implica grandes modificações estruturais, é tirar vantagem da já existente layer de RF (Rádio Frequência) usada para distribuição do pulso de radar pelos módulos.

O objectivo desta tese é investigar OFDM (Orthogonal Frequency Division Multiplexing) como uma das opções para modulação do novo sinal de RF responsável pela informação de controlo e determinar se esta é ou não uma escolha viável. Como prova de conceito, resultados experimentais serão apresentados e discutidos.

Abstract

Currently, all the control data behind the RF front-end modules in phased array radars is transmitted digitally and simultaneously by means of optical fiber, resulting in a massive distribution network. The design of cheaper radars requires alternative ways of transmission to be explored. An intuitive and rather straight approach is to take advantage of the already existent RF layer used for the distribution of the radar pulse.

The aim of this thesis work is to investigate OFDM as a modulation option for that approach and to determine whether or not it is a viable one. As proof of concept, experimental results are presented and discussed.

Contents

Contents	I
List of Abbreviations	V
List of Figures	VII
List of Tables	XIII
1 Introduction	1
1.1 General Phased Array Architecture	1
1.2 Existing Data Distribution Solutions	3
1.3 Motivation	6
1.4 Novelties and Main results	7
1.5 Outline of the thesis	11
2 Orthogonal Frequency Division Multiplexing (OFDM)	13
2.1 OFDM Concept	14
2.2 Out of Band Radiation	18
2.3 Symbol Error Rate (SER)	21
2.4 Synchronization on OFDM signals	23

2.5	RF impairments and their impact on SER	27
2.6	Conclusions	36
3	The Transmitter Chain	37
3.1	On the OOB Radiation Reduction	43
3.2	Amplifier's Non Linearity and PAPR	49
3.3	Experimental Setup	51
3.4	Conclusions	60
4	The Receiver Chain	61
4.1	Demodulating the Carrier of Interest: step-by-step	62
4.2	Experimental Setup	67
4.3	Conclusions and Novelties	75
5	Bringing All Together: a Closed Cycle	77
5.1	Channel Impulse Response	79
5.2	Time Synchronization and Phase Correction	81
5.3	Required SER — Simulations	86
5.4	Two case studies	90
5.5	SER measurements	94
5.6	Conclusions	106
6	Conclusions and Remarks for Future Work	109
6.1	General Conclusions, Novelties and Discussion	109
6.2	A few tips for Hardware Implementation and Optimization	110

A Derivation of the SER for M-QAM	115
B MAXIM 2829 datasheet	119
Bibliography	159

List of Abbreviations

AWG	Arbitrary Waveform Generator
AWGN	Additive White Gaussian Noise
CAZAC	Constant Amplitude Zero Auto-Correlation
CC	cancellation Carriers
CDF	Cumulative Density Function
CIR	Channel Impulse Response
CP	Cyclic Prefix/Postfix
CPE	Common Phase Error
CR	Cognitive Radio
CW	Carrier Weighting
DFT	Discrete Fourier Transform
FFT	Fast Fourier Transform
GB	Guard Band
HPA	High Power Amplifier
IBEND	Information Bit-Energy-to-Noise Density
IBO	Input Back-Off
ICI	Inter Carrier Interference
IDFT	Inverse Discrete Fourier Transform
IFFT	Inverse Fast Fourier Transform
ILR	Image Leakage Ratio
IRR	Image Rejection Ratio

ISI	Inter Symbol Interference
LNA	Low Noise Amplifier
LO	Local Oscillator
M-QAM	M^{th} order Quadrature Amplitude Modulation
MLE	Maximum Likelihood Estimate
MSC	Multiple Sequence Choice
NF	Noise Figure
OBO	Output Back-Off
OFDM	Orthogonal Frequency Division Multiplexing
OFDMA	Orthogonal Frequency Division Multiple Access
OOB	Out of Band
PAPR	Peak to Average Power Ratio
PCB	Printed Circuit Board
PDF	Probability Distribution Function
PLL	Phase Locked Loop
PN	Pseudo Noise
PSD	Power Spectral Density
PSG	Programmable Signal Generator
RF	Radio Frequency
RSG	Radar Signal Generator
RV	Random Variable
SC	Samplig scope
SDR	Software Defined Radio
SER	Symbol Error Rate
SNR	Signal to Noise Ratio
SVD	Singular Value Decomposition
T/R module	Transmit/Receive module
VCO	Voltage Controlled Oscillator
VGA	Variable Gain Amplifier
WLAN	Wireless Local Area Network

List of Figures

1.1	General Phased Array Architecture.	2
1.2	Block diagram of a RF front-end module.	3
1.3	Typical architecture of a T/R channel.	4
1.4	Large X-band Phased Array.	5
1.5	Flat Panel X-band Phased Array.	5
1.6	General Phased Array Architecture with solution implemented.	9
1.7	Block diagram of a RF front-end model with solution implemented.	10
2.1	OFDM scheme proposed by Chang.	14
2.2	Overlapping orthogonal OFDM carriers in the frequency domain, an example for 10 carriers.	15
2.3	Time domain OFDM signal (left) and its spectrum (right).	16
2.4	OFDM spectrum with 6.25% (left) and 12.5% (right) cyclic prefix.	17
2.5	Example of a time domain OFDM symbol with CP (in green).	18
2.6	Windowed OFDM symbols.	19
2.7	Concept of the cancellation carriers algorithm. (figure taken from [1])	21
2.8	Example of a phase noise PSD for the MAX2829 chip from Maxim Integrated, $f_{LO} = 5.25\text{GHz}$	28

2.9	CPE and ICI effects on a constellation. (a) $B_\phi/\Delta f = 0.01$. (b) Constellation (a) after CPE correction. (c) $B_\phi/\Delta f = 1$. (figure taken from [2])	30
2.10	Performance degradation due to phase noise for $\sigma_\phi^2 = 0.015 \text{ rad}^2$ (orange), $\sigma_\phi^2 = 0.1 \text{ rad}^2$ (blue), $\sigma_\phi^2 = 0.4 \text{ rad}^2$ (green), $\sigma_\phi^2 = 0.8 \text{ rad}^2$ (red), $\sigma_\phi^2 = 1 \text{ rad}^2$ (cyan) and $\sigma_\phi^2 = 1.3 \text{ rad}^2$ (magenta).	31
2.11	Mismatches between the I and Q branches.	32
2.12	Received 16-QAM constellations for different phase of the complex-valued leakage parameter $\frac{k_{1,k}}{k_{2,k}}$ and fixed magnitude ($IRR = 15\text{dB}$). (figure taken from [3])	33
2.13	Joint impact of AWGN and IQ imbalance for 64-QAM. (figure taken from [3])	34
2.14	Constellation at the output of the DFT of an OFDM signal distorted by a nonlinear amplifier with $IBO=0\text{dB}$ and no AWGN. (figure taken from [4]) . .	35
3.1	Block diagram of the OFDM transmitter.	38
3.2	Example of a time domain constellation for receiver r^{th}	40
3.3	Example of the mapping of the OFDM carriers with the first constellation point of each receiver.	41
3.4	5 out of the 24 OFDM time domain symbols; inphase (top) and quadrature(bottom).	41
3.5	Example of the OFDM spectrum for one symbol; orthogonal carriers in a linear spectrum (top) and spectrum in dB (bottom).	42
3.6	Example of the averaged OFDM spectrum over the 24 symbols.	42
3.7	Windows under study: Blackman (dark blue), Blackman-Harris (dark green), Tukey (red), Gaussian (cyan), Parzen (purple) and Chebyshev (light green). . .	43
3.8	The first 3 time domain OFDM symbols for the six different windows.	46
3.9	OFDM average spectra over the 24 time domain symbols for the six different windows.	46
3.10	OFDM time domain signal with (green) and without (blue) CCs.	47
3.11	Averaged OFDM spectrum over 24 time domain symbols for different CCs scenarios.	48

3.12	CDF of the PAPR for the original OFDM signal (blue) and OFDM signal with $n_{CC} = 8$ and small α (green), large α and $n_{CC} = 8$ (red) and large α and $n_{CC} = 4$ (black).	49
3.13	HPA's transfer function and required OBO (Output Back-Off) depending on the PAPR.	50
3.14	Block diagram of the transmitter setup.	51
3.15	Analog outputs technical characteristics provided in the AWG N6030A manual.	52
3.16	<i>Infiniium</i> scope's noise floor with no averaging (blue), 512 average sweep (green) and 1024 average sweep (red).	53
3.17	OFDM time domain signal (top) and 500MHz wide measured spectrum (down) at the output of the AWG (left) and computed on MATLAB [®] (right).	54
3.18	OFDM time domain signal (top) and 500MHz wide measured spectrum (down) at the output of the AWG (left) and computed on MATLAB [®] (right) optimized with cancellation carriers.	55
3.19	OFDM time domain signal (top) and 500MHz wide measured spectrum (down) at the output of the AWG (left) and computed on MATLAB [®] (right) optimized with a Gaussian, 70% symbol extension.	56
3.20	OFDM time domain signal (top) and 500MHz wide measured spectrum (down) at the output of the AWG (left) and computed on MATLAB [®] (right) optimized with cancellation carriers combined with a Gaussian window, 70% symbol extension.	57
3.21	500MHz wide OFDM spectrum measured at the output of the AWG with (green) and without (blue) cancellation carriers.	58
3.22	500MHz wide OFDM spectrum measured at the output of the AWG with (green) and without (blue) windowing.	58
3.23	500MHz wide OFDM spectrum measured at the output of the AWG with (green) and without (blue) windowing combined with CCs.	58
3.24	300MHz wide OFDM spectrum transmitted at a central frequency $f_c = 5.4\text{GHz}$ with (blue) and without (black) cancellation carriers.	59
4.1	Block diagram of a receiver Rx_r	61
4.2	Illustration of the signal's spectrum at the output of the narrow filter (left) and the result of sampling with $f_{ADC} > K\Delta f$ (right).	66

4.3	Illustration of the signal's spectrum after extreme downsampling with decimation factor d ; example for a 8 points (left) and 5 points (right) DFT, i.e. $f_{ADC} = 8\Delta f$ and $f_{ADC} = 5\Delta f$, respectively.	66
4.4	Block diagram of the receiver setup.	67
4.5	Block diagram of the MAX2829 chip.	68
4.6	Frequency response of the MAX2829 chip filters for the fine settings (left) and the coarse settings (right).	69
4.7	PSD phase noise curves for carrier 1 (blue), 26 (green), 50 (red), 80 (black) and 105 (cyan) on the left and phase noise PSD curve for $f_{LO} = 5.25\text{GHz}$ provided by Maxim Integrated on the right.	70
4.8	MAX2829 voltage gain (left) and NF (right) typical curves depending on the gain settings for the LNA and the VGA provided by Maxim Integrated.	71
4.9	I and Q time domain signals at the output of the receiver.	73
4.10	OFDM spectrum at the output of the receiver.	73
4.11	Noise spectrum at the output of the receiver.	74
4.12	I&Q time domain signal and spectrum of a 4MHz carrier at the receiver output for $G_{LNA} = \text{Min}$, $G_{VGA} = 26\text{dB}$ and $P_{in} = -23\text{dBm}$	74
4.13	I&Q time domain signal and spectrum of a 4MHz carrier at the receiver output for $G_{LNA} = \text{Mid}$, $G_{VGA} = 20\text{dB}$ and $P_{in} = -31\text{dBm}$	75
5.1	Block diagram of the experimental setup with the transmit-receive cycle closed.	78
5.2	Time domain pulse with a 125ns delay measured at the output of the AWG — I (top) and Q (below) channel.	79
5.3	Time domain pulse with a 125ns delay measured with the sampling scope at the output of the Maxim's board for a 14MHz lowpass filter.	80
5.4	Time domain pulse with a 125ns delay sampled with the digitizer at the output of the Maxim's board for a 14MHz lowpass filter.	80
5.5	Inphase OFDM signal with synchronization symbols at the IDFT output.	82
5.6	Example of a synchronization symbol for receiver Rx_r ; inphase time domain signal (left) and spectrum before upconversion (right).	83

5.7	Example of the correlation output for synchronization at the receiver side. . .	84
5.8	Time domain constellations for receiver Rx_r : sent constellation (left), received constellation with no synchronization (middle) and received constellation after time synchronization (right).	84
5.9	Inphase OFDM time domain signal with appended preamble for phase correction at the output of the IDFT.	85
5.10	Time domain constellations for receiver Rx_r : sent constellation (left) and received constellation after time synchronization without phase correction (middle) and with phase correction (right).	85
5.11	Tx and Rx weighting functions for the phased array antenna.	87
5.12	Radiation patterns with all radiator elements ON.	87
5.13	Radiation pattern with one non radiating element in the middle of the phased array.	88
5.14	Radiation patterns for one failed RF front-end module in the middle, 4 radiator elements switched OFF.	88
5.15	Radiation patterns for 2 RF failed front-end modules on the side, 8 radiator elements switched OFF.	89
5.16	Radiation patterns for 4 failed RF front-end modules, 16 radiator elements switched OFF: one in the middle, and 3 more near the borders.	89
5.17	Radiation patterns for 10 failed RF front-end modules spread around, 40 radiator elements switched OFF.	90
5.18	Theoretical SER curves for the two case studies, 64-QAM with one carrier per receiver (green) and 16-QAM with two carriers per receiver (red).	93
5.19	Block diagram of the experimental test setup including the TCP/IP connection.	94
5.20	Mapping of the OFDM carriers (top) and its spectra (below) for the "no images" experiment.	98
5.21	Theoretical SER curve (black) and measured curves for Rx_1 and case study 64-QAM, 1 allocated carrier: no downsampling (blue), downsampling to 80MHz (green), downsampling to 40MHz (red) and downsampling to 80MHz with no images (cyan).	99

5.22	Theoretical SER curve (black) and measured curves for Rx ₁ and case study 16-QAM, 2 allocated carriers: no downsampling (blue), downsampling to 80MHz (green), downsampling to 40MHz (red) and downsampling to 80MHz with no images (cyan).	100
5.23	Theoretical SER curve (black) and measured curves for Rx ₂₆ and case study 16-QAM, 2 allocated carriers: no downsampling (blue), downsampling to 80MHz (green), downsampling to 40MHz (red) and downsampling to 80MHz with no images (cyan).	100
5.24	Theoretical SER curve (black) and measured curves for Rx ₅₁ and case study 16-QAM, 2 allocated carriers: no downsampling (blue), downsampling to 80MHz (green), downsampling to 40MHz (red) and downsampling to 80MHz with no images (cyan).	101
5.25	Theoretical SER curve (black) and measured curves for Rx ₈₀ and case study 16-QAM, 2 allocated carriers: no downsampling (blue), downsampling to 80MHz (green), downsampling to 40MHz (red) and downsampling to 80MHz with no images (cyan).	101
5.26	Theoretical SER curve (black) and measured curves for Rx ₁₀₅ and case study 16-QAM, 2 allocated carriers: no downsampling (blue), downsampling to 80MHz (green), downsampling to 40MHz (red) and downsampling to 80MHz with no images (cyan).	102
5.27	Theoretical SER curve (black) and measured curves for Rx ₁ (blue), Rx ₂₆ (green), Rx ₅₁ (magenta), Rx ₈₀ (cyan) and Rx ₁₀₅ (red) with downsampling to 80MHz.	102
5.28	Sinc roll-off caused by reconstruction from a staircase signal as a function of carrier index.	105
5.29	Digitizer's step response with markers at multiples of $T_s + T_{CP} = 625\text{ns}$ for the 16-QAM, two carriers per receiver, example.	105
6.1	RF network characterization plots: Port Reflection "RF-Com", S11 dB (1,1); Return loss, S21 and S31 dB (1,2); Port Reflection "Module", S22 and S33 dB (2,1) and Isolation 2-ports I/O, S32 dB (2,2).	111

List of Tables

3.1	Power at the output of the synthesizer, ILR and LO leakage measured for 5 carriers across the wide OFDM bandwidth at a central frequency $f_c = 5.2\text{GHz}$.	60
4.1	Phase noise measurements at different δf offsets away from the carrier for a set of carriers across the OFDM spectrum after downconversion to Δf .	70
4.2	Receiver gain for $G_{VGA} = 26\text{dB}$ and G_{LNA} at minimum and mid levels.	71
5.1	CIR measurements with the sampling scope and with the digitizer and the output of the Maxim's board for different lowpass filters.	80
5.2	SNR measurements for several input powers in the range -64dBm to -34dBm for both case studies, Rx ₁ .	96

Chapter 1

Introduction

In 1887, Heinrich Hertz proved that radio waves could be reflected by solid objects [5]. This was the starting point of a research that was still far to become the RADio Detection And Ranging (RADAR) technology that is known nowadays. Boosted by the Second World War, this technology had a huge development on the beginning of the XX century. When the war was over, its utility for military, civil, security and science applications kept the investigation ongoing. RADAR technology is now able to detect, track and even identify moving and stationary targets under the most adverse conditions.

One of the features that contributed for the improvement of this technology was the use of phased array antennas. By changing the relative amplitudes and phases of the radiating elements, different radiation patterns are produced without actually moving the antenna. It allows to steer the beam into a fixed point in space or rapidly scan in both elevation or azimuth. These characteristics make the phased array RADAR very flexible and capable of performing multiple tasks.

Given the huge interest in using and commercialize phased array RADARs, it is urgent to find ways of making it cheaper to produce.

1.1 General Phased Array Architecture

A general architecture of a phased array radar with active T/R-channels and electronic beamsteering is shown in Figure 1.1.

The phased array antenna consists of radiators, which are arranged in a linear or a planar configuration.

The RF front-end modules containing the T/R-channels are mounted behind the antenna face. At one end, the T/R-channels are connected to the radiators and at the other end they are connected to a RF combiner with one common input/output port and as many individual

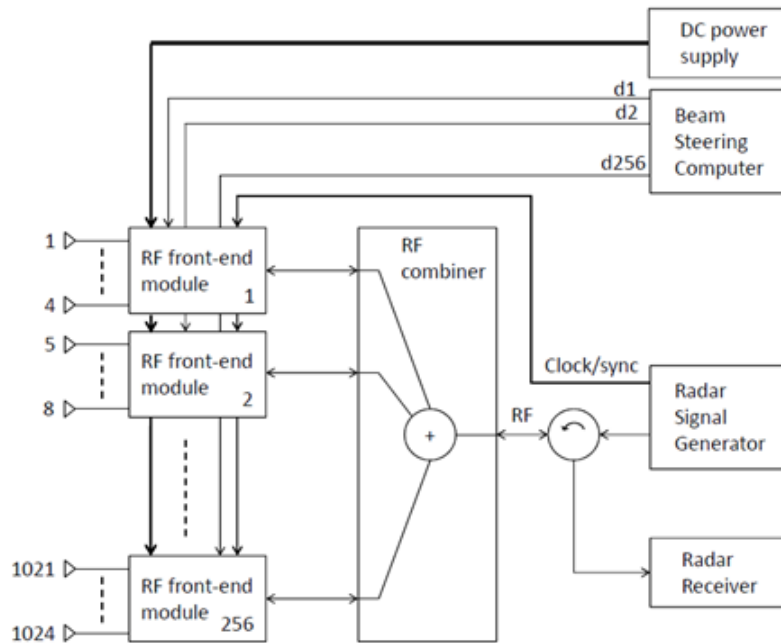


Figure 1.1: General Phased Array Architecture.

input/output ports as RF front-end modules. The common port of the RF combiner is connected to a circulator, which provides the two signal paths for radar transmission and reception.

For radar transmission, the RF signal from the RSG (Radar Signal Generator) is provided to the common port of the RF combiner. The RF combiner distributes the RF signal from the common port to each individual port.

For radar reception, the RF signals from the T/R-channels are provided to the individual ports of the RF combiner. The RF combiner sums the RF signals in phase, and the summed RF signal is provided to the radar receiver via the circulator.

To steer the beam direction and create a specified beam shape, the beamsteering computer computes the gain and phase settings required for each of the radiators. This control data, together with a clock/synchronization signal and DC power has to be provided to the RF front-end modules. The clock/synchronization signal is common for the RF front-end modules, while the control data is specific for each RF front-end module.

To provide typical figures, the number of radiators was chosen to be 1024, the number of RF front-end modules 256 and the number of T/R (Transmit/Receive) channels in each RF front-end module 4.

Figure 1.2 shows a block diagram of a RF front-end module, consisting of 4 T/R-channels and a digital control block that receives the gain and phase settings for the T/R-channels and the clock/synchronization signal. The controller decodes the settings from the beam steering computer into the control bits for the components of the T/R-channel. Internally, the RF

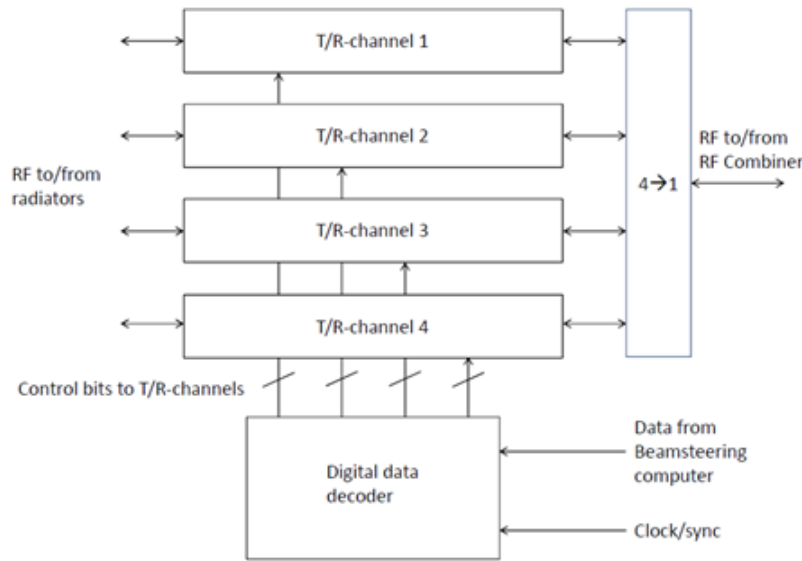


Figure 1.2: Block diagram of a RF front-end module.

signals to/from the 4 T/R-channels are distributed/summed by a 4-to-1 combiner to obtain 1 RF input/output port towards the 256 port RF combiner.

Figure 1.3 shows a typical block diagram of a T/R-channel. For transmission, the upper path is active and is driven with the RF transmit signal from the RF combiner. The upper path consists of a phase shifter for beam steering, a driver amplifier and HPA (High Power Amplifier) to amplify the RF transmit signal to the required power which is provided to the antenna element. For reception, the lower path is active and it receives the RF signal from the antenna element. The lower path consists of a limiter, a LNA (Low Noise Amplifier), a phase shifter and a VGA (Variable Gain Amplifier) to amplify the received signal which is then provided to the RF combiner. The control bits for the phase shifters and the VGA give the gain and phase settings applied to the RF signal for each of the antenna elements, to obtain the desired beam direction and beam shape.

1.2 Existing Data Distribution Solutions

The RADAR world is a secretive one and it is hard to find full disclosures of how the control data distribution is done, nowadays. Conventional solutions that are publicly known are based on serial data links implemented via electrical wiring and fibre optic cables. In this section two existing solutions based on Thales-NL technology will be briefly described.

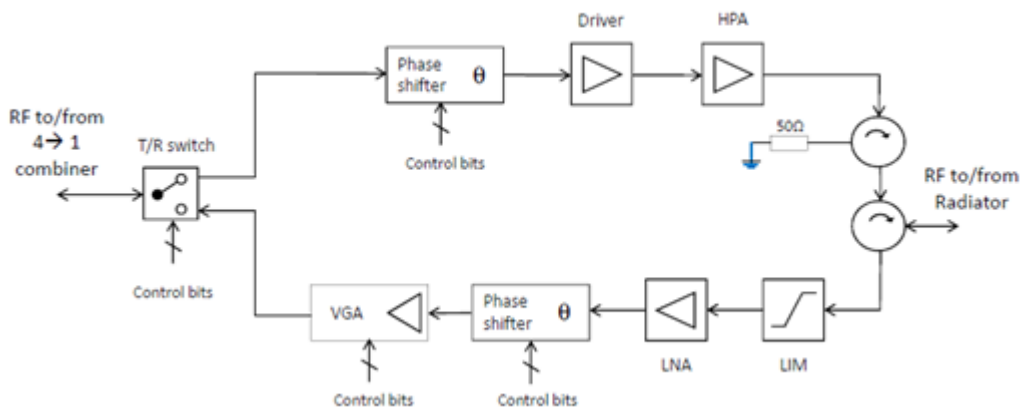


Figure 1.3: Typical architecture of a T/R channel.

Large X-Band Phased Array

Thales' APAR is an example of a large X-band (8–12GHz) phased array with RF analogue beamforming. The array is built with a radiator face in which the RF front-end modules are plugged in perpendicularly to fit on the radiator spacing. One APAR antenna face contains more than 3000 T/R channels.

RF front-end modules are mounted on support frames together with power supply units and data distribution boards. The frames are inserted in the backside of the antenna to connect the T/R channels to the radiators.

In this radar, control data is distributed using fiber optic cables, shielded electrical cables and data distribution boards. RF is distributed and combined separately, using waveguide combiners and stripline combiners. Figure 1.4 shows the backside of the APAR. The amount of cables used to distribute the control data and clock signal with encoded syncs for timing is seen in the lower left compartment.

An alternative solution for data distribution, sharing the RF combiner with the radar RF would eliminate most of the cabling and all the digital data distribution boards (more than 100!). This will result in a reduction of weight, power consumption and cost, and will increase the reliability of the antenna through the reduction of component count. Even though these improvements are useful, the urge to come up with alternative technology is not so strong, since there is a proven solution within the available space.

Flat Panel X-band Phased Array

A flat panel phased array consists of a PCB (Printed Circuit Board) on which RF front-end modules are mounted close together to form the phased array. The RF front-end module includes the radiating element on the top side and all the electrical contacts for RF, DC power, control data and synchronization on the bottom side.

The RF front-end modules fit within a 0.5 wavelength grid and are tightly placed together.



Figure 1.4: Large X-band Phased Array.

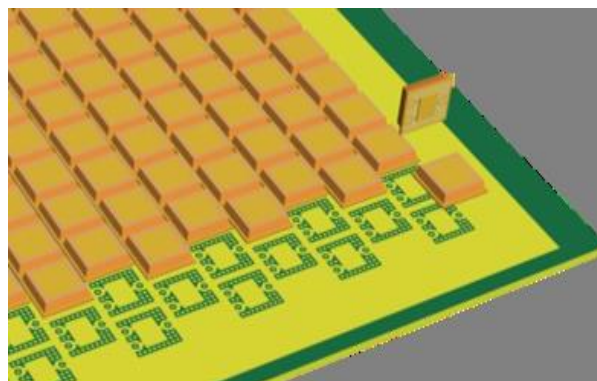


Figure 1.5: Flat Panel X-band Phased Array.

They are a lot smaller than in the APAR case — a RF front-end module with 2 T/R channels has a size of approximately $30 \times 15 \text{ mm}$. It all has to be done in one board, so the all design of RF, control data, DC power and synchronization distribution is much more integrated. The board build-up is a combination of RF layers that can be used up to X-band and board material for the lower frequencies down to DC.

Figure 1.5 is an artist impression of how this phased array will look like. An alternative data distribution solution that can share board layers with the clock/synchronization distribution or the RF distribution would reduce the number of layers in the board and simplify the layout by relieving the design constraints. This is a significant advantage in this highly integrated phased array antenna.

1.3 Motivation

Until this point in time, data distribution to the RF front-end modules is made digitally using electrical wiring or fibre optic cables, adding cost and weight to the system and taking space that may be scarce, especially for high RF (X-band and higher). The multitude of interfaces to the RF front-end modules for DC-power, RF, clock/synchronization signals and control data leads to design constraints and may complicate design optimization.

In particular, the infrastructure for the transport of the control data to the RF front-end modules is cumbersome. The data is specific for each RF front-end module, and has to be transmitted in a short time to all RF front-end modules simultaneously. Typical figures that have to be dealt with are:

- $10\mu\text{s}$ transmission time for 160 to 240 bits per RF front-end module
- 256 RF front-end modules, each requiring one data link

The resulting data rate is 16 to 24 Mbit/s per data link and, in total, 4.10 to 6.14 Gbit/s. For data rates as high as this, fully parallel data distribution is preferred. However, to implement such a distribution, separate clock and data lines to each RF front-end module are necessary, requiring the use of several board layers. Several layers result in a complex layout and add design constraints due to inter-layer interaction.

The data distribution infrastructure could be removed, if it would be possible to use the RF layer to transport the control data to the RF front-end modules.

To do such an implementation using the RF layer, there are two domains to play with: serial/parallel and time/frequency.

Let's take an example on X-band. In principle, a fully serial data distribution would require just one layer and could be done via the RF distribution layer. Unfortunately, there are many obstacles to a solution of this kind. In a fully serial data distribution in time domain, all the control data is concatenated in one data stream and each RF front-end module must extract its own data out of the stream within the available time (less than $10\mu\text{s}$, as mentioned above). Moreover, with data rates as high as seen in the typical figures, data and clock harmonics reach up to X-band where the radar signal is being transmitted. The spectrum is hard to control and the distribution is very sensitive to impedance mismatches, resulting in reflections and degrading signal integrity. Note that the RF distribution layer is optimized for X-band and not for the frequency range that is covered by the main spectral components of this data stream, increasing the risk of the data being distorted. The goal is to find a solution that relieves space by using the RF layer, but there is no interest in making the design or the processing more complex. A serial solution is then discarded and a parallel distribution is evaluated.

Continuing in the time domain, a parallel transmission cannot be considered. All the RF front-end modules receive the same signal via the RF combiner by definition (Figure 1.1) while needing its own specific control data.

It can be concluded that solutions for fully serial and fully parallel data distribution in the time domain are not feasible when the RF combiner is to be used as transmission medium. This leaves a parallel data transmission in the frequency domain as the solution to look for.

To transmit the data in a parallel fashion in the frequency domain, it has to be modulated on a RF carrier with a suitable modulation technique for the total data rate calculated above. OFDM, which is based on the use of a large number of orthogonal modulated carriers, could be a solution. If a high order modulation technique such as M-QAM (M^{th} order Quadrature Amplitude Modulation) is used, OFDM can achieve high data rates within a given bandwidth.

To provide an indication, consider one OFDM carrier assigned to each RF front-end module, i.e. 256 OFDM carriers in total. The OFDM data rate would be of 256x240 bits in $10\mu s$. Using 64-QAM (which represents 6 bits per symbol), 240 bits is transduced into 40 symbols in $10\mu s$, giving a symbol length T_s of $0.25\mu s$. In OFDM, the frequency spacing Δf between the carriers would be $1/T_s = 4\text{MHz}$. As a result, the total bandwidth occupied by the OFDM signal would be $256 \times 4 = 1024\text{MHz}$. This is about twice the bandwidth proposed in "Multi-band OFDM Physical Layer Proposal for IEEE 802.15 Task Group 3a", referred to in [6] and an order of magnitude more than the bandwidth used in common WLAN (Wireless Local Area Network) applications [7]. To relax bandwidth requirements, higher order modulations could be used. Nevertheless, even an order as high as 256-QAM, reducing the number of symbols from 40 to 30, would result on a 768MHz bandwidth for the example assumed above.

Conventional OFDM techniques distribute the total amount of data over all the carriers, and employ receivers which process the entire transmitted bandwidth. OFDMA (Orthogonal Frequency Division Multiple Access) modulates the data for individual users on subsets of the total number of carriers, which fits better with this concept, but still requires receivers which process the entire transmitted spectrum [8]. Thus, using conventional OFDM techniques, each RF front-end module would have to be equipped with a receiver with high speed ADCs (Analogue-to-Digital Converters) and digital signal processing able to process a bandwidth of more than 1 GHz to recover just the 240 bits needed by the RF front-end module. It can be concluded that the conventional OFDM techniques do not provide an effective solution to the technical problem of the control data distribution, since the advantage of eliminating the wiring for control data transport does not outweigh the added complexity in the RF front-end modules.

1.4 Novelties and Main results

A possible solution is an adaptation of the OFDM system which differs from the conventional one in two ways:

1. At the transmit side, the binary data stream for each user is divided into bit-words that can be mapped on a chosen constellation. The constellation points modulate one or a few carriers, which are allocated to that user in an arbitrary, but predefined way;
2. At the receive side, each user employs a receiver with a narrow filter which receives and processes only a small part of the entire OFDM bandwidth.

The difference between the OFDM system developed in this thesis and the conventional OFDM system is explained below for the simple case of one carrier per user at the receiver side.

In the OFDM system of this work, the OFDM principle is used to create K single carrier transmission channels with a frequency spacing Δf , taking advantage of the orthogonality in frequency at the transmitter side to send data simultaneously in time to K single carrier receivers (see Chapter 3 for details).

First, the binary data stream for each of the K receivers is broken up into bit-words that can be mapped on the chosen constellation. This results in K sets of N_w constellation points. Second, the first constellation point of each of the K sets is put on the IFFT (Inverse Fast Fourier Transform) input. The IFFT is performed, resulting in the first time domain symbol of the data stream. The first time domain symbol contains the information of K carriers, modulated with the first constellation point that has to be sent to each of the K receivers. Subsequently, the same operation is performed for the remaining $N_w - 1$ constellation points of each of the K sets. As a result of this mode of operation at the transmitter side, the novel OFDM system modulates the single carrier that is assigned to one user with its constellation points sequentially in time. This is done for all K carriers, resulting in N_w time domain symbols. In other words, the constellation is spread in time and transmitted on one carrier. Each receiver (see Chapter 4 for details) has a narrow filter and demodulates only the single carrier that it is tuned to, by performing the FFT (Fast Fourier Transform) calculation only for the FFT frequency bin in which this carrier is centered. At the output of the single bin FFT, the demodulated constellation points are retrieved sequentially for that user. As a last step, the original bit-words are decoded according to the mapping used at the transmitter side and the data stream is reconstructed.

This simple case can be extended to a case with more than one carrier per receiver, depending on the data rate that is required and the order of the modulation that it was chosen. The orthogonality between the carriers is maintained, and the FFT calculation in the receiver is extended to include more than one frequency bin.

The main difference with existing OFDM(A) systems is that instead of retrieving and processing the entire spectrum, each of these receivers filters and processes just the set of carriers of interest (hence the narrow filter) by tuning the LO to the frequency of that set. This change enables the use of low speed ADCs, resulting in the successful retrieval of data with just a few samples per OFDM symbol. Thus, no high speed signal processing hardware is needed in the receiver.

At the input of the receiver, a band-pass filter may be used to reject signals outside the OFDM bandwidth.

To transport the OFDM signal, the RF combiner is used, providing a wired medium which prevents EMI problems with the RF front-end modules. Furthermore, by sharing the existing RF combiner in the system, the wiring and cabling infrastructure for the data transport can be simplified or removed. This creates space that relieves design constraints on the transport of DC power, RF and clock/synchronization signals.

In Figure 1.6, the general architecture of the phased array is shown again, with the solution implemented. The gain and phase data for all RF front-end modules is provided to the OFDM

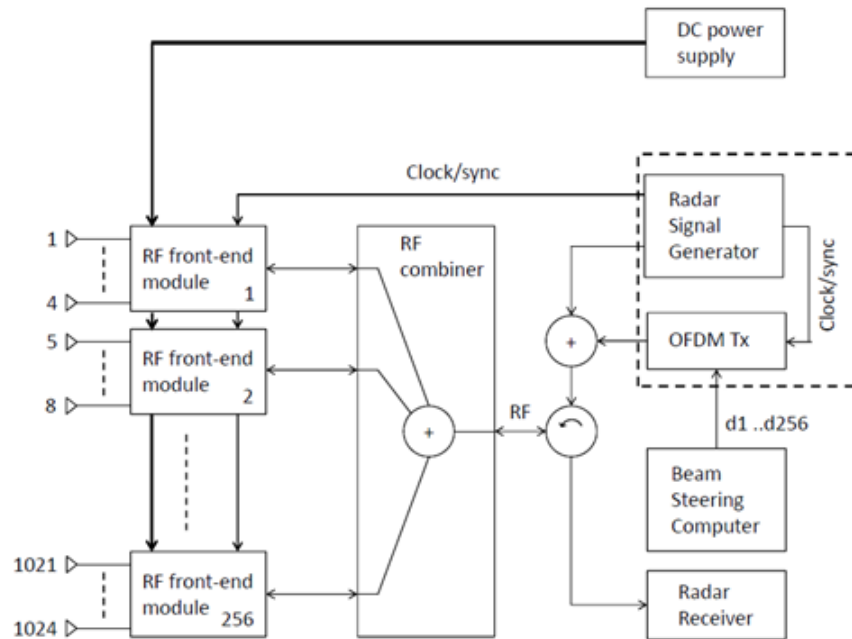


Figure 1.6: General Phased Array Architecture with solution implemented.

Tx, where the data for each RF front-end module is modulated on one or a few predefined carriers of the OFDM signal. The OFDM Tx may be located in the RSG, where the data RF signal is added to the radar RF signal path for distribution to the RF front-end modules via the same RF combiner that is already used as part of the radar RF functionality.

The data RF signal is separated in frequency from the radar RF signals that are transported on the RF combiner to prevent interference. The wiring for the transport of the control data to the RF front-end modules is removed from the system. The distribution of the clock/synchronization signal remains, and may be used to support time synchronization.

In Figure 1.7 the implementation of the solution in the RF front-end modules is shown. In each RF front-end module an OFDM Rx is built-in to receive the OFDM signal, which is taken from the common input/output port using a directional coupler. Each OFDM Rx is centered at a different frequency by means of the tunable LO and is assigned a different set of carriers of the OFDM spectrum. The receiver only demodulates the set of carriers that is assigned to the RF front-end module. The OFDM Rx provides the demodulated control data to the T/R-channels.

The developed system features a fully parallel and simultaneous data transport to all RF front-end modules, equivalent with the conventional solution but with less wiring. This reduces cost and weight of the infrastructure, creates space and alleviates design constraints, allowing a more optimal design of the essential system functionalities.

The solution realizes a data transport capacity of several Gbits/s within a limited part of the frequency spectrum, which is well controlled with techniques known for OFDM(A) systems. This enables the coexistence of the data transport with the other RF signals in the network

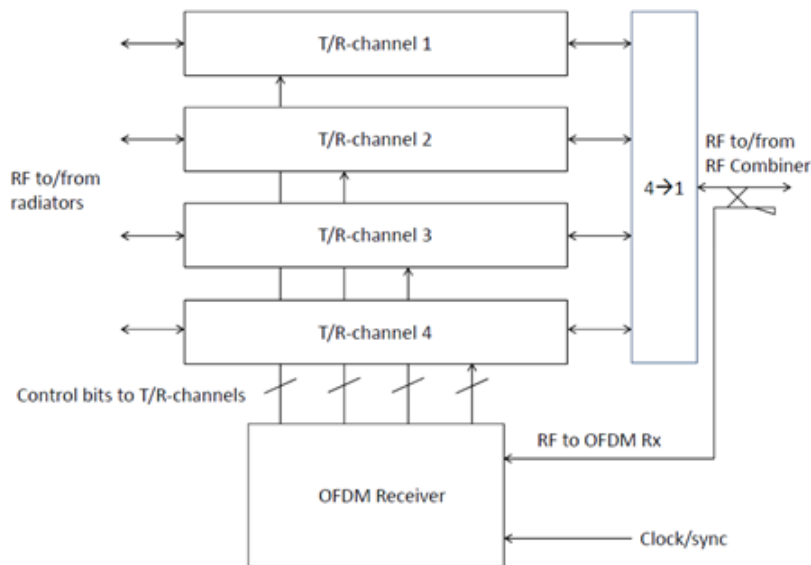


Figure 1.7: Block diagram of a RF front-end model with solution implemented.

and makes it a suitable data transport technique for use in an EMI sensitive environment.

The use of OFDM results in a data transmission that is very tolerant with regard to imperfections of the RF network. This allows the optimization of the RF network for the frequencies that are used in the essential function of the system, while still being able to transport data at another frequency where the RF network is non-optimal.

Even though the scope of this thesis was on phased array RADARs, the presented OFDM system is flexible in a way that it can be used in one-to-multipoint applications, multipoint-to-one applications, and in general for RF sensing systems with distributed RF front-end modules that are connected to a network for transport of RF signals. It is also adaptable to the specific area of application in terms of the number of carriers, the used modulation per receiver depending on the needed data rate (each set of carriers per receiver may be modulated using a different constellation/modulation technique) and the transmitted power per carrier. Plus, the solution allows for different time length messages on each receiver by just nulling the carriers of the users that already have all the information needed or that do not need information at all without affecting the time domain symbol or degrading performance.

Experimental results show that there is no loss in performance when compared to standard OFDM implementations (refer to Chapter 5).

1.5 Outline of the thesis

In Chapter 2, a closer look is taken into Orthogonal Frequency Division Multiplexing (OFDM) as a modulation technique. The conventional transmission and reception schemes are presented. Several spectrum shaping techniques are studied to keep the signal from interfering with the radar RF pulses. The sensitiveness of the OFDM signal to time and frequency synchronization is discussed and state-of-art synchronization algorithms are described. The SER expression for an OFDM signal as function of the system parameters is derived. To conclude, the effect of phase noise and other RF impairments like IQ imbalance and the amplifier's non linearities are shown, as well as their impact on the SER.

A detailed overview of the transmitter path is provided on Chapter 3. Special attention is taken on the implemented algorithms for reduction of the OOB radiation. An estimate of the PAPR and its impact on the amplifier specifications is discussed. The results presented in this section were achieved with the development of a general MATLAB[®]¹ module to generate OFDM signals with adjustable parameters. An experimental setup is put together to compare the real spectrum against the one MATLAB[®] outputs. Measurement results are presented as closure.

Chapter 4 focus on the receiver path. A mathematical overview is made, giving special attention to the DFT matrix transformations, consequence of the new approach. These transformations result in a number of constraints that reflect on the various receiver blocks, from the downconversion to the ADC. Each block soft spot is explained in detail. One of the biggest challenges of the receiver chain is time and frequency synchronization, which will be discussed in Chapter 5 for the closed cycle. The experimental setup used for validation is described, including equipment limitations and a MATLAB[®] module for demodulation.

The final step for proof of concept is to close the cycle and put together on the test setup the single parts mentioned before. Chapter 5 is mainly divided in three sections: solutions implemented for time and frequency synchronization, simulations of the phased array performance to determine minimum required SER and SER measurements of the experimental setup. To conclude, it is determined whether OFDM modulation is a viable implementation or not to satisfy the overall system requirements.

Every choice, from the way the data is organized prior to the carrier assignment to the sampling rate used on the ADC, is a compromise. Every decision hides a trade-off. This means there are a few places in the chain that may be chosen for optimization on the sacrifice of others.

Chapter 6 enclosures the general conclusions and discussion of the work as a whole, as well as some remarks for the next step — hardware implementation and optimization.

The datasheet of the receiver chip used in the test setup may be found in the appendices section.

¹MATLAB[®] is a U.S. registered trademark of The Mathworks Inc.

Chapter 2

Orthogonal Frequency Division Multiplexing (OFDM)

The idea of transmission of multiple waveforms by a multiplexing operation in the frequency domain goes back for more than a century. Early telegraph systems would carry low data rate signals by placing the different carrier frequencies over a wide bandwidth, such that the signals spectra would not overlap and were easily filtered and recovered at the receive side. The spacing between the channels ensured that there would be no interference between the carriers. On the down side, spectral efficiency was low. The first idea to increase the data rate was, instead of transmitting different messages on each channel, to transmit pieces of the same message spread on the frequency domain, but simultaneously in time. Still, this solution would have a lower spectral efficiency than a single wideband channel due to the guard bands between carriers. Research at the time was focused on finding out new ways of making better use of the spectrum. The first OFDM scheme was introduced by Robert W. Chang in 1966 [9].

This chapter begins by giving the OFDM mathematical concept and by describing how modulation and demodulation are conventionally done. The remaining sections will focus on the drawbacks and sensitive points of the technique.

One of the disadvantages found in OFDM is the high out-of-band radiation that the spectrum holds. This is a serious issue when the signal is on a shared spectrum and several techniques to suppress it will be discussed in Section 3.1.

The OFDM concept core lies in the equally spacing of carriers over the available bandwidth, being the key word to ensure orthogonality *equally*. If, due to imperfections of the system or channel effects, the receiver is not tuned to the exact transmitted frequency or if the first sample is not the first sample of the transmitted symbol, the recovered information is distorted. Section 2.4 explains the causes and the most common synchronization methods to mitigate these effects.

All communication systems are designed to satisfy certain requirements, to achieve a desired performance. An usual figure to measure whether the system is on the right track is the SER. The SER depends on the chosen modulation for the individual carriers, on the number

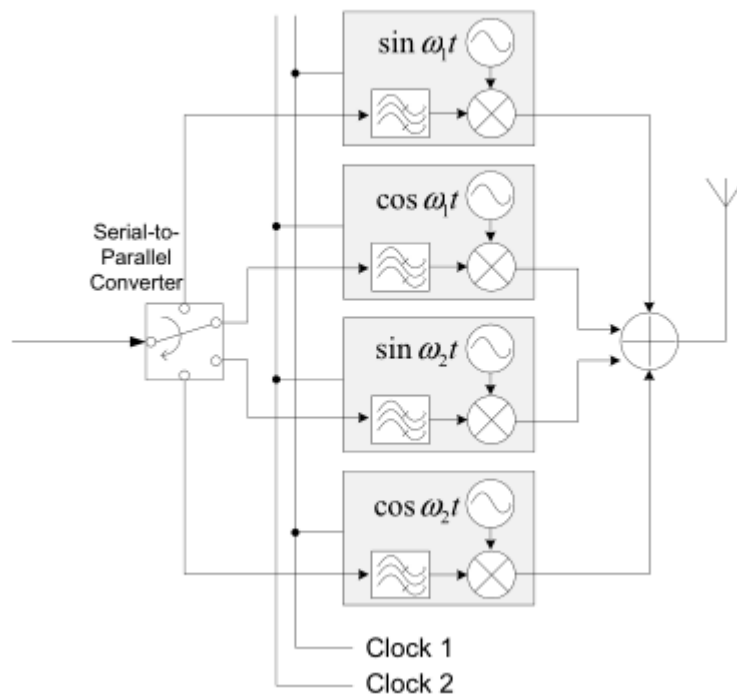


Figure 2.1: OFDM scheme proposed by Chang.

of carriers used and on the existence or not of guard intervals, both in frequency and time domain. Several RF impairments as well as synchronization residual offsets have an impact on this figure, driving the real value away from the ideal one. How each of this impairments affects the SER and how they should be taken into account will be described in Section 2.5.

2.1 OFDM Concept

The first OFDM scheme suggested by Chang was based on the transmission of signals simultaneously in time over a given limited bandwidth without ICI (Inter Carrier Interference) and ISI (Inter Symbol Interference). To do so, he divides the channel into several overlapping narrowband sub-channels of equal width Δf and uses an analogue implementation of the Fourier transform to modulate the rectangular pulses (Figure 2.1).

Each carrier has an integer number of cycles within a given interval $T_s = \frac{1}{\Delta f}$ and the number of cycles by which each adjacent carrier differs is exactly one. Since each carrier has a sinc shape spectrum (note that the Fourier transform of a rectangular pulse is a sinc function), the relation between the number of cycles ensures that, at the peak spectral response of each of them, all the others are identically zero — the system is orthogonal in the frequency domain (Figure 2.2).

Even though Chang's contribution was of major importance, the fact that a bank of filters is needed both on the transmit and the receive side makes it an unsuitable one. As the

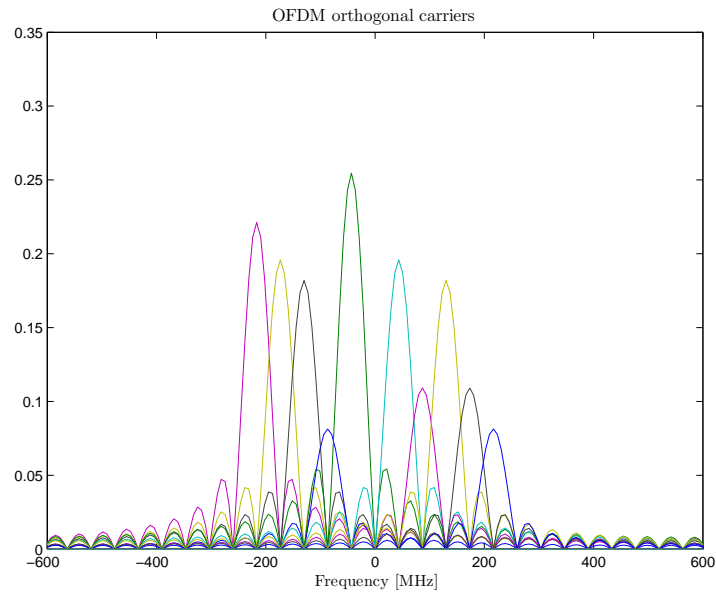


Figure 2.2: Overlapping orthogonal OFDM carriers in the frequency domain, an example for 10 carriers.

number of carriers becomes larger, the synchronization and coherent demodulation becomes unpractical, both due to hardware cost and oscillator drift in the analog components. The orthogonality between the carriers is not maintained and ICI occurrence increases.

The second major contribution to this field was then the one from Weinstein and Ebert in 1971 [10], who came up with the idea of modulating the OFDM carrier's rectangular pulses with an IDFT/DFT to replace the bank of filters. By performing an IDFT, the OFDM carriers are all harmonics of the same fundamental frequency — all of them have an integer number of cycles within T_s and differ by one period like in Chang's scheme. Moreover, this operation may be performed in an efficient way by means of an IFFT/FFT, reducing the number of arithmetic operations from N_{DFT}^2 to $N_{DFT} \log(N_{DFT})$. This is the current implementation in nowadays applications.

Let T_s be the time length of one OFDM symbol, Δf the spacing between carriers and K the total number of carriers. The first step to begin with the generation of the OFDM time domain symbol is to choose a suitable modulation for the individual carriers, which depends on the data rate required by the system to be designed. The chosen modulation and its associated constellation define the set of complex values used to map the binary data stream. Let $\mathbf{x} \in \mathbb{C}$ be the string of complex values to be transmitted, i.e. the amplitudes and phases modulating the OFDM carriers. The IDFT output \mathbf{s} is

$$\mathbf{s} = \mathbf{x} e^{i2\pi \mathbf{k} \frac{n}{N_{IDFT}}} \quad (2.1)$$

Each time sample $n \in [0, N_{IDFT} - 1]$ is determined by the sum of \mathbf{x} over $k \in [0, K]$, i.e. $s(n)$ is the sum of the amplitudes and phases of all K carriers at that point in time n . N_{IDFT} will be the total number of time domain samples on the output of the IDFT \mathbf{s} and is determined by the number of spectral components. $N_{IFFT} = K$ is the critical sampling rate according to the Nyquist sampling criterion. Zero padding in frequency/time domain is used to increase

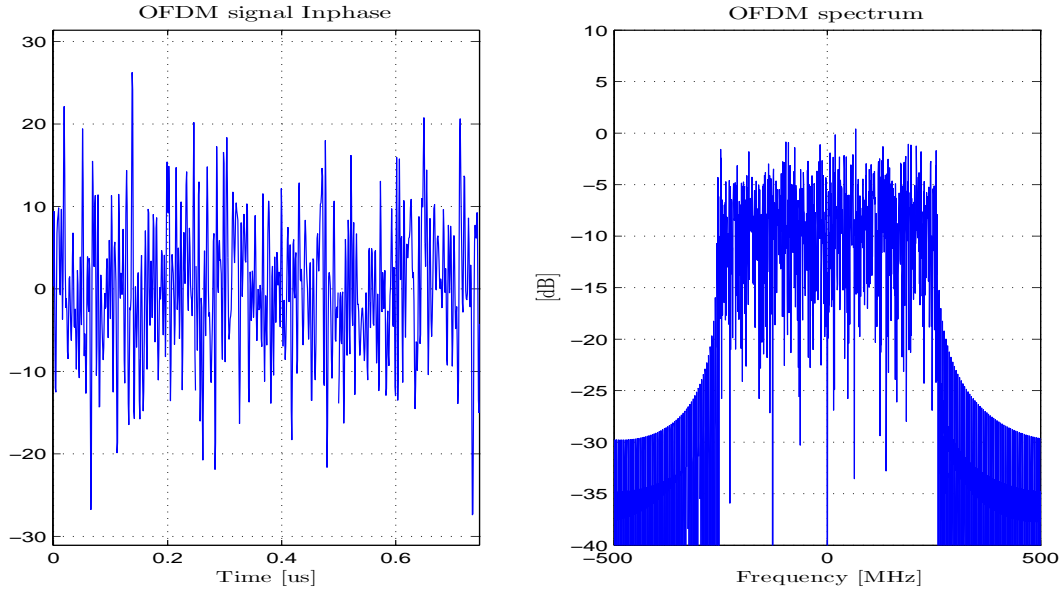


Figure 2.3: Time domain OFDM signal (left) and its spectrum (right).

resolution in time/frequency domain. To increase the resolution, a string of zeros is added to \mathbf{x} either at the beginning, end or middle ($N_{IDFT} > K$). The resulting signal \mathbf{s} is as if interpolated in the time domain. Also, when computing an IFFT instead of an IDFT, zero padding is often used to create a number of frequency samples that is a power of 2, reducing the algorithm computation time.

For demodulation, a DFT is performed over the received time domain signal, \mathbf{r} . To correctly recover the carriers' amplitudes and phases, the DFT window must be exactly aligned with the symbol and cover its entire time length T_s . The DFT output \mathbf{y} is

$$\mathbf{y} = \frac{1}{N_{DFT}} \mathbf{r} e^{-i2\pi \mathbf{k} \frac{\mathbf{n}}{N_{DFT}}} \quad (2.2)$$

Each complex value modulating carrier k on the transmit side is recovered by the sum of \mathbf{r} over \mathbf{n} , i.e. the complex value $y(k)$ is the sum of all the time samples N_{IDFT} of the time signal \mathbf{r} of that frequency k . To recover the complex values used to modulate all the K carriers, N_{DFT} must be at least equal to N_{IDFT} . \mathbf{y} will be a vector of length N_{DFT} with all the K complex values.

Orthogonality between OFDM carriers may be shown by just replacing Equation 2.1 into Equation 2.2. For the simplest case of $N_{DFT} = N_{IDFT} = N$,

$$y(k) = \mathbf{x} e^{-i2\pi(\mathbf{m}-k)\frac{\mathbf{n}}{N}} \quad (2.3)$$

The output of the DFT $y(k)$ is zero when $m \neq k$, i.e. when the exponential term has an integer number of cycles over T_s . When looking at carrier k , all the other carriers are orthogonal to it and do not contribute to the sum over time. Figure 2.3 shows an OFDM signal in time and frequency domain.

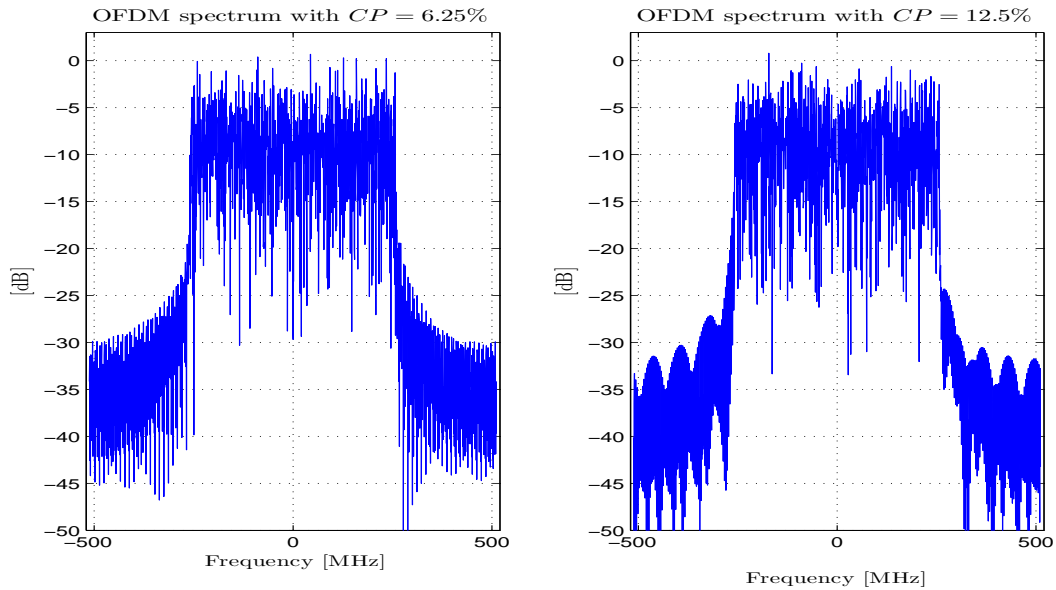


Figure 2.4: OFDM spectrum with 6.25% (left) and 12.5% (right) cyclic prefix.

The Cyclic Prefix — a guard interval in time domain

As mentioned before, to recover the data without distortion, the DFT window should be perfectly aligned with the time domain symbol. In real channels, this almost never happens. Either due to the CIR (Channel Impulse Response), frequency selectivity or time dispersion, the OFDM symbol arrives at the receiver with a certain delay. For instance, in the case of a frequency selective channel, carriers at different frequencies may arrive with different delays. In wireless channels, the received signal is a sum of multiple signals from multiple paths (reflections, scattering, diffraction) with multiple delays; the channel has a certain delay spread. In all cases, parts of the original OFDM symbol appear at the receiver outside the DFT window and neighboring symbols appear inside it.

The phenomenon is known as ISI and it greatly degrades the system performance. As a form of compensation, a guard interval T_{CP} (that should be larger than the channel delay) is added to the beginning or end of the time domain symbol to account for these effects — symbol length is now $T_s + T_{CP}$. To maintain the orthogonality between the carriers, the prefix/postfix is a cyclic extension of the symbol, such that all carriers remain with the same frequency and amplitude. Depending on the prefix/postfix length, the carrier's phase may or not be the same. If not the same, it is translated as a rotation in the constellation and is easily corrected for.

Note that even though the symbol is extended, the DFT window length does not change — the symbol rate is reduced, but the orthogonality is maintained. The ability to trade effective data rate for dispersion robustness is one of the strongest points of OFDM. Due to the extension of the time domain symbols, the carrier's sinc shape is narrower. Narrower sinc shapes mean less overlapping between the carriers, which decreases the out of band radiation. On the other hand, slimmer sines behave as if there were dips between them, which gives the

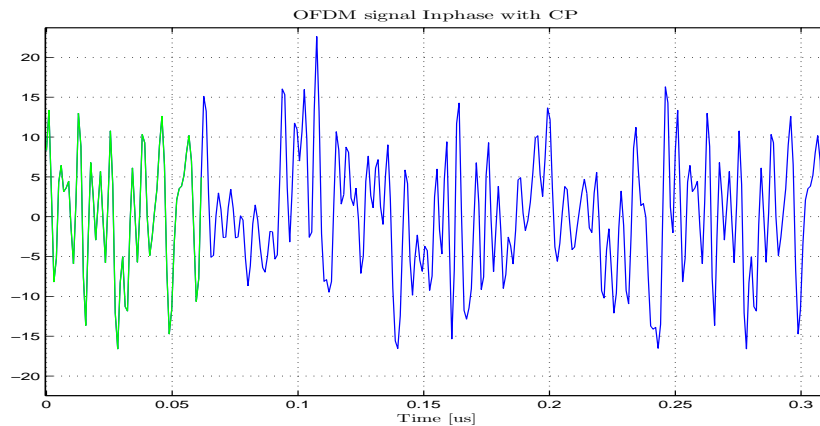


Figure 2.5: Example of a time domain OFDM symbol with CP (in green).

impression of ripple on the OFDM spectrum (Figure 2.4).

The CP (Cyclic Prefix/Postfix) is added in the transmitter chain after computing the IDFT. Figure 2.5 shows an OFDM time domain symbol with cyclic prefix.

2.2 Out of Band Radiation

Practical systems, while transmitting, should comply to the spectral mask requirements as defined by FCC (Federal Communications Commission) / ETSI (European Telecommunications Standards Institute). To fulfill the requirements of a such a mask, it is often necessary to reduce the sidelobes — as seen before, the OOB (Out of Band) radiation can be quite high. A lot of research has been dedicated recently to this subject due to the increasing usage of CR (Cognitive Radio) systems. CR systems are an extension of SDR (Software Defined Radio), adding environment sensing, change tracking and reaction upon findings [11]. It makes use of unused licensed spectrum for its transmission, ensuring that the system performance of the primary user as well as its own is not impacted. Since the spectrum "free" window can be very narrow, it is of huge importance to decrease the OOB radiation as much as possible to prevent interference.

One of the characteristics of the system to which this thesis work applies is that the RF network is shared, which means that the OFDM signal will be transmitted on the same channel as the RADAR signal and (possibly) the clock/synchronization channel. For this reason, it is of high interest to reduce the out of band radiation without adding much complexity to the transmit/receive chain. In this section, several OOB radiation reduction techniques will be briefly described.

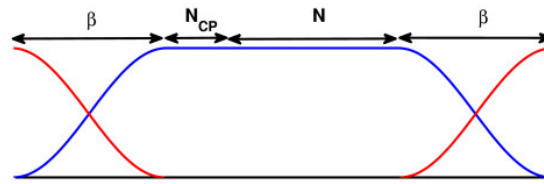


Figure 2.6: Windowed OFDM symbols.

State-of-art techniques for reduction of OOB radiation

The simplest method to achieve lower sidelobe power is to reserve a few edge carriers to serve as spectral buffer, i.e. a GB (Guard Band) of nulled carriers. In spite of being a simple and low complex solution, it is not very spectral efficient – null carriers on the sides are wasted spectrum – and the reduction of OOB radiation is not significant.

One of the reasons OFDM has such a high OOB radiation is the jump between time domain symbols. As seen in Section 2.1, the starting phase of the OFDM signal is the sum of the starting phases of all carriers. Each OFDM symbol has a different starting phase that depends on the complex values the carriers are modulated with. Since there is an integer number of cycles of each carrier within T_s , the end and starting phase of the OFDM symbol is the same and the phase jumps from one symbol to the next can be quite high. This kind of rapid/steep transitions from symbol to symbol translate into high frequency spectral components, increasing the OOB radiation.

One way of suppressing the side band radiation is to smooth the symbol transitions in time domain with what is called a window. For different window descriptions, refer to [12].

Windowing is usually applied to the OFDM's CP time domain samples. The time domain symbol of duration $N + N_{CP}$ (case $N_{DFT} = N_{IDFT} = N$), where N_{CP} is the length in samples of the CP, is cyclically extended with β samples (Figure 2.6).

Consecutive symbols overlapping of β samples yield an effective symbol duration of $N + N_{CP} + \beta$ samples. For the same kind of window, the smoothness of the transition is dictated by β — the larger it is, the smoother the transition. Note that, as β is increased, the symbol rate is reduced — there is no useful information in these samples. The choice of β / reduced OOB radiation is a trade-off.

Advantages are that the chosen window (shape of the transition region) and β value can be dynamically altered and that it is a low complexity method, easy to combine with other OOB radiation reduction techniques.

Another method is the MSC (Multiple Sequence Choice). which is based on the clever mapping of the data to be transmitted onto the OFDM carriers. Multiple mapping scenarios are generated and their sidelobe power is computed. The carrier mapping sequence that accomplishes maximum OOB radiation reduction is chosen. To retrieve the original data at the receive side, de-mapping of the received sequence into the original one is required. To be able to de-map the sequence, the receiver needs to know which one was used on the transmit side — an identification number has to be signalled. The sidelobe suppression achieved with

this method is significant. On the down side, it adds a lot of complexity on the transmit side and slightly reduces throughput due to the signalling index.

Several ways of reducing implementation complexity exist, either by reducing the set of possible sequences or reducing the optimization region. For example, since the carriers responsible for most of the sidelobe power are the ones on the edges, some methods based on the MSC concept focus on the optimization the data arrangement of those ones alone.

For further detail on how this technique is implemented, refer to [13].

Continuing along the methods based on spectrum arrangement, there is another approach of which the essence is to weigh the carriers in such a way that the OOB radiation level is minimized in a certain optimization range. The weighting is done by multiplying the data carriers by optimized real weighting coefficients [14]. At the receiver, the symbols may be viewed as distorted, specially for high values of weighting coefficients. To mitigate this, the authors suggest that a constraint is imposed to the weights.

An advantage of CW (Carrier Weighting) over MSC is that the receiver does not need any additional information to retrieve the original data, so throughput is maintained. BER, however, suffers some loss, since different carriers receive different amounts of power.

As discussed in the MSC technique, different sequence mapping results in different OOB radiation. In [15], a novel method for sidelobe suppression is introduced that once more takes advantage of this characteristic. This technique, instead of re-mapping the sequence, expands the chosen constellation in such a way that the possible mapping of a certain bit word into complex value is no longer a 1 : 1 relation. By doing so, the authors reduce the sidelobe power due to the mapping randomness. The plus point is that the receiver does not need any extra information. The minus is that, using a higher order constellation, the distance between the points is smaller, decreasing the BER performance.

One more approach that tries to shape the OFDM spectrum is the one which adds the so-called cancellation carriers (CC) [1]. CC are carriers appended on both sides of the spectrum to cancel out the sidelobes of the data carriers (see Figure 2.7). The complex values modulating these carriers are the solution of a linear least square problem.

Let \mathbf{s} be the frequency samples of the data carriers of the original signal in the optimization range, \mathbf{C} be the matrix of the frequency samples of the n_{CC} cancellation carriers in the optimization range and \mathbf{g} be the complex weighting factors (modulating complex values) of the CCs. The CCs algorithm is based on the finding of

$$\min_g \|\mathbf{s} + \mathbf{C}\mathbf{g}\|^2 \quad \text{subject to} \quad \|\mathbf{g}\|^2 \leq \alpha \quad (2.4)$$

, i.e. finding \mathbf{g} that minimizes the sum of the squared residuals $(\mathbf{s} + \mathbf{C}\mathbf{g}) - \|\cdot\|^2$ is the 2-norm. α is an added constraint to limit the power used in the CCs' modulation. With a generalized SVD (Singular Value Decomposition), the resulting optimization problem is reduced to a linear system.

This method is rather simple and intuitive and can achieve around 15/20dB of OOB radiation reduction. On the other hand, it slightly degrades the system performance by putting some of the transmitted power on the CCs and increasing the PAPR (Peak to Average Power Ratio). PAPR impact is controlled by α : when α is large, more room power is given to the CCs to

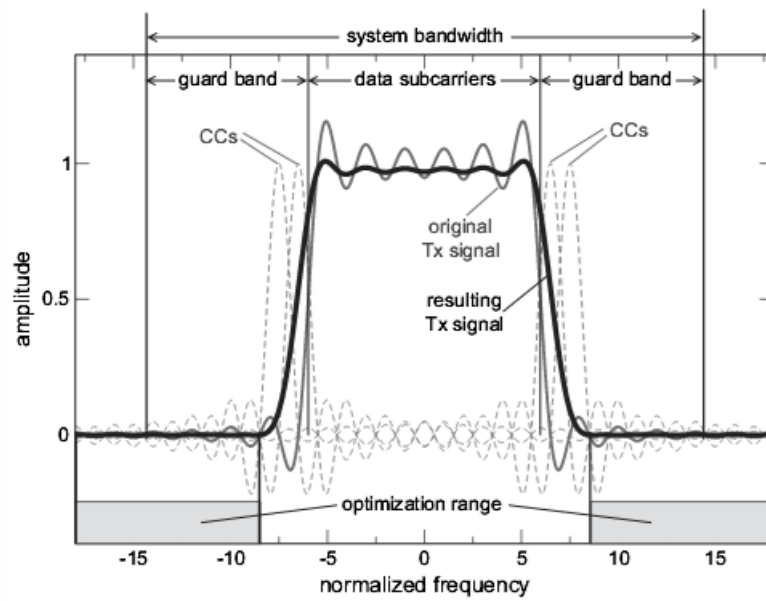


Figure 2.7: Concept of the cancellation carriers algorithm. (figure taken from [1])

cancel out the OFDM sidelobes, increasing the PAPR.

More detail on how this technique is implemented will be given on Chapter 3.

Most OFDM systems with out of band radiation limitations do not use just one of the above described methods. By implementing a combined solution, it is easy to find balance and reduce the negative side effects of the separate parts. Common examples are the combination of CCs with windowing [16], CCs with null carriers [17], CCs with constellation expansion [18], etc.. Note how data dependent and non data dependent methods are paired together as a solution.

2.3 Symbol Error Rate (SER)

Before introducing the definition of SER and its particular expression for an OFDM system, two other quantities must be clearly defined in advance: SNR (Signal to Noise Ratio) and IBEND (Information Bit-Energy-to-Noise Density), E_b/N_0 .

The universally accepted definition for SNR is the ratio of the signal power (P_S) defined in a specified bandwidth, over the locally present noise power (P_N) measured in the same bandwidth [19]. Since both powers are defined in a specific bandwidth, SNR may be used to compare systems with different bands and the definition holds for different filter types. As it is a ratio of identic units, SNR is dimensionless and can be expressed in decibels:

$$snr = \frac{P_S}{P_N} \quad \text{and, in decibels,} \quad SNR = 10 \log_{10}(snr) \text{ dB} \quad (2.5)$$

One should not forget that this definition assumes an ideal filter, with an infinite slope. Powers must be adjusted according to the filter shape.

SNR is often used to assess channel quality, but it is not enough to comment on a digital system performance. Being a ratio of powers, it averages the communication system for an *infinite* time. Hence, another metric working with quantized, *finite* time intervals is needed. IBEND plays this role. Even though it is related to SNR and they are often mistaken as being the same, they are not. The differences begin with the fact that *ibend* is not dependent on bandwidth. As bandwidth is increased, *snr* will decrease while *ibend* will not. The relationship between *snr* and *ibend* is

$$ibend = \frac{E_b}{N_0} \equiv \frac{P_S T_b}{\frac{P_N}{B}} = snr T_b B \quad (2.6)$$

As *snr*, it is also a dimensionless ratio, so it may be expressed in decibels as well. IBEND is then defined as the ratio between the signal power over a period of time and the ratio of the channel noise power over a limited bandwidth. For an uncoded binary signal, *ibend* is related to *snr* by the bandwidth efficiency. To compute information *symbol-energy-to-noise density* (*isend*), where a symbol has $\log_2(M)$ bits, $isend = \log_2(M) \cdot ibend$.

SNR and IBEND defined, it is now possible to start looking at OFDM's SER. Forgetting for a moment how the information is mapped and spread over frequency to increase the data rate for a single receiver, an OFDM system may be seen as nothing more than multiple single carrier systems, whose carriers' frequencies are orthogonal between themselves. Thus, in the simplest case, the OFDM symbol error rate is the symbol error rate of the modulation scheme chosen for the individual carriers.

Later development changed the way the transmitted signal is generated and afterwards demodulated. The use of an IDFT spreads the energy over the spectrum that is later recovered with the DFT computation on the receiver side. This balance is maintained as long as the critical sampling rate is used, $N_{IDFT} = N_{DFT}$. If, either due to zero-padding, null carriers, CCs or any other optimization method, non data carriers are processed in the IDFT, the gain equilibrium is disturbed. This disturbance comes from the fact of the processed bandwidth being larger than the OFDM bandwidth, decreasing *snr*. Since the SER of a single carrier system depends on *isend* that depends on *snr*, system performance is slightly affected. Equation 2.6 shows this dependency on bandwidth, as well as symbol time. Following the same line of thought, the use of a cyclic prefix/postfix, windowing or any other method that extends symbol duration, will also have an impact on the SER. Adapting Equation 2.6 to an OFDM system with symbol extension T_{CP} , K carriers and $\log_2(M)$ bits per carrier symbol,

$$SER\left(\frac{E_S}{N_0}\right) \quad \text{with} \quad \frac{E_S}{N_0} = \log_2(M) \frac{P_S}{P_N} T_S B = \log_2(M) \cdot snr \cdot \left(\frac{T_S}{T_S + T_{CP}}\right) \left(\frac{K}{N_{IDFT}}\right) \quad (2.7)$$

SER is a function of *isend*, which depends on the modulation chosen, and *isend* depends on the OFDM system characteristics.

2.4 Synchronization on OFDM signals

Section 2.1 described how a OFDM signal is modulated, demodulated and the principle it is based on. For the data to be properly recovered, the carriers must be seen by the receiver as orthogonal to each other and the time samples summation of each carrier over T_S must go around the entire complex circle (must be equal to 2π). This makes OFDM systems very sensitive to frequency and time offsets: if the DFT window is not precisely aligned with the time domain symbol or if the receiver's LO (Local Oscillator) is not exactly tuned to the transmitter's, the received information is distorted.

Synchronization errors may be divided in terms of three effects: carrier error, clock error and sampling time error [20].

- Carrier error results from drifting in the LO; there is a difference between the receiver's LO and the transmitter's central frequency. The effect of this offset is displacement of the OFDM spectrum as a whole, shifting all carriers in frequency in a equal manner. If all carriers are shifted by a multiple of the carrier spacing δf , the DFT exponential term will still sum up to zero. Nevertheless, most of the times this is not the case and the orthogonality requirement is no longer fulfilled. The OFDM system suffers from ICI and the signal amplitude is reduced. Since the OFDM carriers are designed to be closely spaced, the tolerable frequency offset is a very small fraction of the total bandwidth, making it very difficult to keep the LO drift acceptable.
- Clock error, as the name suggests, is the difference between the transmitter's and receiver's sampling clock. The receiver's sampling clock depends on the carrier error mentioned before, so these two errors are usually associated and treated as one single offset in the frequency domain.
- Sampling time error is the difference between the sampling time in the receiver and the actual sampling time. The placement of the DFT window and, as a consequence, the existence or not of ISI, is directly related to this error. Symbol delay is usually treated as a separate event from the two above and called timing offset.

Let ε be the frequency offset (ratio of the actual frequency offset and Δf , the carrier spacing) and δ be the timing offset (ratio of the actual time offset and the sampling period). The received symbol \mathbf{y} (Equation 2.2) is,

$$\mathbf{y} = \frac{1}{N_{DFT}} \mathbf{r} e^{-i2\pi(\mathbf{k}+\varepsilon)\frac{(\mathbf{n}+\delta)}{N_{DFT}}} \quad (2.8)$$

Both time and frequency offsets translate into phase rotations — $\varepsilon\delta$ that is the same for all carriers and constant over time, $n\varepsilon$ that varies with the time sample and $k\delta$ that varies with the carrier index — and a spread of the constellation points similar to AWGN (Additive White Gaussian Noise) due to ICI. If $\delta \geq 0$ and a CP was appended to the symbol in the transmitter side, the received constellation is rotated, but there is no ISI. If, however, $\delta < 0$, the receiver is placing the DFT window over two different symbols and ISI is observed. It should be noted that the main role of the CP is to account for channel delays and multipath

and not to relax time synchronization. Timing offset does not degrade the system performance if kept within the CP, but must always be estimated and corrected for. The timing synchronizer requirement is thus determined by the number of samples the CP exceeds the CIR. On the frequency domain, carrier performance decreases as the carrier index increases — carriers further away from the central frequency suffer a higher impact from the synchronization offset [6]. Power distribution schemes over the OFDM carriers are often used to mitigate this behavior.

To design an OFDM system with good performance, the synchronization step cannot be neglected. Several synchronization techniques to estimate and correct these offsets are available in literature and will be described next.

Time & Frequency Synchronization Techniques

A synchronized OFDM system is vital. Synchronization techniques may be divided in two major groups: data aided and non data aided (also known as blind methods). Even inside those two, there are techniques that are only able to synchronize in the time/frequency domain and need to be combined with other techniques to get a fully synchronized system and techniques that are able to synchronize on both domains with a single process.

Moose's algorithm assumes that the symbol timing is known and uses a repeated data symbol to estimate the carrier frequency offset [21]. By transmitting the same data symbol multiple times, the author determines the frequency offset by comparing the carrier's phase shifts between symbols. To do so, a MLE (Maximum Likelihood Estimate) algorithm is used. The maximum estimate is limited by the MLE algorithm to $0.5\Delta f$. Moose describes a way of increasing this range by shortening the data symbol time, but this only works up to some point. As the symbol becomes shorter, the number of samples per symbol to average also decreases and the estimate is not as good. Besides, the symbol must be kept longer than the channel delay spread to get an undistorted estimation — the algorithm range is bounded by the channel characteristics.

A very simple and intuitive algorithm is introduced by Nogami and Nagashima in 1995 [22]. Once more, it assumes that the symbol timing is known and uses a null symbol to find the carrier frequency offset and the sampling period. The drop in received power is detected and the estimation is done in the frequency domain by applying a Hanning window and taking the FFT. PN (Pseudo Noise) sequences are used to widen the acquisition range. This algorithm fails for burst transmission where it would be very hard (if not impossible) to distinguish between the null symbol and the idle period.

Van de Beek's algorithm falls on the non data aided or blind methods. The author uses the already existent CP on the time domain symbol to estimate carrier and timing offset. The method is very simple and it can be implemented with just a correlator and a peak detector. Remember that the CP is a copy of the end of the time domain symbol placed in its front. The autocorrelation of the OFDM symbol will output a peak at the end of the CP, giving the sample in which the data symbol starts.

Schmidl and Cox developed an algorithm for both time and frequency estimation [23]. The acquisition is done in two steps with the use of a two-symbol training sequence; the first step gives the symbol timing and a coarse frequency offset estimate (phase shifts $< \pi$) and the second step is for fine frequency offset estimate (phase shifts $> \pi$ need to be corrected in two steps).

The first training symbol \mathbf{s}_1 transmits a PN sequence on the even frequencies, resulting in a time domain symbol with two identical halves:

$$\mathbf{s}_1 = [\mathbf{a}_L \ \mathbf{a}_L] \quad (2.9)$$

The training symbol is not mistaken with the data symbols which must contain odd frequencies as well. The two identical halves will be unchanged by the channel, except for a phase shift due to the carrier frequency offset. If the conjugate of a sample from the first half is multiplied by the corresponding sample from the second half, the channel effect is canceled out and only the frequency shift remains. At the beginning of the transmission where this symbol is placed, the products of these pair of samples will have approximately the same phase, so the magnitude of the sum will be large. The timing metric M for timing estimation is defined by the sum of the pair of products normalized to the received energy in the second half-symbol (Equation 2.10).

$$M(d) = \frac{\left| \sum_{m=0}^{L-1} r_{d+m}^* r_{d+m+L} \right|^2}{\left(\sum_{m=0}^{L-1} |r_{m+d+L}|^2 \right)^2} = \frac{|P(d)|^2}{R(d)^2} \quad (2.10)$$

Where L is the number of complex samples in one half-symbol (excluding the CP), d is the time index of the first sample in a window of $2L$ samples and m is the index responsible for sliding the window in time as the receiver searches for the first training symbol. The timing metric peak values, where the sum values is larger, determines the beginning of the first training symbol. The timing metric will have a plateau with length equal to the number of samples of the CP minus the CIR. This plateau leads to some uncertainty as to the starting point of the training symbol and is one of the main drawbacks of the algorithm. Another disadvantage is that the peak is not very sharp.

$$P(d+1) = P(d) + (r_{d+L}^* r_{d+2L}) - (r_d^* r_{d+L}) \quad (2.11)$$

The adjacent values difference is determine by $(r_{d+L}^* r_{d+2L}) - (r_d^* r_{d+L})$, which is a rather small value. The values near M 's peak do not reduce fast enough to make it sharp. The coarse frequency offset may be estimated by the phase of the timing metric. If the phase offset is smaller than π , the even frequencies of the second training symbol are not needed.

After Schmidl and Cox, several algorithms base on the same principle – finding the highest correlation point between two repeated sample sequences – were developed to improve its shortcomings. Park's algorithm [24] uses a training symbol that is divided in four identical parts instead of two:

$$\mathbf{s}_1 = [\mathbf{a}_{L/2} \ \mathbf{b}_{L/2} \ \mathbf{a}_{L/2}^* \ \mathbf{b}_{L/2}^*] \quad (2.12)$$

Where \mathbf{b} is symmetric of \mathbf{a} . Even though Park's method gives a much sharper timing metric peak, it needs a synccenter in the training symbol or the maximum cannot be reached. Another drawback is the existence of smaller peaks on the sides of the main one, which may result in wrong peak detection and, consequently, wrong time offset estimation.

In [25], two algorithms are proposed; one to improve Schmidl and Cox's plateau and another one to eliminate Park's side peaks. A comparison of all 4 methods is presented. It is interesting to see that, even with the plateau, Schmidl and Cox's method is the one with better performance for lower SNRs.

These algorithms use a PN sequence spread over frequency, which results in a large PAPR due to the large number of carriers involved. The nonlinear distortion in the amplifier, degrades the performance of the synchronization. As an attempt to overcome this problem, Czylwik proposed an algorithm that uses a constant envelope preamble [26], but the performance is not satisfactory and the methods above described cannot be implemented, since it is not possible to choose the data on the carriers of the constant envelope. Ren reuses the constant envelope idea, proposing a weighting of the preamble with a PN sequence [27]. The constant envelope preamble is generated from the DFT of a CAZAC sequence (more details about the properties of this class of sequences will be given in Chapter 4) and may be described as

$$X_{preamble} = [x_0 x_1 \dots x_{2L-1}] \quad (2.13)$$

x_i are the samples of the preamble in time domain and satisfy $x_i = x_{i+L}$ with $i \in [0, L-1]$ and $\text{mod } x_m \text{ mod } = C$, where C is a constant number. The preamble has two identical halves as in Schmidl and Cox's algorithm, with the difference of now having a constant envelope. This means that the plateau problem is still there and, since a constant envelope is used, variations as the ones presented by Park and Maoquan cannot be used. To solve this, Ren proposes that the constant envelope preamble is weighted by a PN sequence:

$$x'_m = s_m x_m \quad (2.14)$$

s_m is the PN sequence weighted factor of the m^{th} sample of the original preamble x_m . The value of the PN sequence is $+1$ or -1 . The different between adjacent points is then enlarged and the peak becomes narrower. To estimate the timing offset in the receive side, the weighting can be removed by multiplying the preamble by the corresponding PN sequence. The new timing metric is defined as

$$M(d) = \frac{\left| \sum_{m=0}^{L-1} s_m s_{m+L} r_{d+m}^* r_{d+m+L} \right|^2}{\left(\frac{1}{2} \sum_{m=0}^{L-1} |r_{m+d}|^2 \right)^2} = \frac{|P(d)|^2}{R(d)^2} \quad (2.15)$$

Timing and frequency offset are estimated with the same procedure used by Schmidl and Cox; the accuracy is greatly improved. One disadvantage of Ren's method is that it cannot be used on IEEE standards [28].

All the algorithms presented above based on the correlation of repeated sequences are computationally expensive when N , the number of time samples, is very large. In [29], a method to reduce the processing complexity is presented. The reduction is achieved by doing first a rough estimation of where the maximum of the timing metric is (using a large step) and only

after performing a finer search in a smaller interval. For SNR values > -2 , it has been shown that the search step can begin to be as big as $1/3$ without loss in the estimation precision.

Another common class of synchronization algorithms is based on the use of pilots in the frequency domain; an example can be found in [30]. The intention is to avoid the use of time domain pilots, which lower the data rate.

Impact on the SER of Residual Synchronization Offsets

As good as the synchronization algorithm applied may be, there are always residual synchronization offsets that cannot be compensated for and affect the system's SER. The impact of these offsets on the DFT output is the same as the one showed in Equation 2.8, with the difference that ε and δ are now very small.

Assuming that the timing residual error is within the CP and thus negligible, the effects of the residual synchronization offsets are reduced to a slight phase rotation and ICI. The time residual offset sets a SER floor error, since the impact of this error cannot be improved by increasing SNR [31].

By looking at Equation 2.8, it is clear that the impact of the residual offsets depends on the carrier index. Carriers with larger index have worse performance and thus are the ones limiting the SER. Since the SER of an OFDM system is the average of the SER of each individual carrier, the overall SER can be minimized by optimizing the power distribution over the carriers. One way of distributing the power is to adjust it in such a way that the SER of each carrier is the same — more transmission power to the carriers with lower performance. If such a distribution is made, a frequency equalizer has to be used at the receiver as a form of compensation.

As SNR is increased, ICI starts dominating over the channel Gaussian noise. This means that the OFDM's sensitivity to synchronization errors increases with SNR. Modulation schemes that work with higher SNRs require better and more accurate synchronization schemes.

A thorough analysis of the impact of residual errors in the OFDM's SER may be found in [32].

2.5 RF impairments and their impact on SER

Both the transmitter and the receiver non idealities degrade the RF signal. Of most importance to the OFDM system are the disturbances that break the orthogonality requirement. Typical RF impairments that should be accounted for when designing such a system are the effects of the receiver LO's phase noise, IQ imbalance (specially in direct conversion receivers) and non linear devices, with special consideration for the transmitter power amplifier in the end of the chain. In this section, the effects of each of these non-idealities in the OFDM signal will be described, as well as their impact on the system SER. For the analysis, a non-fading time-invariant channel affected only by AWGN is going to be considered.

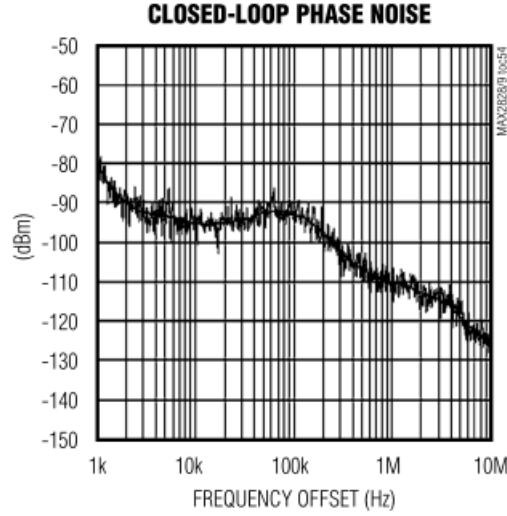


Figure 2.8: Example of a phase noise PSD for the MAX2829 chip from Maxim Integrated, $f_{LO} = 5.25\text{GHz}$.

Effects of Phase Noise

Phase noise effects are introduced by the receiver's local oscillator and will always be present unless the local oscillator itself is improved. Thus, it is important to determine how much phase noise a system can handle to achieve a certain performance and determine the design requirements for the LO accordingly.

The LO's phase noise is so relevant that a common way to determine the LO's quality is by plotting the phase noise PSD (Power Spectral Density) as a function of the offset frequency. A typical PSD curve for a locked LO (with a PLL (Phase Locked Loop) tuning the VCO (Voltage Controlled Oscillator) to the required frequency) is shown in Figure 2.8.

Phase noise may be modeled as a zero-mean and wide-sense stationary process with a narrow-band PSD $S_\phi(f)$ (Equation 2.16) and a finite variance σ_ϕ^2 (Equation 2.17) [33].

$$S_\phi(f) = 10^{-c} + \begin{cases} 10^{-a}, & |f| < f_l \\ 10^{-(f-f_l)\left(\frac{b}{f_h-f_l}\right)-a}, & f > f_l \\ 10^{(f+f_l)\left(\frac{b}{f_h-f_l}\right)-a}, & f < -f_l \end{cases} \quad (2.16)$$

a determines the noise level within the PLL bandwidth, b determines the noise roll-off rate from f_l (PLL bandwidth) to f_h (where noise floor starts to dominate) and c determines the white noise floor. Given that the phase noise has zero mean, its variance may be defined as

$$\sigma_\phi^2 = 2 \int_0^{B_\phi} \frac{S_\phi(f)}{C} df \quad (2.17)$$

where C denotes carrier power and B_ϕ is the phase noise bandwidth.

Let \mathbf{s} be the transmitted OFDM signal (Equation 2.1). The received OFDM signal in the absence of AWGN and in the presence of phase noise ϕ is,

$$\mathbf{r} = \mathbf{s}e^{i\phi} \quad (2.18)$$

Carriers are produced at nominal frequency with a time-varying frequency offset ϕ . For ϕ small, $\cos(\phi) \approx 1$ and $\sin(\phi) \approx \phi \Rightarrow e^{i\phi} \approx 1 + i\phi$. In this case, an arbitrary OFDM symbol at the output of the DFT (for $N_{DFT} = N_{IDFT} = N$) is

$$\begin{aligned} y(k) &= \frac{1}{N} \sum_{n=0}^{N_{DFT}-1} r(n) e^{i\phi(n)} e^{-i2\pi k \frac{n}{N}} \\ &\approx \frac{1}{N} \sum_{n=0}^{N-1} \left(\sum_{m=0}^{N-1} x(m) e^{i2\pi m \frac{n}{N}} \right) (1 + i\phi(n)) e^{-i2\pi k \frac{n}{N}} \\ &\approx s(k) + \frac{i}{N} \sum_{m=0}^{N-1} s(m) \sum_{n=0}^{N-1} \phi(n) e^{i2\pi(m-k) \frac{n}{N}} \approx s(k) + c(k) \end{aligned} \quad (2.19)$$

Each carrier k has an associated error $c(k)$ that results from a combination of errors from all the carriers. This error $c(k)$ may be divided in two scenarios:

- Common Phase Error (CPE) for $m = k$

$$c(k) = \frac{i}{N} \sum_{m=0}^{N-1} s(m) \sum_{n=0}^{N-1} \phi(n) e^{i2\pi \frac{n}{N} \cdot 0} = i s(k) \Phi \quad (2.20)$$

Every carrier has a common error proportional to Φ (average of the phase noise) that is translated into a rotation of the overall constellation. The phase noise that contributes to this error is the *low frequency* phase noise, the phase noise within the carrier spacing band. All carriers are affected by the low frequency phase noise in the same way, so it can be estimated and corrected for — it remains constant over Δf (and thus over T_S) and is equal to all carriers.

- Inter Carrier Interference for $m \neq k$

$$c(k) = \frac{i}{N} \sum_{m=0, m \neq k}^{N-1} s(m) \sum_{n=0}^{N-1} \phi(n) e^{i2\pi(m-k) \frac{n}{N}} \quad (2.21)$$

Each carrier suffers from the phase noise skirt of all the other carriers. ICI is a summation of the data of all the other $N-1$ carriers, each multiplied by a complex number that comes from an average of the phase noise with a spectral shift, resulting in a behavior similar to gaussian noise. The spectral components of phase noise that contribute to the magnitude of this error are those from Δf up to B_ϕ . Due to its random nature, it

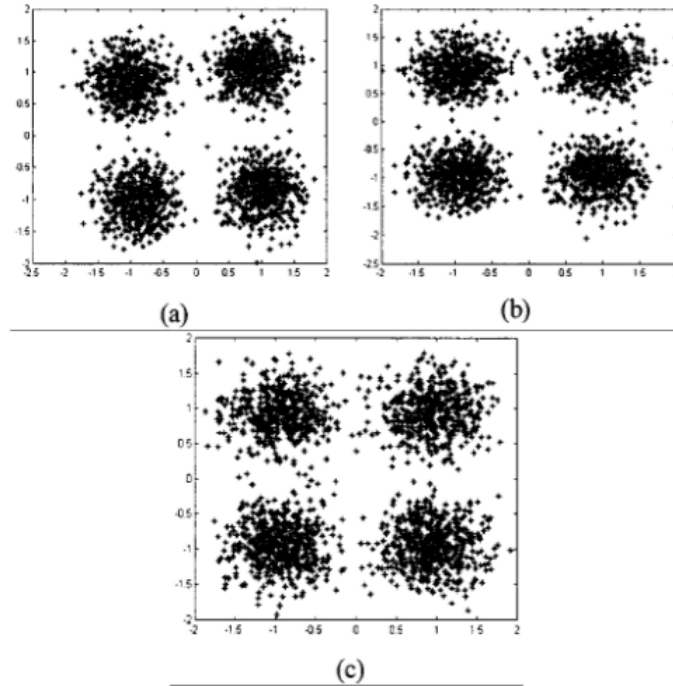


Figure 2.9: CPE and ICI effects on a constellation. (a) $B_\phi/\Delta f = 0.01$. (b) Constellation (a) after CPE correction. (c) $B_\phi/\Delta f = 1$. (figure taken from [2])

cannot be corrected for. Nevertheless, there has been some research on how to model this behavior so that some sort of compensation could be applied [33].

Figure 2.9 shows the effects of CPE and ICI on a constellation. In [2], it is argued that the commonly considered degradation in SNR due to phase noise (Equation 2.22) is only true when no correction is applied. Note that this expression suggests that the degradation does not depend on any characteristics of the OFDM system, but only on the phase noise variance.

$$\text{degrSNR} = 10\log_{10}\left(1 + \sigma_\phi^2 \frac{E_S}{N_0}\right) \quad (2.22)$$

Based on simulations, Armada concludes that if $B_\phi > \Delta f$, ICI dominates (both over CPE and gaussian noise) and compensating for CPE has no effect: the performance after correction is not improved. On the other hand, if $B_\phi < \Delta f$, the correction scheme has a positive result and, since the ICI is a sum of the contributions of all carriers, the system with the lowest number of carriers will have the best SER [34].

Correcting for CPE will change the phase noise spectral mask and thus decrease the phase noise variance σ_ϕ^2 . The system performance will always degrade due to phase noise as SNR increases (Equation 2.7), but how fast this degradation is depends on the final σ_ϕ^2 after CPE correction (Equation 2.22). Figure 2.10 illustrates this dependence for different variance values. The correction will delay the start of the degradation and decrease the slope depending on the variance improvement [2].

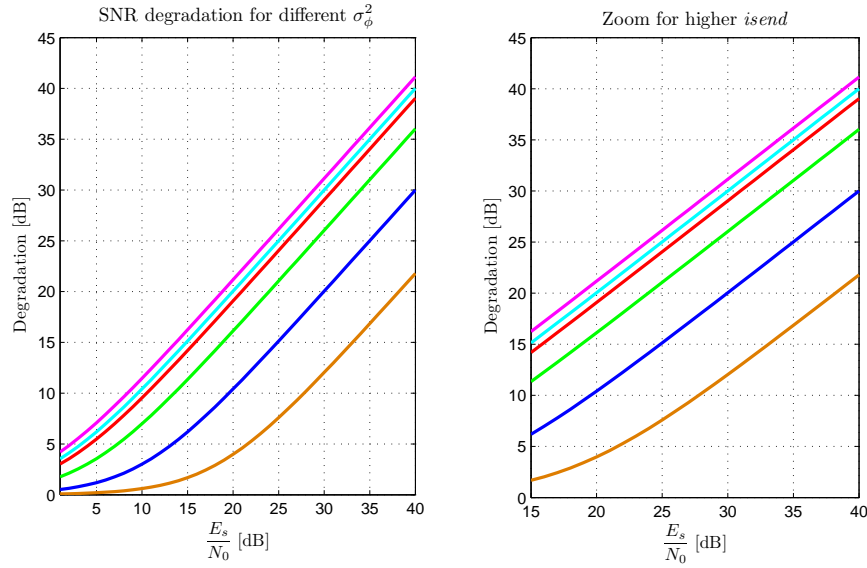


Figure 2.10: Performance degradation due to phase noise for $\sigma_\phi^2 = 0.015 \text{ rad}^2$ (orange), $\sigma_\phi^2 = 0.1 \text{ rad}^2$ (blue), $\sigma_\phi^2 = 0.4 \text{ rad}^2$ (green), $\sigma_\phi^2 = 0.8 \text{ rad}^2$ (red), $\sigma_\phi^2 = 1 \text{ rad}^2$ (cyan) and $\sigma_\phi^2 = 1.3 \text{ rad}^2$ (magenta).

IQ Imbalance

IQ imbalance is a common issue in complex down-converters found in the receiver chain. A complex down-converter basically multiplies the RF signal by the complex waveform $e^{-i2\pi f_{LO}}$, where f_{LO} is the local oscillator frequency at the receiver. To perform a complex down-conversion, both the sine and the cosine waves (Inphase, I and Quadrature, Q) are necessary — both inphase and quadrature versions of the LO. The receiver is then divided in two branches (I and Q) that do the analogue processing of the complex baseband signal after down-conversion. For the conversion to baseband to be correctly performed, both inphase and quadrature versions of the LO need to have exactly 90° phase difference and exactly the same amplitude. That's the ideal system. In an actual design, there is always what is called a mismatch between the branches, an imbalance between I and Q. Multi carrier systems and, in particular, systems that use a direct conversion receiver architecture, are very sensitive to it. It is of high importance to model how much IQ imbalance the design can tolerate to achieve a certain performance. The coming analysis is made based on [3].

Let y_k and x_k be the received and transmitted signal in frequency domain respectively (Equation 2.1 and 2.2), h_k be the channel coefficients (for generality) and w_k the channel AWGN — the carrier index k is used to emphasize that the IQ imbalance parameters may be frequency dependent. The received frequency domain signal y_k is

$$y_k = h_k x_k + w_k \quad (2.23)$$

It has been shown in literature that the IQ imbalance in direct conversion receivers translates

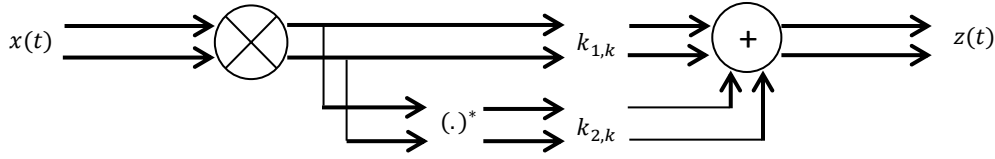


Figure 2.11: Mismatches between the I and Q branches.

into a mutual interference between each pair of carriers located symmetrically with respect to DC. This interference is of carrier y_{-k} on carrier y_k and vice-versa. The undesirable leakage z_k due to imbalance is then modeled as

$$z_k = k_{1,k}y_k + k_{2,k}y_{-k}^* \quad (2.24)$$

The complex weighting factors $k_{1,k}$ and $k_{2,k}$ are determined by the gain μ and phase λ imbalance and are a characteristic of each receiver (Figure 2.11):

$$\begin{aligned} k_{1,k} &= \cos(\lambda) + i\mu \sin(\lambda) \\ k_{2,k} &= \mu \cos(\lambda) - i \sin(\lambda) \end{aligned} \quad (2.25)$$

To quantify the receiver's robustness against IQ mismatches, two quantities are commonly used: *IRR* (Image Rejection Ratio, Equation 2.26) and *ILLR* (Image Leakage Ratio, Equation 2.27).

$$IRR_k = \left| \frac{k_{1,k}}{k_{2,k}} \right|^2 \quad (2.26)$$

$$ILLR_k = \left| \frac{k_{2,k}}{k_{1,k}} \right|^2 \quad (2.27)$$

In an ideal receiver, *IRR* tends to infinity, while *ILLR* tends to zero. Each symbol x_k is rotated and scaled by both the channel h_k and $k_{1,k}$ (Figure 2.12). Note how a phase rotation of $\pi/4$ put the corner symbols closer to the decision boundaries.

Assuming a zero-forcing equalizer,

$$\begin{aligned} \tilde{s}_k &= \frac{1}{k_{1,k}h_k} z_k = \frac{1}{k_{1,k}h_k} [k_{1,k}h_k s_k + k_{1,k}w_k + k_{2,k}h_{-k}^* s_{-k}^* + k_{2,k}w_{-k}^*] \\ &= s_k + \frac{1}{h_k} w_k + \frac{k_{2,k}}{k_{1,k}} \frac{h_{-k}^*}{h_k} s_{-k}^* + \frac{k_{2,k}}{k_{1,k}} \frac{1}{h_k} w_{-k}^* \end{aligned} \quad (2.28)$$

Which results in an error vector Δ_k of

$$\Delta_k = \tilde{s}_k - s_k = \frac{1}{h_k} \left[\frac{k_{2,k}}{k_{1,k}} h_{-k}^* s_{-k}^* + w_k + \frac{k_{2,k}}{k_{1,k}} w_{-k}^* \right] \quad (2.29)$$

For simplicity, let $\frac{k_{2,k}}{k_{1,k}} = k_k$ and $h_k = h_{-k} = 1$. w_k and w_{-k} are modeled as complex-values

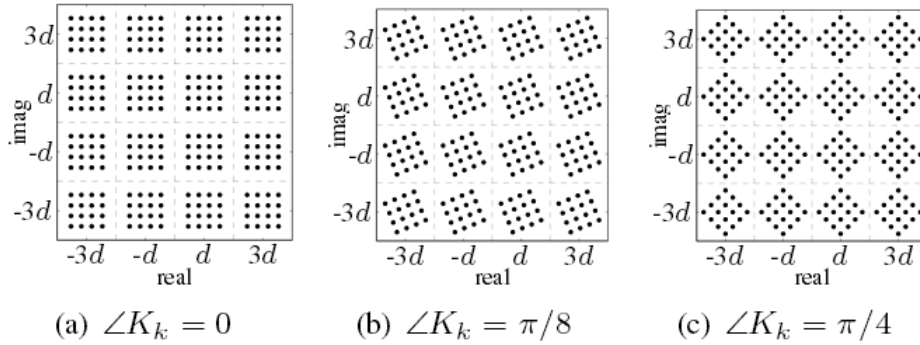


Figure 2.12: Received 16-QAM constellations for different phase of the complex-valued leakage parameter $\frac{k_{1,k}}{k_{2,k}}$ and fixed magnitude ($IRR = 15\text{dB}$). (figure taken from [3])

RVs (Random Variable) and are assumed to be uncorrelated zero-mean gaussian distributed RVs with equal power σ_w^2 , i.e. $E|w_k|^2 = 2\sigma_w^2$ for each k . $\Delta_k = x + iy$ is a linear transformation of jointly gaussian distributed RVs. The joint pdf is then

$$f_{xy}(x, y) = \frac{1}{2\pi\sigma_{\Delta_k}^2} e^{-\frac{1}{2\pi\sigma_{\Delta_k}^2} |(x+iy) - \mu_k|^2} \quad (2.30)$$

with

$$\begin{aligned} \mu_k &= \mu_{R,k} + i\mu_{I,k} = k_k s_{-k}^* \\ \sigma_{\Delta_k}^2 &= (1 + |k_k|^2)\sigma_w^2 = (1 + ILLR_k)\sigma_w^2 \end{aligned} \quad (2.31)$$

Even though the noise variance is increased by $(1 + ILLR_k)$, the impact on the system performance is not significant, since $ILLR_k$ is usually $\ll 1$. Also, the mean error is shifted from 0 to $k_k s_{-k}^*$. The impact of this shift on the SER will depend on its magnitude when compared to the minimum distance between constellation points.

To give an idea of typical figures, $ILLR$ should be lower than -30dB for a $\text{SNR} > 30\text{dB}$ and a $\text{SER} < 10^{-7}$ in an OFDM system modulated with 64-QAM [35]. Since such values of $ILLR$ are achievable with careful design, it is concluded that IQ imbalance is of secondary importance in non-fading AWGN case. To conclude, Figure 2.13 gives SER curves for different $ILLR$ s for 64-QAM modulation suffering of both AWGN and IQ imbalance. As SNR increases, IQ imbalance effects dominate over AWGN; for higher modulation orders, this behavior is more evident and the SER floor is higher.

Several IQ imbalance compensation schemes are available in literature. In [36], a good overview of pre and pos-FFT compensation algorithms and their impact on SER may be found.

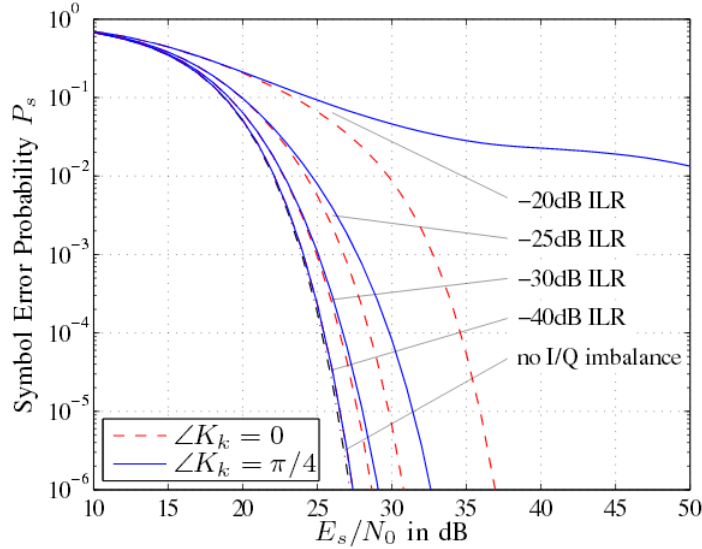


Figure 2.13: Joint impact of AWGN and IQ imbalance for 64-QAM. (figure taken from [3])

OFDM in non linearity

In OFDM systems, non linearities have, in general, two main causes: either the transmitter HPA was driven too hard, i.e. at or near saturation, or the signal was clipped somewhere in the path IFFT output \leftrightarrow DFT input. When a non linear event occurs, the multi carrier signal is distorted and the system performance is degraded. There is a trade-off between high power and distortion requirements, between the back-off (amplifier efficiency) and the maximum degradation allowed.

Let κ_0 the complex linear gain and \mathbf{n}_d the non linear distortion noise. The amplified baseband signal to be up-converted for transmission \mathbf{s}_{amp} is

$$\mathbf{s}_{amp} = \kappa_0 \mathbf{s} + \mathbf{n}_d \quad , \text{ with } \mathbf{s}_{[1 \times N]} \text{ consisting of } N \text{ time samples} \quad (2.32)$$

And the signal at the input of the receiver \mathbf{r} is

$$\mathbf{r} = \kappa_0 \mathbf{s} + \mathbf{n}_d + \mathbf{w} \quad (2.33)$$

Where \mathbf{w} is a gaussian random variable representing the channel's AWGN.

A baseband equivalent polynomial model for a nonlinear power amplifier is

$$\mathbf{s}_{amp} = \sum_{u=1}^U \alpha_u \mathbf{s} |\mathbf{s}|^{u-1} \quad (2.34)$$

Being \mathbf{s}_{amp} and \mathbf{s} the output and input of the amplifier respectively, U the order of the nonlinearity and α_u the complex nonlinear coefficients. Odd order linearities cause the most in-band

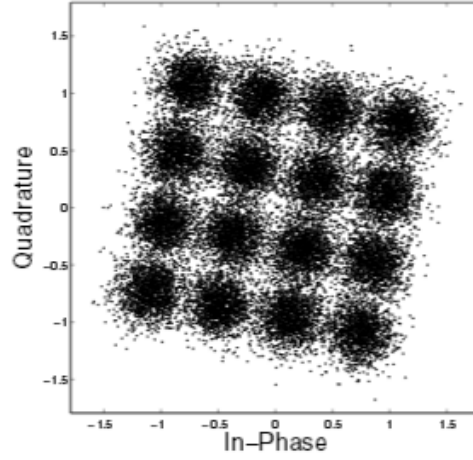


Figure 2.14: Constellation at the output of the DFT of an OFDM signal distorted by a nonlinear amplifier with IBO=0dB and no AWGN. (figure taken from [4])

distortion due to the intermodulation products IM3, IM5, etc.. As a good approximation, the nonlinearities will be restricted to the odd harmonics with most weight,

$$\mathbf{s}_{amp} = \alpha_1 \mathbf{s} + \alpha_3 \mathbf{s} |\mathbf{s}|^2 \quad (2.35)$$

Thus, the received symbol \hat{y}_k will be

$$\hat{y}_k = \alpha_1 \sum_{n=0}^{N-1} s e^{-i2\pi k \frac{n}{N}} + \alpha_3 \sum_{n=0}^{N-1} s |s|^2 e^{-i2\pi k \frac{n}{N}} + w_k \quad (2.36)$$

where w_k has variance σ_0^2 . Figure 2.14 shows how a constellation of a signal distorted by a nonlinear amplifier would like for an IBO (Input Back-Off) of 0dB in the absence of AWGN. After some manipulation (see [4] for details), \hat{y}_k can be written as

$$\hat{y}_k = y_k \mu + \eta + w_k \quad (2.37)$$

with

$$\begin{aligned} \text{complex phase shift } \mu &= \alpha_1 + \frac{\alpha_3}{N} \sum_{n=0}^{N-1} |s|^2 = \alpha_1 + \alpha_3 P_{av} \\ \text{nonlinear noise component } \eta &= \frac{\alpha_3}{N} \sum_{m=0, m \neq k}^{N-1} y_m \left[\sum_{n=0}^{N-1} |s|^2 e^{i2\pi(-k+m) \frac{n}{N}} \right] \end{aligned} \quad (2.38)$$

The amount of phase shift of the original signal depends on α_1 and α_3 , as well as on the power of the OFDM signal $P_{av} = \frac{P}{N}$. μ can be estimated and compensated for before demodulation.

η is the sum of $N - 1$ identically distributed random variables, being reasonable to assume the nonlinear noise to be complex Gaussian with variance σ_{NL}^2 given by

$$\sigma_{NL}^2 = E[|\eta|^2] = |\alpha_3|^2 P_{av}^3 \left(\frac{3N^2 - 11N + 12}{N} \right) \quad (2.39)$$

The nonlinear noise variance strongly depends on the OFDM signal power and on α_3 . The degraded snr of each carrier is

$$snr = \frac{P|\mu|^2}{\sigma_{NL}^2 + \sigma_0^2} \quad (2.40)$$

The snr at the output of the DFT depends on the HPA parameters α_1 and α_3 and the chosen operating point, i.e. the average transmitted power. By controlling P_{av} , the IBO can be adjusted for optimum performance.

2.6 Conclusions

The OFDM story was told, from its very beginning with Chang through out its evolution until what it is today. Though OFDM is a promising modulation scheme with a lot of potential, it is a coin with two sides. OFDM's sensitivities and minus points were explained one by one and a brief description of state-of-art techniques to compensate for those was made. It has been shown that the RF impairments and residual synchronization offsets often translate into a rotation of the overall constellation. This means that, after demodulation, it is very hard to tell apart the causes of distortion. A careful modeling of the system performance should be made before the design to determine how much synchronization errors, phase noise, IQ imbalance and nonlinearities the OFDM signal can handle to achieve a desired SER.

Chapter 3

The Transmitter Chain

In Chapter 1, Section 1.4, a general idea of how the solution should work was given. On the transmit side, the OFDM signal is generated in a conventional way, but with a data organization that goes back to the very beginning, before data rate was an issue. In a very simple way, each receiver Rx_r has an allocated band that can go from 1 OFDM carrier to K_r , with

$$\begin{aligned} r \in [1, R] \quad \text{for } R \text{ RF front-end modules} \\ \text{and} \quad K \geq \sum_{r=1}^R K_r \end{aligned} \tag{3.1}$$

The binary data stream designated to each Rx_r is always sent over that same band and, if it does not fit in one time domain symbol, it is spread over time. When all the necessary data has been sent to Rx_r , its allocated carriers are put to zero. The overall OFDM spectrum modulated on the transmit side is a concatenation of all these bands to all the RF front-end modules. This is the point where the work developed in this thesis touches the OFDMA concept: allocation of bands to different users. The number of carriers K of the OFDM signal thus depends on the number of RF front-end modules in the antenna and their required data rate — the required data rate for each module determines the number of carriers it needs in its band. Each module may have a different number of allocated carriers and may choose a different modulation technique. All bands are independent of each other, being the only thing connecting them together the fact that they are all inputs of the same IDFT that generates the OFDM signal. It cannot be stressed enough that these are independent communication links taking advantage of the orthogonality in the frequency domain and of the simplicity of the IDFT/DFT process to achieve so.

Figure 3.1 is a block diagram of the transmitter chain. At first sight, and putting apart for a second how the data is organized, it is just like a conventional OFDM transmitter. The binary data stream is fed as input to the block transmitter, which divides it into the data blocks for each RF front-end module. Each of the binary data blocks is mapped onto the appropriate constellation of the modulation in use for its receiver Rx_r . These constellations represent the modulated data to be transmitted to each RF front-end module between

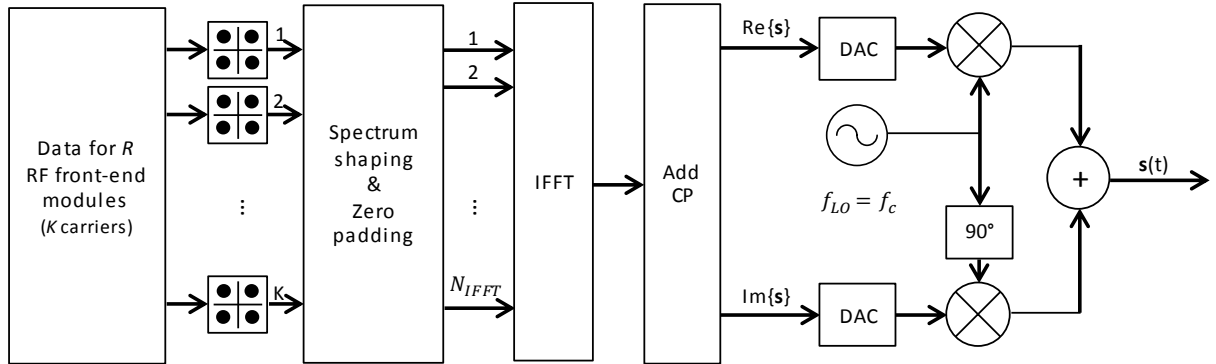


Figure 3.1: Block diagram of the OFDM transmitter.

RADAR pulses, as explained in Section 1.4. For receiver r , the first K_r complex values of its constellation are put in the IDFT input; the same is done to all receivers until all the OFDM carriers are attributed a complex value.

The next step before performing the actual IDFT is zero-padding. Zero-padding has two main advantages that are actually consequence of each other. First, by increasing the number of points in the frequency domain (by increasing the IDFT input length) the resolution in time domain is improved. Second, zero-padding ends up working as spectrum guard-bands (see Section 2.2), helping in the reduction of out-of-band radiation and relaxing the passband filter requirements.

Spectrum shaping to decrease the sidelobes power may take different places in the chain, depending on the technique applied. If shaping of the rectangular pulses is chosen, the shaping is done before the IDFT. If expanded constellations are used, the shaping done during the mapping of the binary data stream into the constellations. Other methods like, MSC, CCs or subcarrier weighting, require an DFT after the IDFT to determine the OOB radiation power and apply their reduction algorithm; after optimizing the data/power distribution in the frequency domain, the final IDFT is done to generate the OFDM signal.

After finally having the IDFT output, the time domain OFDM symbol, the last step before upconversion is to add the cyclic prefix/postfix. The length of the CP depends on the channel and receiver characteristics. For the RADAR application in particular, it will depend on how the RF network behaves at the frequency range in which the OFDM signal will be distributed and on the receiver module's characteristics. With the CP added, the signal is then upconverted to its central frequency f_c and amplified for transmission.

For proof of concept, an example based on the possibilities with available laboratory equipment and components was assumed:

- OFDM bandwidth $B \in [100, 600]$ MHz
- Total transmission time between RADAR pulses $< 18\mu s$
- Number of RF front-end modules $R = 128$

- Binary bit stream for each receiver Rx_r of 144bits per RADAR pulse
- Central frequency for OFDM transmission f_c around 5GHz

For the allocation of carriers and modulations, two cases were studied: 64-QAM with one carrier for each RF front-end module and 16-QAM with two carriers for each RF front-end module. QAM modulation was chosen mainly for convenience reasons: the control data in the RF front-end models is given as 6 bit inputs, so using 64-QAM for each receiver, for instance, would be an elegant way of transmitting one of those inputs in one time domain symbol alone. Besides, QAM is a high spectral efficiency modulation scheme, suitable for the typical data rates desired for the RADAR system.

For simplicity, the same modulation, number of allocated carriers and amount of data per burst was chosen for all receivers. However, since the receivers work independently of each other, they may have their own distinct modulation and number of allocated carriers. Basically, the system may be widened to the case where there are R frequency-orthogonal subsystems working at different data rates, and the data rates can be adjusted to the RF front-end modules' needs. If the receiver's design is optimized for the higher modulation orders they may eventually need, this exchange of constellation types for different desired rates can be done without loss in performance. All the conclusions and descriptions of the remaining chapters can be extended to those scenarios unless stated otherwise.

64-QAM Modulation with one carrier per RF front-end module, an example

To generate the OFDM signal, a MATLAB[®] module was developed. Bandwidth, total transmission time, guard interval length, binary data and QAM order are fed as input. The user also sets whether the limitation should be put on used bandwidth or transmission time. On top of these specifications, a few choices for optimization that will be discussed in Section 3.1 are also available. The output of the module is the OFDM message with all the symbols to be transmitted over time to all Rx_r .

The binary data is mapped onto the set of complex values of a 64-QAM constellation. Gray coding was used. Since each RF front-end module receives 144 bits per burst and has one allocated carrier, it takes $144/\log_2(64) = 24$ time domain symbols to transmit all the data. Figure 3.2 shows an example of a constellation for the receiver Rx_r . Note that, even though the constellation looks sparse, it does not mean that the spectrum is not being used in its full capacity. The constellation of interest is the one of a particular receiver and, for that reason, of the transmitted symbols over time. It will have as many points as time domain symbols necessary to transmit all the data with its allocated band.

After having all the constellations for all R receivers, the data is mapped onto the OFDM carriers. In this case, only one carrier is dedicated to each receiver, so only one point of its constellation will be mapped per time domain symbol. Figure 3.3 shows the OFDM carriers for the first time domain symbol; zero-padding was already done. The carrier at DC is not used for robustness purposes.

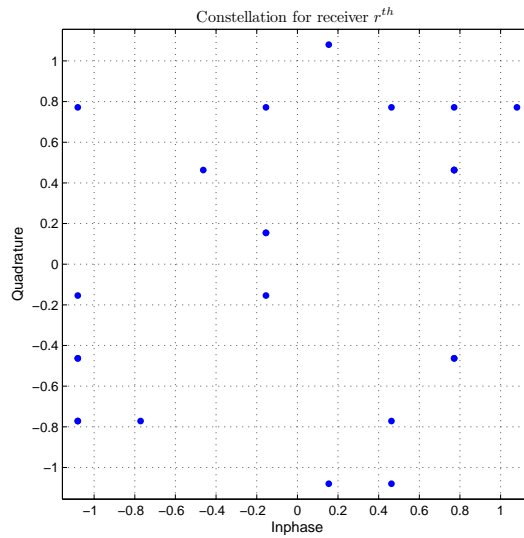


Figure 3.2: Example of a time domain constellation for receiver r^{th} .

This process is repeated for all constellation points, creating as many frequency vectors as time domain symbols to be transmitted. In this case, 24 frequency vectors are created to be fed as input to the IDFT. Since there are 128 receiver modules and the frequency points were doubled with zero-padding, the IDFT input is a matrix of 256 frequency points X 24. An IDFT is performed over each column of the matrix, generating 24 time domain symbols with 256 time domain samples each (Figure 3.4). If needed, a CP may be added to each of the time domain symbols after the IDFT (Figure 2.5).

The modulated orthogonal carriers and the respective OFDM spectrum for one time domain symbol can be seen in Figure 3.5. Figure 3.6 shows the average of the spectra of the 24 symbols.

Optimization techniques used to lower the OOB radiation will be discussed in the next section.

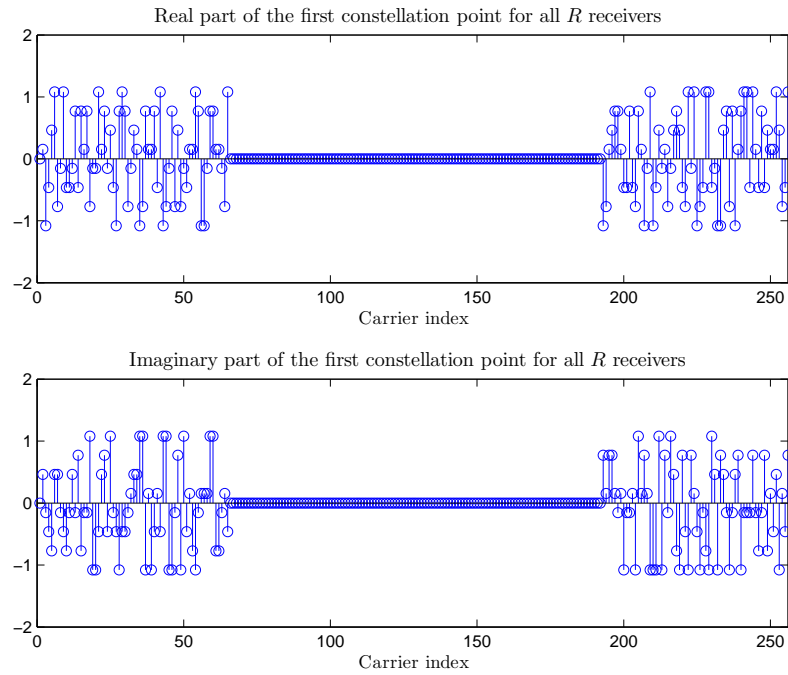


Figure 3.3: Example of the mapping of the OFDM carriers with the first constellation point of each receiver.

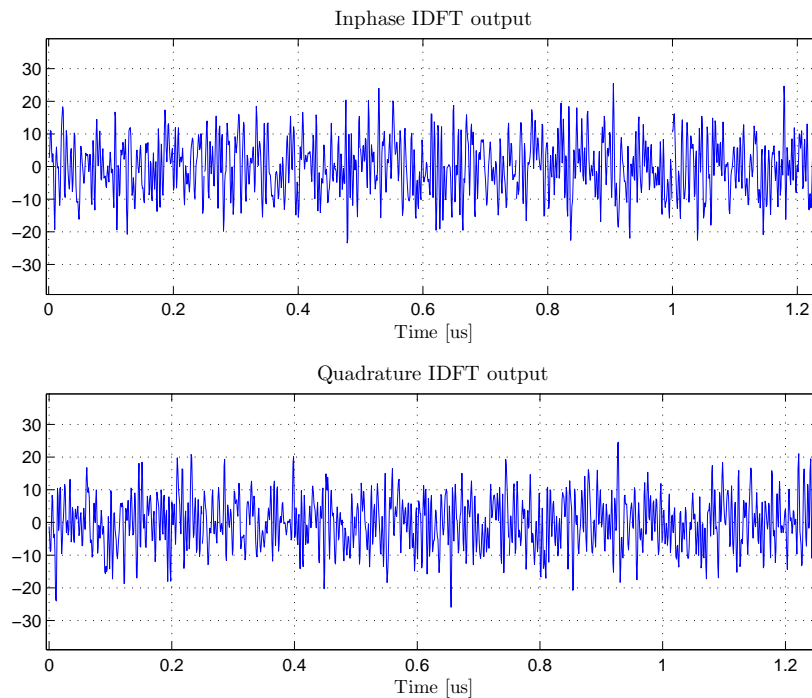


Figure 3.4: 5 out of the 24 OFDM time domain symbols; inphase (top) and quadrature(bottom).

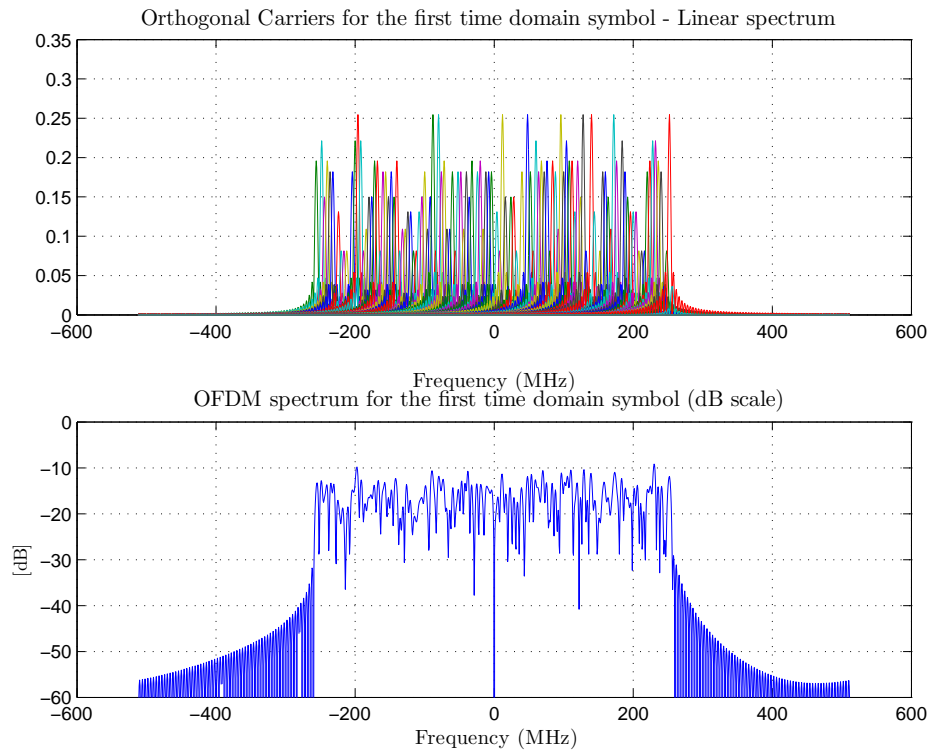


Figure 3.5: Example of the OFDM spectrum for one symbol; orthogonal carriers in a linear spectrum (top) and spectrum in dB (bottom).

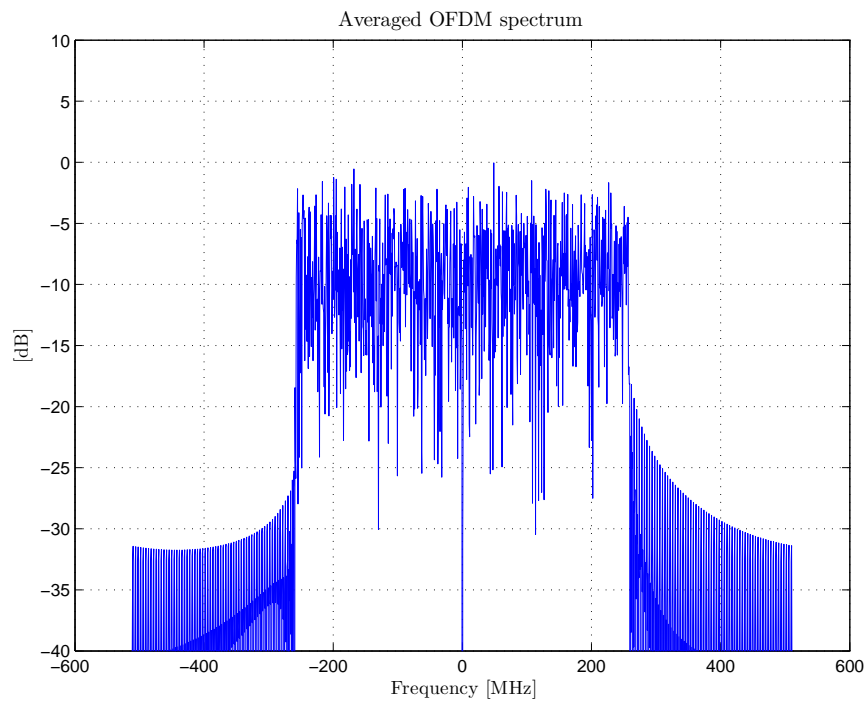


Figure 3.6: Example of the averaged OFDM spectrum over the 24 symbols.

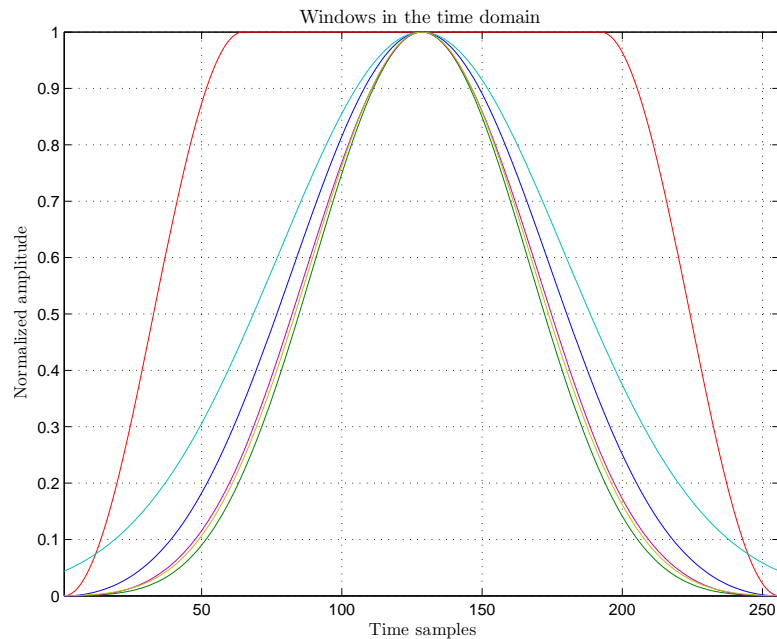


Figure 3.7: Windows under study: Blackman (dark blue), Blackman-Harris (dark green), Tukey (red), Gaussian (cyan), Parzen (purple) and Chebyshev (light green).

3.1 On the OOB Radiation Reduction

Among the methods for reduction of out-of-band radiation described in Section 2.2, two were chosen for this study: windowing and cancellation carriers. The criteria to choose these two and not others was low complexity of implementation on the receiver side and the promising reduction if combined [16]. Even though it will not be mentioned in this section, the guard band method is applied by zero-padding the data before the IDFT.

Windowing

To window the OFDM spectrum, different windows were applied to the OFDM time domain symbols. Let β be the window's time domain samples. If $\beta < \text{CP}$, the symbol is extended by β samples and the window is applied. The main goal is to find windows that for a known finite duration achieve a narrow spectral lobe. Six different windows were used to see the effect of windowing on the spectrum (see Figure 3.7).

For the remaining of this section, let $w(n)$ be the window coefficients, with time samples $n \in [1, N]$ where $N = N_{IDFT} + \beta$. For instance, a rectangular window is defined with $w(n) = 1$ for all n .

The higher form generalized cosine windows are of the form

$$w(n) = \sum_{k=0}^K a_k \cos\left(\frac{2\pi kn}{N-1}\right) \quad (3.2)$$

and only have $2K + 1$ non-zero coefficients. These windows may be seen as the summation of $2K - 1$ shifted sinc pulses (rectangular window). The Hamming and Hanning windows are special cases of this family. Another special case is the Blackman window for $K = 3$ and is defined as

$$w(n) = 0.42 + 0.5 \cos\left(\frac{2\pi}{N}n\right) + 0.08 \cos\left(\frac{2\pi}{N}2n\right) \quad \text{for } -\frac{N}{2} \leq n \leq \frac{N}{2} \quad (3.3)$$

Note that the coefficients sum zero at the boundaries: $0.42 - 0.5 = 0.08 = 0$. The Blackman window is continuous with a continuous first derivative.

The Blackman-Harris window principle is to minimize the sidelobe's level. It is one more window of this family for $K = 4$ and is defined as

$$w(n) = a_0 - a_1 \cos\left(\frac{2\pi}{N}n\right) + a_2 \cos\left(\frac{2\pi}{N}2n\right) - a_3 \cos\left(\frac{2\pi}{N}3n\right) \quad n \in [0, N-1] \quad (3.4)$$

with $a_0 = 0.35875$, $a_1 = 0.48829$, $a_2 = 0.14128$ and $a_3 = 0.01168$.

The Tukey window is the result of a rectangular window of width $(1 - \alpha/2)N$ convolved with a cosine lobe of width $(\alpha/2)N$ and is defined as:

$$w(n) = \begin{cases} 1 & 0 \leq |n| \leq \alpha \frac{N}{2} \\ \frac{1}{2} \left[1 + \cos\left(\pi \frac{n - \alpha \frac{N}{2}}{2(1-\alpha)\frac{N}{2}}\right) \right] & \alpha \frac{N}{2} \leq |n| \leq \frac{N}{2} \end{cases} \quad (3.5)$$

By changing α , the Tukey window's shape can be modeled more like a rectangular window ($\alpha = 0$) or a Hanning window ($\alpha = 1$). Hence, increasing α , smoothens the time domain window and makes the main lobe narrower.

The Gaussian pulse is known by its minimum time-bandwidth product, which makes it a good candidate for a window. When the pulse is used as window though, it has to be truncated. This truncation breaks the minimum time-bandwidth product property. However, if the truncation is kept after the 3σ point, where σ is the standard deviation of the gaussian distribution, the error should be small and the approximation good. The Gaussian window is defined as

$$w(n) = e^{-\frac{1}{2}\left(\alpha \frac{2n}{N}\right)^2} \quad (3.6)$$

Here, α is the reciprocal of the standard deviation σ . Increasing α decreases the window width, which makes the spectrum main lobe larger and the sidelobes higher.

Parzen windows, also known for de la Vall-Poisson windows, are a piecewise cubic approximation of a Gaussian window. They can also be seen as self-convolving two triangles of half extent or four rectangles of one-fourth extent [12] and are defined as

$$w(n) = \begin{cases} 1 - 6 \left(\frac{2n}{N}\right)^2 \left(1 - \frac{2|n|}{N}\right) & 0 \leq |n| \leq \frac{N}{4} \\ 2 \left(1 - \frac{2|n|}{N}\right)^3 & \frac{N}{4} \leq |n| \leq \frac{N}{2} \end{cases} \quad (3.7)$$

The last window to be presented in this section is the Chebyshev window. Unlike the previously described windows, this window is defined in the frequency domain and only afterwards the time domain window is derived. The Chebyshev window is the closed-form solution for a minimum mainlobe width for a given sidelobe level and is defined (in the frequency domain) as

$$W(k) = (-1)^k \frac{\cos \left[N \cos^{-1} \left(\beta \cos \left(\pi \frac{k}{N} \right) \right) \right]}{\cosh(N \cosh^{-1}(\beta))} \quad 0 \leq |k| \leq (N-1) \quad (3.8)$$

with $\beta = \cosh \left[\frac{1}{N} \cosh^{-1}(10^\alpha) \right]$

The parameter α is the log of the ratio of mainlobe to sidelobe level required.

The time domain OFDM signals after windowing and their respective spectra are shown in Figure 3.8 and 3.9. All windows were applied with approximately the same β samples extension (in this case, the symbol length was approximately doubled). By applying the same extension for all windows, some are not being plotted in their best case scenario. However, it holds a fair comparison by imposing the same conditions to all windows.

The two extreme cases are the Tukey window and the Gaussian window. In the first case, the fact that the window is a convolution of a cosine lobe with a rectangular pulse, makes it the less effective window for radiation reduction; in the time domain plot, it can be seen that there's almost no processing gain lost. On the other hand, for the Gaussian window, the behavior is exactly the opposite. The time domain pulse is very narrow for that particular extension, which results in a lot of gain loss — this can be seen in both time and frequency domain. From the six studied windows, the one that offers the best trade-off between needed symbol length extension / spectrum shaping is the Blackman-Harris. From Figure 3.8, it is observed that the resulting time domain symbol is a nice midterm between the Gaussian and the Tukey window. As a result from the balanced extension/smooth symbol transition, it gives one of the best spectrum shapes (Figure 3.9).

For further details on windows and their performance, please refer to [12].

To study the different windows' effects, the transmit MATLAB[®] module has extra inputs to choose the kind of window, the desired symbol time extension for windowing (in percentage) and the desired minimum amplitude for the useful information window (where the DFT on the receiver side is performed). Based on the chosen window, the program tries to tune the window's function parameters to meet most of the required specifications. For the final design, the use of windowing was discarded. The reasoning behind it is heavy symbol rate reduction when transmission time is a limiting factor.

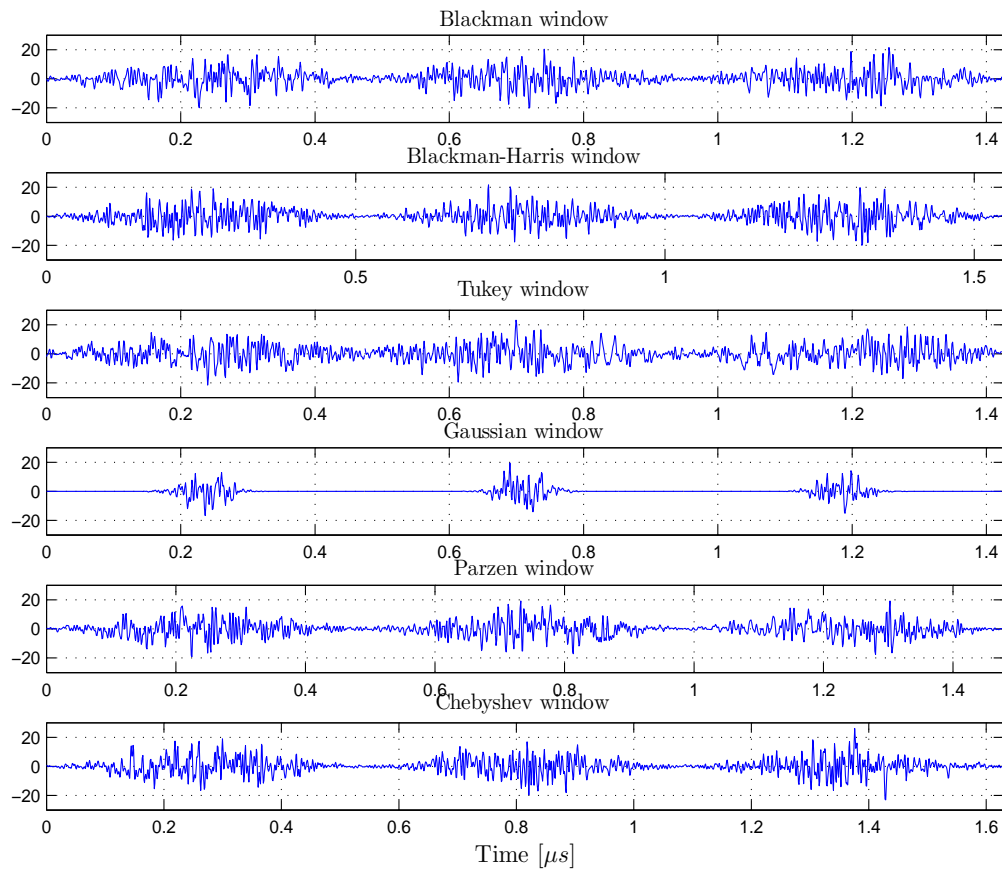


Figure 3.8: The first 3 time domain OFDM symbols for the six different windows.

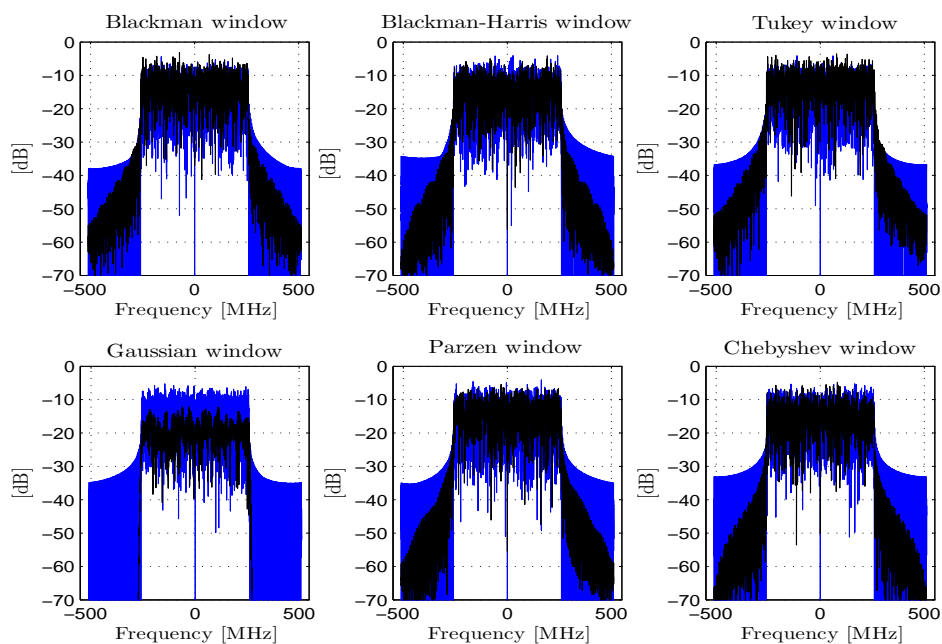


Figure 3.9: OFDM average spectra over the 24 time domain symbols for the six different windows.

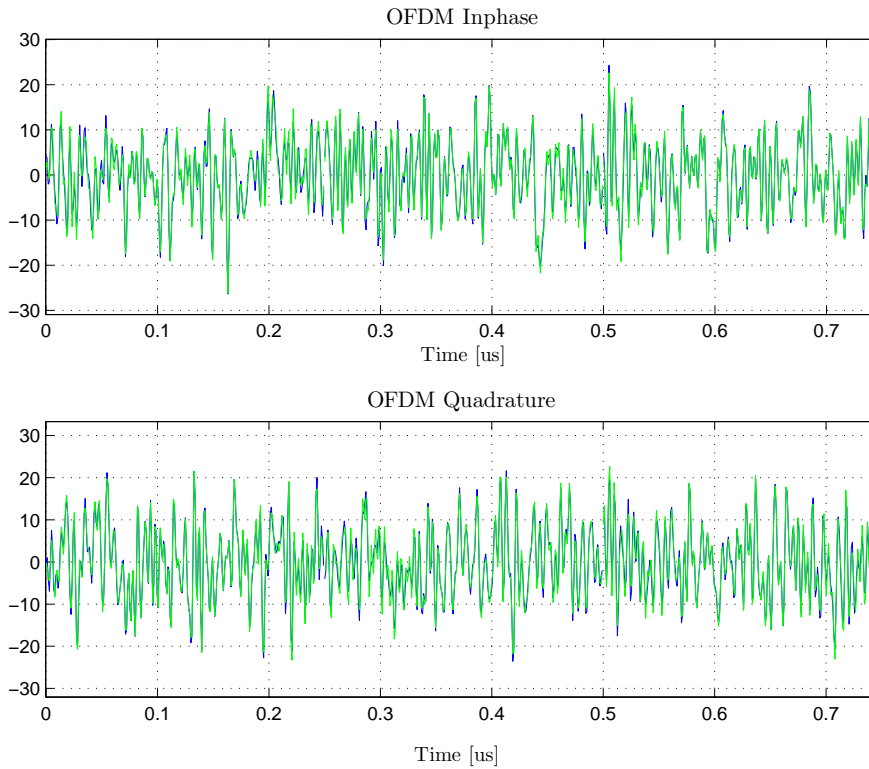


Figure 3.10: OFDM time domain signal with (green) and without (blue) CCs.

Cancellation Carriers

The theory behind the cancellation carriers algorithm was introduced in Section 2.2. The implementation of the algorithm on the transmit side is divided into three steps. On the first step, a DFT of the just computed IDFT is taken to determine the sidelobe power for a selected optimization range. Second, the linear least square problem (Equation 2.4) is solved for that same optimization range, computing the CCs' modeling coefficients \mathbf{g} that minimize the power in it. As last step, those modeling coefficients, which are the data to be carried by the CCs, are added to the original frequency domain data vector $\mathbf{x} = [d_1, \dots, d_N]$ (Equation 2.1) and weighted to create \mathbf{x}_{new}

$$\begin{aligned} \mathbf{x}_{new} &= \sqrt{A}[g_1, \dots, g_{n_{CC}/2}, d_1, \dots, d_N, g_{n_{CC}/2+1}, \dots, g_{n_{CC}}] \quad \text{with} \\ A &= \frac{\|d\|^2}{\|d\|^2 + \|g\|^2} \leq 1 \end{aligned} \quad (3.9)$$

The weighting factor A assures that the transmit power stays the same after the addition of the cancellation carriers. The spectrum wise optimized OFDM signal for transmission is the IDFT output of \mathbf{x}_{new} (see Figure 3.10). Note how, in contrast to the windowing algorithm, the time domain signal remains almost unchanged. The computational complexity introduced by the algorithm can be reduced by considering just a few samples per sidelobe.

Several OFDM spectra for different conditions may be seen in Figure 3.11. The first row

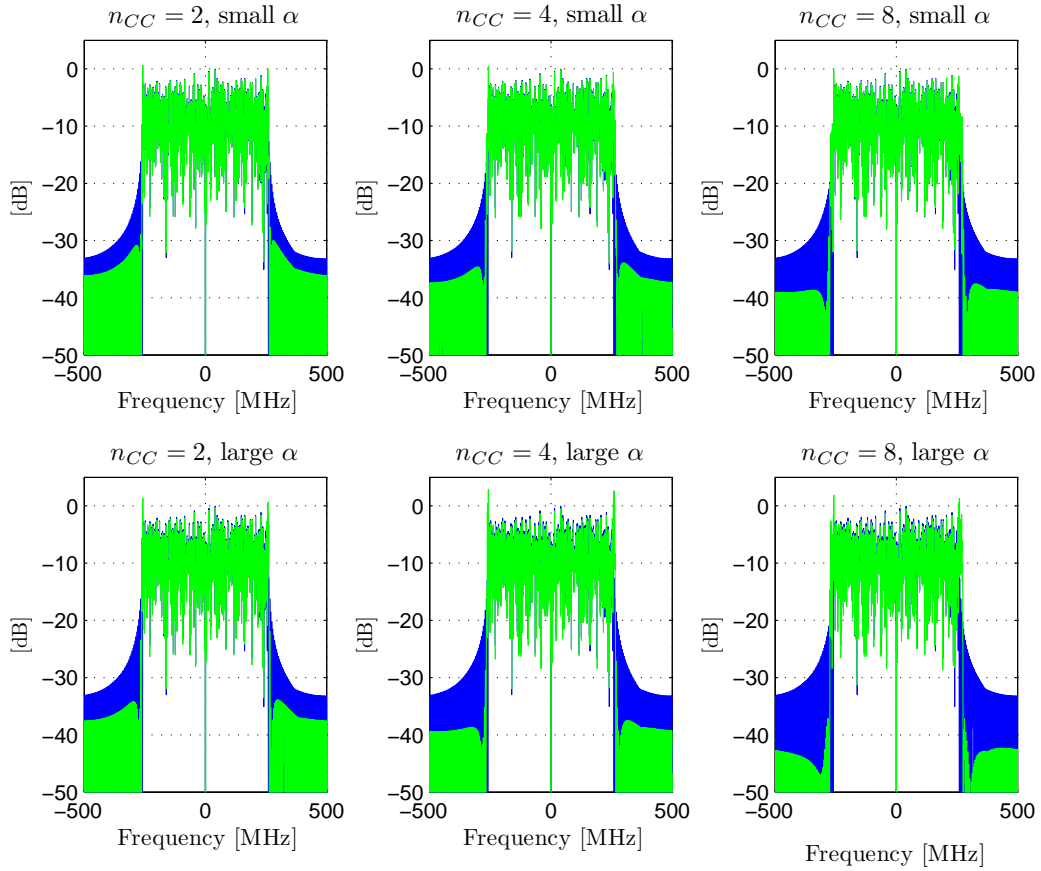


Figure 3.11: Averaged OFDM spectrum over 24 time domain symbols for different CCs scenarios.

is for very small α (small portion of the power dedicated to the CCs) and the second row for a slight more larger value of α , but still low enough to avoid a large increase on PAPR. The sidelobe power decreases with the increase of the number of used CCs (over the columns) and with the increase of available power (over the rows). PAPR, spectral efficiency and the reduction of out-of-band radiation are tightly together, it is a trade-off triangle. An important remark is that the performance of this algorithm is highly dependent on the OFDM data. For the same algorithm parameters, two different transmissions will have different optimized spectra.

Since the OFDM data is normalized by A , the power used for the "useful" data transmission is less and the signal to noise ratio decreases. The degradation in SNR is shown to be [1]

$$SNR_{degr} = 10 \log_{10} \left(\frac{1}{A} \right) \quad (3.10)$$

SNR loss can be controlled by properly choosing α . The maximum degradation is achieved when the cancellation carriers use all the power available for the optimization, i.e. $\|g\|^2 = \alpha$, for all OFDM symbols.

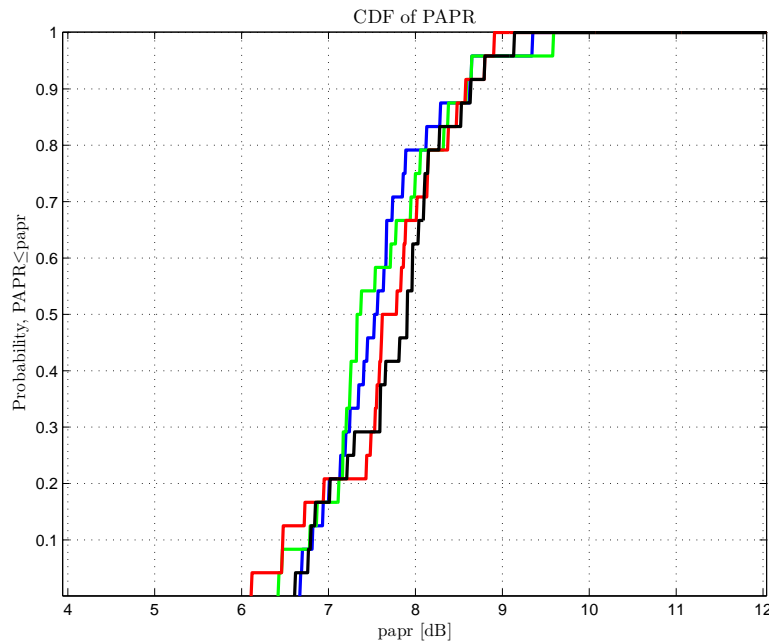


Figure 3.12: CDF of the PAPR for the original OFDM signal (blue) and OFDM signal with $n_{CC} = 8$ and small α (green), large α and $n_{CC} = 8$ (red) and large α and $n_{CC} = 4$ (black).

3.2 Amplifier's Non Linearity and PAPR

Peak-to-Average Power Ratio is defined as [37]

$$PAPR = \frac{\max |\mathbf{s}|^2}{E\{|\mathbf{s}|^2\}} \quad (3.11)$$

Theoretically, the difference of PAPR between a multi carrier system and a single carrier system using the same carrier modulation depends on the number of carriers K as $\Delta(\text{dB}) = 10 \log_{10}(K)$. This ends up being an overestimate of the reality, since the OFDM data is random enough to never reach this maximum value, specially when the constellation size is large.

The CDF (Cumulative Density Function) of the PAPR for the 64-QAM OFDM signal described in the beginning of this chapter may be seen in Figure 3.12 in blue. Together, there are three more curves for signals generated with cancellation carriers.

From the green, black and red curve, it is observed that, for the same α , the PAPR decreases if the power dedicated to the CCs is spread over more carriers. Since the simulations were done with random data, it can be concluded that with or without cancellation carriers, the PAPR should not be larger than 9/10dB.

An OFDM signal peak is obtained by the alignment at some point in time of a considerable subset of the K carriers. Thus, clipping these peaks has a distorting effect on all the carriers

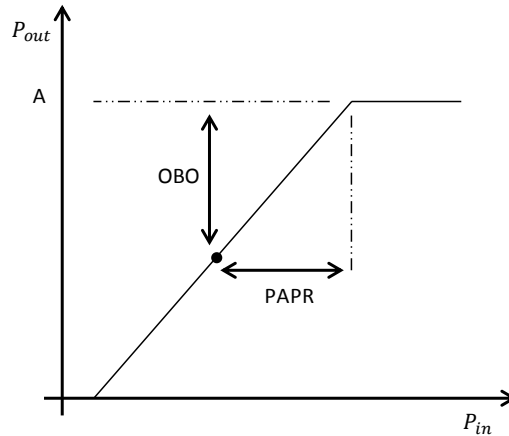


Figure 3.13: HPA's transfer function and required OBO (Output Back-Off) depending on the PAPR.

from that subset at once (refer to Section 2.5). To ensure that the OFDM signal peaks stay within the amplifier's linear range so that the signal does not clip, the average output power has to be backed off for at least the PAPR estimation (see Figure 3.13) [38].

In reality, the amplifier's transfer function is never linear near the saturation point, which means that the $OBO \neq PAPR$. However, the estimation is considered to be good enough, specially if a reasonable safe margin is added. This safe margin will be different for each amplifier, depending on its transfer function near saturation. The required P_{-1dB} compression point and amplifier gain may only be determined after complete knowledge of the receiver characteristics (see Chapter 5).

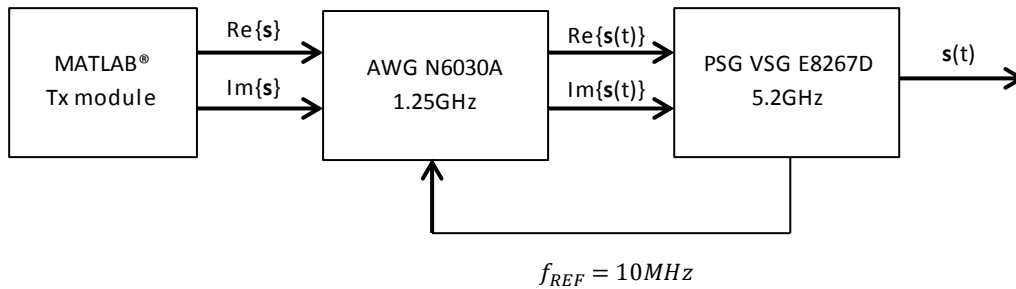


Figure 3.14: Block diagram of the transmitter setup.

3.3 Experimental Setup

For the transmitter module, the setup consists of an AWG (Arbitrary Waveform Generator) and a PSG (Programmable Signal Generator) vector signal generator to create the OFDM signal (Figure 3.14).

The AWG N6030A from Agilent has a defined set of control functions in MATLAB® for ease of integration. The transmitter MATLAB® module mentioned throughout this chapter is loaded on the AWG as well. The AWG has an internal clock of 1.25GS/s, so this is the adopted sampling frequency for the moment. To enable the use of such a sampling frequency without limiting the transmitter module’s freedom for different scenarios, the OFDM signal is always oversampled. Thus, the MATLAB® transmitter module puts on the output two time domain vectors I and Q upsampled to 1.25GHz and these are the vectors loaded into the AWG. For the output analog signals I and Q, two wideband channels of 500MHz each are available. The AWG is used in continuous mode, so the N_w symbols length OFDM message is played in a loop. One of the AWG features worth spending a few words on is the pre-distortion function. In the AWG’s manual [39], the following is said

The pre-distortion function compensates for the variation in the magnitude of the output response as a function of frequency. This variation is the result of the $\sin x/x$ (sinc) roll-off of the internal DAC and the frequency response of the reconstruction filter. The correction method uses filters to level the amplitude response and to create a linear phase response at the front panel of the AWG. This process attenuates the signal as a function of frequency, but cannot increase the signal above the maximum output voltage. Therefore, it is necessary to attenuate the lower frequency signals. This results in a reduced output voltage and dynamic range at all frequencies, but with uniform response across the full frequency range.

Hence, for the OFDM spectrum, this would mean less power attributed to the lower frequency carriers. Figure 3.15 shows the technical characteristics for the AWG’s analog outputs as provided by the Agilent’s manual. Without the pre-distortion filter, the variation over frequency accounting for the uncompensated roll-off and reconstruction filter is stated to be within $\pm 1dB$ for the range DC to 200MHz and within ± 3.5 for the range DC to 500MHz. Since the

Analog output

Output connector: SMA female
Output impedance: ~50 ohms

Analog output levels

The following output levels are specified into 50 ohms:

	Single-Ended	Differential
Passive Mode	0.5V p-p	1V p-p
Active Mode	1V p-p with +/-0.2V p-p	N/A

Uncorrected passband flatness: +/- 1 dB DC - 200 MHz; +/- 3.5 dB DC - 500 MHz (with 1.25 GHz clock)
Uncorrected passband group delay: +/- 500 ps DC - 200 MHz; +/- 1 ns DC - 500 MHz (with 1.25 GHz clock)

Reconstruction filters

500 MHz and 250 MHz realized as 7-pole elliptical filters plus thru-line output

Figure 3.15: Analog outputs technical characteristics provided in the AWG N6030A manual.

attenuation for the lower frequency carriers would be higher and only up to 300MHz are used on each channel, the pre-distortion feature was disabled.

The AWG's outputs are fed into the E8267D synthesizer from Agilent [40] where they are upconverted to a pre-determined frequency. At the PSG VSG's single ended output, there is a real signal $s(t)$ with a bandwidth centered at a frequency chosen by the user.

The following measurements were made at baseband with no resort to the synthesizer. The sampling scope used was the *Infiniium* DSO80304B scope from Agilent. Figure 3.16 shows the sampling scope's noise floor measured with 50Ω loads on the channel's inputs. The sampling scope alone should allow to measure spectra down to -100dB with no averaging. The spectra and time domain signals with and without cancellation carriers and windowing measured with the scope on the output of the AWG are given side to side with the ones from MATLAB[®] on Figures 3.17 to 3.20. It can be concluded that the spectra follow the expected behavior, but it is not possible to measure more than 50/60dB lower than the in-band level due to the presence of a wideband noise floor imposed by the AWG. The time domain OFDM signals are well reproduced and no clipping or distortion is observed. On Figures 3.19 and 3.20 a 70% symbol extension is used. For the 24 symbol length message example, these would represent a total transmission time of about $10\mu\text{s}$, which is very close to the limit of the typical figures given in Chapter 1. Since the factor with most weight to improve windowing performance is to increase the symbol extension even more, it becomes an unviable option.

The overlapped spectra measured with the scope on the output of the AWG for the scenarios

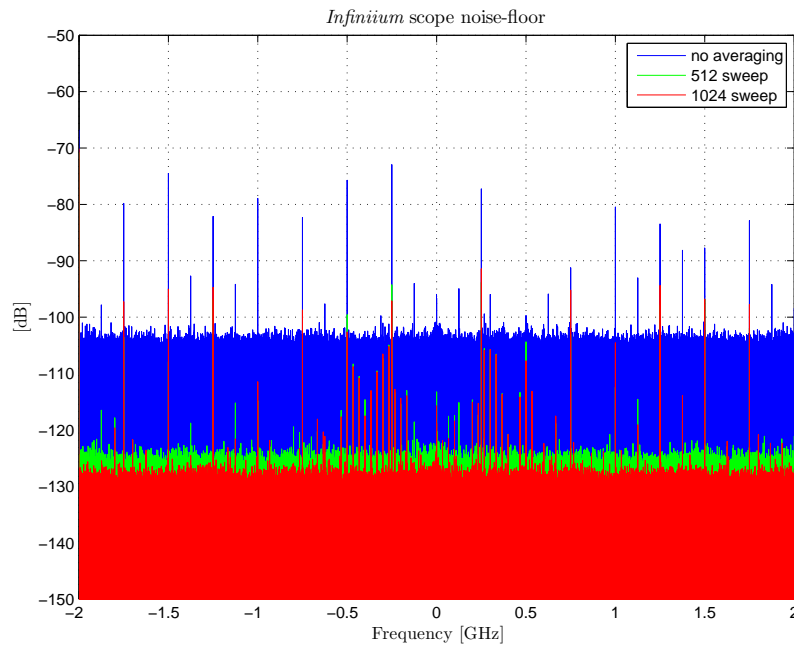


Figure 3.16: *Infiniium* scope's noise floor with no averaging (blue), 512 average sweep (green) and 1024 average sweep (red).

with and without CCs, with and without windowing and with a combined solution are shown in Figure 3.21 for $n_{CC} = 6$, Figure 3.22 for a Gaussian window with 70% symbol extension and Figure 3.23, respectively. An improvement of around 20dB for CCs, 10dB for windowing and 15dB for the combined solution is accomplished. It is here clear that the cancellation carriers have a greater impact right near the spectrum edges, while windowing reduces the out-of-band radiation progressively away from the OFDM spectrum. The combined solution has the best of the two methods, reducing the sidelobe power right at the edge and continuously reducing it further away.

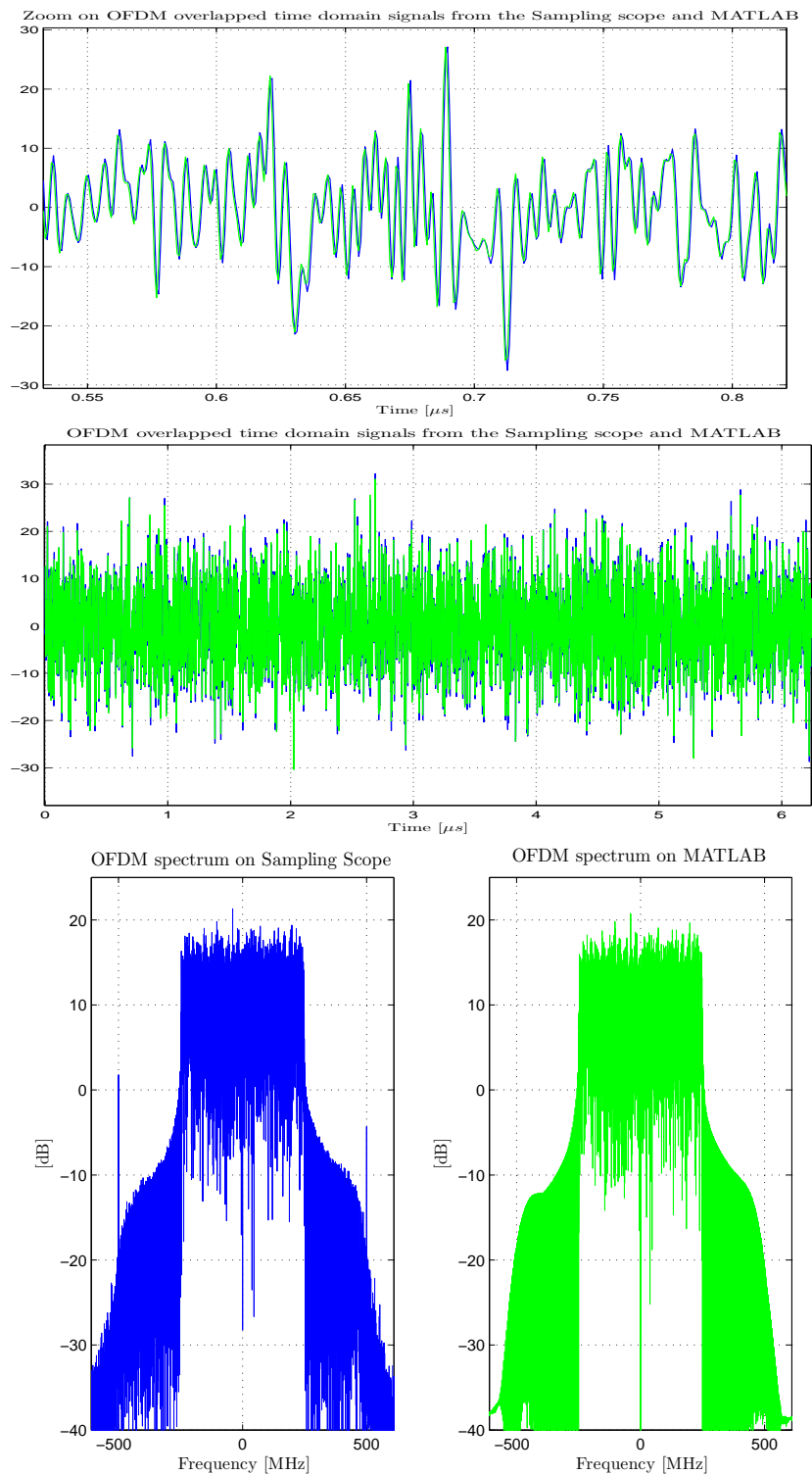


Figure 3.17: OFDM time domain signal (top) and 500MHz wide measured spectrum (down) at the output of the AWG (left) and computed on MATLAB[®] (right).

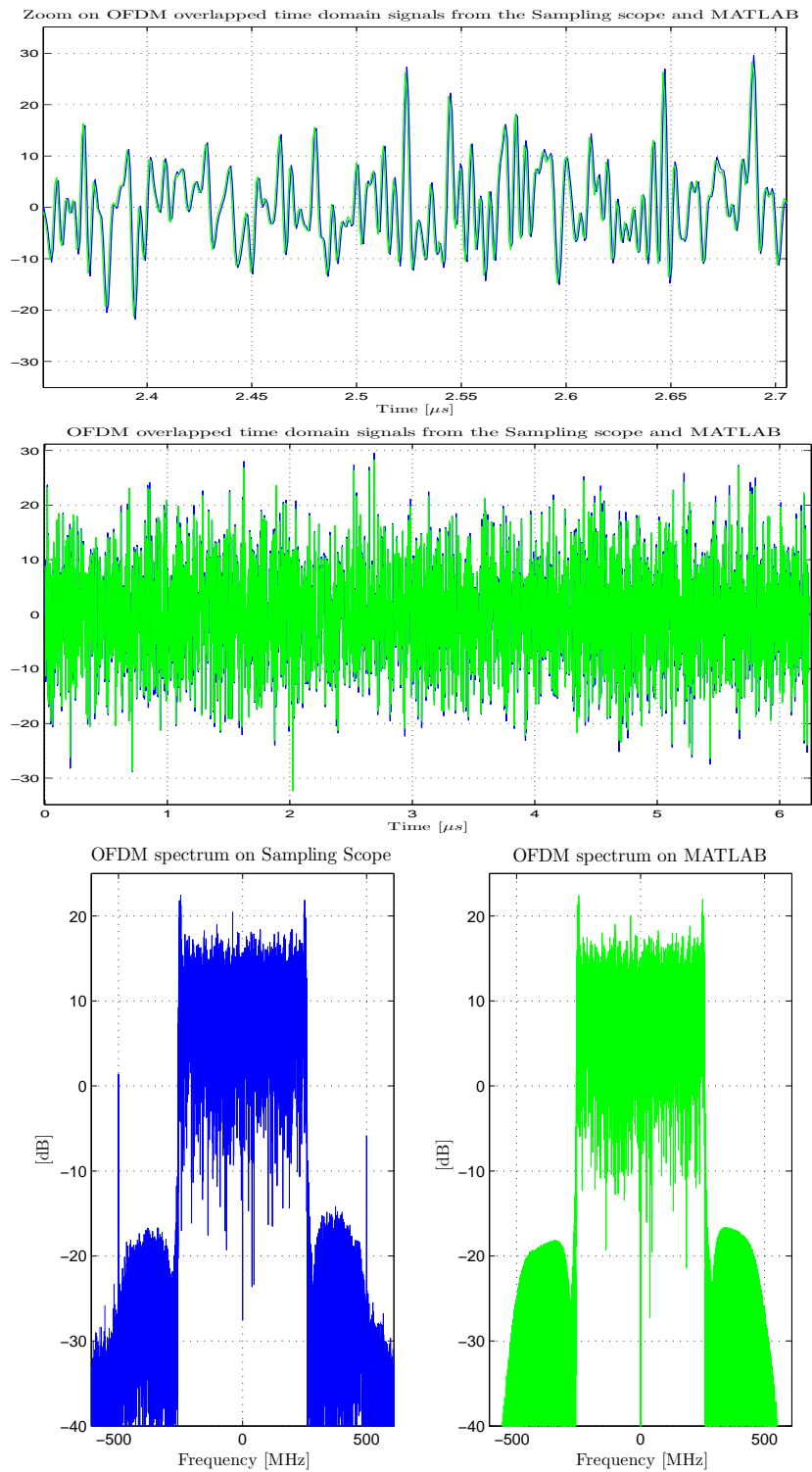


Figure 3.18: OFDM time domain signal (top) and 500MHz wide measured spectrum (down) at the output of the AWG (left) and computed on MATLAB[®] (right) optimized with cancellation carriers.

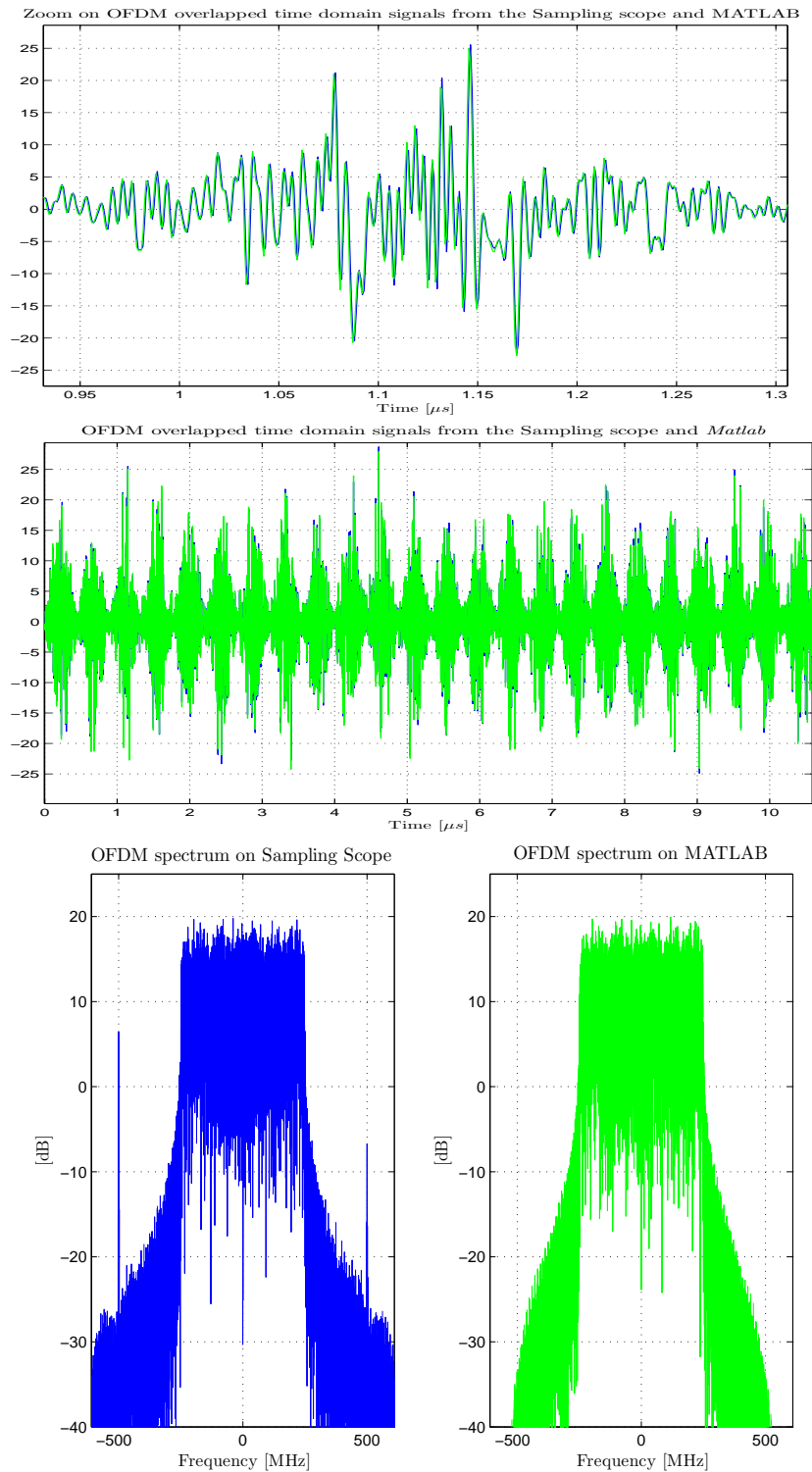


Figure 3.19: OFDM time domain signal (top) and 500MHz wide measured spectrum (down) at the output of the AWG (left) and computed on MATLAB[®] (right) optimized with a Gaussian, 70% symbol extension.

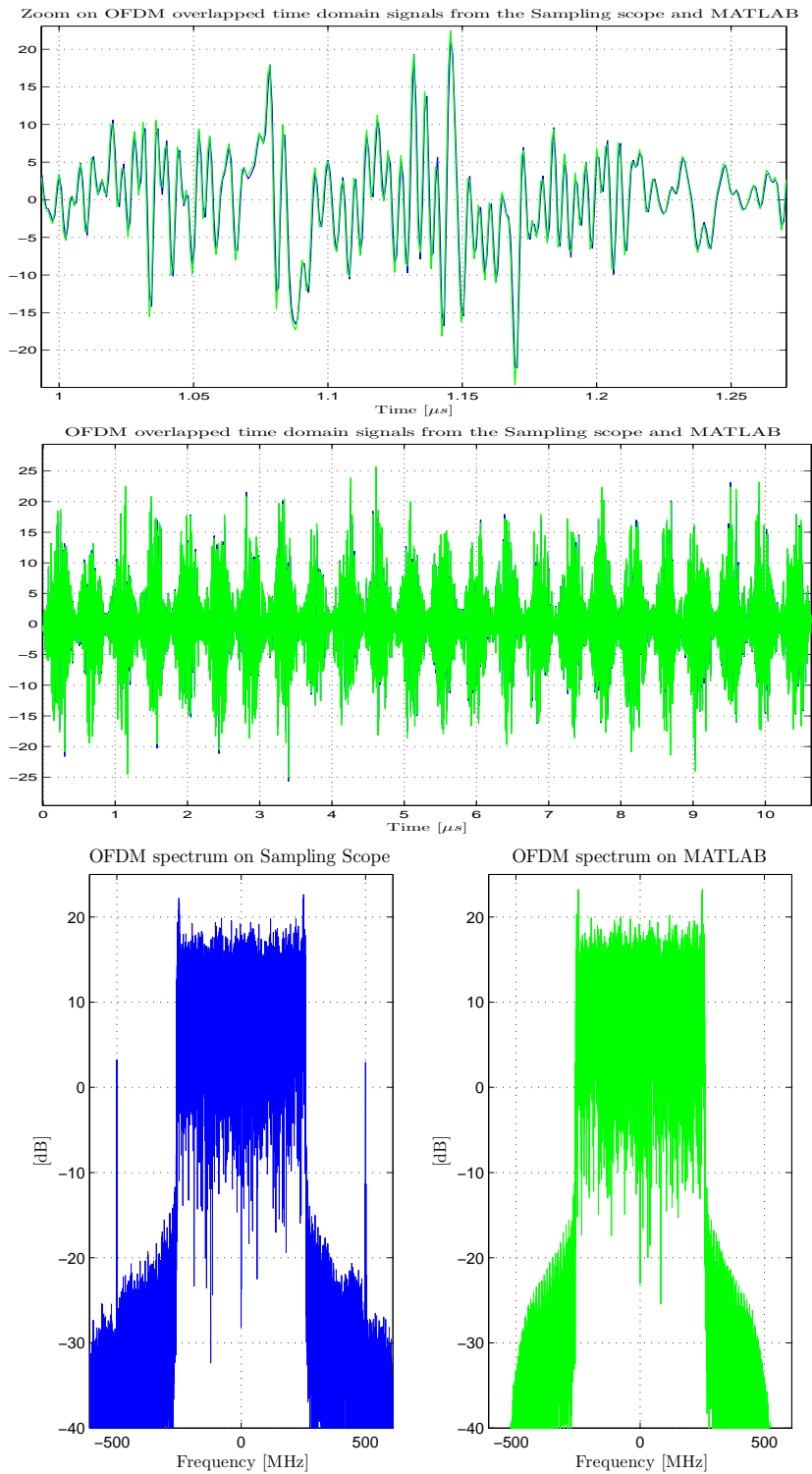


Figure 3.20: OFDM time domain signal (top) and 500MHz wide measured spectrum (down) at the output of the AWG (left) and computed on MATLAB[®] (right) optimized with cancellation carriers combined with a Gaussian window, 70% symbol extension.

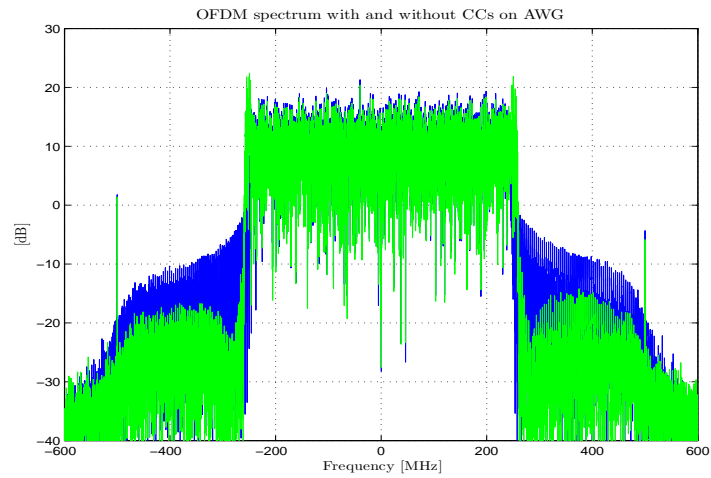


Figure 3.21: 500MHz wide OFDM spectrum measured at the output of the AWG with (green) and without (blue) cancellation carriers.

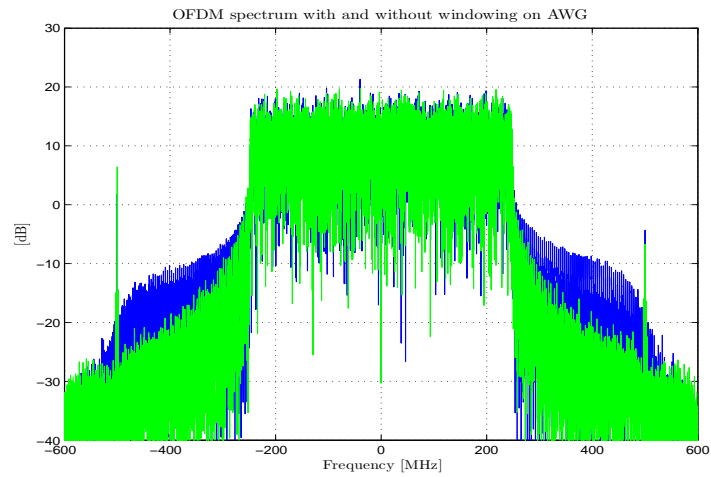


Figure 3.22: 500MHz wide OFDM spectrum measured at the output of the AWG with (green) and without (blue) windowing.

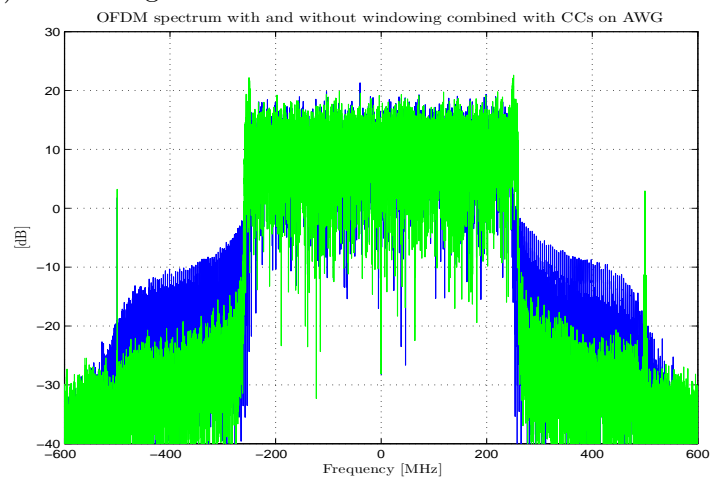


Figure 3.23: 500MHz wide OFDM spectrum measured at the output of the AWG with (green) and without (blue) windowing combined with CCs.

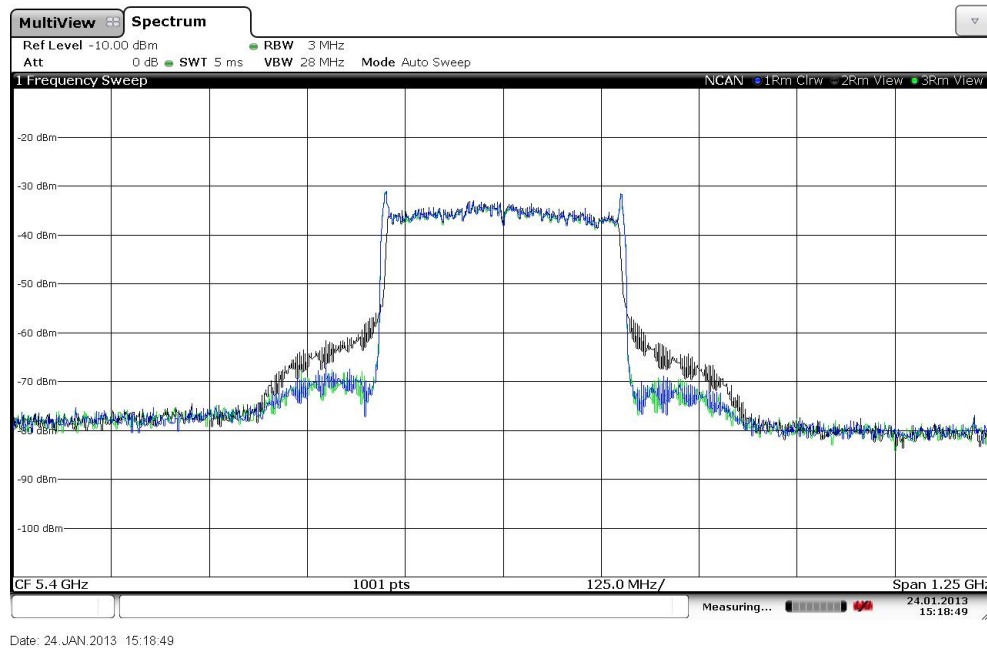


Figure 3.24: 300MHz wide OFDM spectrum transmitted at a central frequency $f_c = 5.4\text{GHz}$ with (blue) and without (black) cancellation carriers.

To wrap up the OFDM spectrum analysis, a final measurement was made using a Rhode&Schwartz FSW-26 spectrum analyzer for a 300MHz wide spectrum centered at 5.4GHz with and without cancellation carriers (Figure 3.24). It can be concluded that the synthesizer responsible for the up conversion does not have a significant contribution to the noise floor and that the overall transmitter chain is linear, giving the output expected from the MATLAB[®] simulations. It is observed a slight roll-off of the spectrum, consequence for not enabling the pre-distortion feature on the AWG. The roll-off seems to be about $\approx 2\text{dB}$, which is inline with the specifications.

The last task before moving on to the receiver chain, is to calibrate the I and Q channels of the synthesizer. IQ imbalance is usually defined as a problem on the receiver side, but due to the way the signal is generated in this setup, mismatches between the I and Q branches may occur on the transmitter side as well, more specifically in the analog part of the AWG and on the vector modulator built in the synthesizer. To check the ILR across the OFDM spectrum, 5 carriers were considered. Going back to the 64-QAM with one allocated carrier per receiver, the parameters were K (total number of carriers in the OFDM spectrum) equal to R (total number of receiver modules), were $R = 128$. Thus, to have a good idea of the I and Q imbalances along the spectrum, carriers 1, 26, 51, 80 and 105 were measured. In a 520MHz wide spectrum (260MHz for each side around f_c), for instance, this is the same as measuring at $f_c + 4\text{MHz}$, $f_c + 104\text{MHz}$, $f_c + 204\text{MHz}$, $f_c - 96\text{MHz}$ and $f_c - 196\text{MHz}$ for $\Delta f = \frac{520 \cdot 10^6}{R+2} = 4\text{MHz}$. To minimize the images at the output of the synthesizer, the gain on the I and Q branches and the phase difference between them relatively to 90° can be adjusted. To cancel out the LO leakage, the DC offset can be tuned. Table 3.1 gives the ILR measured for a single carrier at the above mentioned frequencies, as well the measured LO leakage, after

	$f_c - f$ [MHz]	P_{out} [dBm]	ILR [dBc]	LO [dB]
k_1	4	-23.2	-53	-63
k_{26}	104	-23.2	-45	-50
k_{51}	204	-23.5	-38	-45
k_{80}	-196	-23.2	-42	-46
k_{105}	-96	-23.0	-48	-52

Table 3.1: Power at the output of the synthesizer, ILR and LO leakage measured for 5 carriers across the wide OFDM bandwidth at a central frequency $f_c = 5.2\text{GHz}$.

calibration.

The ILR values are a bit tight for 64-QAM [35]. Hardware limitations was one of the reasons to try the two different scenarios for proof of concept — 64-QAM, one carrier per receiver, and 16-QAM, two carriers per receiver. 16-QAM is more robust to RF impairments (not only IQ imbalance in particular) and gives a nice, simple example for $K_r > 1$. LO leakage is now clear as one of the reasons to not modulate the carrier at f_c . Chapter 5 will give more details on this matter.

3.4 Conclusions

The concept used behind the transmission and its impact on the way the data is organized is explained. A step by step description of the OFDM signal's generation is made by breaking the transmitter chain into blocks for analysis. The techniques used for reduction of the out-of-band radiation were presented in Section 3.1. Given that the total transmission time is one of the limiting factors of the system where this work could be implemented, cancellation carriers were chosen over windowing. A brief overview of the PAPR of this solution and the impact of the cancellation carriers on it was made. It was concluded that the HPA at the end of the chain should have an OBO of around 10dB to preserve the OFDM signal linearity. To finalize, the experimental setup was described and measurement results were given. The measured spectrum behaves accordingly to what was expected with MATLAB[®].

Chapter 4

The Receiver Chain

The receiver side is where the difference to conventional OFDM (Chapter 2) is seen. Each receiver Rx_r is realized to only recover the data from its assigned band and for that, it only filters out a smaller band containing its K_r allocated carriers. Thus, instead of processing the entire OFDM bandwidth just to extract the data from a much smaller set of interest, this implementation processes just the K_r carriers of each receiver Rx_r and not more. The signal processing speed is greatly reduced with no loss in performance when compared to standard solutions.

A block diagram of the receiver section is given in Figure 4.1. Each receiver Rx_r consists of an LNA, followed by a quadrature mixer, which down-converts the received signal $r(t)$ to the complex IF signal $R_{IF}(t)$ using the tunable LO. The LO of each OFDM receiver is locked to the clock signal (see Figure 1.6) to maintain synchronization and it is chosen such that it tunes the desired band to a defined position within the bandwidth of the receiver filter (IF). Each output of the quadrature mixer is connected to the narrow filter which selects the set of carriers of interest K_r , and is followed by a low speed ADC. The ADC sampling

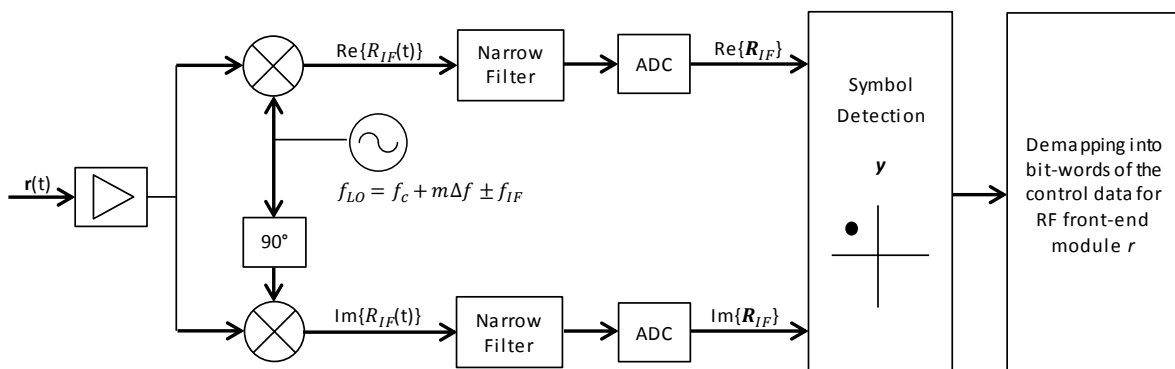


Figure 4.1: Block diagram of a receiver Rx_r .

rate is determined by the bandwidth of the narrow filter and the IF used. Each received OFDM symbol only carries as many constellation points for receiver Rx_r , as allocated carriers K_r . From the sampled IF OFDM symbol \mathbf{R}_{IF} , the transmitted K_r constellation points are retrieved. The receiver sequentially processes the incoming OFDM symbols until it has received the entire constellation for the control data message containing the RF front-end module settings for the coming RADAR transmission. For each RADAR transmission, a new OFDM message is sent and processed.

Due to limitations imposed by the available hardware, the proof of concept solution uses a direct conversion receiver architecture. To avoid a direct conversion of any of the carriers of interest to DC, the LO is tuned to the carrier left of the first carrier of interest. Nevertheless, this is not to be seen as a limitation of the concept. The concept can be extended without any added limitations to different architectures and downconversion solutions (as described in the above paragraph for the more general case).

In the next sections, the demodulation is explained step by step for an ideal channel with no RF impairments. Unless stated otherwise, the same example used in Chapter 3 for 64-QAM OFDM, one carrier per receiver Rx_r , will be assumed.

4.1 Demodulating the Carrier of Interest: step-by-step

After the LNA, the first block in the receiver is the quadrature mixer. The LO controlling the mixer is tuned to

$$f_{LO} = f_c + m\Delta f - f_{IF} \quad \text{with } m \in \left[-\frac{K}{2}, \frac{K}{2}\right] \quad (4.1)$$

For the example case, IF is Δf and, since each receiver only has one dedicated carrier that is downconverted to the first place right of DC, $m = r$ for receiver Rx_r . However, since the receivers are numbered from 1 to R ($R = K$, for this example) and the OFDM carriers are placed around f_c from $[-\frac{K}{2}, \frac{K}{2}]$, the index must be adjusted accordingly for $r > \frac{K}{2}$. For receiver r^{th} ,

$$f_{LO} = \begin{cases} f_c + (r - 1)\Delta f & \text{if } r \leq \frac{K}{2} \\ f_c + (r - K - 2)\Delta f & \text{if } r > \frac{K}{2} \end{cases} \quad (4.2)$$

The first step of the demodulation is then the downconversion of the carrier of interest to baseband. The complex baseband OFDM symbol is defined as

$$R_{IF}(t) = r(t)e^{-2\pi f_{LO}t} \quad (4.3)$$

with $IF = \Delta f$. The OFDM symbol is thus divided into two signals: Inphase (I) and Quadrature (Q). Each signal is afterwards filtered with a lowpass narrow filter of bandwidth B_{NF} and converted to the digital domain by a low speed ADC. The trade-offs between the filter bandwidth B_{NF} and the ADC's sampling rate will be discussed later in this section.

The second step of the demodulation is performed in the digital domain over the sampled complex baseband signal \mathbf{R}_{IF} . From all the K frequencies composing the OFDM symbol, the receiver Rx_r looks to its carrier frequency k_r that is now at Δf . The symbol y_r is determined as

$$y_r = \mathbf{R}_{IF} e^{-i2\pi k_r \frac{n}{N_{DFT}}} \quad (4.4)$$

with $k_r = \Delta f$. If $K_r > 1$, k_r is no longer Δf but a vector \mathbf{k}_r consisting of the K_r carrier frequencies of receiver Rx_r . For that case, y_r is also not a single symbol, but a vector of K_r symbols. N_{DFT} is determined by the ADC's sampling rate.

An unconventional receiver

There are two details that may go unnoticed if attention is not paid to them. One, is the fact that the DFT is performed in two steps instead of a single summation operation. The second, is the undersampling by the ADC, allowed by the narrow filter, which makes $N_{DFT} \ll N_{IDFT}$. Both will be explained in the following paragraphs for the general case, not restricted to the one introduced in the beginning of this section.

While in a standard DFT the symbol on carrier k is retrieved by summing all the time samples (i.e., sampled phases) of the frequency $k\Delta f$ of the OFDM symbol, in this implementation the symbol is retrieved in two separate sets of summation operations. The first is when the signal is downconverted and the second is on the digital processing part of the ADC output. For the two separate sets of summation operations to be equivalent to the single standard DFT sum, both summations must start at the same phase for each symbol. This may not be the case when a CP is added to the transmitter block.

In conventional OFDM receivers, the CP is not an issue, because the appended copy is taken out of the sampled signal before the DFT operation. Assuming no synchronization errors and an ideal channel, all carriers start with the phase defined in the transmitter and the sum of all time samples for each carrier results in the vector of complex values originally used on the IDFT input. In this implementation, however, the first part of the DFT is the downconversion itself, which uses a continuously running oscillator and an unprocessed OFDM signal, i.e. the OFDM symbol still has its CP. Since the oscillator is always running on the background as different symbols arrive, it will be at a different phase at the start of each them.

A further detailed explanation is given in Thales' internal appendix.

The second detail concerns the low speed ADC. To understand how the undersampling works and how it is related with the narrow filter bandwidth B_{NF} , the explicit matrix form of the IDFT/DFT will be considered. For this explanation only, let $x(n)$ be the IDFT output/DFT input and $X(k)$ be the IDFT input/DFT output. Time samples are represented by $n \in [0, N - 1]$ and frequency samples are represented by $k \in [0, N - 1]$. Assume the mixer's LO tuned such that the spectrum after downconversion is centered at f_{IF} (4.1). If $f_{mix} = |f_{LO} - f_c|$ is not a multiple of Δf , f_{IF} will not be at a frequency bin of the OFDM spectrum. Let ξ be the frequency distance of f_{IF} to the next OFDM carrier and \mathbf{W}_N^{kn} to be

$$\mathbf{W}_N^{kn} = e^{-i2\pi k \frac{n}{N}} \quad (4.5)$$

The IDFT and the DFT are then defined as

$$\begin{cases} \text{IDFT:} & x(n) = \sum_{k=0}^{N-1} X(k)w_N^{-kn} \\ \text{DFT:} & X(k) = \frac{1}{N} \sum_{n=0}^{N-1} e^{-i2\pi\frac{f_{LF}+\xi}{\Delta f}\frac{n}{N}} x(n)w_N^{kn} \end{cases} \quad (4.6)$$

and may be seen in matrix form as

$$\begin{bmatrix} x(0) \\ x(1) \\ \vdots \\ x(N-2) \\ x(N-1) \end{bmatrix} = \begin{bmatrix} 1 & 1 & \dots & 1 \\ 1 & w_N^{-1} & \dots & w_N^{(N-1)(-1)} \\ \vdots & \vdots & \ddots & \vdots \\ 1 & w_N^{(-1)(N-1)} & \dots & w_N^{-(N-1)(N-1)} \end{bmatrix} \begin{bmatrix} X(0) \\ X(1) \\ \vdots \\ X(N-2) \\ X(N-1) \end{bmatrix} \quad (4.7)$$

and

$$\begin{bmatrix} X(0) \\ X(1) \\ \vdots \\ X(N-2) \\ X(N-1) \end{bmatrix} = \begin{bmatrix} 1 & 1 & \dots & 1 \\ 1 & w_N^1 & \dots & w_N^{(N-1).1} \\ \vdots & \vdots & \ddots & \vdots \\ 1 & w_N^{(N-1).1} & \dots & w_N^{(N-1)(N-1)} \end{bmatrix} \text{diag} \left(e^{-i2\pi\frac{f_{LF}+\xi}{\Delta f}\frac{n}{N}} \right) \begin{bmatrix} x(0) \\ x(1) \\ \vdots \\ x(N-2) \\ x(N-1) \end{bmatrix} \quad (4.8)$$

,respectively. $\text{diag}(\cdot)$ is a diagonal matrix of size $N \times N$.

If there are no synchronization errors and the channel is ideal, the time domain signal in the receiver after downconversion to IF may be represented as in the IDFT with an extra frequency shift: $\mathbf{x}_n = e^{i2\pi\frac{f_{LF}+\xi}{\Delta f}\frac{n}{N}} \mathbf{W}_N^{-kn} \mathbf{x}_k$ (note that, in the transmit side, the IDFT defined by Equation 4.7 to generate the OFDM signal is performed at baseband). Filtering $K_f = B/\Delta f$ carriers is the same as selecting K_f columns in the matrix \mathbf{W}_N^{-kn} that defines the time domain signal, i.e. the new time domain signal is composed of K_f frequencies and only those frequencies have a real contribution to the DFT. Filtering K_f carriers of the time domain signal is the same as changing the matrix \mathbf{W}_N^{-kn} representing \mathbf{x}_n to

$$\mathbf{W}_N^{-kn} = \begin{bmatrix} 1 & 1 & \dots & 1 & 1 & \dots & 1 \\ 1 & w_N^{-1} & \dots & w_N^{-\frac{K_f}{2}} & w_N^{-(-\frac{K_f}{2}+1)} & \dots & w_N^{(-1)} \\ \vdots & \vdots & \dots & \vdots & \vdots & \dots & \vdots \\ 1 & w_N^{-(N-1)} & \dots & w_N^{-(N-1)(\frac{K_f}{2})} & w_N^{-(N-1)(-\frac{K_f}{2}+1)} & \dots & w_N^{-(N-1)(-1)} \end{bmatrix} \quad (4.9)$$

The changes on the time domain signal represented by using the \mathbf{W}_N^{-kn} matrix, give an immediate visual understanding of how its hermitian on the DFT side will look like. Filtering K_f carriers on the time domain signal, reduces the available spectral information from K to K_f . Thus, the remaining data after the filter may be retrieved with a smaller DFT matrix of size $[K_f \times N]$. This matrix \mathbf{W}_N^{kn} may be reduced even further if the receiver is only interested

in a number of carriers $K_r < K_f$. In this case, the matrix only needs to have K_r rows (note that \mathbf{W}_N^{kn} is the hermitian of \mathbf{W}_N^{-kn}). To give an example, consider the 16-QAM, two carriers per receiver, case study. The carriers of interest $k_{r,1}$ and $k_{r,2}$ are on the first two places starting on f_{IF} to the right. To recover the data, the performed DFT is

$$\begin{bmatrix} X(k_{r,1}) \\ X(k_{r,2}) \end{bmatrix} = \begin{bmatrix} 1 & w_N^1 & \dots & w_N^{(N-1).1} \\ 1 & w_N^2 & \dots & w_N^{(N-1).2} \end{bmatrix} \text{diag} \left(e^{-i2\pi \frac{f_{IF} + \xi}{\Delta f} \frac{n}{N}} \right) \begin{bmatrix} x(0) \\ x(1) \\ \vdots \\ x(N-2) \\ x(N-1) \end{bmatrix} \quad (4.10)$$

There are still N time domain samples. This matrix transformation englobing only K_f carriers makes it theoretically possible to reduce the ADC sampling rate to the limit, where the digital time domain signal has as many samples as filtered carriers. For instance, for the above mentioned example, if the narrow filter would let through 2 carriers on each side of f_{IF} , only 5 time domain samples per symbol would be necessary to recover the data for any of the 5 carriers. The described scenario is equivalent to have a square \mathbf{W}_N^{-kn} matrix with dimensions $[K_f \times K_f]$ representing the time domain signal at the output of the ADC. Hence, \mathbf{W}_N^{kn} matrix with size $[K_r \times K_f]$ may be used to perform the DFT and recover the information from the K_r allocated carriers of interest. As filtering is translated in selection of columns, downsampling is translated in selection of rows for the time domain matrix \mathbf{W}_N^{-kn} . It goes without saying that the selection of rows must be done in equal steps, i.e. if the sampling rate is such that $N_{ADC} = N/2$, rows 1, 3, ..., $N-4$, $N-2$ or rows 2, 4, ..., $N-3$, $N-1$ should be selected. It is not necessary for the first sample in the undersampled signal to be the first sample in the original time domain signal, as long as the low rate samples N_{ADC} are equally spaced over time in such a way that their sum in phase over the symbol length T_s is 2π .

The explanation above with the given image of downsampling by selection of rows may lead to the conclusion that the ADC sampling rate is conditioned to $\text{rem}(N_{IDFT}, N_{ADC}) = 0$. However, this is not the case. As stated before, the real condition is that the sum in phase of all samples equals 2π . For that to happen, they do not necessarily need to be placed at multiples of $\frac{1}{N_{IDFT}}$. For the sum to be equal to 2π , only an integer number of samples equally spaced over the OFDM time domain symbol is needed.

This approach of understanding, though pessimist in a way, is also optimist in the way that it suggests that is possible to sample down to K_f samples. It would be possible, indeed, but only in the ideal case where each carrier is a pulse of infinitesimal bandwidth and the receiver has a brick wall narrow filter. Practical systems do not fulfill these requirements. Figure 4.2 gives an illustration of how the filtered spectrum would be in a more realistic scenario. The example of 5 carriers within the designated band is reused from two paragraphs above. As it can be seen, besides the desired filtered carriers, there are a few more attenuated carriers and sidelobes in the filter's transition band until the actual stop band. As f_{ADC} is decreased, the green carriers start to fold on top of the red ones. This does not represent a problem while the carriers folding were way beyond the filter stop band and not folding on top of the carriers to be demodulated. However, if the ADC is to sample at the lowest extreme sampling rate, the less attenuated carriers will fold into the carriers of interest, degrading the signal

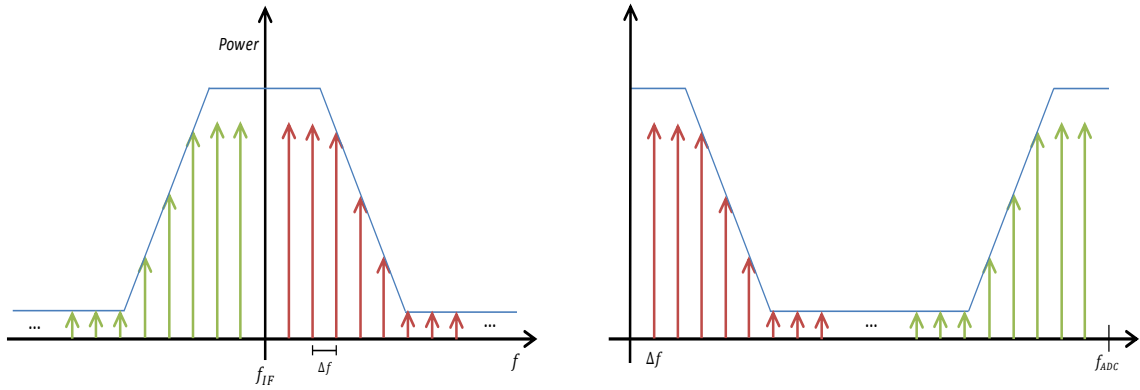


Figure 4.2: Illustration of the signal’s spectrum at the output of the narrow filter (left) and the result of sampling with $f_{ADC} > K\Delta f$ (right).

(see Figure 4.3) or even preventing the retrieval of data. How bad the folding affects the

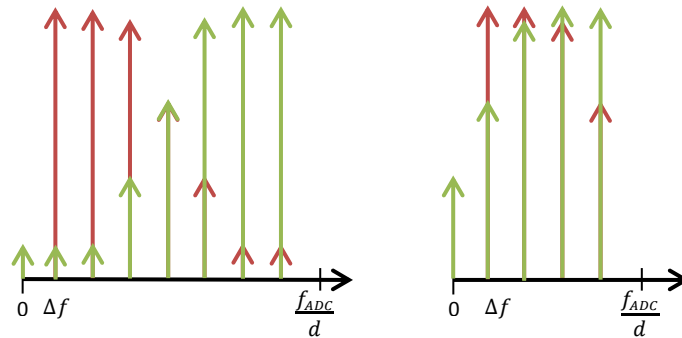


Figure 4.3: Illustration of the signal’s spectrum after extreme downsampling with decimation factor d ; example for a 8 points (left) and 5 points (right) DFT, i.e. $f_{ADC} = 8\Delta f$ and $f_{ADC} = 5\Delta f$, respectively.

signal will depend on its sensitivity to IQ imbalance. Indeed, the folding of carriers is not IQ imbalance per se, but when it is folded into the carrier the receiver is looking at, it has exactly the same effect. The type of modulation used will determine the maximum interfering power that can be tolerated at that frequency and thus determine the stop band required for the narrow filter. The stop band together with the steepness of the filter’s slope and the IQ imbalance sensitivity of the modulation will determine the minimum possible sampling rate for the ADC. However, a trade-off is hidden. If the filter’s slope is made too steep to decrease the ADC’s sampling rate to the maximum, the channel impulse responde is made larger and larger, increasing the length of the required CP and, consequently, the total transmission time of the OFDM message. Since total transmission time is a limitation of the system were this work would be integrated, a balance between the filter specifications and ADC sampling rate should be found.

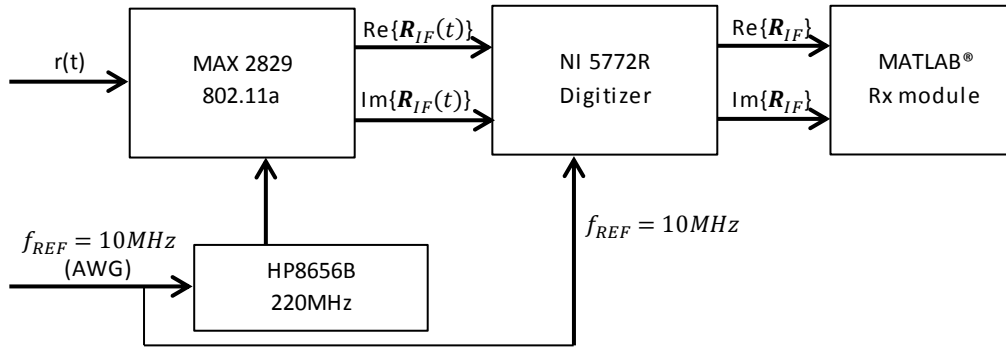


Figure 4.4: Block diagram of the receiver setup.

4.2 Experimental Setup

The receiver chain is modeled by two blocks: a MAX2829 chip from Maxim Integrated (Appendix B) and a 12bit ADC from National Instruments (NI 5772R) [41]. A block diagram of the experimental setup is given in Figure 4.4.

The MAX2829 chip is a single-chip designed for dual-band OFDM 802.11a/g WLAN applications. In this setup, band *a* that goes from 4.9GHz to 5.875GHz will be used. The integrated circuit provides a fully integrated receive path, VCO, frequency synthesizer and baseband control interface (Figure 4.5).

The Maxim chip is integrated in an evaluation kit to ease the testing. The kit includes 50Ω inputs/outputs for all RF and baseband signals on SMA connectors. Differential-to-single-ended line drivers are provided to convert the differential high impedance I and Q baseband outputs of the MAX2829 chip back to single-ended 50Ω ports with a voltage gain of 1. The conversion as it is done, results in an available power gain on board level that is equal to the voltage gain of the Maxim chip in dB. The evaluation kit is connected to the PC through a 3-wire interface. A user friendly control software is available. With the control software, LO frequency, filter bandwidth, VCO subband, VGA and LNA gain are easily tuned from the PC.

In particular, the VGA has an adjustable gain of 62dB in 31 steps and the same setting is used on the I and Q branch, i.e. a gain setting of G dB is actually $2G$ dB for the total VGA gain, considering both branches. The LNA gain is more difficult to control. Three windows are given — *Min*, *Mid* and *High* — with three different ranges: *High* to *Min* is specified as a -30.5 dB step and *High* to *Mid* is specified as a -15.5 dB step. Since the maximum voltage gain of the receiver is said to be 94dB of which the VGA is responsible for 62dB, it is reasonable to assume that $G_{LNA} = Min \approx (94 - 62) - 30.5 = 1.5$ dB, $G_{LNA} = Mid \approx (94 - 62) - 15.5 = 16.5$ dB and $G_{LNA} = High \approx (94 - 62) = 32$ dB.

For the lowpass filter bandwidth, there is a coarse setting that allows to choose between 7.5MHz, 9.5MHz, 14MHz or 18MHz bandwidth and a fine setting that adjusts the -3 dB corner of filter to 90%, 95%, 100%, 105% or 110% of the coarse setting (see Figure 4.6). For more information on the tuning ranges, refer to Appendix B.

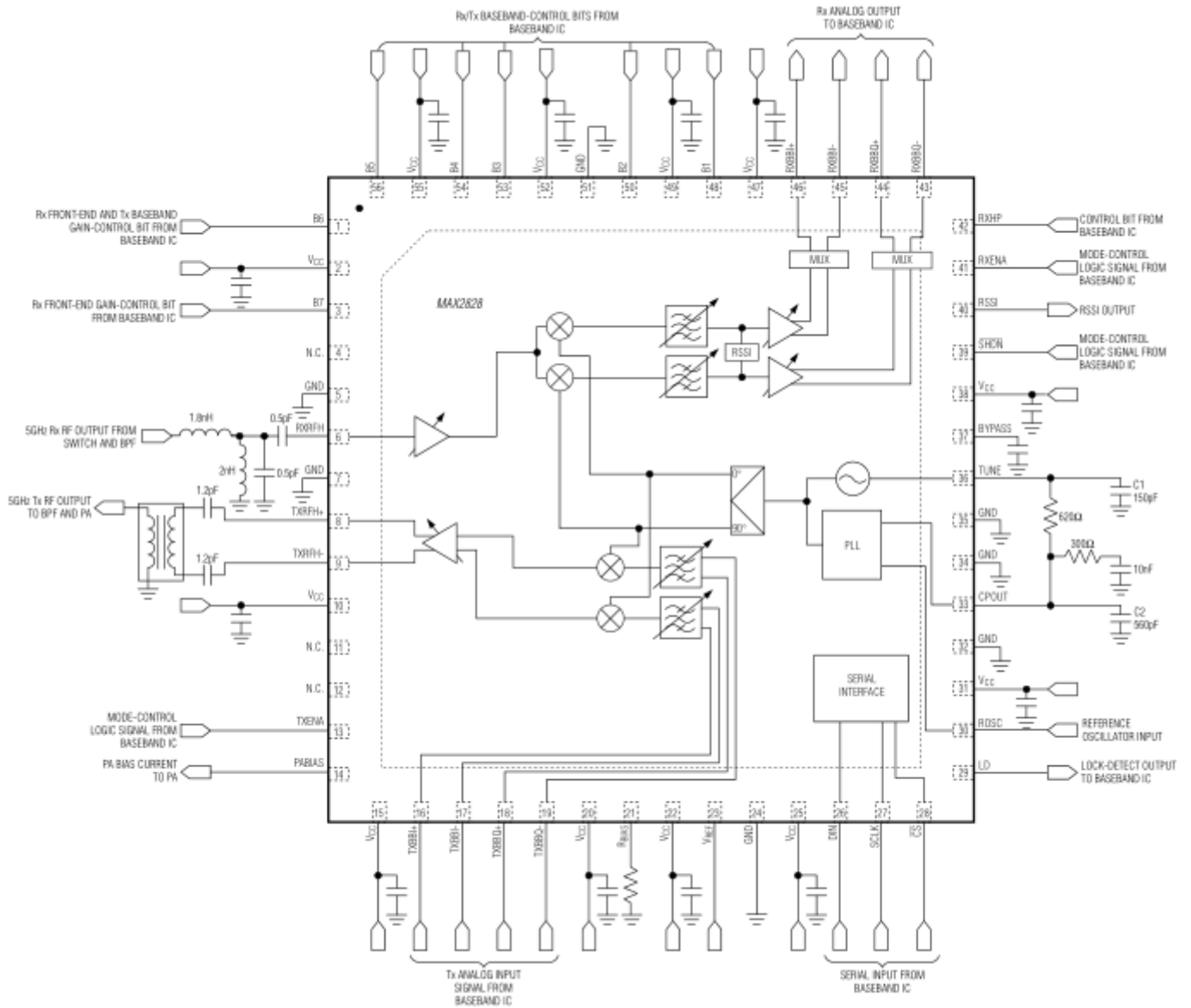


Figure 4.5: Block diagram of the MAX2829 chip.

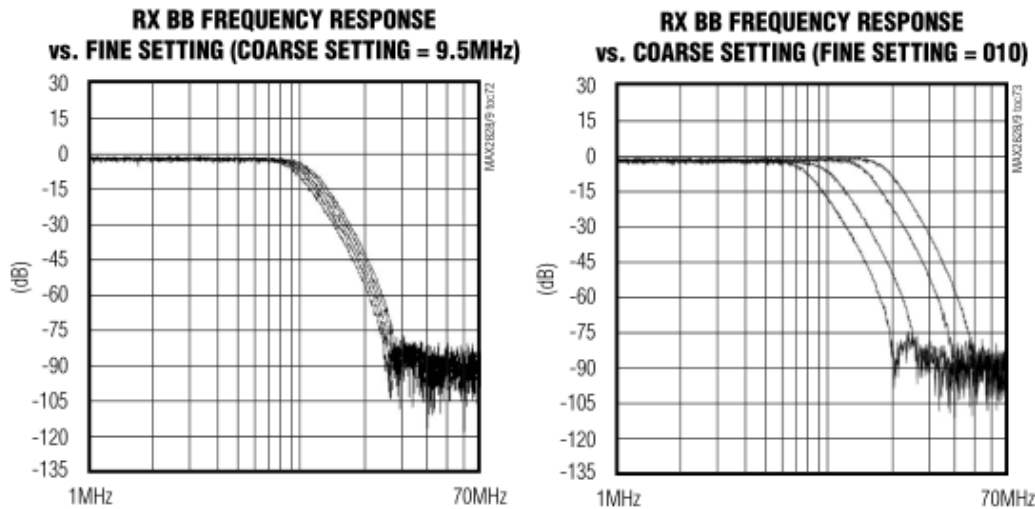


Figure 4.6: Frequency response of the MAX2829 chip filters for the fine settings (left) and the coarse settings (right).

The NI 5772R digitizer was designed to work together with NI FlexRIO FPGA module. It has two analog input channels with 12bit resolution and samples rates from 400MS/s up to 800MS/s when using both channels and 1.6GS/s if only one is used. The FPGA can be programmed with LabView for data acquisition. Besides the two analog inputs, it also has a trigger and a clock input that will be used later for the closed cycle measurements described on Chapter 5. The data retrieved with the digitizer can be post processed on MATLAB[®].

Before closing the cycle, a few figures are important to know that concern the receiver alone. Those are phase noise, NF (Noise Figure) and gain. For the following measurements, the vector modulator output is connected to the evaluation kit. To measure phase noise and gain, I or Q output of maxim chip is connected to a spectrum analyzer. For NF, both I and Q are connected to the digitizer, which output is digitally processed on MATLAB[®]. The transmission central frequency is $f_c = 5.2\text{GHz}$.

To confirm that different carriers along the spectrum have the same phase noise PSD and that those curves are in accordance with the ones given by the datasheet, the same carrier frequencies used in Section 3.3 for ILR measurements were considered. The measurements were done after downconversion to Δf , IF frequency considered for the proof of concept examples described in Chapter 3. For the downconversion, the LO was tuned to 5.2GHz, 5.3GHz, 5.4GHz, 5.0GHz and 5.1GHz for carrier 1, 26, 51, 80 and 105, respectively. VGA gain was set to 26dB and LNA gain was set to *Min*. Figure 4.7 is the plot of the overlapped phase noise power measurements given on Table 4.1 for each carrier.

All curves more or less follow the curve provided by Maxim Integrated, except for carrier 51 that has the same curve but higher values. In the Maxim's chip, the 802.11a band is divided into two sub bands; carriers 1, 26, 80 and 105 belong to the first sub band and $f_{LO} = 5.4\text{GHz}$ is not included in either of them. The performance of the LO is not specified for frequencies

δf [kHz]	k_1 [dBc/Hz]	k_{26} [dBc/Hz]	k_{51} [dBc/Hz]	k_{80} [dBc/Hz]	k_{105} [dBc/Hz]
1	-86.5	-85.7	-81.9	-86.5	-85.4
5	-95.5	-94.4	-87.5	-92.5	-95.0
10	-97.3	-95.0	-88.5	-94.7	-96.4
50	-96.4	-93.4	-88.1	-93.6	-95.4
100	-94.6	-92.5	-93.5	-92.3	-93.3
1000	-106.3	-108.1	-110.3	-106.8	-106.6

Table 4.1: Phase noise measurements at different δf offsets away from the carrier for a set of carriers across the OFDM spectrum after downconversion to Δf .

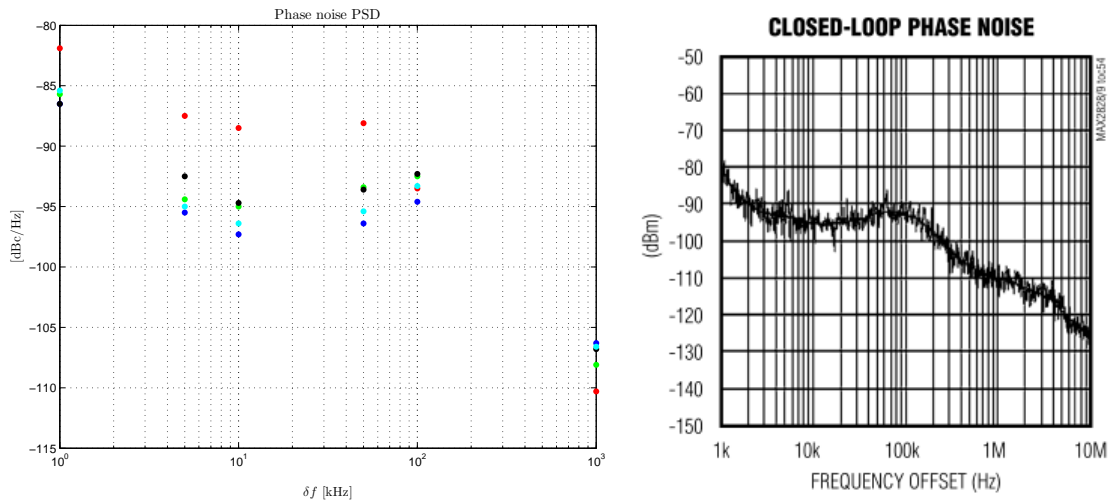


Figure 4.7: PSD phase noise curves for carrier 1 (blue), 26 (green), 50 (red), 80 (black) and 105 (cyan) on the left and phase noise PSD curve for $f_{LO} = 5.25\text{GHz}$ provided by Maxim Integrated on the right.

outside these sub bands.

Regarding the impact of phase noise on this receiver approach, not all of what was said on Section 2.5 can be directly applied. Each carrier is still affected by the phase noise close to the carrier, slow phase noise, which gives an error equal to all carriers and that does not depend on how many OFDM carriers there are. ICI due to phase noise further away from the carrier, fast phase noise, is however reduced. Not only because just a part of the spectrum is filtered, but also because the only carriers contributing to it will be the ones demodulated by receiver R_{x_r} , K_r . In the example of just one carrier per receiver, it may see the phase noise tail of the adjacent carriers with an effect similar to gaussian noise, but it won't see this kind of ICI. More on this matter will be discussed in Chapter 5.

To measure the receiver gain, the power of a carrier at the output of the receiver was measured and compared with the power set in the vector modulator for transmission at the input of the maxim chip. With the VGA gain set to 13dB per channel, the average measured gain for different carriers was of 27.9dB for LNA with *Min* gain (1.5dB) and 43.6dB for LNA

	$G_{LNA} = Min = 1.5dB$			$G_{LNA} = Mid = 16.5dB$		
	P_{in} [dBm]	P_{out} [dBm]	Gain [dB]	P_{in} [dBm]	P_{out} [dBm]	Gain [dB]
k_1	-23.2	4.9	28.1	-40.3	3.2	43.5
k_{26}	-23.3	4.4	27.7	-40.5	3.0	43.5
k_{51}	-23.5	4.0	27.5	-40.7	2.8	43.5
k_{80}	-23.3	4.9	28.2	-40.3	3.7	44.0
k_{105}	-23.0	4.9	27.9	-40.2	3.5	43.7

Table 4.2: Receiver gain for $G_{VGA} = 26dB$ and G_{LNA} at minimum and mid levels.

with *Mid* gain (16.5dB) (Table 4.2). The measured values are in line with the ones expected by looking at the gain curves provided by Maxim Integrated for different gain settings (Figure 4.8, on the left): $G = 26 + 1.5 = 27.5dB$ and $G = 26 + 16.5 = 42.5dB$, respectively.

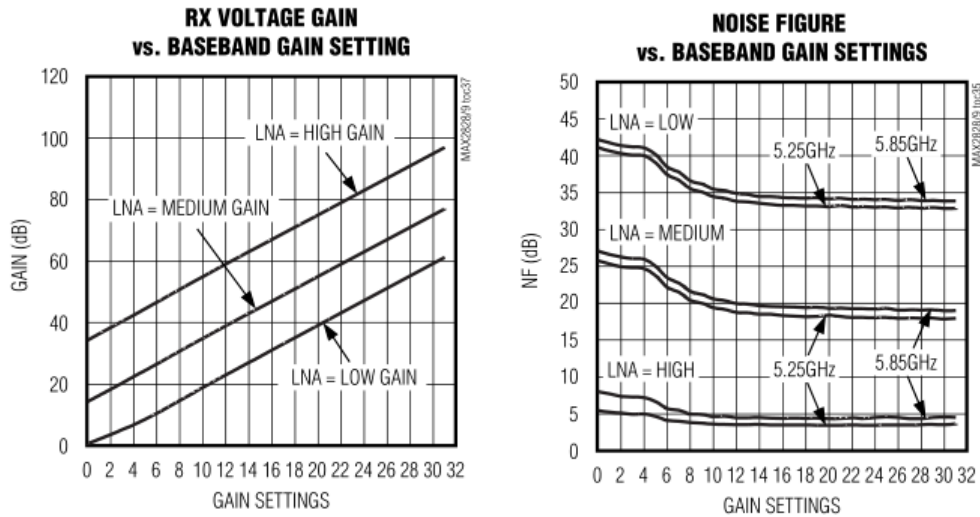


Figure 4.8: MAX2829 voltage gain (left) and NF (right) typical curves depending on the gain settings for the LNA and the VGA provided by Maxim Integrated.

The noise factor F of a device is defined by Friis [42] as the ratio of the available SNR at the device's input to the available SNR at the device's output. To derive the noise factor's expression, Friis defines four other figures first: available signal power, gain, available noise power and effective bandwidth.

The available signal power is divided in two parts: S_{in} , available signal power at the device's input, and S_{out} , available signal power at the device's output. The linear gain of the device G is the ratio between these two powers,

$$G = \frac{S_{in}}{S_{out}} \quad (4.11)$$

The available noise power is also divided in two: available noise power at the output N and available noise power at the input of the device. N is the power due to all the noise sources inside the device. The available noise power at the input is defined as κT , the noise

power between two terminals of a passive network when all parts are at the same temperature T . The contribution of this noise to the output noise is $G\kappa TB$, where $\kappa = 1.38 \times 10^{-23}$ is the Boltzman constant, T is the absolute temperature in Kelvin and B is the device's "operating" bandwidth in Hz. Note that, in this case, it is considered an ideal filter with flat gain G over B .

The noise factor F is then defined as

$$F = \frac{\frac{S_{in}}{\kappa TB}}{\frac{S_{out}}{N}} = \frac{S_{in}}{\kappa TB} \frac{N}{S_{out}} = \frac{1}{G} \frac{N}{\kappa TB} \quad (4.12)$$

For $T = 290K$, $\kappa T = -174\text{dBm/Hz}$ and the receiver's noise figure is

$$NF = 10\log_{10}(F) = 10\log_{10}\left(\frac{N}{B}\right) - G_{dB} - 174 \quad (4.13)$$

where $P_N = \frac{N}{B}$ is the noise power density in dBm/Hz at the receiver's output.

To measure the receiver's NF, a MATLAB[®] script was used to process the data acquired by the digitizer. Figure 4.9 shows the I and Q OFDM time domain signals and noise. Figures 4.10 and 4.11 show the receiver's OFDM output spectrum and noise, respectively. Noise measurements are made by putting I and Q to zero on the AWG inputs. From Figure 4.11, it can be concluded that the digitizer noise is about 20dB lower than the receiver, and thus that it does not have a relevant contribution to SNR degradation. The average measured NF for different carriers was of 15dB for G_{LNA} at mid level and of 30dB for G_{LNA} at minimum level. Typical curves on the MAX2829 datasheet show NF values in this range (Figure 4.8, on the right).

Another important topic is the harmonics. The harmonics of each single OFDM carrier will fall in the main bin of the nearby carriers and cause interference, so it is essential to assure that the spurious levels are well below the IQ imbalance sensitivity of the system. Figure 4.12 and 4.13 show the spectrum for a single carrier downconverted to $\Delta f = 4\text{MHz}$ for $G_{LNA} = \text{Min} = 1.5\text{dB}$, $G_{VGA} = 26\text{dB}$ and $P_{in} = -23\text{dBm}$ and $G_{LNA} = \text{Mid} = 16.5\text{dB}$, $G_{VGA} = 20\text{dB}$ and $P_{in} = -31\text{dBm}$, respectively. Central frequency for transmission is $f_c = 5.2\text{GHz}$. Sampling frequency of the sampling scope is 10GS/s. Orthogonality in OFDM is assured by placing the carriers at frequencies that are integer multiples of each other, so the harmonics of each carrier will fall right on top of the remaining OFDM carriers. These spectral components at multiples of the fundamental frequency will sum up with the images and degrade the SNR of each single carrier. On top of that, they will also contribute to the folding in the downsampling step. The measured levels are close to the ILR values from Table 3.1. Both these effects together turn the system even more unfriendly for 64-QAM, though still good enough for 16-QAM.

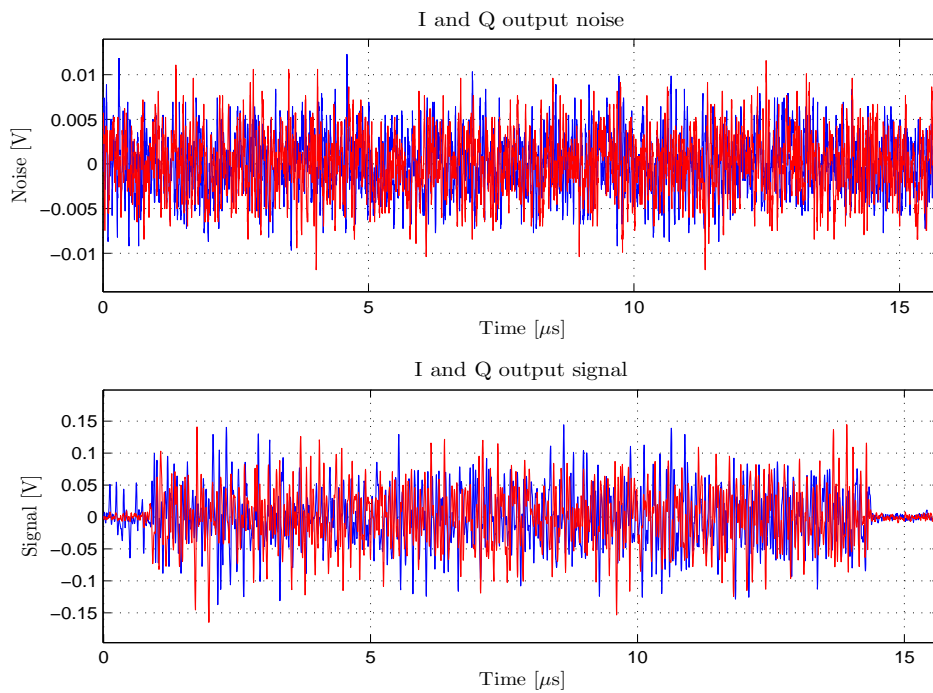


Figure 4.9: I and Q time domain signals at the output of the receiver.

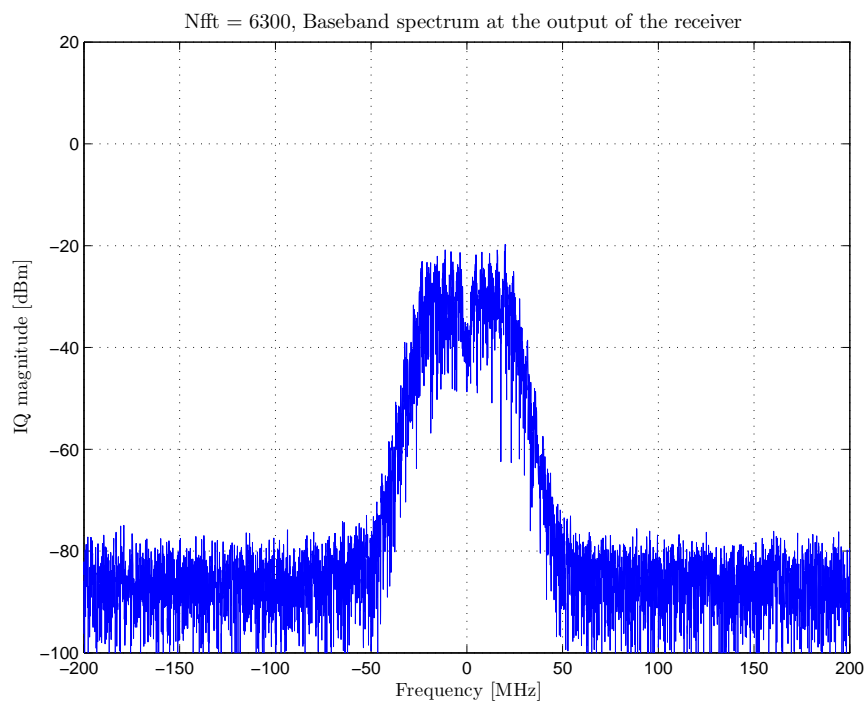


Figure 4.10: OFDM spectrum at the output of the receiver.

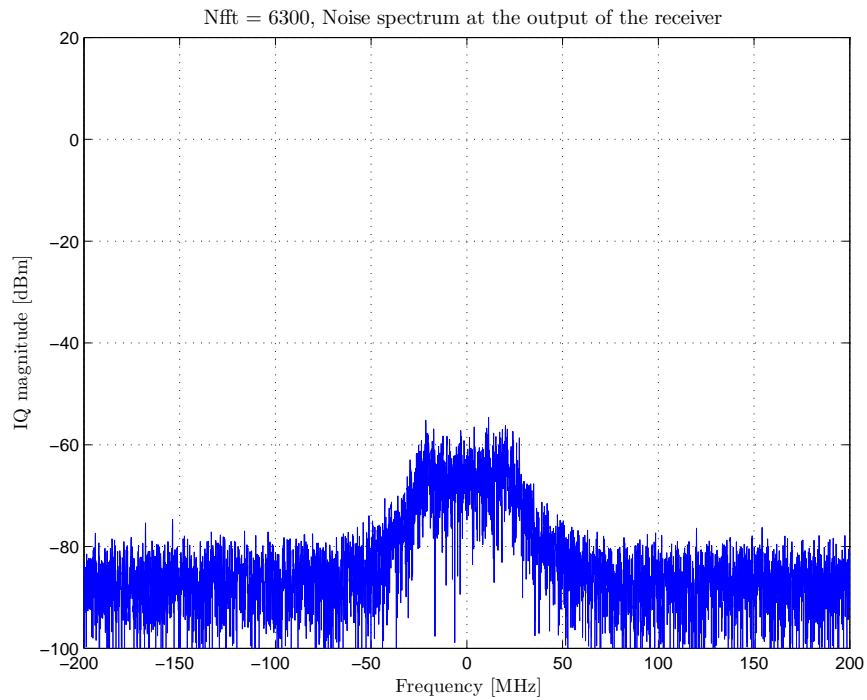


Figure 4.11: Noise spectrum at the output of the receiver.

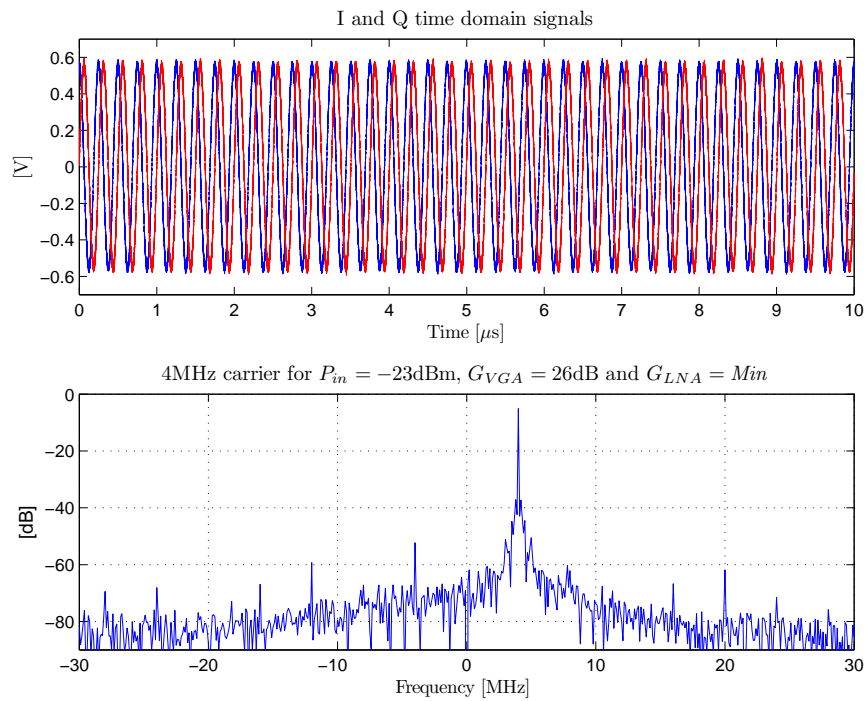


Figure 4.12: I&Q time domain signal and spectrum of a 4MHz carrier at the receiver output for $G_{LNA} = Min$, $G_{VGA} = 26\text{dB}$ and $P_{in} = -23\text{dBm}$.

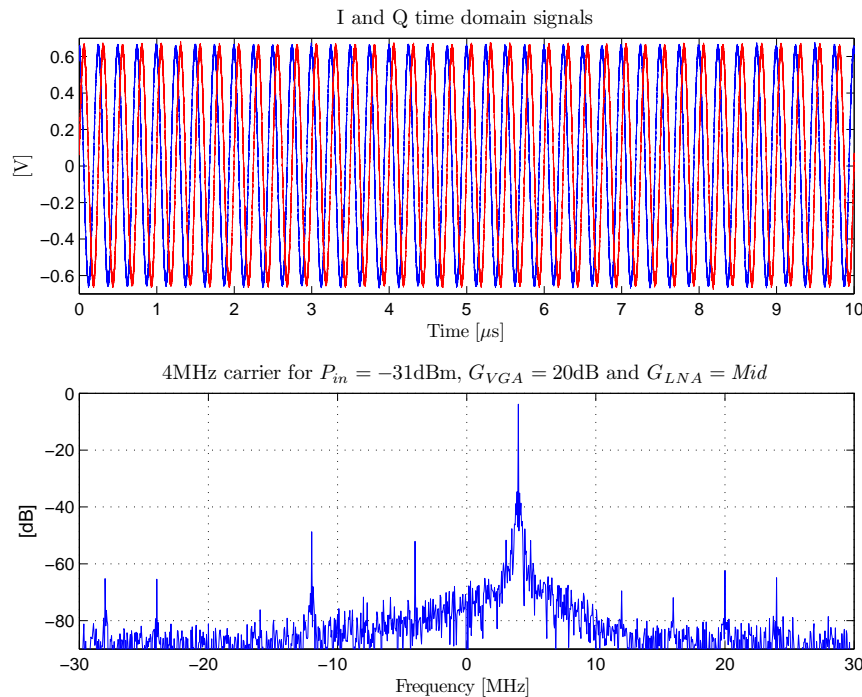


Figure 4.13: I&Q time domain signal and spectrum of a 4MHz carrier at the receiver output for $G_{LNA} = Mid$, $G_{VGA} = 20\text{dB}$ and $P_{in} = -31\text{dBm}$.

4.3 Conclusions and Novelties

The receiver chain was introduced with a description and specifications of its main blocks. The differences from the standard OFDM solution were explained, taking particular care of the effects of performing the DFT in two steps and of describing filtering and downsampling transformations in the IDFT/DFT matrix form. It was concluded that the data from the filtered carriers may be retrieved with just a few time domain samples per symbol. In the extreme case, only as many samples as carriers of interest are needed to successfully recover the transmitted information. The trade-off between ADC sampling rate, filter requirements and CIR was discussed. To conclude, the experimental setup for the receiver module was described and measurements that characterize the available hardware are presented.

From the discussed RF impairments in Chapter 2, Section 2.5, the HPA on the Tx was already considered in Chapter 3, leaving out two other to link: Phase noise and IQ imbalance. It was seen that folding due to too much decimation may have the same impact on the retrieved constellation as IQ imbalance. Folded carriers that fall on top of carriers of interest interfere in the same way as images do. This means that the maximum acceptable ILR given for M-QAM standard OFDM should for this case be seen as the maximum image's level plus folded carriers level for a given performance. For the given example of 64-QAM, a maximum ILR value of -30dB was given in [35] for a $\text{SER} = 10^{-7}$. Since the receiver of the test setup has an image level of -45dB (Figure 4.13), folding is allowable until up to 15 more dBs before the performance starts to degrade.

It is more difficult to estimate the impact when it comes to the setup's phase noise. The measured spectral masks indicate a phase noise variance $\sigma_{\phi}^2 \approx 0.015 \text{rad}^2$ (Equation 2.17). A variance of this magnitude shouldn't be a problem for an OFDM system, though it may result in an SNR degradation between 4 and 15dB for *isends* higher than 20dB (Figure 2.10, orange curve), if not corrected for. Compensating for CPE will help decrease the variance even more, but the improvement will depend on how frequently it is estimated and corrected for. The phase noise variance after correction will determine how fast the system's performance degrades with increasing *isend*, which is proportional to SNR (Equation 2.22 and 2.7). More on this matter will be discussed in Chapter 5.

Chapter 5

Bringing All Together: a Closed Cycle

After introducing the transmitter and the receiver separately, it is time to close the cycle. The block diagram of the experimental setup with the transmitter and receiver path together is shown in Figure 5.1. The final setup includes an Agilent N6030A AWG controllable with MATLAB[®], an Agilent E8267D synthesizer with built-in vector modulator with I&Q inputs, an evaluation kit for MAX2829 chip from Maxim Integrated, a National Instruments 5772R high-speed digitizer with FlexRIO FPGA module programmable with LabView, two RF synthesizers and a DC power supply. All the equipment is frequency locked. For demodulation, a MATLAB[®] script was developed.

To ensure that the setup was properly locked, the equipment was put together and checked up step by step without the Maxim board.

The first figure measured after closing the cycle was the channel impulse response. The CIR will depend mostly on the Maxim's board due to the narrow filters and it is the factor with most weight on the choice of the CP length. A brief description on how the measurements were done and their results are presented in Section 5.1.

When closing the cycle, another important topic for recovery of undistorted information is time synchronization and phase correction. Frequency synchronization is not an issue, because the entire setup is locked. This setup characteristic will not affect the final conclusion regarding implementation viability of the system, since the RADAR application has a similar context (Section 1.1). Different possibilities for synchronization and how they mainly work are explained in Section 5.2.

To evaluate the required SER of the OFDM distribution network, simulations of the Phased Array RADAR performance for different RF front-end failure scenarios were done. When one symbol of the OFDM message is wrong for receiver Rx_r , that module is "shut down" and does not transmit nor receive. Thus, the interesting figure to measure is *Symbol* error rate and not *Bit* error rate — how many bits are wrong within one symbol, how distant

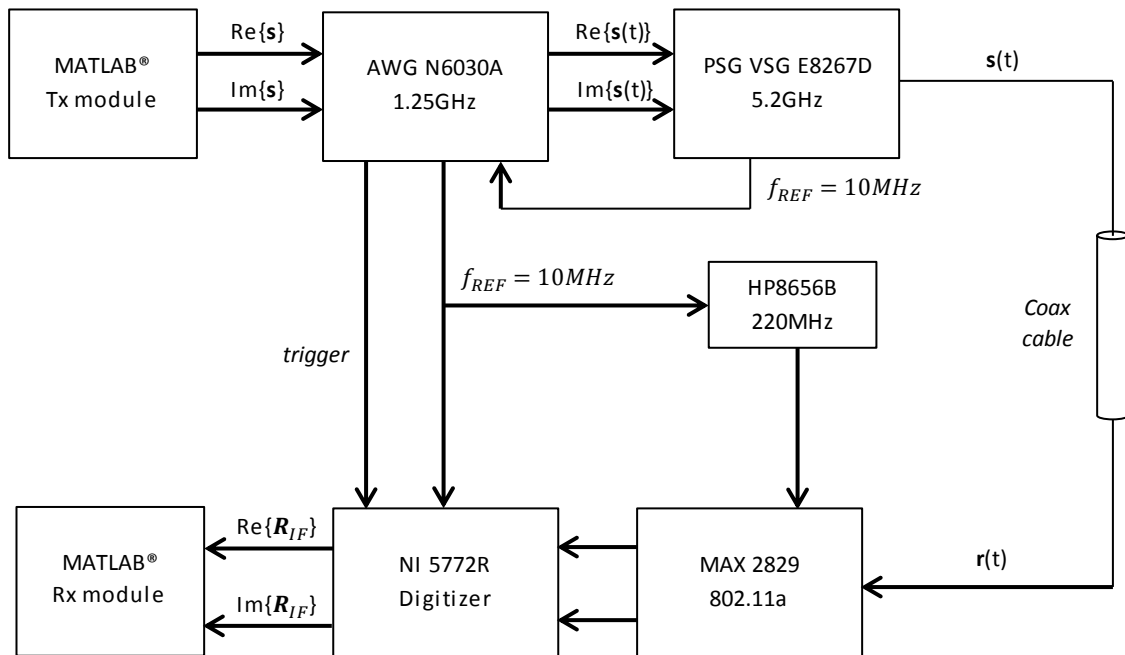


Figure 5.1: Block diagram of the experimental setup with the transmit-receive cycle closed.

in the constellation the received symbol is from the transmitted one, is irrelevant. How many modules can be OFF for an acceptable RADAR functionality determines the minimum required SER per receiver. Section 5.3 will show some of the results of these simulations, explain how the minimum SER was estimated and why it is just a rough approximation.

Finally, Section 5.5 encloses the SER measurements for different parts of the spectrum to mimic the behavior of different receivers — note that a different part of the spectrum is allocated for each receiver. A full explanation of the setup, chosen OFDM parameters for both examples (64-QAM, one carrier per receiver and 16-QAM, two carriers per receiver) and how the SER measurements were performed is given. SER curves for different scenarios are drawn and it is shown that filtering and downsampling holds no degradation for the recovered data.

5.1 Channel Impulse Response

To measure the channel impulse response, a pulse was generated in MATLAB® with a delay of 125ns (Figure 5.1). Figure 5.2 shows the pulse measured with the sampling scope right at the output of the AWG. As it can be seen, the pulse has the same delay of 2.8ns for both I

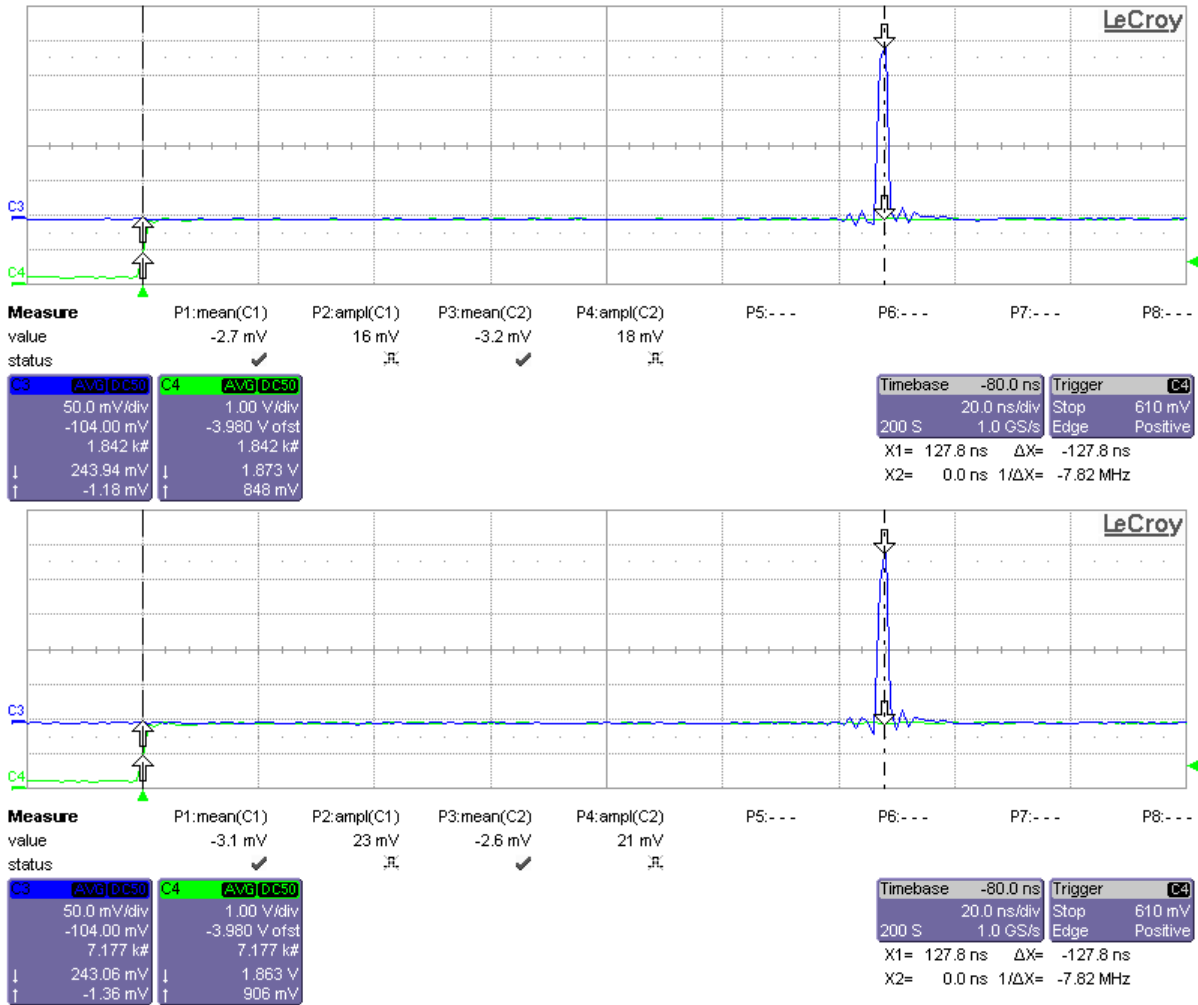


Figure 5.2: Time domain pulse with a 125ns delay measured at the output of the AWG — I (top) and Q (below) channel.

and Q channel at the output of the AWG. To measure the CIR, the pulse was measured with the sampling scope (SC) and with the digitizer at the output of the Maxim board. Figure 5.3 and 5.4 are representative figures of those measurements. Table 5.1 gives the measurement’s results for both scenarios and for the four MAX2829’s lowpass filter bandwidths (B_{LPP}): 7.5MHz, 9.5MHz, 14MHz and 18MHz (see Appendix B). On average, the digitizer introduces a 18 clock cycles delay in the chain, around 20ns for a 800MS/s sampling rate. The measured CIR will determine the needed CP to be added to each OFDM symbol for successful demodulation.

B_{LPF} [MHz]	CIR_{SC} [ns]	CIR_{dig} [ns]
7.5	121	140
9.5	98	120
14	73	96
18	63	85

Table 5.1: CIR measurements with the sampling scope and with the digitizer and the output of the Maxim’s board for different lowpass filters.

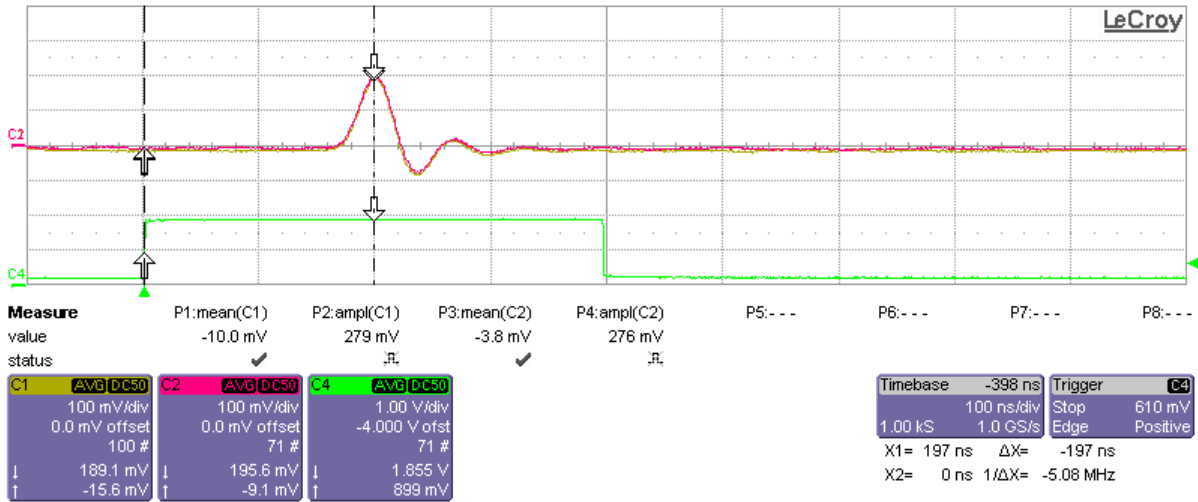


Figure 5.3: Time domain pulse with a 125ns delay measured with the sampling scope at the output of the Maxim’s board for a 14MHz lowpass filter.

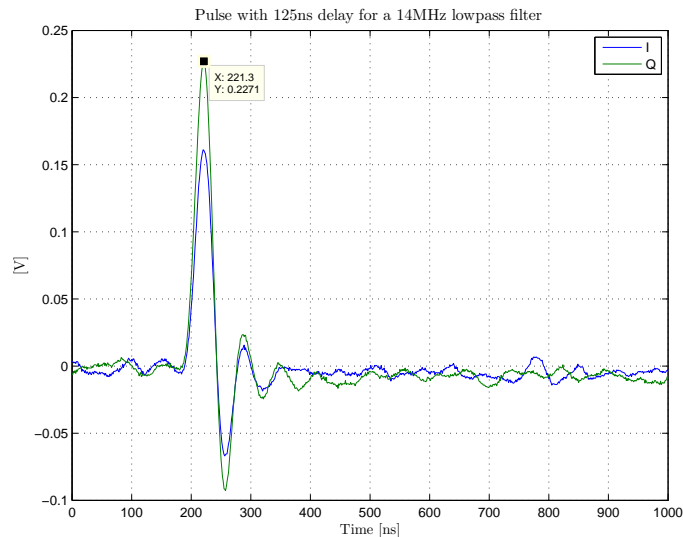


Figure 5.4: Time domain pulse with a 125ns delay sampled with the digitizer at the output of the Maxim’s board for a 14MHz lowpass filter.

5.2 Time Synchronization and Phase Correction

Time synchronization was one of the big challenges of this thesis work. Not by the implemented solution itself, but by how the adopted OFDM demodulation scheme limits the use of known synchronization techniques in literature. Section 2.4 described several of the available synchronization algorithms. Careful reading will make clear that all those techniques imply absolute knowledge of the entire spectrum, i.e. that the entire spectrum is received on the other end. By definition of the system under development, this does not happen. The core of this work is exactly the fact that each receiver filters around its own allocated band alone and discards the rest before any data process. The consequence is that each receiver sees a different time domain signal, since it filters a different part of the spectrum, and that none of them sees the same time domain signal or spectrum that was sent on the transmit side. Hence, any synchronization techniques that rely on the correlation between transmitted and received signals or on the transmission of pilots both in frequency or time domain cannot be applied. One solution that eventually could be used would be the placement of pilots in the frequency domain. However, since each receiver would need at least one pilot, the transmission would become highly inefficient. Consider the extreme case of one carrier per receiver: half the spectrum would consist of pilots. Another method that could work would be blind synchronization by autocorrelation of each symbol, detecting the output peak due to the presence of a CP. Since each receiver always filters the same band (filter bandwidth is fixed), the autocorrelation should still work, even though the CP is no longer equal to the one transmitted.

To overcome the described problems, an algorithm should be found that does not depend on the specific part of the spectrum the receiver sees and does not require any knowledge of the original time domain symbol. Plus, the receiver should be designed as simply as possible, so low complexity architectures with minimum digital signal processing are preferred.

The first key point is that the synchronization, due to the reasons mentioned above, cannot be done during the data transmission period without great loss in data rate. Thus, the receivers should be synchronized at system startup. It is possible to do it this way due to the high stability of the RF network over time. The channel may be considered time-invariant. The second key point is that there is a clock/synchronization signal integrated in the RADAR system with encoded syncs available for synchronization of Tx/Rx switching in the T/R-channels. The syncs may be encoded in the clock by means of pulse width modulation. This existent signal may be used to help in the OFDM synchronization.

The simplest idea that came to mind was to use one dedicated symbol for synchronization at the beginning of each OFDM message. The carriers should be modulated in such a way that their sum will generate a peak somewhere within the symbol length. Since the distance of the peak relative to the beginning of the symbol is known in advance by the receiver, the delay could be computed by determining the difference between that distance and the one given by the peak detection output minus the transmission starting time marked by the RADAR's clock/synchronization signal. This solution allowed all the receivers to be synchronized in parallel and at the beginning of each message. Since the spectrum is filtered, all the carriers must be modulated with one of corner constellation points (maximum amplitude and phase)

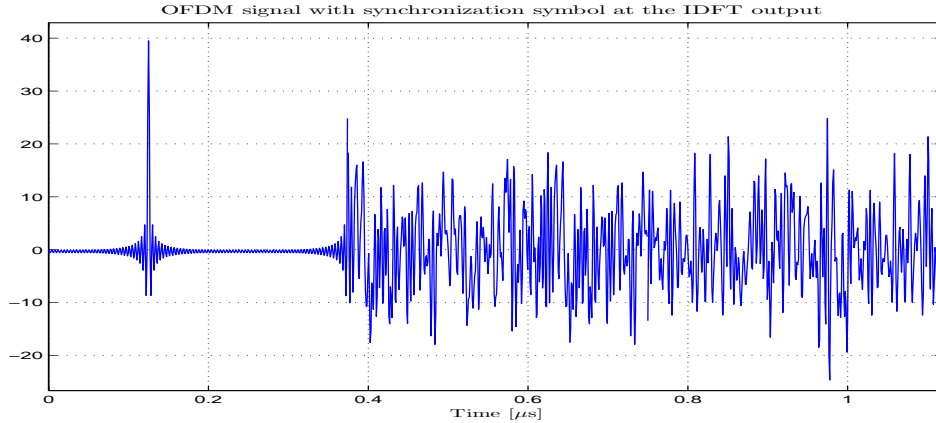


Figure 5.5: Inphase OFDM signal with synchronization symbols at the IDFT output.

for the filtered symbols to have detectable peaks. This, of course, is a problem at the transmit side. If all the carriers are modulated with maximum energy, the PAPR ratio of that symbol is huge (Figure 5.5). The peaks cannot be clipped, or the precision decreases. To ensure the linearity of the transmission of those peaks, the dynamic range left for the OFDM signal is very small. This together with the fact that the precision was not great, lead this method to be discarded.

The second idea was to use a Zadoff-Chu sequence. Zadoff-Chu sequences are known as CAZAC sequences, which are the same sequences used in Czylwik's method. These are complex-valued sequences that result in constant amplitude time domain signals. This characteristic is specially advantageous for OFDM systems, since it helps to assure that the synchronization step does not contribute to the increase of the PAPR.

These sequences were first introduced by Frank and Zadoff in [43] and earlier by Heimiller [44]. Basically, the sequences are polyphase codes with good periodic correlation properties, meaning that the autocorrelation function of the periodic sequence is zero everywhere except at multiples of its period, where the autocorrelation function has a single maximum. Heimiller described the code of length L^2 , where L is a prime number. Frank showed that codes with the same properties could be created without the restriction of L being prime. However, the sequences were still squared (of length L^2). Later, Chu [45] generalized these code sequences for any size N . The polyphase sequences \mathbf{a}_k of length L are defined as

$$\begin{cases} \mathbf{a}_k = e^{j \frac{M\pi k^2}{P}} & \text{for } P \text{ even} \\ \mathbf{a}_k = e^{j \frac{M\pi k(k+1)}{P}} & \text{for } P \text{ odd} \end{cases} \quad (5.1)$$

where $k \in [0, P - 1]$ and M is an integer relatively prime to P . Cyclic shifts, addition of constants on the exponent of the exponential defining \mathbf{a}_k or conjugating the entire code, do not affect the autocorrelation function. More important to conclude is that discrete fourier transforms do not affect these codes' properties. Further elaboration on the use of Zadoff sequences can be found in Thales' internal appendix.

For the experimental setup used for proof of concept, a Zadoff-Chu sequence is created

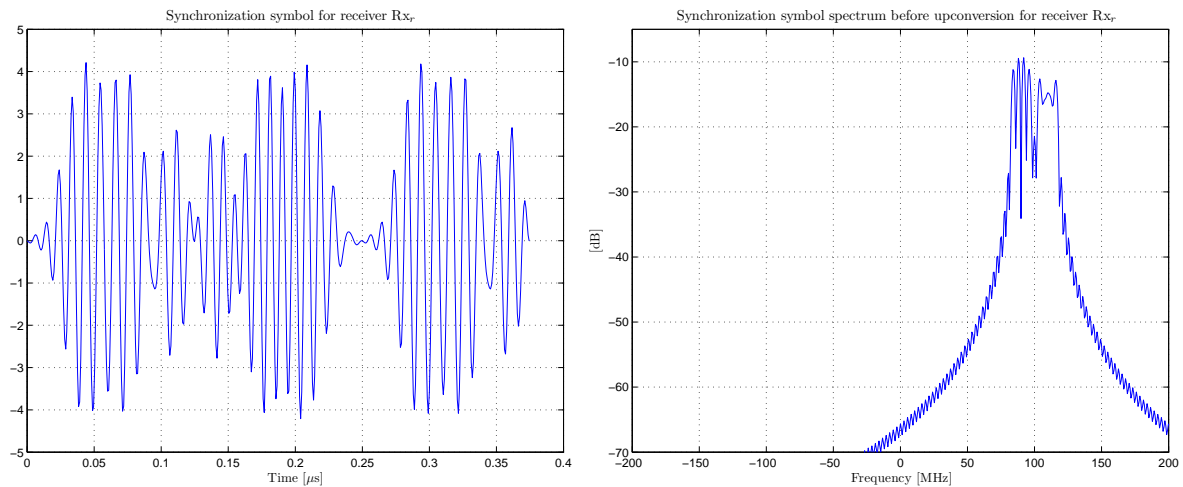


Figure 5.6: Example of a synchronization symbol for receiver Rx_r ; inphase time domain signal (left) and spectrum before upconversion (right).

and placed around the frequency under test. The LO is tuned to $f_c + (r - 1)\Delta f$ for receiver Rx_r and the Zadoff-Chu sequence is placed at the IDFT input around $(r - 1)\Delta f$ MHz, with as many elements as carriers the receiver's lowpass filter allows to go through. An example of a synchronization symbol for receiver Rx_r is given in Figure 5.6. Figure 5.7 shows the correlation output. The single peak can be made sharper by increasing the number of carriers for the same Δf .

After the peak detection, the time delay τ is stored. The sampled received signal \mathbf{R}_{IF} is delayed by τ samples,

$$\mathbf{R}_{IF, sync} = R_{IF}(n + \tau) \quad (5.2)$$

Time synchronization is the first step for any measurement. Only after the DFT window is correctly placed, the symbols may be demodulated. Due to the stability of the test setup, the system is synchronized one time only at the beginning. The stored delay τ may then be used for days. This helps to prove that, if the RADAR system is as stable as this test setup, there should be no loss in performance for synchronizing only at system startup. How the constellation over time is received for receiver Rx_r with and without time synchronization is shown in Figure 5.8. Note that at this time, no phase correction is applied yet, so the constellations are still rotated and equal constellation points are a bit dispersed.

Only after all the receivers have been synchronized, the phase offsets can be corrected for. This step faces the same frequency and time domain challenges described for the time synchronization algorithms. The simplest way to compensate for phase offsets is, without a doubt, to work with transmission of known constellation points. At the receiver side, a simple complex division of the received constellation point by the known transmitted one results in the right phase rotation to apply for each retrieved data point in that message. Once more, since each receiver filters just part of the spectrum and each carrier may have a different frequency/phase shift, all allocated carriers must be modulated with known constellation

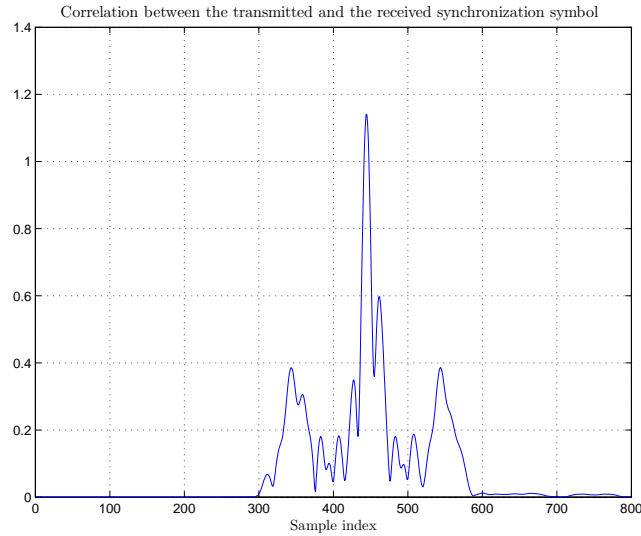


Figure 5.7: Example of the correlation output for synchronization at the receiver side.

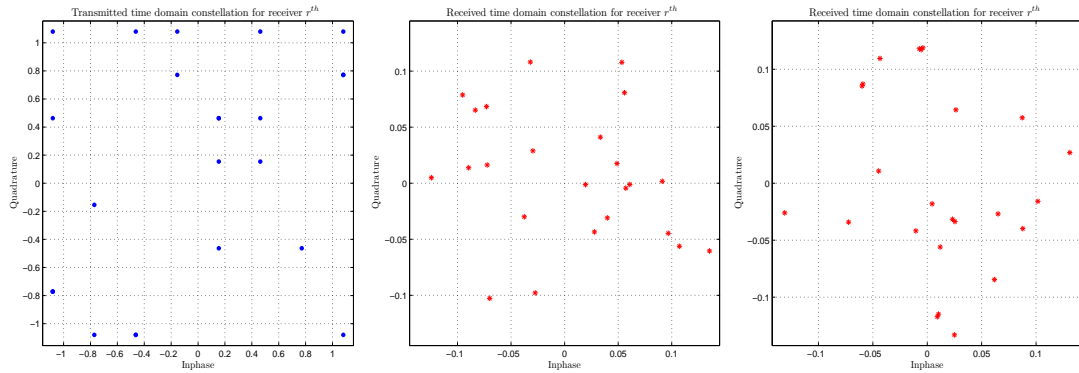


Figure 5.8: Time domain constellations for receiver Rx_r : sent constellation (left), received constellation with no synchronization (middle) and received constellation after time synchronization (right).

points at the beginning of each OFDM message. Since the system is frequency locked and time-invariant, it is reasonable to assume that the determined phase offset for each carrier remains constant within the message time period.

All allocated carriers are transmitting known constellation points, so it is necessary to choose these points in such a way that peaks are avoided; otherwise, the same problem illustrated in Figure 5.5 occurs. The details of the design of the preamble are explained in Thales' internal appendix.

A part of an OFDM message with an appended preamble for phase correction is shown in Figure 5.9. The preamble consists of two OFDM symbols and each carrier is modulated with a different constellation point for each symbol. The phase offset estimation ϕ is the mean of the individual phase offsets determined for each symbol. To compensate for the phase offset, the DFT's second step (Equation 4.4) should be modified to

$$y_r = \mathbf{R}_{IF} e^{-i2\pi k_r \frac{n}{N_{DFT}}} e^{-i\phi} \quad (5.3)$$

Received constellations after time synchronization with and without phase correction are given in Figure 5.10 (sent constellation is the same as in Figure 5.8).

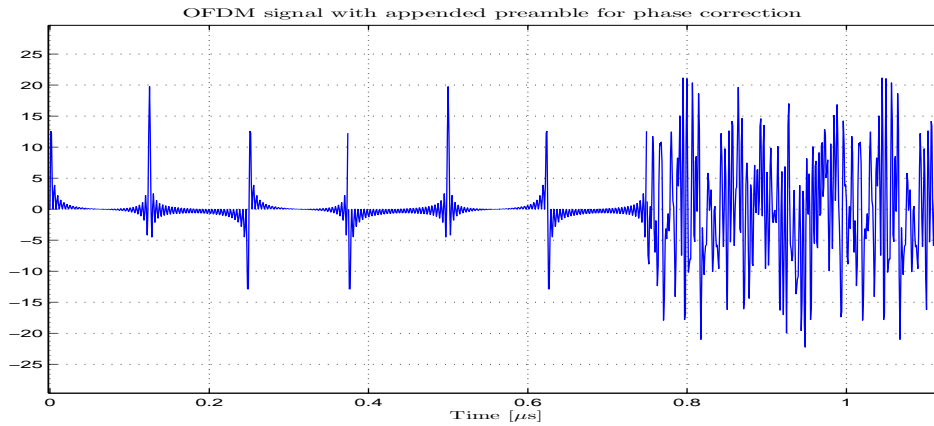


Figure 5.9: Inphase OFDM time domain signal with appended preamble for phase correction at the output of the IDFT.

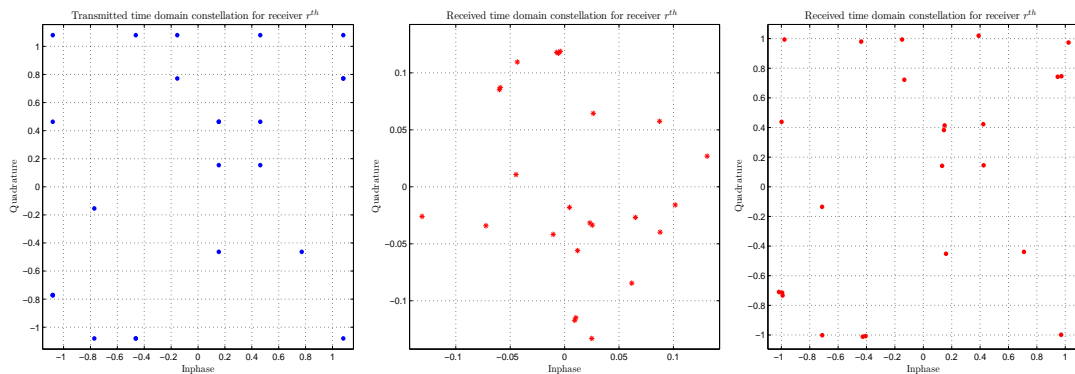


Figure 5.10: Time domain constellations for receiver Rx_r : sent constellation (left) and received constellation after time synchronization without phase correction (middle) and with phase correction (right).

The time synchronization and phase correction are then performed in two steps: at system startup the time delay is computed once, being stored and re-used for $> 10^6$ messages, and phase correction is estimated at beginning of each message, being re-used for as many symbols as the OFDM message has.

Note that, unlike in standard wideband OFDM receivers [6], it is not expected for the performance to degrade with increasing carrier index. Residual synchronization offsets have the same impact on all receivers: each receiver downconverts its allocated band, so all of them look to the same distance around IF, giving the same exponent weight to the eventual residual error.

5.3 Required SER — Simulations

As mentioned before, the SER should be low enough to guarantee that the frequency/number of RF front-end modules shutting down has a negligible impact on the overall system performance. Skolnik [46] estimates that if 0.1% of the radiators are OFF, the disturbance in the antenna sidelobes is $> 50\text{dB}$ below the mainlobe, which is still acceptable. For the typical figures and general architecture given in Chapter 1, the phased array would have 256 RF front-end modules, 1024 radiator elements — it could be allowed for one T/R channel to be switched OFF. At the same time, it only takes one symbol error for one entire RF front-end module, i.e. 4 radiator elements, to be switched OFF. This fact alone, no longer ensures that the disturbance will be $> 50\text{dB}$ below the mainlobe, but since one module controls four T/R channels, it is the minimum allowable without an extra algorithm to control the channels independently, it is the worst case scenario. Still using the given typical figures, each RF front-end module requires 240 bits, which are 40 symbols per pulse using 64-QAM, one carrier per receiver. The total number of symbols sent to the $R = 256$ RF front-end modules is $256 \times 40 = 10240$ symbols. To allow for only one of these symbols to go wrong is to require a minimum SER of 10^{-4} .

This is a very rough and optimistic approximation. Even though the transmission is done with uniform weighting, creating a pattern rather insensitive to which radiator is turned OFF, the impact on the antenna radiation pattern for receiving is highly dependent on the radiator's place in the phased array (Figure 5.11). The Tx/Rx pattern for the case with no errors is given in Figure 5.12. Figure 5.13 gives an example of the impact of one non radiating element on the Rx pattern of a phased array using a non-uniform weighting. Peak sidelobes increase up to $\approx -43\text{dB}$, which is already too high for a RADAR application. Thus, the determination of the required SER is not as simple as put by Skolnik. Going back to the discussed RADAR example, the situation is even worse, because one RF front-end module switched OFF implies 4 non radiating elements. If the RF front-end module that happens to receive the wrong symbol is the one right in the middle, the sidelobe level of the Rx pattern is severely degraded. At the same time, radiators in the corners or laterals of the array could be switched OFF all the time without noticeable loss in performance. Figure 5.14 to 5.17 give the Tx/Rx diagram for different error scenarios.

From these simulation results, it is clear that the Rx pattern sidelobes increase when elements near the center of the array are not radiating. Also, it shows how misleading it can be to say that only one element can be switched OFF: it is better to have several non radiating elements in the laterals than one in the middle (Figure 5.14). Comparing Figure 5.16 and 5.14, it is clear that having one switched OFF RF front-end module in the middle (4 non radiating elements) versus one switched OFF RF front-end module in the middle together with a few in the laterals results in almost the same pattern. For an extreme case, see Figure 5.17: even with 10 switched OFF RF front-end modules (40 non radiating elements), the pattern does not get much worse than the one with one 4 non radiating elements in the center (one RF front-end module switched off). When the non radiating elements are placed in the corners/laterals, it does not matter whether it is 1, 2 or more RF front-end modules that are not transmitting/receiving — the impact in the system performance is always negligible (Figure 5.15).

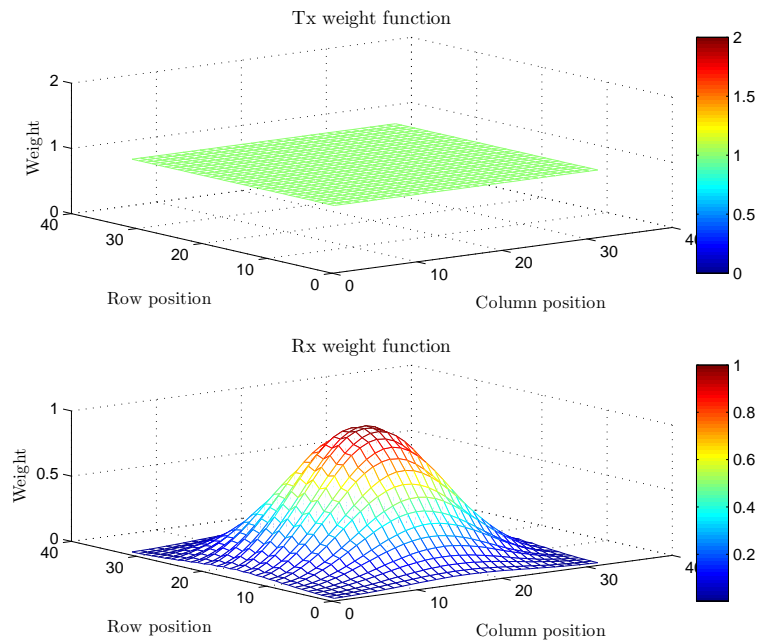


Figure 5.11: Tx and Rx weighting functions for the phased array antenna.

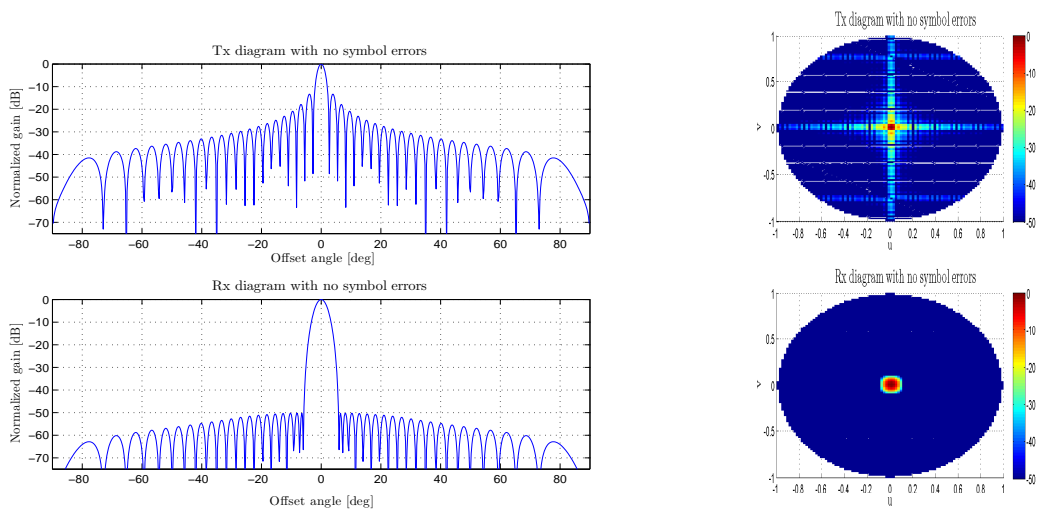


Figure 5.12: Radiation patterns with all radiator elements ON.

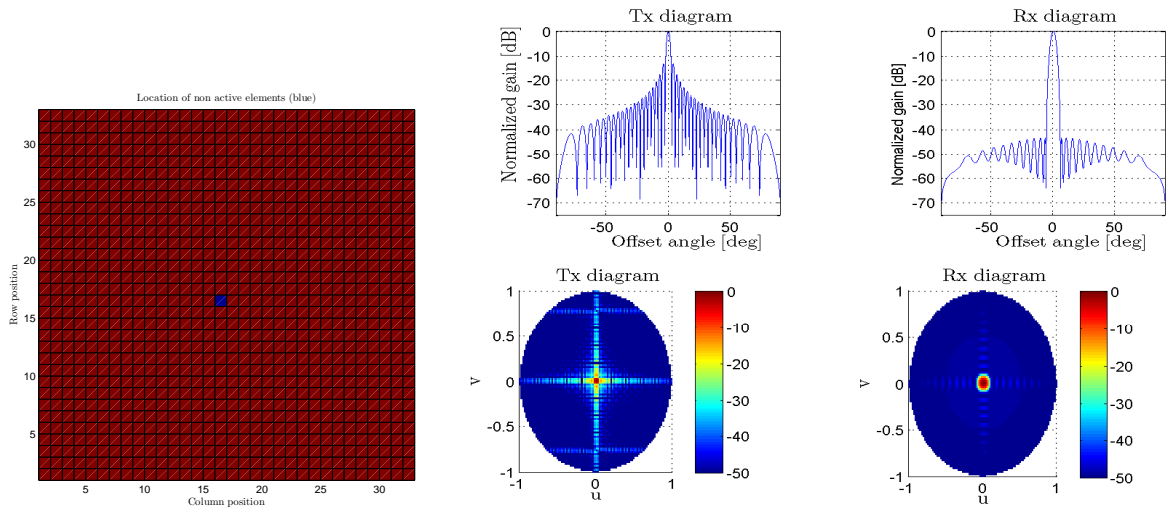


Figure 5.13: Radiation pattern with one non radiating element in the middle of the phased array.

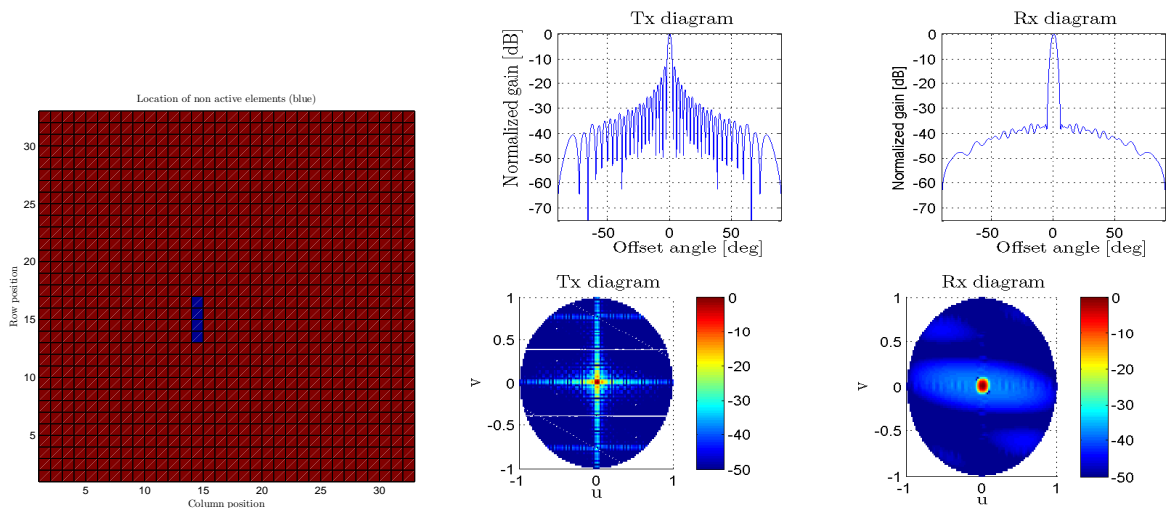


Figure 5.14: Radiation patterns for one failed RF front-end module in the middle, 4 radiator elements switched OFF.

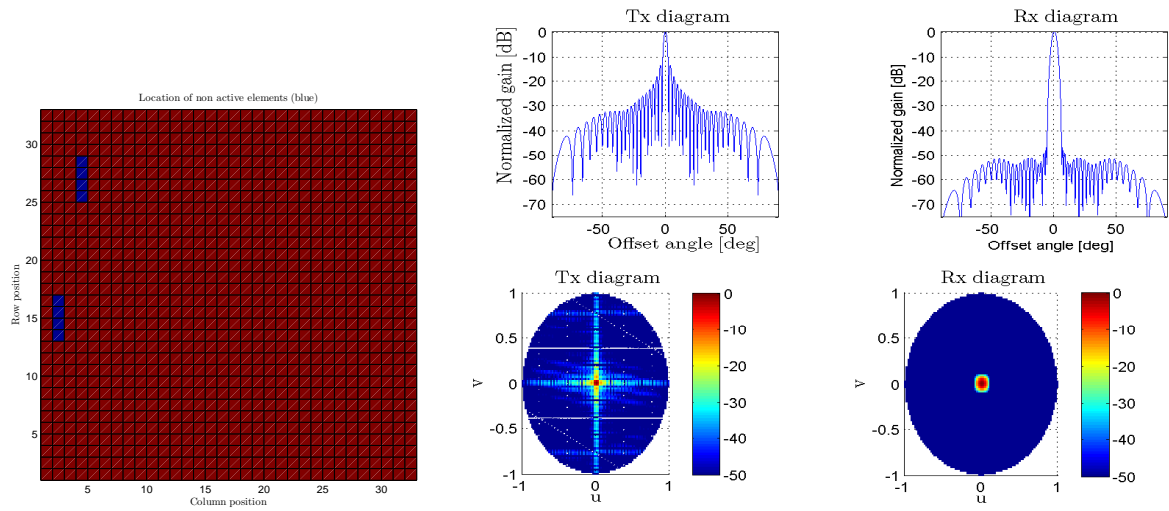


Figure 5.15: Radiation patterns for 2 RF failed front-end modules on the side, 8 radiator elements switched OFF.

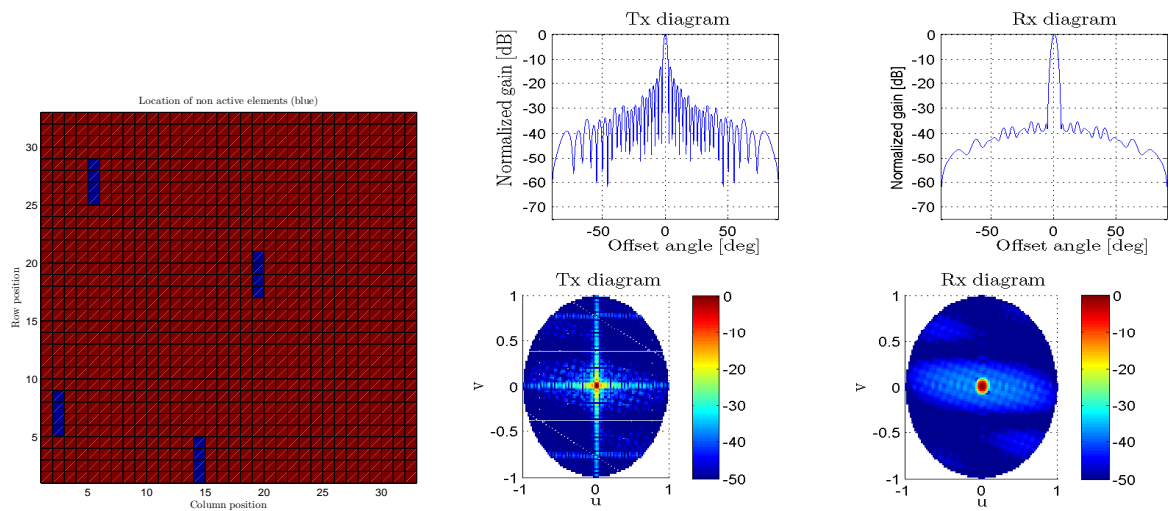


Figure 5.16: Radiation patterns for 4 failed RF front-end modules, 16 radiator elements switched OFF: one in the middle, and 3 more near the borders.

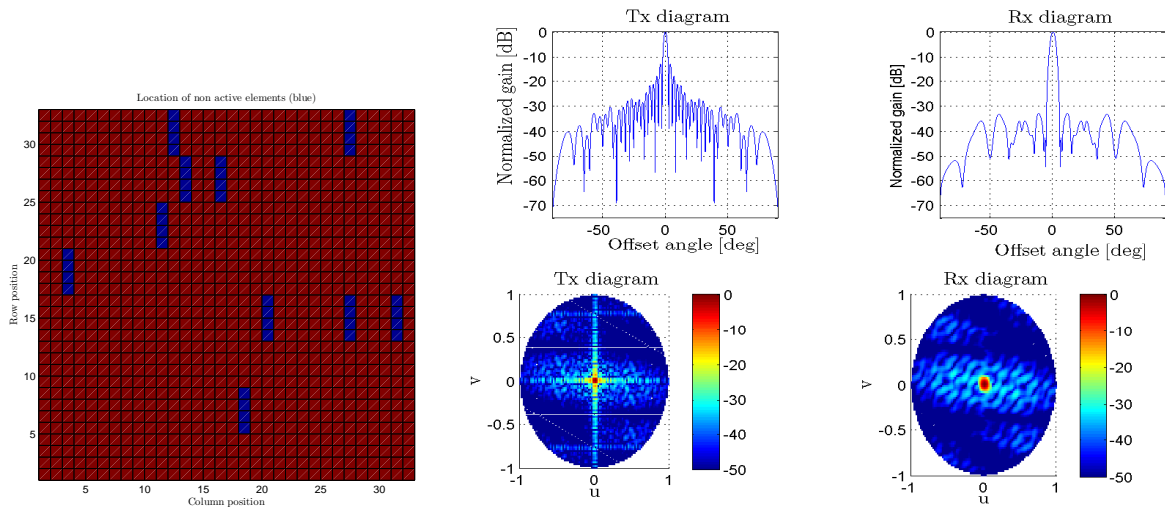


Figure 5.17: Radiation patterns for 10 failed RF front-end modules spread around, 40 radiator elements switched OFF.

For the Tx diagram, note how the radiation pattern remains almost constant for the different scenarios, proving its insensitivity to the spatial arrangement of the non radiating elements.

The radiation patterns were simulated for different SER values, taking as a starting point a SER of 10^{-4} as indicated by Skolnik's assumption. Since the patterns can only be simulated for one receiver at a time, a 256 messages window was taken to have an overview of what would happen for the given example of $R = 256$ RF front-end modules. It was observed for several simulation rounds that one up to a few symbol errors occurred over the 256 messages, i.e. cases as the ones illustrated from Figure 5.14 to 5.16 would occur frequently, resulting in an average sidelobe degradation of 10 to 15dB. Indeed, Skolnik's approximation is too optimistic for this RADAR application. After extensive simulations with a large number of radar transmissions and randomly generated errors, it was concluded that a SER of $5 \cdot 10^{-6}$ should be enough to guarantee a negligible effect of the errors on the radar performance. To have a more accurate and reliable estimation of the required SER, a statistical model of the phased array behavior for different failure scenarios should be developed. Section 6.2 in Chapter 6 will have some discussion on how the knowledge of this relation position/relevance for transmission/reception can be used combined with the RF network characteristics for better performance of the overall system.

5.4 Two case studies

For the SER measurements, two case studies (already mentioned in previous sections) were considered: 64-QAM with one carrier per receiver and 16-QAM with two carriers per receiver.

Common choices for both studies are

- OFDM bandwidth $B = 520\text{MHz}$
- Number of RF front-end modules (aka Rx) $R = 128$
- Bit stream of 144 bits per Rx_r
- Zero padding in the frequency domain for twice the resolution
- Number of cancellation carriers $n_{CC} = 4$
- Preamble for phase correction of 2 OFDM symbols
- Lowpass filter bandwidth $B_{NF} = B_{LPF} = 18\text{MHz}$

The widest lowpass filter was chosen to have the shortest CIR. However, as it will be seen later, the CIR of 85ns for the $B_{LPF} = 18\text{MHz}$ will still be quite long relative to the OFDM symbol time T_s . Another detail is that, since the carrier at DC is not modulated, the total number of OFDM carriers K will be $K = K_r R + 2K_r$.

For the 64-QAM, one carrier per receiver case, the total number of carriers will be $K = 128 + 2 = 130$. The carrier spacing is then $\Delta f = B/K = 4\text{MHz}$, which results in a symbol time T_s of 250ns. With a carrier spacing $\Delta f = 4\text{MHz}$ and a lowpass filter of 36MHz complex bandwidth, $36/4 - 1 = 8$ carriers are used for the Zadoff-Chu sequence for time synchronization. A CIR of 85ns imposes a CP $> 85/250 = 34\%$. Since ratios of a power of 2 are preferred, a 50% CP is used.

Each receiver Rx_r needs 144 bits per OFDM message. With one carrier per receiver and using 64-QAM, $144/\log_2(64) = 24$ time domain symbols are required to transmit all the data. Accounting for the preamble for phase correction, each OFDM message consists of 26 symbols. The total transmission time is $T_{total} = 26T_s(1 + 0.5) = 9.75\mu\text{s}$.

The other case study with 16-QAM, two carriers per receiver, was designed to occupy exactly the same bandwidth, keeping the same spacing between the receiver's allocated band, but doubling the number of carriers. The total number of OFDM carriers is now $K = 256 + 4 = 260$ and the carrier spacing $\Delta f = 2\text{MHz}$. The same lowpass filter fits 16 carriers for this carrier spacing, so a Zadoff-Chu sequence with 16 elements is used.

The symbol time is now doubled $T_s = 500\text{ns}$, but the total transmission will not be. To transmit the 144 bits, $144/(2\log_2(16)) = 18$ OFDM symbols are needed and, since the symbol time is now longer, the CP percentage can be reduced to $25\% > 100(85/500)$. With two symbols for phase correction, the total transmission time is $T_{total} = 20T_s(1 + 0.25) = 12.5\mu\text{s}$. By doubling the number of carriers per receiver, it is possible to use a much more robust modulation order, with just a $\approx 20\%$ increase in the OFDM message time period.

Since the phase rotation is only estimated once per OFDM message, only phase noise slower than $9\mu\text{s}$ ($< 112\text{KHz}$) for 64-QAM with one carrier per receiver and $11.25\mu\text{s}$ ($< 89\text{KHz}$) for 16-QAM two carriers per receiver, can be corrected for [2]. This is still within the plateau seen in Figure 4.7, also known as slow phase noise or CPE, for the phase noise effect's study.

Before going into the real measurements, one important thing to draw are the theoretical SER curves for each case. In Chapter 2, the theoretical SER expression for an OFDM system

was introduced (Equation 2.7). At that point, it was only said that the SER would depend on the *isend* and that this dependence would vary with the modulation used. For a single carrier modulated with M-QAM, the SER is defined as

$$SER = 2 \left(1 - \frac{1}{\sqrt{M}} \right) \operatorname{erfc} \left(n_f \sqrt{\operatorname{isend}} \right) - \left(1 - \frac{2}{\sqrt{M}} + \frac{1}{M} \right) \operatorname{erfc}^2 \left(n_f \sqrt{\operatorname{isend}} \right)$$

$$\text{with } n_f = \sqrt{\left(\frac{3}{2(M-1)} \right)}$$

$$\text{and } \operatorname{erfc}(x) = \frac{2}{\pi} \int_x^{\infty} e^{-t^2} dt$$
(5.4)

n_f is a scaling factor to normalize the constellation's energy to one and erfc is the complementary error function. For the derivation of these expressions, refer to Appendix A. The expression for *isend* as given in Equation 2.7 was

$$\operatorname{isend} = \frac{E_S}{N_0} = \log_2(M) \frac{P_S}{P_N} T_s B = \log_2(M) \cdot \operatorname{snr} \cdot \left(\frac{T_S}{T_S + T_{CP}} \right) \left(\frac{K}{N_{IDFT}} \right)$$
(5.5)

The main difference between the regular OFDM system and this one, is the narrow filter in the receiver. With this narrow filter, the ratio in B is no longer K/N_{IDFT} as in K being the total number of OFDM carriers and N_{IDFT} the number of time domain samples at the output of the IDFT on the transmit side. In this case, $K \equiv K_r$ and $N_{IDFT} \equiv K_f$. Since the filter is not ideal, the ratio's denominator that after all represents the noise bandwidth the K_r carriers see, is a bit larger. To know exactly how much to consider, is not an easy task. If the filter was ideal, the ratio should be around $4/36 = 1/9$, so that was taken as a starting point. However, looking at the noise spectrum (Figure 4.11, Chapter 4), it is clear that it extends way beyond 36MHz. To have a good approximation of the actual system ratio B for the *isend* expression, the equivalent square filter bandwidth that accounts for the noise as it is seen in the plot should be determined. To do so, the total noise power is computed from $[-50, 50]$ MHz, where there is a spectral step that indicates the stop band of the filter and only the digitizer's wideband noise is present. Afterwards, the noise power density within the $-3dB$ band of the lowpass filter is extended to $\pm\infty$ and is filtered with the equivalent square filter. Finally, the bandwidth of the equivalent square filter that passes through the same noise power as the original filter over $[-50, 50]$ MHz is determined. Following this line of thought, a ≈ 58.3 MHz complex bandwidth was considered (about $2/3$ more than the 36MHz considered before), resulting in an approximate ratio of $1/13$. For the theoretical curves drawn in Figure 5.18, the following expressions were used:

$$64 - \text{QAM, one carrier per receiver: } \frac{E_S}{N_0} = \log_2(64) \operatorname{snr} \frac{1}{1.5} \frac{1}{13}$$

$$16 - \text{QAM, two carriers per receiver: } \frac{E_S}{N_0} = \log_2(16) \operatorname{snr} \frac{1}{1.25} \frac{1}{13}$$
(5.6)

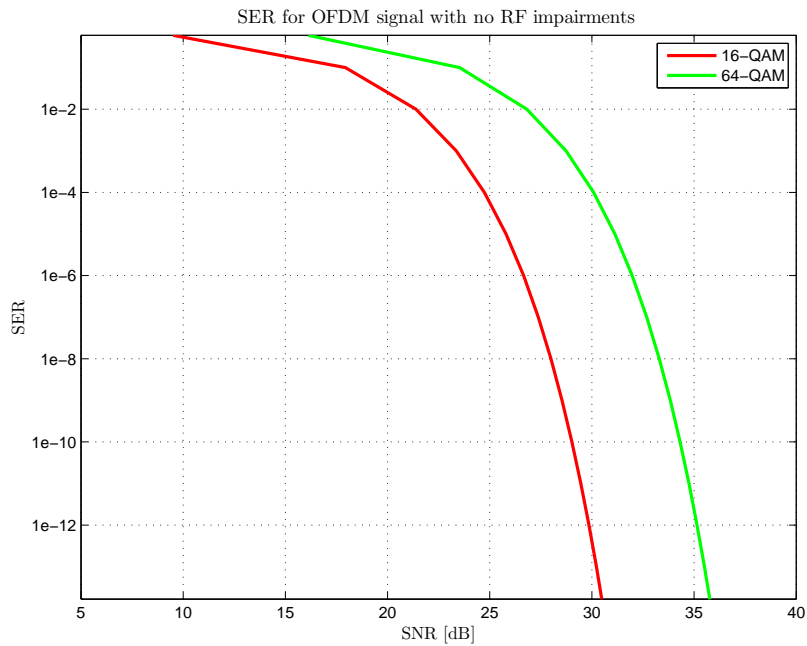


Figure 5.18: Theoretical SER curves for the two case studies, 64-QAM with one carrier per receiver (green) and 16-QAM with two carriers per receiver (red).

The measurement's goal will be to verify if the two case studies follow these curves and if the curve is the same for the different receivers tuned at different f_{LO} along the spectrum. If so, it can be concluded that the unconventional solution does not degrade the system performance when compared to the standard OFDM approach and that all the receivers Rx_r inside the RF front-end modules will respond in the same way.

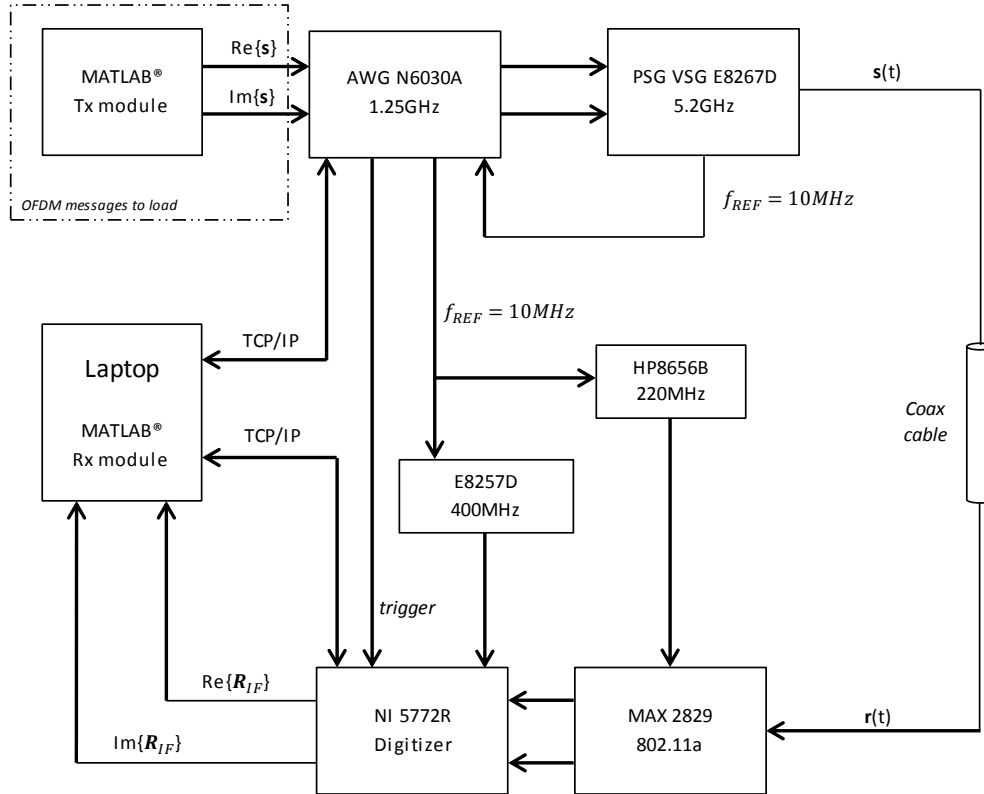


Figure 5.19: Block diagram of the experimental test setup including the TCP/IP connection.

5.5 SER measurements

To run the SER measurements, the entire setup was linked via a TCP/IP connection. An extra laptop running MATLAB[®] played the server role to command the AWG and the client role to receive the acquired data from the digitizer. Figure 5.19 illustrates the final test setup with the TCP/IP connection included. The ADC is running at $f_s = 400\text{MS/s}$ and the gain settings for the MAX2829 chip are $G_{VGA} = 26\text{dB}$ and $G_{LNA} = \text{Mid} = 16.5\text{dB}$, so there is a total voltage gain of 42.5dB in the receiver chain. The central frequency for upconversion is $f_c = 5.2\text{GHz}$. Due to data rate limitations, the AWG couldn't receive in real time random OFDM messages per loop, so a set of 100 random messages plus 1 synchronization message is previously loaded in its memory. Each waveform has an ID number, that works as a pointer to the list of waveforms. From here on, a loop will be defined as the entire cycle from the command to play the second waveform, first OFDM message, to the retrieval of the full constellation for all the 100 waveforms in memory, i.e. transmitting and receiving 100 OFDM messages. As the SNR is increased by increasing the input power with the synthesizer, the SER decreases, the occurrence of errors decreases, and more loops have to be played in a row. For the SER goal of $5 \cdot 10^{-6}$, the setup had to run for days — with the TCP/IP connection, the processing rate was of 4 messages per second. A SER of $5 \cdot 10^{-6}$ is equivalent to 1 symbol error in 200 thousand symbols: $2 \cdot 10^5 / 2400 \approx 84$ loops for 64-QAM with one carrier per receiver and

$2 \cdot 10^5 / 1800 \approx 112$ loops for 16-QAM with two carriers per receiver. If one order is increased to step out of the limit zone, 1000 loops (100 thousand messages) should be played to confirm the required SNR for the desired SER. To reach even lower SERs to follow the theoretical curves without much extrapolation, more loops should be played and so on.

The MATLAB[®] script running on the laptop controlling the cycle can be summarized into the following steps:

1. Compute constants

Compute all demodulation constants for one run of several N_{loop} loops and initialize error counters. Constants include the OFDM general transmission parameters and relevant reception constants that change for each receiver Rx_r or, in this case, for each f_{LO} frequency.

2. Establish TCP/IP connection

Connect to AWG and to digitizer. Some settings in digitizer are previously fixed as the sampling rate $f_s = 400\text{MS/s}$ and the existence of the external trigger from the AWG.

3. Initialize AWG

Send command to initialize AWG and wait for feedback confirmation

4. Load OFDM messages

Load synchronization signal plus the 100 OFDM messages to be played in loop into the AWG and wait for feedback confirmation.

5. Synchronize

- Send settings to digitizer: number of samples.
- Send command to AWG to play waveform 1, the synchronization signal and wait for confirmation.
- Read data from the digitizer.
- Correlate the received signal with the stored one and compute the time delay τ .

6. Process 100 messages loop

- Send settings to digitizer: number of samples.
- Send command to AWG to play waveform $z + 1$, $z \in [1, 100]$, and wait for confirmation.
- Read data from the digitizer (includes one entire OFDM message).
- Shift the received signal from the digitizer by τ samples and slice into the number of OFDM symbols in one message (26 or 20 for these two case studies).
- Take CP out.
- Scale and correct for phase offset.
- Compute the modified DFT to demodulate the data in the K_r carriers of interest.
- Map back the demodulated symbols into bit words.
- Count bit errors and bit errors per symbol to count for wrong symbols.

- Update error counters.
- Plot constellation. (optional)
- Increment z : $z = z + 1$
- Run inner loop while $z \leq 100$.

7. Run loop N_{loop} times

- Store messages with errors.
- Reset z to 1.
- Go back to step 6.
- Run the 100 messages loop N_{loop} times.

8. Compute SER and BER

Before starting with the measurements per se, the SNR was measured for different transmit powers. The transmit powers were set in the synthesizer. Table 5.2 gives the SNR values for the two case studies.

P_{in} [dBm]	SNR 16-QAM [dB]	SNR 64-QAM [dB]
-64	8.9	—
-62	11.4	—
-60	12.8	—
-58	14.9	14.6
-56	17.7	16.7
-54	18.6	18.8
-52	20.9	21.0
-50	23.1	22.5
-48	25.1	24.8
-46	27.1	27.4
-44	28.5	28.7
-42	31.3	31.2
-40	33.0	32.8
-38	—	35.2
-36	—	37.4
-34	—	39.4

Table 5.2: SNR measurements for several input powers in the range -64 dBm to -34 dBm for both case studies, Rx₁.

There were mainly two factors limiting the measurements: the TCP/IP connection that greatly increased the computation time per loop and the receiver dynamic range that didn't allow to measure for higher SNRs. For the test setup to mimic the behavior of different receivers Rx _{r} , f_{LO} was tuned to different frequencies: 5.0GHz, 5.1GHz, 5.2GHz, 5.3GHz and 5.4GHz. These LO frequencies correspond to testing receiver $r = 80$, $r = 105$, $r = 1$, $r = 26$ and $r = 51$, respectively. For each case study and for each receiver, four scenarios

were studied: demodulation with no downsampling, demodulation with downsampling to 80MHz, demodulation with downsampling to 40MHz and demodulation with downsampling to 80MHz and no images. By no images, it is meant that only half of the spectrum around f_c is modulated and the other half is put to zero, i.e. for receivers 1, 26 and 51 the left part of the spectrum is put to zero and for receivers 80 and 105, the right part of the spectrum is put to zero (Figure 5.20). The reason for this last measurement is to study the influence of IQ imbalance on both case studies. By nulling half the spectrum, the images generated by the vector modulator in the synthesizer at the upconversion step are put to zero. If the SER curves for this scenario and the regular one overlap, then the images' level is low enough to not have an impact on the system performance and this impairment can be discarded for the results' analysis. The down side of this experiment is that it only works nicely for Rx₁. All the other receivers will tune their LO to a frequency $f_{LO} \neq f_c$, which means that, even though the images problem at the transmitter is avoided, new images will appear after downconversion in the receiver (see Figure 4.13). These images generated in the analogue domain by IQ imbalance will add up to other carriers that can be folded back on top of the demodulated carrier(s) during downsampling. Carriers that fold back into the carriers of interest have the same impact on the retrieved constellation as IQ imbalance (see Chapter 4), so it is not possible to completely set apart the analog impairment from folding caused in the digital domain by too much decimation.

Another detail worth mentioning before proceeding to the measurement results is the special case of Rx₁ and Rx_R. As explained in Chapter 3, the carrier at DC is not modulated, which is the adjacent carrier left of carrier 1 and right of carrier K . As a consequence, Rx₁ and Rx_R will (theoretically) always be the receivers with better performance — they are on one side sidelobe-interference free. Being on one side sidelobe-interference free means that, not only do the receivers have one less carrier adding to the interference, but also the phase noise and folding that would come from that carrier is gone.

The SER results for the two case studies introduced in the previous section follow.

64-QAM, one carrier per receiver, case study

As it was mentioned in previous chapters, the experimental setup specifications (IQ imbalance, phase noise,...) were right on the edge to achieve the desired SER with 64-QAM. Measurements were made for the four different scenarios for Rx₁; Figure 5.21 shows the measured SER curves.

The fact that decimation does not degrade the system performance is shown by the overlapping of the curves in blue and green. However, as it is observed by the red curve, if the downsampling rate is too close to Nyquist and the filter boundaries are as relaxed as in this chip (refer to Figure 4.6), the folding of carriers becomes dominant, i.e. the power of the carrier folding back into the carrier of interest together with the image of the spectral opposite carrier is higher than the maximum acceptable ILR. Figure 4.10 is an example of the receiver's OFDM spectrum at the output of the filter. For instance, for a 40MHz decimation, the carrier at -36 MHz with a power level of ≈ -28 dBc will fold back; -28 dBc is already

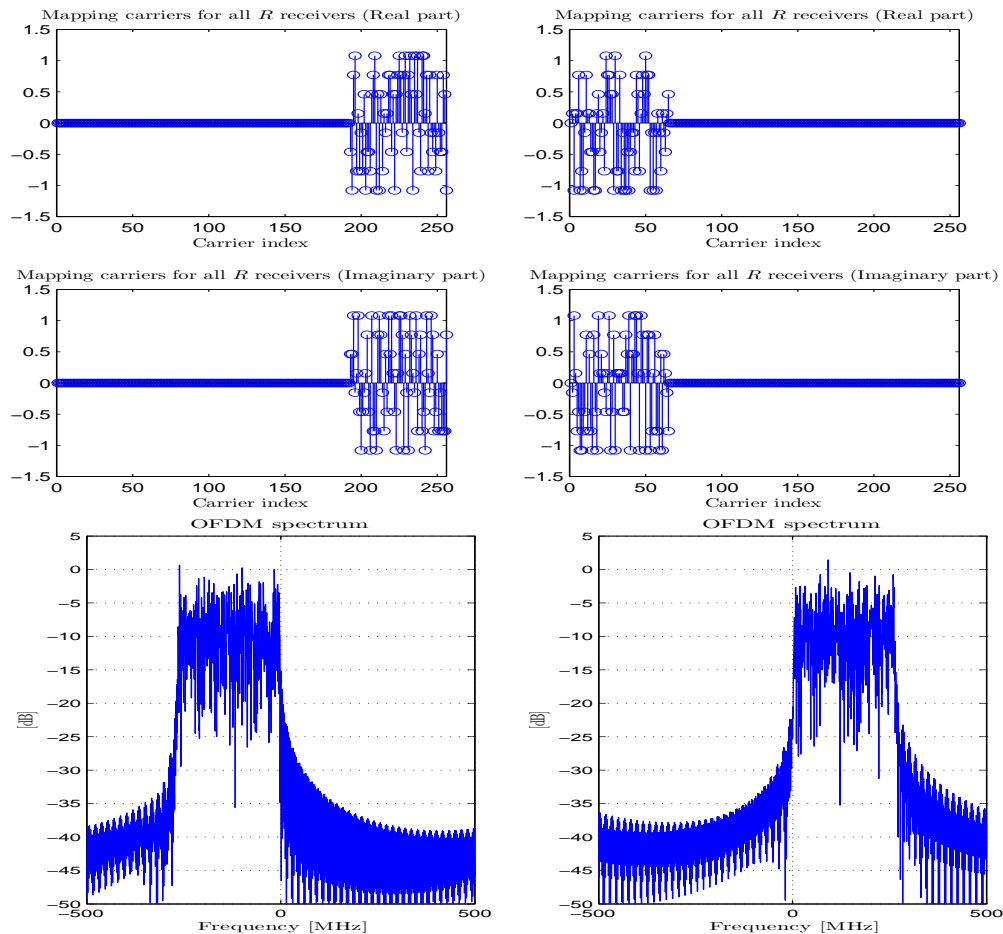


Figure 5.20: Mapping of the OFDM carriers (top) and its spectra (below) for the "no images" experiment.

quite high for 64-QAM. As a result, the SER curve "saturates" — there is an error floor that cannot be improved by increasing SNR.

Another interesting point is that, even though it was seen in literature [35] that the ILR of the setup over the entire OFDM bandwidth was quite close to the level acceptable for 64-QAM, there is no improvement in the SER curve when the images are put to zero (curve in cyan). This means that the image level created by the receiver ($\approx -48\text{dBc}$, Figure 4.13) together with the image created by the vector modulator ($\approx -50\text{dBc}$, Table 3.1) is still below the maximum ILR for the desired SER for 64-QAM (see Section 2.5 on IQ imbalance, example for 64-QAM). It is not possible to conclude that this would still be true for the other carriers, since the image's level after downconversion may be frequency dependent; the -48dBc value given in Chapter 4 is for $f_{LO} = f_c$.

A tendency seen in all curves is to get further away from the theoretical curve as SNR is increased. This means that the white gaussian noise and the ICI due to fast phase noise quickly dominate, making the SER curve less steep. These are system characteristics that

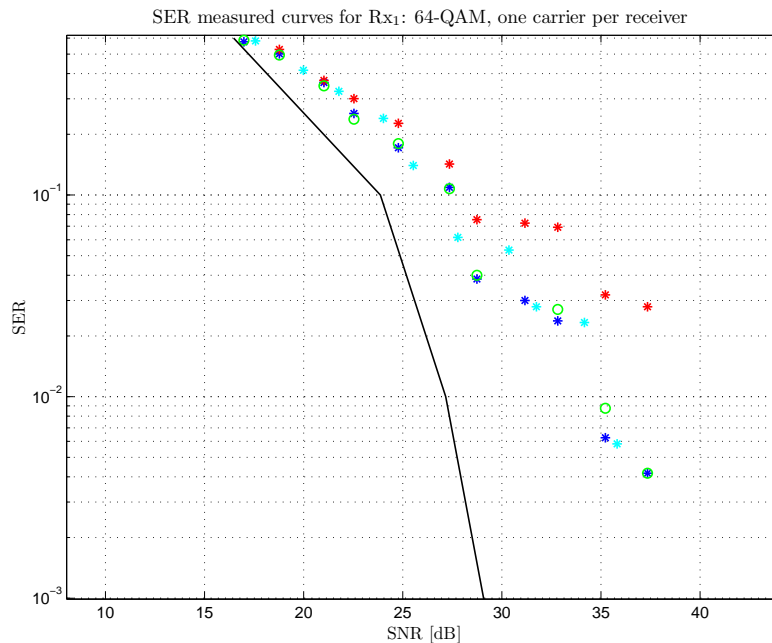


Figure 5.21: Theoretical SER curve (black) and measured curves for Rx₁ and case study 64-QAM, 1 allocated carrier: no downsampling (blue), downsampling to 80MHz (green), downsampling to 40MHz (red) and downsampling to 80MHz with no images (cyan).

cannot be corrected for. The only way to attenuate their effect is to statistically model and compensate for them before demodulation or to improve the LO design.

It was concluded that the performance is limited by folding when decimating to 40MHz; otherwise, phase noise plays the main role. More conclusions could have been drawn if lower SERs could have been measured. However, the SNR was already as high as it could be (39.4dB) without clipping the OFDM signal. Note that the receiver's maximum output power with no clipping is +5dBm.

From these measurements, it was clear that the available test setup would not allow to measure SER values in the order of 10^{-6} for the 64-QAM case study. For that reason, only carrier $k = 1$ was measured.

16-QAM, two carriers per receiver, case study

The measurements of the SER curves for this case study were performed in the same way as previously described. Figures 5.22 through 5.26 give the measured curves of the four different scenarios for receivers Rx₁, Rx₂₆, Rx₅₁, Rx₈₀ and Rx₁₀₅, respectively.

As in the previous case study, decimation does not affect the system performance. For all receivers under test, it can be seen that the blue (no decimation) and green (80MHz decimation) curves overlap. Moreover, even though the folding effects shown by the red curve (40MHz decimation) are barely noticeable, proving the expected higher robustness of

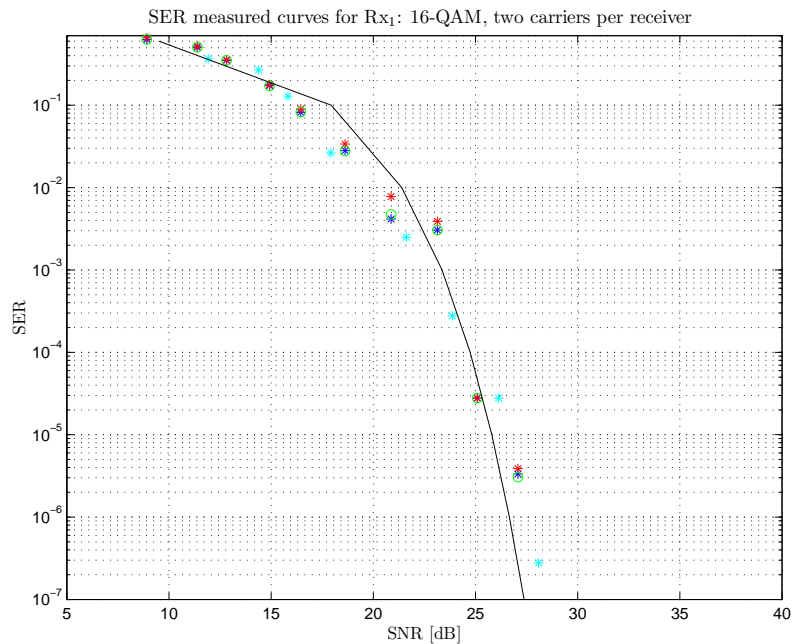


Figure 5.22: Theoretical SER curve (black) and measured curves for Rx_1 and case study 16-QAM, 2 allocated carriers: no downsampling (blue), downsampling to 80MHz (green), downsampling to 40MHz (red) and downsampling to 80MHz with no images (cyan).

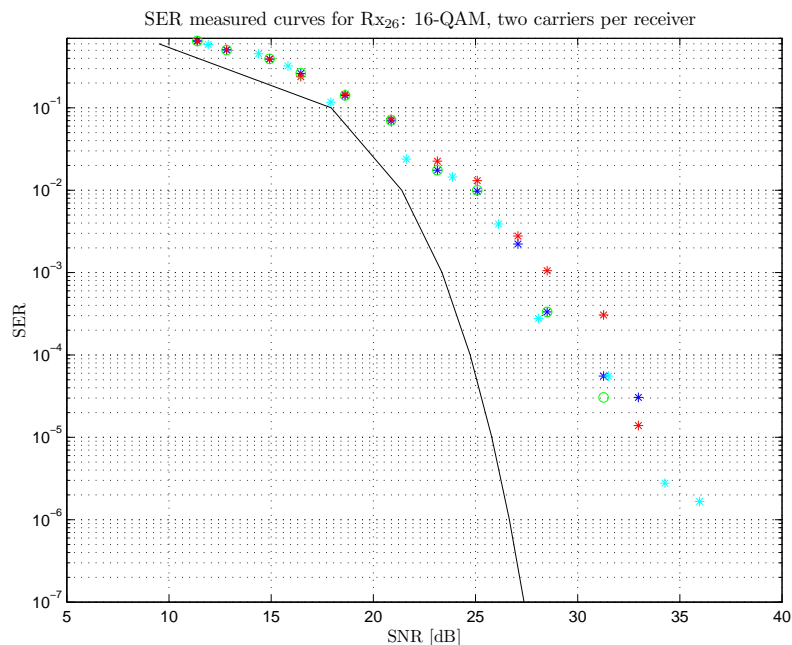


Figure 5.23: Theoretical SER curve (black) and measured curves for Rx_{26} and case study 16-QAM, 2 allocated carriers: no downsampling (blue), downsampling to 80MHz (green), downsampling to 40MHz (red) and downsampling to 80MHz with no images (cyan).

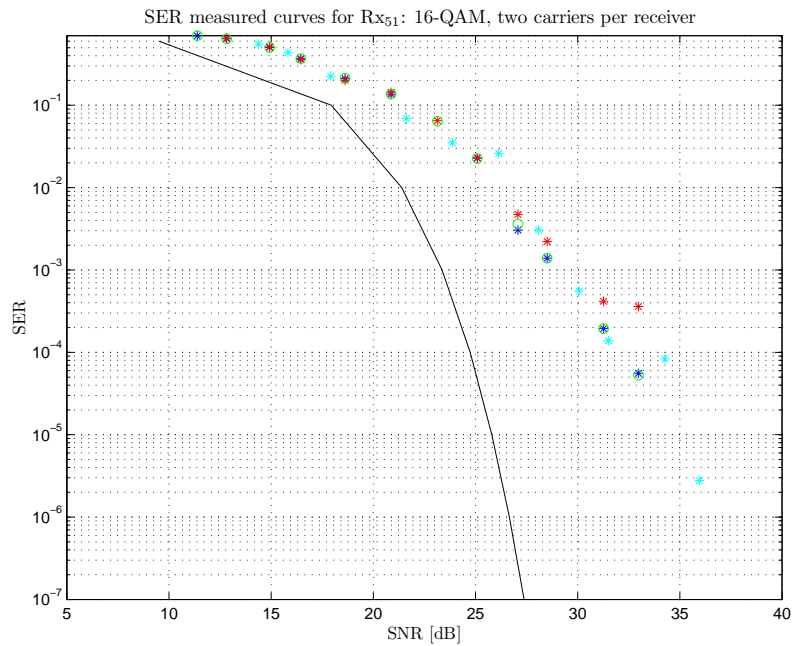


Figure 5.24: Theoretical SER curve (black) and measured curves for Rx₅₁ and case study 16-QAM, 2 allocated carriers: no downsampling (blue), downsampling to 80MHz (green), downsampling to 40MHz (red) and downsampling to 80MHz with no images (cyan).

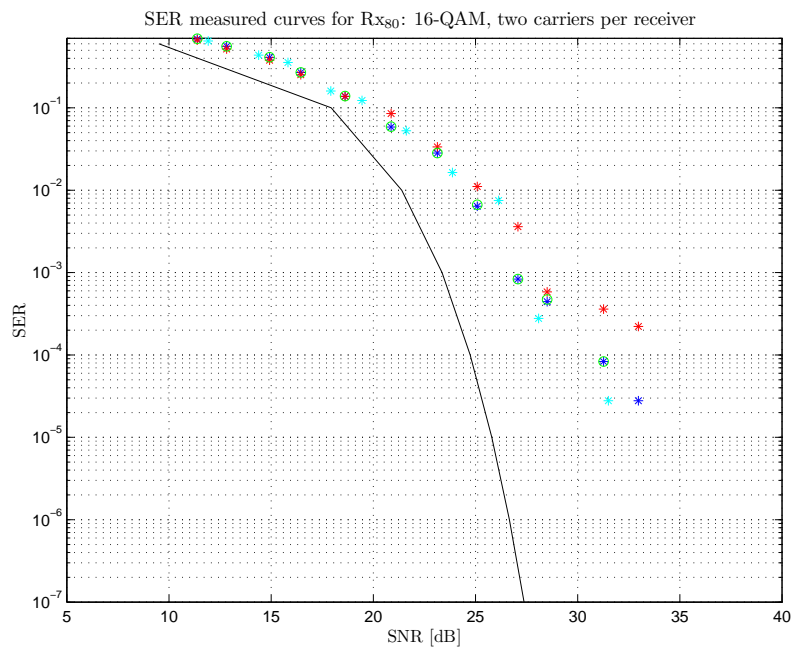


Figure 5.25: Theoretical SER curve (black) and measured curves for Rx₈₀ and case study 16-QAM, 2 allocated carriers: no downsampling (blue), downsampling to 80MHz (green), downsampling to 40MHz (red) and downsampling to 80MHz with no images (cyan).

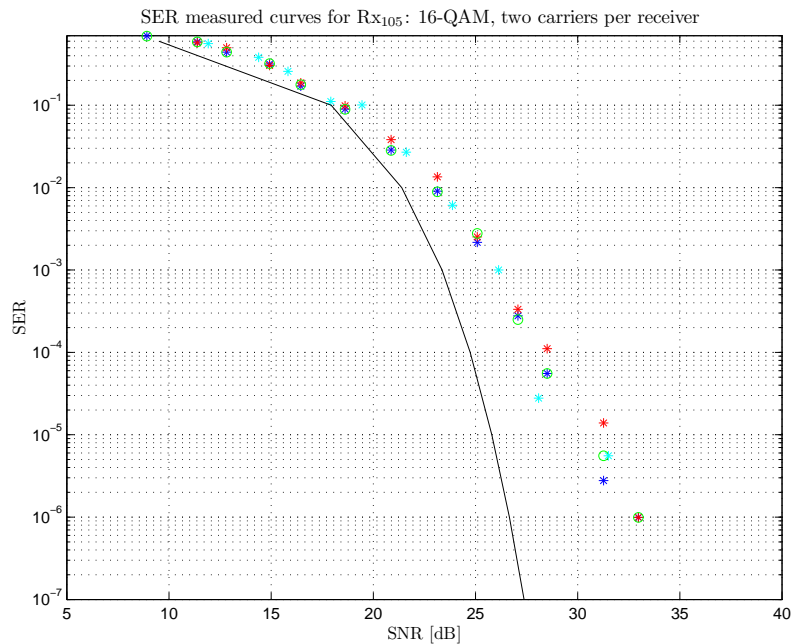


Figure 5.26: Theoretical SER curve (black) and measured curves for Rx₁₀₅ and case study 16-QAM, 2 allocated carriers: no downsampling (blue), downsampling to 80MHz (green), downsampling to 40MHz (red) and downsampling to 80MHz with no images (cyan).

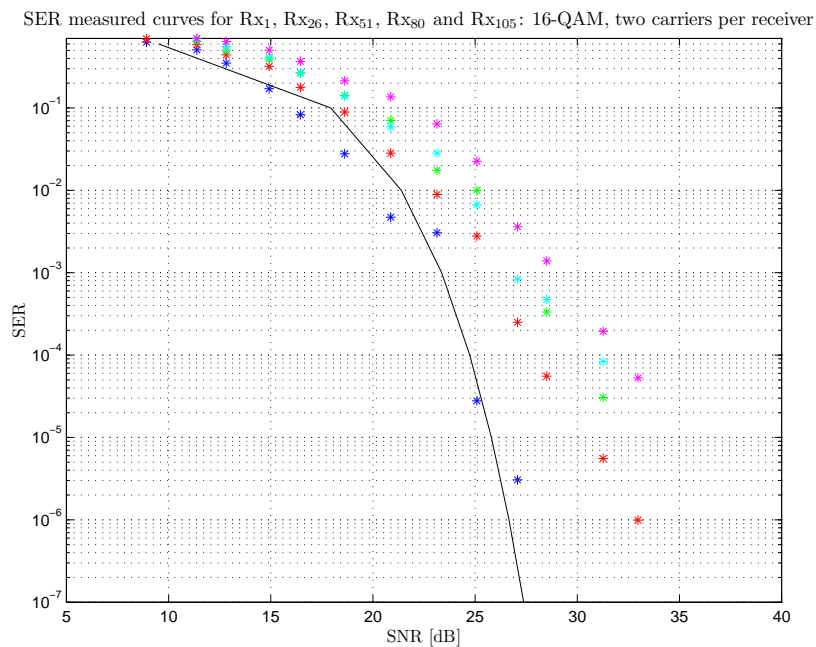


Figure 5.27: Theoretical SER curve (black) and measured curves for Rx₁ (blue), Rx₂₆ (green), Rx₅₁ (magenta), Rx₈₀ (cyan) and Rx₁₀₅ (red) with downsampling to 80MHz.

16-QAM over 64-QAM to folded carriers, there are some differences for each f_{LO} . The tip that each receiver will eventually feel the impact of different amounts of folding on its over downsampled SER curve is given by Figure 5.24 and 5.25. For these two cases, "saturation" of the red SER curve can be anticipated. More important than the event itself is the fact that their error floor is for different SER values. The adjacent carriers around the carriers of interest for different f_{LO} s were modulated with random data, which means that each mimicked receiver, when decimating at extreme low rates, was subject to folded carriers with different amplitudes and phases. Thus, a data dependent error floor in the SER curve is observed. The folding effect limits the performance and this limit is set by the adjacent modulated data together with the receiver's images' level.

Proving the robustness against images is the overlapping of the cyan curve (no images) to all curves. The "no images" is actually an experiment that only ends up making sense to Rx₁, as already discussed. All the other receivers downconvert their assigned band around f_{LO} , which will include carriers on both sides. For instance, the carriers at $f_{LO} - \Delta f$ and $f_{LO} - 2\Delta f$, due to their own IQ imbalance, will generate new images at Δf and $2\Delta f$ after downconversion. Since the cyan curve overlaps with the remaining, it is reasonable to assume that these new images' level (Figure 4.13) will be below the maximum ILR acceptable for 16-QAM, specially since they have already been proven to be acceptable for 64-QAM.

A common trend to the SER curves for different scenarios of each receiver under test is that they all deviate from the theoretical curve as SNR increases. However, it is important to notice as well that this does not happen to Rx₁. As SNR increases, ICI due to fast phase noise starts to dominate over the compensated CPE. Rx₁ has one less carrier contributing to the ICI, so the SER curves are expected to deviate less from the theoretical shape — SER curves for $r = 1$ are steeper than the ones from $r = 26$ to 105. Even though Rx₁ suffers less from ICI, this difference is only enough for a slight change in the SER curve shape to be observed and not enough to justify the large deviation between Rx₁ SER curves and the others for $f_{LO} \neq f_c$.

The measured curves with downsampling to 80MHz for the different tested parts of the spectrum are given in Figure 5.27. Theoretically, the curves for different f_{LO} s should overlap, since all receivers are under the same hardware conditions. However, it was observed that except for Rx₁ that follows the theoretical curve, all the other receivers deviate from it for a few dBs and that this distance increases with SNR.

Even though phase noise is not estimated as often as in Armada's analysis, it is not expected for this impairment to be responsible for the deviation. The reasoning behind this assumption is that, since Rx₁ stays close to the theoretical SER curve, whatever is pushing the other curves away is something that is present on the other 5 receivers and not on this one. Since all carriers have approximately the same phase noise spectral mask (Figure 4.7) before correction, one less carrier contributing for ICI due to fast phase noise (which has lower power density) should not make a 5 to 7dB difference between the curves. For one correction per OFDM message, CPE is corrected up to $\approx 90KHz$, which results in a variance decrease to $\sigma_\phi^2 \approx 0.01rad^2$. This variance magnitude is too small to be the major responsible for the deviation — note that all receivers suffer from the same amount of phase noise, being the difference between Rx₁ and the others one less carrier contributing to ICI.

If it is not phase noise or clipping (note that P_{in} was kept low enough to give room for

the OFDM signal's amplitude peaks), only IQ imbalance/folding and the use of different f_{LO} s is left. The fact that Rx₁ has one sidelobe-interference free side should have a limited impact on the SER curve and, in theory, it should not even be noticed unless orthogonality is compromised. Image and folded carriers' amplitude and phase influence the SER curve and depend on the adjacent carriers' data that goes through the narrow filter. Since the OFDM data for the modulation of carriers is random, each receiver will be differently influenced by this impairment. It should be noted that folding is negligible for the 80MHz sampling frequency used in Figure 5.27, and that the combined ILR of the Tx and Rx is low enough for 16-QAM. Thus, the deviation between the SER curves should be minimal and not the 5 to 7dB deviation seen between Rx₁ and receivers $r = 26$ to $r = 105$. The search for what is causing the deviation and different behavior among the carriers should likely be steered in two directions:

1. Something frequency dependent in the test setup that was overlooked; however, this dependence should not be proportional to frequency, since the curves do not have a mirrored performance, and should be considerably better around f_c .
2. Anything that compromises the orthogonality; it could explain why receivers under similar conditions slightly deviate from each other and all, as a whole, deviate more from Rx₁, which receives no carrier directly left of the carriers of interest.

One particular detail falling on the first direction that may be contributing to this deviation and was not yet pointed out as a possible cause is the disabled pre-distortion filter mentioned in Section 3.3. Without the compensation, the spectrum rolls-off towards the edges, due to the reconstruction DAC [47]. Figure 5.28 illustrates this effect as a function of the carrier index. For the carriers under study, the attenuation is rather small (under -0.4dB). On top of that, if this factor was the main reason for deviation, it would be expected for carriers at the same distance from f_c to overlap. Even if this analysis is put aside and the AWG's technical specifications are taken into account alone, the amplitude ripple is limited to $\pm 1\text{dB}$ up to 200MHz (Figure 3.15), which is the maximum tested f_{mix} ; $\pm 1\text{dB}$ is not enough for the observed behavior. Spectrum roll-off may have a small contribution, but does not play the main role.

Falling on the second search path is another hardware detail that belongs to none of the mentioned impairment categories. A digitizer was chosen over a sampling scope due to its better resolution, lower noise and user friendly control interface. However, the digitizer also has a AC coupled input with a 100KHz cut-off frequency, which corresponds to a $1.6\mu\text{s}$ time constant. This detail was overlooked until the analysis of the SER measurements results. Even though the carrier at DC is not modulated on the Tx side, there is always a carrier at DC for any $f_{LO} \neq f_c$ after downconversion on the Rx side. It is not a carrier of interest, indeed, but if there is something disturbing the DC signal, this carrier's phase samples will not sum up to 2π over the DFT window and it will compromise orthogonality, resulting in a distorted DFT output. When $f_{LO} \neq f_c$, the OFDM signal has a voltage offset determined by the complex value modulating the carrier that is downconverted to DC, hence it is an offset that changes from symbol from symbol. Every time there is a DC voltage step from one symbol to the next, the digitizer responds with a transient followed by a decay of the DC

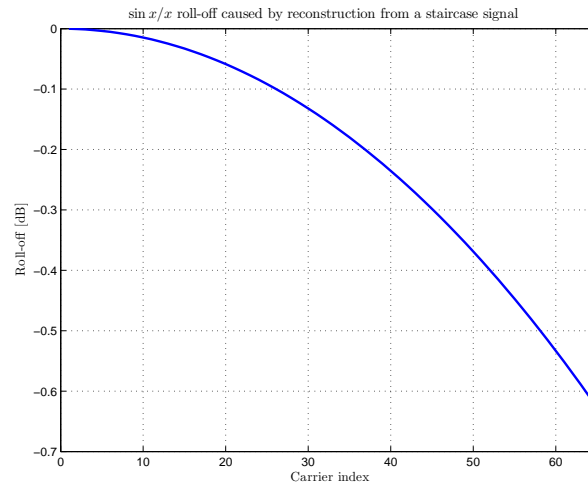


Figure 5.28: Sinc roll-off caused by reconstruction from a staircase signal as a function of carrier index.

voltage. The steepest part of the decay is always at the beginning of the symbol and is longer than the used CP (Figure 5.29). For all the receivers under test except for Rx₁, there is a carrier downconverted to DC which is more or less compromised depending on the distance between its constellation points for adjacent symbols.

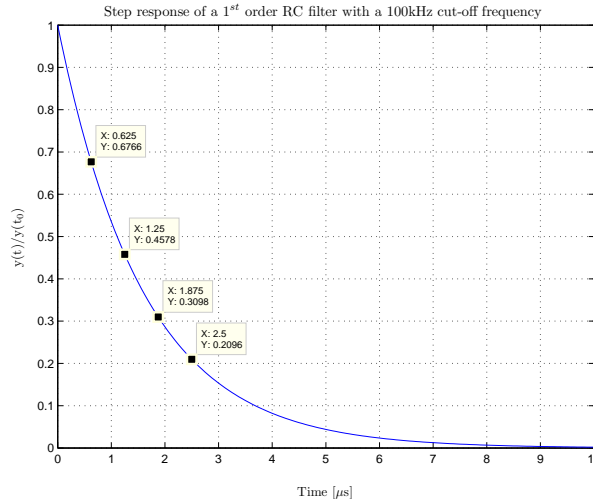


Figure 5.29: Digitizer's step response with markers at multiples of $T_s + T_{CP} = 625\text{ns}$ for the 16-QAM, two carriers per receiver, example.

The available measurements are not sufficient to go deeper on the analysis and explore all fronts. For this case study, the factor limiting the SER measurements was time. It was still possible to increase SNR (last point is for $\text{SNR} \approx 33\text{dB}$, $P_{in} = -40\text{dBm}$), but it would have required more than 10 thousand loops (1 million messages) to measure SERs in the order of 10^{-7} . It would take about 3 days to run 1 million messages for each power level. Multiplying

these for 1 or 2 more power levels for 4 different scenarios for 5 different f_{LOS} , the total time to have more 2 SER values would be around 120 days, 4 months. Optimizing the test setup to run SER measurements is thus crucial for further study of the system.

5.6 Conclusions

The experimental test setup was explained in detail, starting with an overall equipment description and ending with an overview of the SER measurements for two different case studies.

To close the cycle, time synchronization and phase correction methods were developed regarding the receiver's characteristics. For time synchronization a Zadoff-Chu sequence is placed at each receiver's allocated band and the time delay is computed in samples by means of a cross correlation operation. Time synchronization is performed once at system startup. For phase correction, two OFDM symbols are appended as a preamble in the OFDM message. The offset rotation for compensation is estimated once per message, meaning that only phase noise slower than $N_w(T_s + T_{CP})$ is compensated for all symbols. If the plateau in the LO's phase noise PSD extends beyond $[N_w(T_s + T_{CP})]^{-1}$, correcting for CPE will not be enough to have a clean constellation with regard to phase noise. For the particular case of this test setup, most of the phase noise power is within a frequency offset $< [N_w(T_s + T_{CP})]^{-1}$. It was shown that one estimation and correction per OFDM message reduces the phase noise variance to $\sigma_\phi^2 \approx 0.01 rad^2$, which is good enough for both 64 and 16-QAM.

The required SER for negligible impact in the system performance was determined. It was concluded that in phased array antennas with non uniform Tx/Rx weighting functions, Skolnik's approximation of a degradation 50dB below the mainlobe for 0.1% of the radiators switched OFF is too optimistic. A statistical model should be developed to predict the influence in the RADAR performance of the spatial arrangement of the failed RF front-end modules.

Through extensive simulations for different scenarios, a SER of $5 \cdot 10^{-6}$ was considered to be an acceptable value for proof of concept.

For the SER measurements, two cases were studied: 64-QAM with one allocated carrier per receiver and 16-QAM with two allocated carriers per receiver. To verify if all receivers inside the different RF front-end modules behave the same as theoretically expected, the SER was measured for 5 different LO frequencies. It was shown that the SER curves follow the expected theoretical curve shape and that decimation does not degrade the system performance. For the case of over decimation, each receiver will suffer from different amounts of folding and thus perform better or worse depending on the data of its adjacent carriers. Different SER error floors for the red curves for different f_{LOS} were observed. Note that the constellation points modulating the adjacent carriers contribute to degradation in two ways: with their images at downconversion and as themselves when folded. There is however a part of the folding that is predictable, independent of the data and can be minimized in the design (see Section 4.1).

Regarding the different behavior of Rx₁ and the other receivers observed for the second case study, the common RF impairments were ruled out as reason for the deviation in the SER curves: phase noise was way below what 16-QAM OFDM can tolerate for the desired performance, image's plus folded carriers' level was lower than the maximum ILR value and SNR was not high enough for non linearities effects to appear. It was concluded that the cause of the phenomenon is most likely related to a hardware factor compromising the orthogonality of the carrier downconverted to DC, which is modulated for all receivers except $r = 1$.

In the end, it appears that the measurements for the different receivers were done under different conditions, so it is hard to prove that all receivers may follow the theoretical curve as Rx₁ when in an optimum situation. To understand what exactly contributes to this phenomenon and their individual influence, further measurements for multiple scenarios should be done. Chapter 6 will give some suggestions for future work.

Considering a well designed system were each receiver behaves on average as Rx₁ of this test setup, a SNR of around 26dB should be enough to achieve the required SER. Since the eventual application of this work consists of a wired well controllable medium, to drive the system for high SNRs is not an issue.

Now that an approximation of the required SNR exists, the minimum output power in the Tx chain may be calculated. The equivalent noise power at the receiver's input is

$$P_{N,in} = -174 + NF + 10\log_{10}(B) \quad (5.7)$$

where -174dBm/Hz is the reference noise floor. For a certain SNR, the OFDM power needed at the receiver's input is

$$P_{Rx,in} = P_{N,in} + SNR \quad (5.8)$$

The minimum output power at the Tx chain should be $P_{Rx,in}$ plus the losses L in the RF network connecting the Tx output to each Rx input. To account for the PAPR, the amplifier should be designed to have a P_{-1dB} compression point of

$$P_{-1dB} = P_{Rx,in} + L + OBO \quad (5.9)$$

Chapter 6

Conclusions and Remarks for Future Work

6.1 General Conclusions, Novelties and Discussion

An alternative way to distribute the control data behind the phased array antennas was developed, allowing all the wiring and fiber optic cables to be removed. The data is generated in a beam steering computer and is fed as input to the OFDM Tx located in the RSG, where both the RADAR signal and the OFDM generated signal are added for distribution to the several RF front-end modules via the same RF network. To ensure that the RADAR and the OFDM do not interfere, cancellation carriers are used to reduce the out-of-band radiation of the OFDM signal. In each RF front-end module, an OFDM Rx is built-in for analog and digital processing. Each OFDM Rx is centered by means of a tunable LO to its allocated band and demodulates only the carriers modulated with the control data to its T/R channels. The selection of its designated band is done by means of a narrow filter, which enables the use of low speed ADCs, i.e. it allows the time domain signal to be decimated to the point of just a few time domain samples per OFDM symbol. No high speed signal processing hardware is needed on the receiver side. Depending on the LO's phase noise PSD, the frequency of phase offset estimations can be adjusted. For this particular system, the OFDM message time period is short enough to allow for just one correction per message without much loss relative to other methods found in literature. Since time domain symbols are used for phase correction, spectral efficiency is not reduced by use of pilots in the frequency domain. Due to the stability of the RF network, the system is synchronized once at startup and can use the same time delay for days.

A complete test setup was built for proof of concept and SER measurements. It was concluded that decimation does not affect the system performance as long as the sampling rate is such that the level of the folded carriers together with eventual existing images is contained within the chosen modulation's tolerance to IQ imbalance. It was also shown that, for carriers under similar conditions, the performance is the same for all of them, i.e. it does not degrade with the carrier index as it does in a conventional OFDM system.

An overview of the most common RF impairments in an OFDM system and the bridge of how they apply for this approach is built. Based on that study, the impact of each impairment may be separately considered on a simulation environment and theoretically predicted for several scenarios.

The developed system features a fully parallel and simultaneous data transport to all RF front-end modules, equivalent with the conventional solution but with less wiring. This reduces cost and weight of the infrastructure, creates space and alleviates design constraints, allowing a more optimal design of the essential system functionalities. The use of OFDM results in a data transmission that is very tolerant with regard to imperfections of the RF network. This allows the optimization of the RF network for the frequencies that are used in the essential function of the RADAR system, while still being able to transport data at another frequency where the RF network is non-optimal.

Even though the scope of this thesis was on phased array RADARs, the developed OFDM system concept is flexible enough for general RF sensing systems with distributed RF front-end modules that are connected to a network for transport of RF signals. It is also adaptable to the specific area of application in terms of the number of carriers, the used modulation per receiver depending on the needed data rate (each set of carriers per receiver may be modulated using a different constellation/modulation technique) and the transmitted power per carrier.

6.2 A few tips for Hardware Implementation and Optimization

If the system turns out to be implemented in hardware, there are a few trade-offs and clever choices that should be kept in mind. Most of the trade-offs are related with the receiver architecture and were already mentioned in Chapter 4. These are related with the narrow filter characteristics, ADC sampling rate and CIR.

The fact that modulated carriers are downconverted to DC for all cases except for the receivers with its allocated bands next to f_c , special care should be taken to avoid compromising orthogonality. As long as the carriers of interest are not directly converted to DC, offsets are of no concern. However, any transient responses to DC changes should always be accounted for, since they may disturb the OFDM signal when longer than the selected CP length. One way to avoid this would be to downconvert the allocated band to the minimum IF possible that would allow a narrow bandpass filter to eliminate the DC component before the ADC input.

Another set of considerations that was not discussed yet is how to handle the RF network reflections and return loss and how to take advantage of that knowledge to distribute the transmission power across the OFDM spectrum and the OFDM carriers over the RF front-end modules. Figure 6.1 shows four plots that do an exemplary S-parameter characterization of a RF network. There is clearly an optimum frequency f_{opt} for which the network is optimized and that corresponds to the frequency used for the RADAR transmission. The

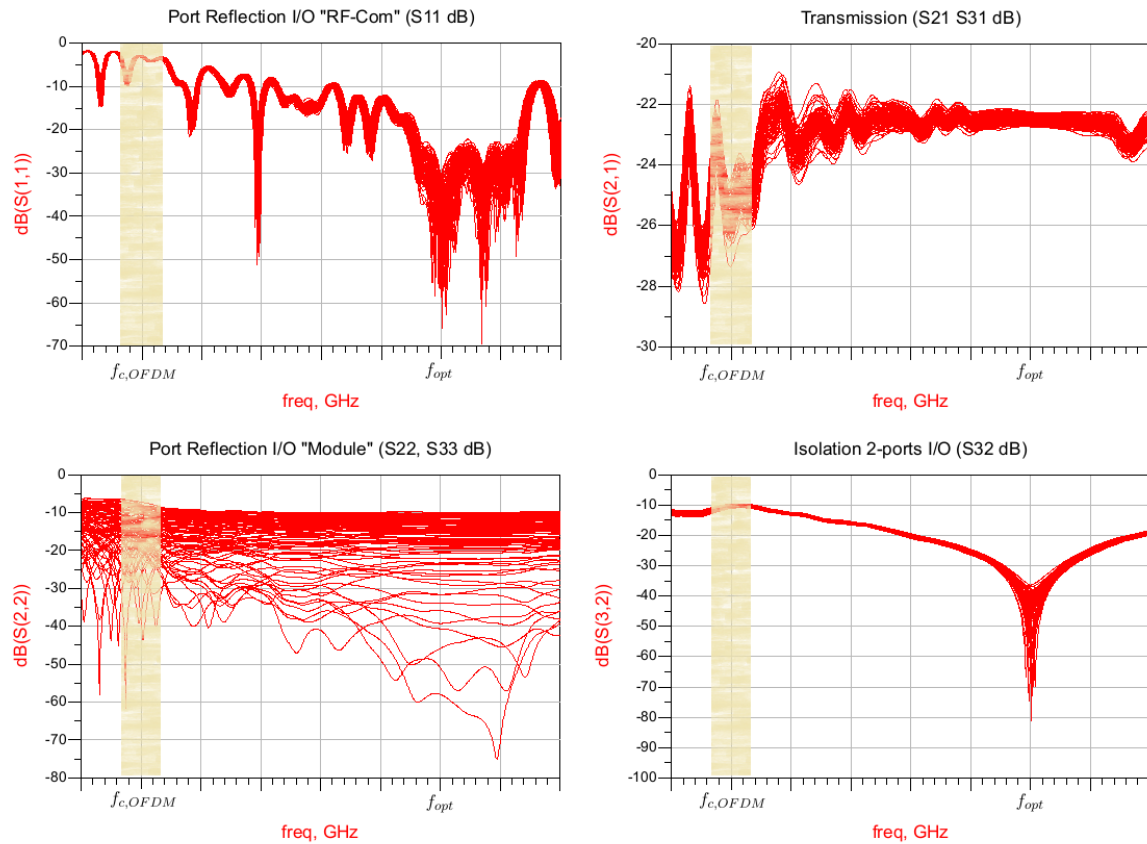


Figure 6.1: RF network characterization plots: Port Reflection "RF-Com", S11 dB (1,1); Return loss, S21 and S31 dB (1,2); Port Reflection "Module", S22 and S33 dB (2,1) and Isolation 2-ports I/O, S32 dB (2,2).

OFDM signal is transmitted with central frequency $f_{c,OFDM}$, where the losses and reflections are higher and the isolation is worse. It is also observed that the losses are not constant over the OFDM bandwidth, which means that different carriers will suffer different losses. To compensate for this loss variation across the OFDM spectrum, the transmission power can be distributed over the carriers in such a way that carriers at frequencies that have a higher insertion loss have a higher transmission power and carriers that have a lower insertion loss are attributed less power in the transmitter. The knowledge of which carriers are more likely to behave worse or better should be used to distribute the OFDM spectrum over the RF front-end modules. Frequency ranges that behave worse should be assigned to the modules on the borders of the array and ranges that behave better should be dedicated to the middle (Section 5.3). Another factor that varies along the OFDM spectrum are the reflections. Since the CP length is common to all carriers, the minimum length should be enough to cover the worst reflection point within the OFDM bandwidth. In principal, for central frequencies around a few GHz, these reflections will always be much shorter than the CIR, that will be dominated by the narrow band receiver.

It was clear from Chapter 5 that there is still not a full understanding of what was causing

carrier $k = 1$ to behave so differently from the remaining carriers. The measuring time was limited and the results not sufficient to elaborate solid conclusions on this matter. To further optimize the system and carefully study the RF impairments and their influence, future work should include

- Tx and Rx design optimization. The best way to optimize the Tx and Rx design is to build a RF model of the OFDM system. In the model, the RF impairments can be added one by one, so that the effects of each one can be studied in separate and compared with the theoretical predictions. Moreover, a RF distribution network can be added between the Tx and the R Rxs, giving the possibility to simulate what would happen if, for example, one branch of the RF combiner is not working and starts reflecting all the power that comes in. In parallel with the test setup, RF "obstacles" may be added to the system enabling a constant simulation/measurement validation for each addition.
- For the SER measurements tryout different scenarios to exclude some of the possible reasons for the observed deviation in Section 5.5 and explore the impairments impact and the system's trade-offs. Testing scenarios may include
 - ▷ Phase offset estimation and correction for every OFDM symbol, increasing the frequency at which the phase rotation is compensated for. This will reduce σ_{ϕ}^2 even more and thus decrease the degradation of the SNR for increasing $isend$. If there was still a significant amount of phase noise in the system, the SER curves will improve, deviating less from the theoretical curve slope. However, it is not expected to solve the deviation problem between carrier $k = 1$ and the others.
 - ▷ For the "no images" experiment, put to zero all carriers left of the carriers of interest (assuming that the band will be downconverted to $f_{IF} > 0$). This way, there will be no new images created at downconversion and all carriers will be put under the same conditions as carrier $k = 1$ was at this point — it will be possible to show for a real "no image" case scenario that 16-QAM is robust enough to the present image and folding level.
 - ▷ Following this line of thought, another interesting experiment is to put to zero only the carrier at f_{LO} for each f_{LO} under test, assuming the carriers of interest placed from Δf upwards, as in the given examples in Chapter 5. All carriers would have the exact same interference as carrier $k = 1$ had with the unmodulated carrier at DC. This would be the ultimate test to verify if the deviation disappears. If so, it is proven that the reason for the 5dB deviation between curves has to do with the downconverted carrier to DC. Nevertheless, it does not explain how modulation on the carrier at DC influences the SER and what effect compromises the orthogonality. The RF model should help to fill this gap.
 - ▷ It was shown in literature that the amplitude and the phase of the images (and carriers folding back, in this case) greatly influences the SER curve (Section 2.5, Figure 2.13). Moreover, that the impact of the image's phase is proportional to the image's amplitude. The closing test to put all the possible downconversions with the same narrow filter bandwidth and decimation under the same folding and images conditions, would be to modulate all the carriers with the same data.

- ▷ Slowly increase the input power until the OFDM signal starts to clip at the receiver's output, study the SER reaction and validate with the theoretical analysis.
 - ▷ In the same way the synthesizer can be calibrated, its I and Q channels' amplitude and phase may also be tuned to increase the imbalance. Perform SER measurements for different I and Q amplitude and phase offsets and validate the results with the theoretical predictions.
 - ▷ Measure all these scenarios for more carriers spaced along the OFDM bandwidth, so that the conclusion that the performance is constant across the spectrum is better supported.
 - ▷ Develop a pre-distortion filter to eliminate the roll-off of the spectrum when the AWG's function is disabled / attenuation of lower frequencies when it is enabled as a cause for SER worse performance.
 - ▷ Explore the different combinations of number of carriers / modulation types and their trade-offs, supporting them with experimental results.
- Work in a optimized hardware implementation of the receiver's digital block on a FPGA. This would improve the test setup and allow real time SER measurements with shorter computation time per loop, enabling the analysis of the SER curves further down.
 - Establish a synchronization protocol that includes the clock/synchronization signal available in the RADAR system.
 - Develop a statistical model for the impact in the RADAR performance of non radiating elements and their spatial position.
 - Expand the concept to multipoint-to-one applications and to wireless mediums.

Appendix A

Derivation of the SER for M-QAM

Let the number of points of the M-QAM constellation be $M = 2^b$, where b is the number of bits defining each constellation symbol. To restrict the derivation to square constellations, b is defined as an positive even integer.

In a square M-QAM constellation, the alphabets α usually used are

$$\alpha_{\text{M-QAM}} = \{\pm(2m+1) \pm i(2m-1)\} \quad \text{where } m \in \left[1, \frac{\sqrt{M}}{2}\right] \quad (\text{A.1})$$

For the case $M = 64$, m would take values from the set $\{1, 2, 3, 4\}$.

The first step will be to compute the average energy of a M-QAM constellation and derive the normalizing factor n_f .

The sum of the energy E of each alphabet is

$$E_\alpha = \sum_{m=1}^{\frac{\sqrt{M}}{2}} |(2m-1) + i(2m-1)|^2 = \frac{\sqrt{M}}{3}(M-1) \quad (\text{A.2})$$

and each alphabet is used $2\sqrt{M}$ times. Hence, the average energy for M constellation points is

$$E_{\text{M-QAM}} = \frac{1}{M} 2\sqrt{M} E_\alpha = \frac{2}{3}(M-1) \quad (\text{A.3})$$

and the scaling/normalization factor for a M-QAM constellation is defined as

$$n_f = \frac{1}{\sqrt{E_{\text{M-QAM}}}} = \sqrt{\frac{3}{2(M-1)}} \quad (\text{A.4})$$

Let the received symbol y be

$$y = n_f \sqrt{E_s} X + n \quad (\text{A.5})$$

where E_s is the symbol energy, X is the transmitted symbol and n is AWGN. As it is commonly known, the AWGN follows the PDF (Probability Distribution Function)

$$p(x) = \frac{1}{\sqrt{2\pi\sigma^2}} e^{-\frac{(x-\mu)^2}{2\sigma^2}} \quad (\text{A.6})$$

with mean $\mu = 0$ and variance $\sigma^2 = \frac{N_0}{2}$.

To derive the SER expression, the M-QAM constellation will be divided into four sections: $N_{corner} = 4$ corner constellation points, $N_{lateral} = 4(\sqrt{M} - 2)$ points in the borders parallel to the imaginary and real axis (except the corners) and $N_{inside} = (\sqrt{M} - 2)(\sqrt{M} - 2)$ remaining central points (without the borders).

The probability that one symbol is wrongly decoded within the entire M-QAM constellation is the average of the probabilities of one symbol being wrongly decoded in each of the above zones

$$\begin{aligned} SER &= P(e|\text{M-QAM}) \\ &= \frac{N_{inside}p(e|inside) + N_{corner}p(e|corner) + N_{lateral}p(e|lateral)}{M} \end{aligned} \quad (\text{A.7})$$

As an example, the probability of a wrong decision for a symbol in the *inside* zone is derived.

The PDF of y given that the transmitted symbol is $\{+n_f\sqrt{E_s}, +n_f\sqrt{E_s}\}$ is

$$p(y|inside) = \frac{1}{\sqrt{\pi N_0}} e^{-\frac{(y-n_f\sqrt{E_s})^2}{N_0}} \quad (\text{A.8})$$

The received symbol is correctly decoded if its real and imaginary part are each between 0 and 2. Thus, the probability of y being correctly demodulated $p(c|inside)$ is

$$p(c|inside) = p(\Re(y) > 0 \wedge \Re(y) \leq 2n_f\sqrt{E_s} + 1) \cdot p(\Im(y) > 0 \wedge \Im(y) \leq 2n_f\sqrt{E_s} + 1) \quad (\text{A.9})$$

To find the probability of the real/imaginary part of y lying between 0 and 2, one just needs to integrate the y 's PDF from 2 to $+\infty$, from $-\infty$ to 0 and subtract the sum from the total probability, which is 1.

$$\begin{aligned} p(\Re(y) > 0 \wedge \Re(y) \leq 2n_f\sqrt{E_s} + 1) &= 1 - \left[\frac{1}{\sqrt{\pi N_0}} \int_{-\infty}^0 e^{-\frac{(y-n_f\sqrt{E_s})^2}{N_0}} dy + \frac{1}{\sqrt{\pi N_0}} \int_{2n_f\sqrt{E_s}}^{+\infty} e^{-\frac{(y-n_f\sqrt{E_s})^2}{N_0}} dy \right] \\ &= 1 - \text{erfc} \left(n_f \sqrt{\frac{E_s}{N_0}} \right) \end{aligned} \quad (\text{A.10})$$

Similarly,

$$p(\Im(y) > 0 \wedge \Im(y) \leq 2n_f\sqrt{E_s} + 1) = 1 - \text{erfc} \left(n_f \sqrt{\frac{E_s}{N_0}} \right) \quad (\text{A.11})$$

The probability of y being wrongly demodulated is then

$$\begin{aligned}
 p(e|inside) &= 1 - p(c|inside) = 1 - \left[1 - \operatorname{erfc} \left(n_f \sqrt{\frac{E_s}{N_0}} \right) \right]^2 \\
 &= 2\operatorname{erfc} \left(n_f \sqrt{\frac{E_s}{N_0}} \right) - \operatorname{erfc}^2 \left(n_f \sqrt{\frac{E_s}{N_0}} \right)
 \end{aligned} \tag{A.12}$$

The same procedure is used to derive $p(e|corner)$ and $p(e|lateral)$. In the end, all probabilities are replaced in Equation A.7 and the SER expression is obtained

$$SER = 2 \left(1 - \frac{1}{\sqrt{M}} \right) \operatorname{erfc} \left(n_f \sqrt{\frac{E_s}{N_0}} \right) - \left(1 - \frac{2}{\sqrt{M}} + \frac{1}{M} \right) \operatorname{erfc}^2 \left(n_f \sqrt{\frac{E_s}{N_0}} \right) \tag{A.13}$$

Appendix B

MAXIM 2829 datasheet

MAX2828/MAX2829

Single-/Dual-Band 802.11a/b/g World-Band Transceiver ICs

General Description

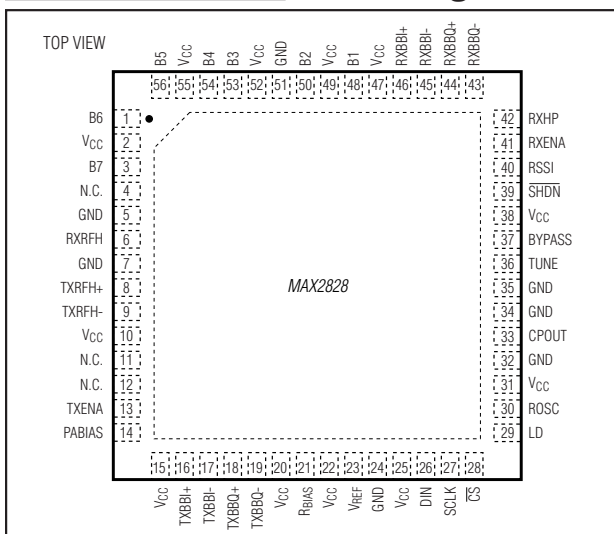
The MAX2828/MAX2829 single-chip, RF transceiver ICs are designed specifically for OFDM 802.11 WLAN applications. The MAX2828 is designed for single-band 802.11a applications covering world-band frequencies of 4.9GHz to 5.875GHz. The MAX2829 is designed for dual-band 802.11a/g applications covering world-bands of 2.4GHz to 2.5GHz and 4.9GHz to 5.875GHz. The ICs include all circuitry required to implement the RF transceiver function, providing a fully integrated receive path, transmit path, VCO, frequency synthesizer, and baseband/control interface. Only the PA, RF switches, RF bandpass filters (BPF), RF baluns, and a small number of passive components are needed to form the complete RF front-end solution.

Each IC completely eliminates the need for external SAW filters by implementing on-chip monolithic filters for both the receiver and transmitter. The baseband filtering and the Rx/Tx signal paths are optimized to meet the 802.11a/g IEEE standards and cover the full range of the required data rates (6, 9, 12, 18, 24, 36, 48, and 54Mbps for OFDM; 1, 2, 5.5, and 11Mbps for CCK/DSSS), at receiver sensitivity levels up to 10dB better than 802.11a/g standards. The MAX2828/MAX2829 transceivers are available in the small 56-pin, exposed paddle thin QFN package.

Applications

Single-/Dual-Band 802.11a/b/g Radios
4.9GHz Public Safety Radios
2.4GHz/5GHz MIMO and Smart Antenna Systems

Pin Configurations



Features

- ◆ **World-Band Operation**
MAX2828: 4.9GHz to 5.875GHz (802.11a)
MAX2829: 2.4GHz to 2.5GHz and 4.9GHz to 5.875GHz (802.11a/b/g)
- ◆ **Best-In-Class Transceiver Performance**
-75dBm Rx Sensitivity at 54Mbps (802.11g)
-46dB (802.11g)/-51dB (802.11a) Tx Sideband Suppression
1.5% (802.11g) and 2% (802.11a) Tx EVM
-100dBc/Hz (802.11g)/-95dBc/Hz (802.11a) LO Phase Noise
Programmable Baseband Lowpass Filters
Integrated PLL with 3-Wire Serial Interface
93dB (802.11g)/97dB (802.11a) Receiver Gain-Control Range
200ns Rx I/Q DC Settling
60dB Dynamic Range Rx RSSI
30dB Tx Power-Control Range
Tx/Rx I/Q Error Detection
I/Q Analog Baseband Interface for Tx and Rx
Digital Mode Selection (Tx, Rx, Standby, and Power Down)
Supports Both Serial and Parallel Gain Control
- ◆ **MIMO and Smart Antenna Compatibility**
Coherent LO Phase Among Multiple Transceivers
- ◆ Support 40MHz Channel Bandwidth (Turbo Mode)
- ◆ Single +2.7V to +3.6V Supply
- ◆ 1µA Low-Power Shutdown Mode
- ◆ Small 56-Pin TQFN Package (8mm x 8mm)

Ordering Information

PART	TEMP RANGE	PIN-PACKAGE
MAX2828 ETN	-40°C to +85°C	56 TQFN-EP* (T5688-2)
MAX2829 ETN	-40°C to +85°C	56 TQFN-EP* (T5688-2)

*EP = Exposed paddle.

Pin Configurations continued at end of data sheet.

For pricing, delivery, and ordering information, please contact Maxim Direct at 1-888-629-4642, or visit Maxim's website at www.maximintegrated.com.

MAX2828/MAX2829


Single-/Dual-Band 802.11a/b/g

World-Band Transceiver ICs

ABSOLUTE MAXIMUM RATINGS

V_{CC}, TXRFH₋, TXRFL₋ to GND.....-0.3V to +4.2V
 RXRFH, RXRFL, TXBBI₋, TXBBQ₋, ROOSC, RXBBI₋, RXBBQ₋,
 RSSI, PABIAS, V_{REF}, CPOUT, RXENA, TXENA, SHDN, CS,
 SCLK, DIN, B₋, RXHP, LD, RBIAS,
 BYPASS to GND-0.3V to (V_{CC} + 0.3V)
 RXBBI₋, RXBBQ₋, RSSI, PABIAS, V_{REF}, CPOUT,
 LD Short-Circuit Duration.....10s

RF Input Power+10dBm
 Continuous Power Dissipation (T_A = +70°C)
 56-Pin Thin QFN (derate 31.3mW/°C above +70°C)....2500mW
 Operating Temperature Range-40°C to +85°C
 Junction Temperature+150°C
 Storage Temperature Range-65°C to +160°C
 Lead Temperature (soldering, 10s)+300°C

 **CAUTION!** ESD SENSITIVE DEVICE

Stresses beyond those listed under "Absolute Maximum Ratings" may cause permanent damage to the device. These are stress ratings only, and functional operation of the device at these or any other conditions beyond those indicated in the operational sections of the specifications is not implied. Exposure to absolute maximum rating conditions for extended periods may affect device reliability.

DC ELECTRICAL CHARACTERISTICS

(MAX2828/MAX2829 evaluation kits: V_{CC} = 2.7V to 3.6V, Rx/Tx set to maximum gain, RBIAS = 11kΩ, no signal at RF inputs, all RF inputs and outputs terminated into 50Ω, receiver baseband outputs are open, no signal applied to Tx I/Q BB inputs in Tx mode, f_{REFOSC} = 40MHz, registers set to default settings and corresponding test mode, T_A = -40°C to +85°C, unless otherwise noted. Typical values are at V_{CC} = +2.7V and T_A = +25°C, unless otherwise noted.) (Note 1)

PARAMETERS	CONDITIONS		MIN	TYP	MAX	UNITS	
Supply Voltage			2.7		3.6	V	
Supply Current	Shutdown mode, reference oscillator not applied, V _{IL} = 0			1	100	μA	
	Standby mode	802.11g MAX2829	T _A = +25°C	37	47		
			T _A = -40°C to +85°C		51		
		802.11a MAX2828/MAX2829	T _A = +25°C	44	51		
			T _A = -40°C to +85°C		55		
	Rx mode	802.11g MAX2829	T _A = +25°C	118	151		
			T _A = -40°C to +85°C		158		
		802.11a MAX2828/MAX2829	T _A = +25°C	135	180		
			T _A = -40°C to +85°C		188		
	Tx mode	802.11g MAX2829	T _A = +25°C	124	164		
			T _A = -40°C to +85°C		175		
		802.11a MAX2828/MAX2829	T _A = +25°C	142	184		
			T _A = -40°C to +85°C		197		
	Standby mode (MIMO) (Note 2)	802.11g MAX2829	T _A = +25°C	65			mA
			T _A = +25°C	70			
		802.11a MAX2828/MAX2829	T _A = +25°C	136			
			T _A = +25°C	154			
802.11g MAX2829		T _A = +25°C	139				
		T _A = +25°C	157				
Tx calibration mode, T _A = +25°C		802.11g MAX2829	129				
		802.11a MAX2828/MAX2829	147				
RX calibration mode, T _A = +25°C		802.11g MAX2829	188				
		802.11a MAX2828/MAX2829	210				
Rx I/Q Output Common-Mode Voltage	T _A = +25°C		0.80	0.9	1.05	V	

MAX2828/MAX2829

Single-/Dual-Band 802.11a/b/g World-Band Transceiver ICs

DC ELECTRICAL CHARACTERISTICS (continued)

(MAX2828/MAX2829 evaluation kits: $V_{CC} = 2.7V$ to $3.6V$, Rx/Tx set to maximum gain, $R_{BIAS} = 11k\Omega$, no signal at RF inputs, all RF inputs and outputs terminated into 50Ω , receiver baseband outputs are open, no signal applied to Tx I/Q BB inputs in Tx mode, $f_{REFOSC} = 40MHz$, registers set to default settings and corresponding test mode, $T_A = -40^\circ C$ to $+85^\circ C$, unless otherwise noted. Typical values are at $V_{CC} = +2.7V$ and $T_A = +25^\circ C$, unless otherwise noted.) (Note 1)

PARAMETERS	CONDITIONS	MIN	TYP	MAX	UNITS
Rx I/Q Output Common-Mode Voltage Variation	$T_A = -40^\circ C$ (relative to $+25^\circ C$)		-25		mV
	$T_A = +85^\circ C$ (relative to $+25^\circ C$)		20		
Tx Baseband Input Common-Mode Voltage Operating Range		0.9		1.3	V
Tx Baseband Input Bias Current				13	μA
Reference Voltage Output	$-1mA < I_{OUT} < +1mA$		1.2		V
Digital Input-Voltage High, V_{IH}		$V_{CC} - 0.4$			V
Digital Input-Voltage Low, V_{IL}				0.4	V
Digital Input-Current High, I_{IH}		-1		+1	μA
Digital Input-Current Low, I_{IL}		-1		+1	μA
LD Output-Voltage High, V_{OH}	Sourcing $100\mu A$	$V_{CC} - 0.4$			V
LD Output-Voltage Low, V_{OL}	Sinking $100\mu A$			0.4	V

AC ELECTRICAL CHARACTERISTICS—802.11g Rx Mode (MAX2829)

(MAX2829 evaluation kit: $V_{CC} = +2.7V$, $f_{IN} = 2.437GHz$; receiver baseband I/Q outputs at $112mV_{RMS}$ ($-19dBV$), $f_{REFOSC} = 40MHz$, $\overline{SHDN} = \overline{RXENA} = \overline{CS} = \text{high}$, $RXHP = \overline{TXENA} = \overline{SCLK} = \overline{DIN} = \text{low}$, $R_{BIAS} = 11k\Omega$, registers set to default settings and corresponding test mode, $T_A = +25^\circ C$, unless otherwise noted. Unmodulated single-tone RF input signal is used, unless otherwise indicated.) (Tables 1, 2, 3)

PARAMETER	CONDITIONS	MIN	TYP	MAX	UNITS
RECEIVER SECTION: LNA RF INPUT TO BASEBAND I/Q OUTPUTS					
RF Input Frequency Range		2.412		2.500	GHz
RF Input Return Loss	With 50Ω external match	LNA high-gain mode (B7:B6 = 11)		-22	dB
		LNA medium-gain mode (B7:B6 = 10)		-24	
		LNA low-gain mode (B7:B6 = 0X)		-12	
Total Voltage Gain	Maximum gain, B7:B1 = 1111111	$T_A = +25^\circ C$	87	94	dB
		$T_A = -40^\circ C$ to $+85^\circ C$ (Note 1)	85		
RF Gain Steps	From high-gain mode (B7:B6 = 11) to medium-gain mode (B7:B6 = 10) (Note 3)		-15.5		dB
	From high-gain mode (B7:B6 = 11) to low-gain mode (B7:B6 = 0X) (Note 3)		-30.5		
Gain Variation Over RF Band	$f_{RF} = 2.412GHz$ to $2.5GHz$			3	dB
Baseband Gain Range	From maximum baseband gain (B5:B1 = 111111) to minimum baseband gain (B5:B1 = 00000)		62		dB

MAX2828/MAX2829

Single-/Dual-Band 802.11a/b/g World-Band Transceiver ICs

AC ELECTRICAL CHARACTERISTICS—802.11g Rx Mode (MAX2829) (continued)

(MAX2829 evaluation kit: $V_{CC} = +2.7V$, $f_{IN} = 2.437GHz$; receiver baseband I/Q outputs at $112mV_{RMS}$ (-19dBV), $f_{REFOSC} = 40MHz$, $\overline{SHDN} = \overline{RXENA} = \overline{CS} = \text{high}$, $RXHP = \overline{TXENA} = \overline{SCLK} = \overline{DIN} = \text{low}$, $R_{BIAS} = 11k\Omega$, registers set to default settings and corresponding test mode, $T_A = +25^\circ C$, unless otherwise noted. Unmodulated single-tone RF input signal is used, unless otherwise indicated.) (Tables 1, 2, 3)

PARAMETER	CONDITIONS		MIN	TYP	MAX	UNITS
DSB Noise Figure	Voltage gain $\geq 65dB$, with B7:B6 = 11			3.5		dB
	Voltage gain = 50dB, with B7:B6 = 11			4		
	Voltage gain = 45dB, with B7:B6 = 10			16		
	Voltage gain = 15dB, with B7:B6 = 0X			36		
Output P-1 _{dB}	Voltage gain = 90dB, with B7:B6 = 11			3.2		V _{P-P}
Out-of-Band Input IP3	-35dBm jammers at 40MHz and 78MHz offset; based on IM3 at 2MHz	Voltage gain = 60dB, with B7:B6 = 11		-10		dBm
		Voltage gain = 45dB, with B7:B6 = 10		-2		
		Voltage gain = 40dB, with B7:B6 = 0X		21		
In-Band Input P-1 _{dB}	Voltage gain = 40dB, with B7:B6 = 11			-29		dBm
	Voltage gain = 25dB, with B7:B6 = 10			-14		
	Voltage gain = 5dB, with B7:B6 = 0X			2		
In-Band Input IP3	Tones at 7MHz and 8MHz, IM3 at 6MHz and 9MHz, P _{IN} = -40dBm per tone	Voltage gain = 40dB, with B7:B6 = 11		-17		dBm
		Voltage gain = 25dB, with B7:B6 = 10		-5		
		Voltage gain = 5dB, with B7:B6 = 0X		14		
I/Q Phase Error	B7:B1 = 1101110, 1 σ variation			± 0.5		degrees
I/Q Gain Imbalance	B7:B1 = 1101110, 1 σ variation			± 0.1		dB
Tx-to-Rx Conversion Gain for Rx I/Q Calibration	B7:B1 = 0010101 (Note 4)			-4		dB
I/Q Static DC Offset	RXHP = 1, B7:B1 = 1101110, 1 σ variation			± 2		mV
I/Q DC Droop	After switching RXHP to 0, D2 = 0 (see the <i>RX Control/RSSI Register Definition</i> section)			± 1		mV/ms
RF Gain-Change Settling Time	Gain change from high gain to medium gain, high gain to low gain, or medium gain to low gain; gain settling to within $\pm 2dB$ of steady state			0.4		μs
Baseband VGA Settling Time	Gain change from B5:B1 = 10111 to B5:B1 = 00111; gain settling to within $\pm 2dB$ of steady state			0.1		μs
Rx I/Q Output Load Impedance	Minimum differential resistance			10		k Ω
	Maximum differential capacitance			8		pF
Spurious Signal Emissions at LNA Input	RF = 1GHz to 26.5GHz			-67		dBm

MAX2828/MAX2829

Single-/Dual-Band 802.11a/b/g World-Band Transceiver ICs

AC ELECTRICAL CHARACTERISTICS—802.11g Rx Mode (MAX2829) (continued)

(MAX2829 evaluation kit: $V_{CC} = +2.7V$, $f_{IN} = 2.437GHz$; receiver baseband I/Q outputs at 112mV_{RMS} (-19dBV), $f_{REFOSC} = 40MHz$, $\overline{SHDN} = \overline{RXENA} = \overline{CS} = \text{high}$, $RXHP = \overline{TXENA} = \overline{SCLK} = \overline{DIN} = \text{low}$, $R_{BIAS} = 11k\Omega$, registers set to default settings and corresponding test mode, $T_A = +25^\circ C$, unless otherwise noted. Unmodulated single-tone RF input signal is used, unless otherwise indicated.) (Tables 1, 2, 3)

PARAMETER	CONDITIONS		MIN	TYP	MAX	UNITS
RECEIVER BASEBAND FILTERS						
Baseband -3dB Corner Frequency	(See the <i>Lowpass Filter Register</i> section)	Narrowband mode		7.5		MHz
		Nominal mode		9.5		
		Turbo mode 1		14		
		Turbo mode 2		18		
Baseband Filter Rejection (Nominal Mode)	$f_{BASEBAND} = 15MHz$			20		dB
	$f_{BASEBAND} = 20MHz$			39		
	$f_{BASEBAND} > 40MHz$			84		
RSSI						
RSSI Minimum Output Voltage	RXHP = 1, low range (D11 = 0, see the <i>Rx Control/RSSI Register Definition</i> section)			0.5		V
	RXHP = 1, high range (D11 = 1, see the <i>Rx Control/RSSI Register Definition</i> section)			0.52		
RSSI Maximum Output Voltage	RXHP = 1, low range (D11 = 0, see the <i>Rx Control/RSSI Register Definition</i> section)			2		V
	RXHP = 1, high range (D11 = 1, see the <i>Rx Control/RSSI Register Definition</i> section)			2.5		
RSSI Slope	RXHP = 1, low range (D11 = 0, see the <i>Rx Control/RSSI Register Definition</i> section)			22.5		mV/dB
	RXHP = 1, high range (D11 = 1, see the <i>Rx Control/RSSI Register Definition</i> section)			30		
RSSI Output Settling Time	To within 3dB of steady state	+40dB signal step		0.2		μs
		-40dB signal step		0.7		

MAX2828/MAX2829

Single-/Dual-Band 802.11a/b/g

World-Band Transceiver ICs

AC ELECTRICAL CHARACTERISTICS—802.11a Rx Mode (MAX2828/MAX2829)

(MAX2828/MAX2829 evaluation kits: $V_{CC} = +2.7V$, $f_{IN} = 5.25GHz$; receiver baseband I/Q outputs at $112mV_{RMS}$ (-19dBV), $f_{REFOSC} = 40MHz$, $\overline{SHDN} = \overline{RXENA} = \overline{CS} = \text{high}$, $\overline{RXHP} = \overline{TXENA} = \overline{SCLK} = \overline{DIN} = \text{low}$, $R_{BIAS} = 11k\Omega$, registers set to default settings and corresponding test mode, $T_A = +25^\circ C$, unless otherwise noted. Unmodulated single-tone RF input signal is used, unless otherwise indicated.) (Tables 1, 2, 3)

PARAMETER	CONDITIONS		MIN	TYP	MAX	UNITS
RECEIVER SECTION: LNA RF INPUT TO BASEBAND I/Q OUTPUTS						
RF Input Frequency Range	802.11a low-band mode		4.900		5.350	GHz
	802.11a high-band mode		5.470		5.875	
RF Input Return Loss	With 50 Ω external match	LNA high-gain mode (B7:B6 = 11)		-15		dB
		LNA medium-gain mode (B7:B6 = 10)		-11		
		LNA low-gain mode (B7:B6 = 0X)		-7		
Total Voltage Gain	Maximum gain, B7:B1 = 1111111	$T_A = +25^\circ C$	91	97		dB
		$T_A = -40^\circ C$ to $+85^\circ C$ (Note 1)	88			
	Minimum gain, B7:B1 = 0000000	$T_A = +25^\circ C$		0	3	dB
RF Gain Steps	From high-gain mode (B7:B6 = 11) to medium-gain mode (B7:B6 = 10) (Note 3)			-19		dB
	From high-gain mode (B7:B6 = 11) to low-gain mode (B7:B6 = 0X) (Note 3)			-34.5		
Gain Variation Relative to 5.25GHz	$f_{RF} = 4.9GHz$			-0.3		dB
	$f_{RF} = 5.35GHz$			0.4		
	$f_{RF} = 5.875GHz$			-4		
Baseband Gain Range	From maximum baseband gain (B5:B1 = 11111) to minimum baseband gain (B5:B1 = 00000)			62		dB
DSB Noise Figure	Voltage gain $\geq 65dB$, with B7:B6 = 11			4.5		dB
	Voltage gain = 50dB, with B7:B6 = 11			4.8		
	Voltage gain = 45dB, with B7:B6 = 10			15		
	Voltage gain = 15dB, with B7:B6 = 0X			36		
Output P-1 _{dB}	Voltage gain = 90dB, with B7:B6 = 11			3.2		V _{P-P}
Out-of-Band Input IP3	-35dBm jammers at 40MHz and 78MHz offset; based on IM3 at 2MHz	Voltage gain = 60dB, with B7:B6 = 11		-15		dBm
		Voltage gain = 45dB, with B7:B6 = 10		0.5		
		Voltage gain = 40dB, with B7:B6 = 0X		20		
In-Band Input P-1 _{dB}	Voltage gain = 35dB, with B7:B6 = 11			-32		dBm
	Voltage gain = 20dB, with B7:B6 = 10			-12		
	Voltage gain = 5dB, with B7:B6 = 0X			3		

MAX2828/MAX2829

Single-/Dual-Band 802.11a/b/g

World-Band Transceiver ICs

AC ELECTRICAL CHARACTERISTICS—802.11a Rx Mode (MAX2828/MAX2829) (continued)

(MAX2828/MAX2829 evaluation kits: $V_{CC} = +2.7V$, $f_{IN} = 5.25GHz$; receiver baseband I/Q outputs at $112mV_{RMS}$ (-19dBV), $f_{REFOSC} = 40MHz$, $\overline{SHDN} = \overline{RXENA} = \overline{CS} = \text{high}$, $\overline{RXHP} = \overline{TXENA} = \overline{SCLK} = \overline{DIN} = \text{low}$, $R_{BIAS} = 11k\Omega$, registers set to default settings and corresponding test mode, $T_A = +25^\circ C$, unless otherwise noted. Unmodulated single-tone RF input signal is used, unless otherwise indicated.) (Tables 1, 2, 3)

PARAMETER	CONDITIONS		MIN	TYP	MAX	UNITS
In-Band Input IP3	Tones at 7MHz and 8MHz, IM3 at 6MHz and 9MHz, $P_{IN} = -40dBm$ per tone	Voltage gain = 35dB, with B7:B6 = 11		-24		dBm
		Voltage gain = 20dB, with B7:B6 = 10		-5		
		Voltage gain = 5dB, with B7:B6 = 0X		13		
I/Q Phase Error	B7:B1 = 1101110, 1σ variation			± 0.4		degrees
I/Q Gain Imbalance	B7:B1 = 1101110, 1σ variation			± 0.1		dB
Tx-to-Rx Conversion Gain for Rx I/Q Calibration	B7:B1 = 0001111 (Note 4)			0		dB
I/Q Static DC Offset	RXHP = 1, B7:B1 = 1101110, 1σ variation			± 2		mV
I/Q DC Droop	After switching RXHP to 0, D2 = 0 (see the <i>Rx Control/RSSI Register Definition</i> section)			± 1		mV/ms
RF Gain-Change Settling Time	Gain change from high gain to medium gain, high gain to low gain, or medium gain to low gain; gain settling to within $\pm 2dB$ of steady state			0.4		μs
Baseband VGA Settling Time	Gain change from B5:B1 = 10111 to B5:B1 = 00111; gain settling to within $\pm 2dB$ of steady state			0.1		μs
Rx I/Q Output Load Impedance	Minimum differential resistance			10		k Ω
	Maximum differential capacitance			8		pF
Spurious Signal Emissions at LNA input	RF = 1GHz to 26.5GHz			-50		dBm
RECEIVER BASEBAND FILTERS						
Baseband -3dB Corner Frequency	(See the <i>Lowpass Filter Register Definition</i> section)	Narrow-band mode		7.5		MHz
		Nominal mode		9.5		
		Turbo mode 1		14		
		Turbo mode 2		18		
Baseband Filter Rejection (Nominal Mode)	$f_{BASEBAND} = 15MHz$			20		dB
	$f_{BASEBAND} = 20MHz$			39		
	$f_{BASEBAND} > 40MHz$			80		

MAX2828/MAX2829

Single-/Dual-Band 802.11a/b/g

World-Band Transceiver ICs

AC ELECTRICAL CHARACTERISTICS—802.11a Rx Mode (MAX2828/MAX2829) (continued)

(MAX2828/MAX2829 evaluation kits: $V_{CC} = +2.7V$, $f_{IN} = 5.25GHz$; receiver baseband I/Q outputs at $112mV_{RMS}$ (-19dBV), $f_{REFOSC} = 40MHz$, $\overline{SHDN} = \overline{RXENA} = \overline{CS} = \text{high}$, $RXHP = TXENA = SCLK = DIN = \text{low}$, $R_{BIAS} = 11k\Omega$, registers set to default settings and corresponding test mode, $T_A = +25^\circ C$, unless otherwise noted. Unmodulated single-tone RF input signal is used, unless otherwise indicated.) (Tables 1, 2, 3)

PARAMETER	CONDITIONS	MIN	TYP	MAX	UNITS
RSSI					
RSSI Minimum Output Voltage	RXHP = 1, low range (D11 = 0, see the <i>Rx Control/RSSI Register Definition</i> section)		0.5		V
	RXHP = 1, high range (D11 = 1, see the <i>Rx Control/RSSI Register Definition</i> section)		0.52		
RSSI Maximum Output Voltage	RXHP = 1, low range (D11 = 0, see the <i>Rx Control/RSSI Register Definition</i> section)		2		V
	RXHP = 1, high range (D11 = 1, see the <i>Rx Control/RSSI Register Definition</i> section)		2.5		
RSSI Slope	RXHP = 1, low range (D11 = 0, see the <i>Rx Control/RSSI Register Definition</i> section)		22.5		mV/dB
	RXHP = 1, high range (D11 = 1, see the <i>Rx Control/RSSI Register Definition</i> section)		30		
RSSI Output Settling Time	To within 3dB of steady state	+40dB signal step	0.2		μs
		-40dB signal step	0.7		

AC ELECTRICAL CHARACTERISTICS—802.11g Tx Mode (MAX2829)

(MAX2829 evaluation kit: $V_{CC} = +2.7V$, $f_{OUT} = 2.437GHz$, $f_{REFOSC} = 40MHz$, $\overline{SHDN} = \overline{TXENA} = \overline{CS} = \text{high}$, $RXENA = SCLK = DIN = \text{low}$, $R_{BIAS} = 11k\Omega$, 100mV_{RMS} sine and cosine signal (or 100mV_{RMS}, 54Mbps IEEE 802.11g I/Q signals wherever OFDM is mentioned) applied to baseband I/Q inputs of transmitter, registers set to default settings and corresponding test mode, $T_A = +25^\circ C$, unless otherwise noted.) (Table 4)

PARAMETER	CONDITIONS	MIN	TYP	MAX	UNITS
TRANSMIT SECTION: Tx BASEBAND I/Q INPUTS TO RF OUTPUTS					
RF Output Frequency Range, f_{RF}		2.412		2.500	GHz
Output Power	54Mbps 802.11g OFDM signal	1.5% EVM	-2.5		dBm
		B6:B1 = 111011	-4.5		
Output Power (CW)	$V_{IN} = 100mV_{RMS}$ at 1MHz I/Q CW signal, B6:B1 = 111111		-2		dBm
Output Power Range	B6:B1 = 111111 to B6:B1 = 000000		30		dB
Carrier Leakage	Without DC offset cancellation		-27		dBc
Unwanted Sideband Suppression	Uncalibrated		-46		dBc
Tx Output ACP	Measured with 1MHz resolution bandwidth at 22MHz offset from channel center (B6:B1 = 111011), OFDM signal		-69		dBm/MHz
RF Output Return Loss	With external 50 Ω match		-14		dB

MAX2828/MAX2829

Single-/Dual-Band 802.11a/b/g World-Band Transceiver ICs

AC ELECTRICAL CHARACTERISTICS—802.11g Tx Mode (MAX2829) (continued)

(MAX2829 evaluation kit: $V_{CC} = +2.7V$, $f_{OUT} = 2.437GHz$, $f_{REFOSC} = 40MHz$, $\overline{SHDN} = TXENA = \overline{CS} = high$, $RXENA = SCLK = DIN = low$, $R_{BIAS} = 11k\Omega$, $100mV_{RMS}$ sine and cosine signal (or $100mV_{RMS}$, 54Mbps IEEE 802.11g I/Q signals wherever OFDM is mentioned) applied to baseband I/Q inputs of transmitter, registers set to default settings and corresponding test mode, $T_A = +25^\circ C$, unless otherwise noted.) (Table 4)

PARAMETER	CONDITIONS		MIN	TYP	MAX	UNITS
RF Spurious Signal Emissions	B6:B1 = 111011, OFDM signal	$2/3 \times f_{RF}$		-64		dBm/ MHz
		$4/3 \times f_{RF}$		-61		
		$5/3 \times f_{RF}$		-63		
		$8/3 \times f_{RF}$		-52		
Baseband -3dB Corner Frequency	(See the <i>Lowpass Filter Register Definition</i> section)	Nominal mode		12		MHz
		Turbo mode 1		18		
		Turbo mode 2		24		
Baseband Filter Rejection	At 30MHz, in nominal mode (see the <i>Lowpass Filter Register Definition</i> section)			60		dB
Tx Baseband Input Impedance	Minimum differential resistance			60		k Ω
	Maximum differential capacitance			0.7		pF
TRANSMITTER LO LEAKAGE AND I/Q CALIBRATION USING LO LEAKAGE AND SIDEBAND DETECTOR (SEE THE Tx/Rx CALIBRATION MODE SECTION)						
Tx BASEBAND I/Q INPUTS TO RECEIVER OUTPUTS						
LO Leakage and Sideband-Detector Output	Calibration register, D12:D11 = 11, A3:A0 = 0110	Output at $1 \times f_{TONE}$ (for LO leakage = -29dBc), $f_{TONE} = 2MHz$, $100mV_{RMS}$		-3		dBV _{RMS}
		Output at $2 \times f_{TONE}$ (for sideband suppression = -40dBc), $f_{TONE} = 2MHz$, $100mV_{RMS}$		-13		
Amplifier Gain Range	D12:D11 = 00 to D12:D11 = 11, A3:A0 = 0110			26		dB
Lower -3dB Corner Frequency				1		MHz

MAX2828/MAX2829

Single-/Dual-Band 802.11a/b/g World-Band Transceiver ICs

AC ELECTRICAL CHARACTERISTICS—802.11a Tx Mode (MAX2828/MAX2829)

(MAX2828/MAX2829 evaluation kits: $V_{CC} = +2.7V$, $f_{OUT} = 5.25GHz$, $f_{REFOSC} = 40MHz$, $SHDN = TXENA = \overline{CS} = high$, $RXENA = SCLK = DIN = low$, $R_{BIAS} = 11k\Omega$, 100mV_{RMS} sine and cosine signal (or 100mV_{RMS}, 54Mbps IEEE 802.11a I/Q signals wherever OFDM is mentioned) applied to baseband I/Q inputs of transmitter, registers set to default settings and corresponding test mode, $T_A = +25^{\circ}C$, unless otherwise noted.) (Table 4)

PARAMETER	CONDITIONS		MIN	TYP	MAX	UNITS
TRANSMIT SECTION: Tx BASEBAND I/Q INPUTS TO RF OUTPUTS						
RF Output Frequency Range, f_{RF}	802.11a low-band mode		4.900		5.350	GHz
	802.11a high-band mode		5.470		5.875	
Output Power	54Mbps 802.11a OFDM signal	2% EVM		-5		dBm
		B6:B1 = 111100		-6.5		
Output Power (CW)	$V_{IN} = 100mV_{RMS}$ at 1MHz I/Q CW signal, B6:B1 = 111111			-4.5		dBm
Output Power Variation Relative to 5.25GHz	$f_{RF} = 4.9GHz$			-6		dB
	$f_{RF} = 5.35GHz$			-0.5		
	$f_{RF} = 5.875GHz$			-1		
Output Power Range	B6:B1 = 111111 to B6:B1 = 000000			30		dB
Carrier Leakage	Without DC offset cancellation			-27		dBc
Unwanted Sideband Suppression	Uncalibrated			-51		dBc
Tx Output ACP	Measured with 1MHz resolution bandwidth at 30MHz offset from channel center (B6:B1 = 111100), OFDM signal			-80		dBm/MHz
RF Output Return Loss	With external 50 Ω match			-16		dB
RF Spurious Signal Emissions	B6:B1 = 111100, OFDM signal	4/5 x f_{RF}		-55		dBm/MHz
		6/5 x f_{RF}		-64		
		7/5 x f_{RF}		-65		
		8/5 x f_{RF}		-49		
Baseband -3dB Corner Frequency	(see the <i>Lowpass Filter Register Definition</i> section)	Nominal mode		12		MHz
		Turbo mode 1		18		
		Turbo mode 2		24		
Baseband Filter Rejection	At 30MHz, in nominal mode (see the <i>Lowpass Filter Register Definition</i> section)			60		dB
Tx Baseband Input Impedance	Minimum differential resistance			60		k Ω
	Maximum differential capacitance			0.7		pF
TRANSMITTER LO LEAKAGE AND I/Q CALIBRATION USING LO LEAKAGE AND SIDEBAND DETECTOR (SEE THE Tx/Rx CALIBRATION MODE SECTION)						
Tx BASEBAND I/Q INPUTS TO RECEIVER OUTPUTS						
LO Leakage and Sideband-Detector Output	Calibration register, D12:D11 = 1, A3:A0 = 0110	Output at 1 x f_{TONE} (for LO leakage = -29dBc), $f_{TONE} = 2MHz$, 100mV _{RMS}		-4.5		dBV _{RMS}
		Output at 2 x f_{TONE} (for sideband suppression = -40dBc), $f_{TONE} = 2MHz$, 100mV _{RMS}		-14.5		
Amplifier Gain Range	D12:D11 = 00 to D12:D11 = 11, A3:A0 = 0110			26		dB
Lower -3dB Corner Frequency				1		MHz

MAX2828/MAX2829

Single-/Dual-Band 802.11a/b/g World-Band Transceiver ICs

AC ELECTRICAL CHARACTERISTICS—Frequency Synthesis

(MAX2828/MAX2829 evaluation kits: $V_{CC} = +2.7V$, $f_{RF} = 2.437GHz$ (802.11g) or $f_{RF} = 5.25GHz$ (802.11a), $f_{REFOSC} = 40MHz$, $\overline{SHDN} = \overline{CS} = \text{high}$, $SCLK = \overline{DIN} = \text{low}$, PLL loop bandwidth = 150kHz, $R_{BIAS} = 11k\Omega$, $T_A = +25^\circ C$, unless otherwise noted.)

PARAMETER	CONDITIONS		MIN	TYP	MAX	UNITS	
FREQUENCY SYNTHESIZER							
RF Channel Center Frequency	802.11g mode		2412		2500	MHz	
	802.11a low-band mode		4900		5350		
	802.11a high-band mode		5470		5875		
Charge-Pump Comparison Frequency				20		MHz	
f_{REFOSC} Input Frequency			20		44	MHz	
Reference-Divider Ratio			1		4		
f_{REFOSC} Input Levels	AC-coupled		800			mV _{P-P}	
f_{REFOSC} Input Impedance				10		k Ω	
Closed-Loop Phase Noise	802.11g	$f_{OFFSET} = 1kHz$		-87		dBc/Hz	
		$f_{OFFSET} = 10kHz$		-103			
		$f_{OFFSET} = 100kHz$		-99			
		$f_{OFFSET} = 1MHz$		-112			
		$f_{OFFSET} = 10MHz$		-125			
	802.11a	$f_{OFFSET} = 1kHz$		-84			
		$f_{OFFSET} = 10kHz$		-95			
		$f_{OFFSET} = 100kHz$		-92			
		$f_{OFFSET} = 1MHz$		-108			
		$f_{OFFSET} = 10MHz$		-124			
Closed-Loop Integrated Phase Noise	RMS phase jitter, integrate from 10kHz to 10MHz offset		802.11g		0.6	degrees	
			802.11a		1		
Charge-Pump Output Current				4		mA	
Charge-Pump Output Voltage	>70% of I_{CP}		0.5		$V_{CC} - 0.5V$	V	
Reference Spurs	20MHz offset		802.11g		-65	dBc	
			802.11a		-58		
VOLTAGE-CONTROLLED OSCILLATOR							
VCO Tuning Voltage Range			0.4		2.3	V	
LO Tuning Gain	802.11g	$V_{TUNE} = 0.4V$		135		MHz/V	
		$V_{TUNE} = 2.3V$		62			
	802.11a	Low band	$V_{TUNE} = 0.3V$		324		
			$V_{TUNE} = 2.2V$		167		
		High band	$V_{TUNE} = 0.3V$		330		
			$V_{TUNE} = 2.2V$		175		

MAX2828/MAX2829

Single-/Dual-Band 802.11a/b/g World-Band Transceiver ICs

AC ELECTRICAL CHARACTERISTICS—Miscellaneous Blocks

(MAX2828/MAX2829 evaluation kits: $V_{CC} = +2.7V$, $f_{RF} = 2.437GHz$ (802.11g) or $f_{RF} = 5.25GHz$ (802.11a), $f_{REFOSC} = 40MHz$, $\overline{SHDN} = \overline{CS} = \text{high}$, $SCLK = DIN = \text{low}$, $R_{BIAS} = 11k\Omega$, $T_A = +25^\circ C$, unless otherwise noted.)

PARAMETER	CONDITIONS	MIN	TYP	MAX	UNITS
PA BIAS DAC					
Number of Programmable Bits			6		Bits
Minimum Output Sink Current	D5:D0 = 000000 (see the <i>PA Bias DAC Register Definition</i> section)		0		μA
Maximum Output Sink Current	D5:D0 = 111111 (see the <i>PA Bias DAC Register Definition</i> section), output voltage = 0.8V		313		μA
Turn-On Time	D9:D6 = 0000 (see the <i>PA Bias DAC Register Definition</i> section)		0.2		μs
DNL			1		LSB
ON-CHIP TEMPERATURE SENSOR					
Output Voltage	D11 = 1 (see the <i>Rx Control/RSSI Register Definition</i> section)	$T_A = -40^\circ C$		0.5	V
		$T_A = +25^\circ C$		1.05	
		$T_A = +85^\circ C$		1.6	

AC ELECTRICAL CHARACTERISTICS—Timing

(MAX2828/MAX2829 evaluation kits: $V_{CC} = 2.7V$, $f_{RF} = 2.437GHz$ (802.11g) or $f_{RF} = 5.25GHz$ (802.11a), $f_{REFOSC} = 40MHz$, $\overline{SHDN} = \overline{CS} = \text{high}$, $SCLK = DIN = \text{low}$, PLL loop bandwidth = 150kHz, $R_{BIAS} = 11k\Omega$, $T_A = +25^\circ C$, unless otherwise noted.)

PARAMETER	CONDITIONS	MIN	TYP	MAX	UNITS
SYSTEM TIMING (See Figure 1)					
Turn-On Time	From \overline{SHDN} rising edge (PLL locked)		50		μs
Shutdown Time			2		μs
Channel Switching Time	$f_{RF} = 2.412GHz$ to 2.5GHz		25		μs
	$f_{RF} = 5.15GHz$ to 5.35GHz		35		
	$f_{RF} = 5.45GHz$ to 5.875GHz		130		
	$f_{RF} = 4.9GHz$ to 5.875GHz		130		
Rx/Tx Turnaround Time	Measured from Tx or Rx enable rising edge; signal settling to within $\pm 2dB$ of steady state	Rx to Tx		1	μs
		Tx to Rx, RXHP = 1		1.2	
Tx Turn-On Time (From Standby Mode)	From Tx enable rising edge; signal settling to within $\pm 2dB$ of steady state		1		μs
Rx Turn-On Time (From Standby Mode)	From Rx enable rising edge; signal settling to within $\pm 2dB$ of steady state		1.2		μs

MAX2828/MAX2829

Single-/Dual-Band 802.11a/b/g World-Band Transceiver ICs

AC ELECTRICAL CHARACTERISTICS—Timing (continued)

(MAX2828/MAX2829 evaluation kits: $V_{CC} = 2.7V$, $f_{RF} = 2.437GHz$ (802.11g) or $f_{RF} = 5.25GHz$ (802.11a), $f_{REFOSC} = 40MHz$, $\overline{SHDN} = \overline{CS} = \text{high}$, $SCLK = DIN = \text{low}$, PLL loop bandwidth = 150kHz, $R_{BIAS} = 11k\Omega$, $T_A = +25^\circ C$, unless otherwise noted.)

PARAMETER	CONDITIONS	MIN	TYP	MAX	UNITS
3-WIRE SERIAL INTERFACE TIMING (SEE FIGURE 2)					
SCLK-Rising-Edge to \overline{CS} -Falling-Edge Wait Time, t_{CSO}			6		ns
Falling Edge of \overline{CS} to Rising Edge of First SCLK Time, t_{CSS}			6		ns
DIN-to-SCLK Setup Time, t_{DS}			6		ns
DIN-to-SCLK Hold Time, t_{DH}			6		ns
SCLK Pulse-Width High, t_{CH}			6		ns
SCLK Pulse-Width Low, t_{CL}			6		ns
Last Rising Edge of SCLK to Rising Edge of \overline{CS} or Clock to Load Enable Setup Time, t_{CSH}			6		ns
\overline{CS} High Pulse Width, t_{CSW}			20		ns
Time Between the Rising Edge of \overline{CS} and the Next Rising Edge of SCLK, t_{CS1}			6		ns
Clock Frequency, f_{CLK}			40		MHz
Rise Time, t_R			2		ns
Fall Time, t_F			2		ns

Note 1: Devices are production tested at +85°C only. Min and max limits at temperatures other than +85°C are guaranteed by design and characterization.

Note 2: Register settings for MIMO mode. A3:A0 = 0101 and A3:A0 = 0010, D13 = 1.

Note 3: The expected part-to-part variation of the RF gain step is $\pm 1dB$.

Note 4: Tx I/Q inputs = 100mV_{RMS}. Set Tx VGA gain to max.

Table 1. Receiver Front-End Gain-Control Settings

B7	B6	GAIN
1	1	High
1	0	Medium
0	X	Low

Table 2. Receiver Baseband VGA Gain Settings

B5:B1	GAIN
11111	Max
11110	Max - 2dB
11101	Max - 4dB
:	:
00000	Min

MAX2828/MAX2829

Single-/Dual-Band 802.11a/b/g

World-Band Transceiver ICs

Table 3. Receiver Baseband VGA Gain Step Control

BIT	GAIN STEP (typ)
B1	2dB
B2	4dB
B3	8dB
B4	16dB
B5	32dB

Table 4. Tx VGA Gain Control Settings

NUMBER	B6:B1	OUTPUT SIGNAL POWER
63	111111	Max
62	111110	Max - 0.5dB
61	111101	Max - 1.0dB
:	:	:
49	110001	Max - 7dB
48	110000	Max - 7.5dB
47	101111	Max - 8dB
46	101110	Max - 8dB
45	101101	Max - 9dB
44	101100	Max - 9dB
:	:	:
5	000101	Max - 29dB
4	000100	Max - 29dB
3	000011	Max - 30dB
2	000010	Max - 30dB
1	000001	Max - 30dB
0	000000	Max - 30dB

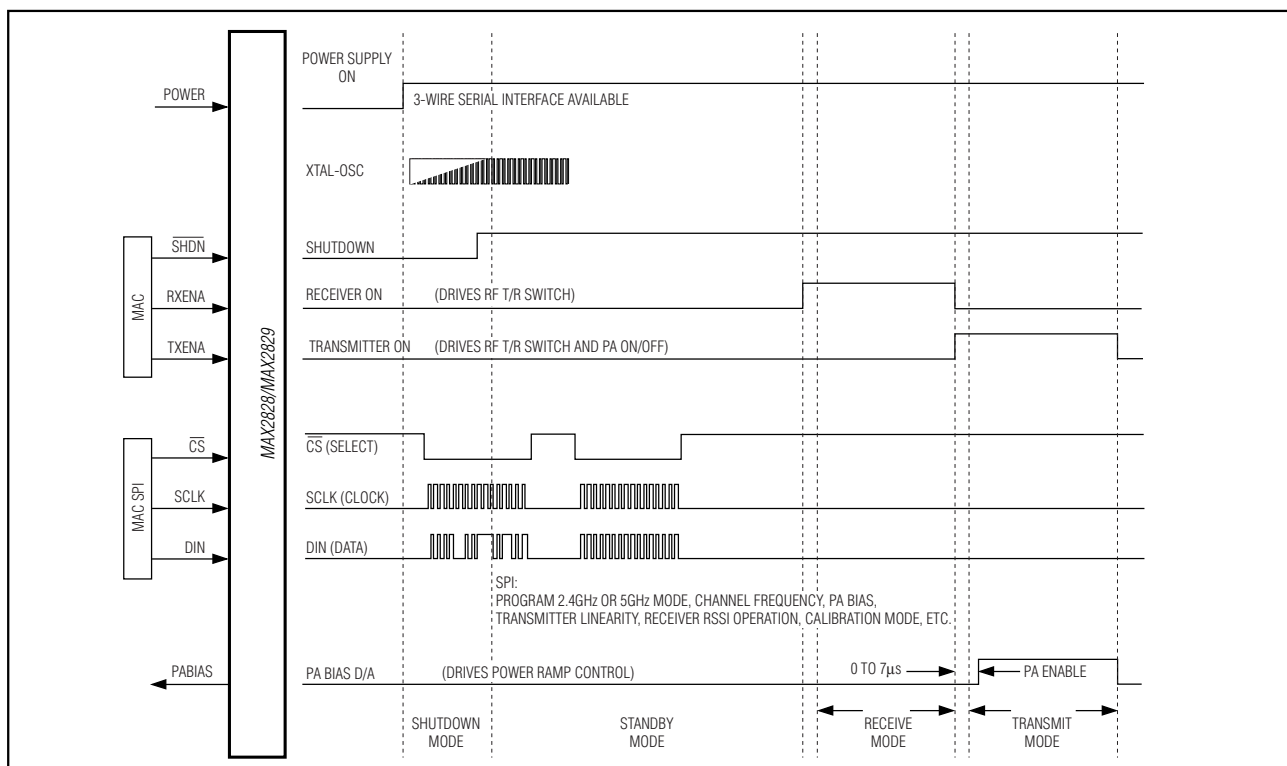


Figure 1. System Timing Diagram

MAX2828/MAX2829

Single-/Dual-Band 802.11a/b/g

World-Band Transceiver ICs

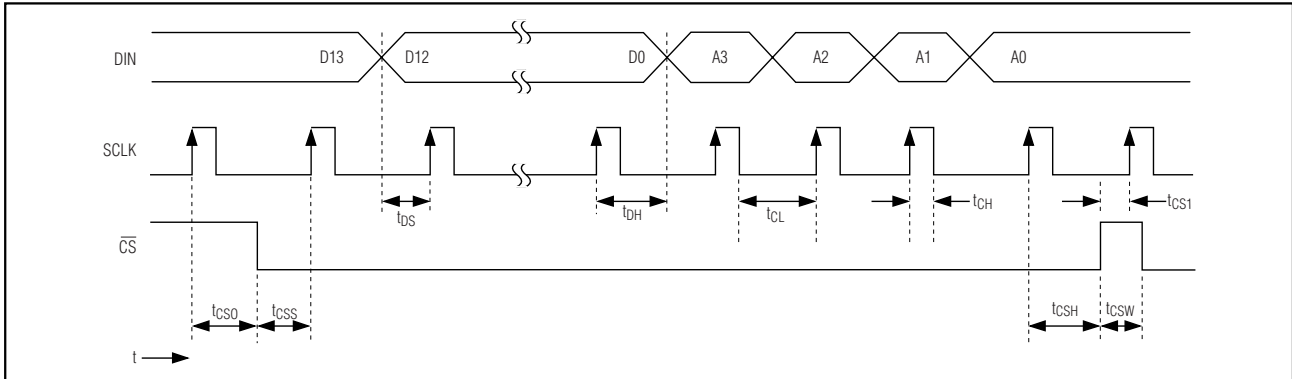
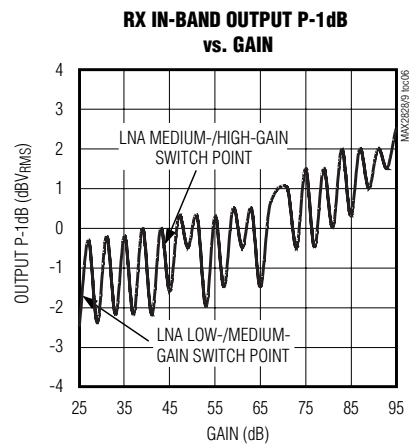
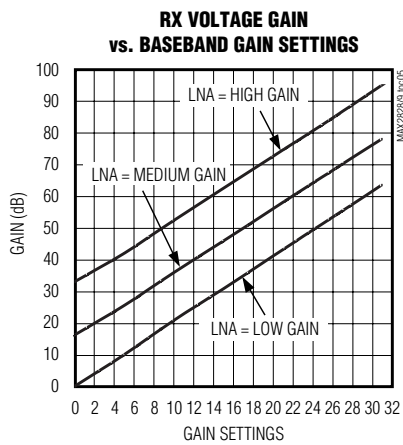
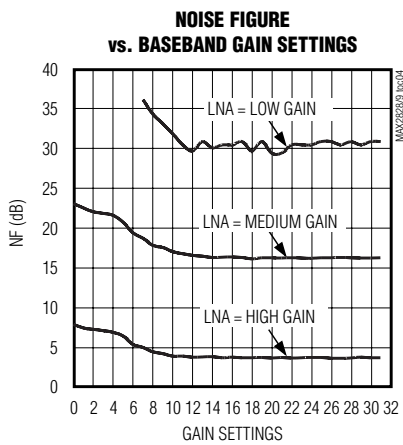
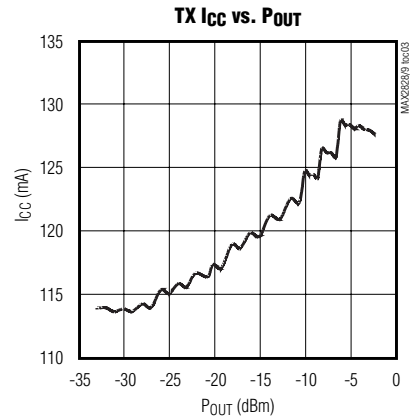
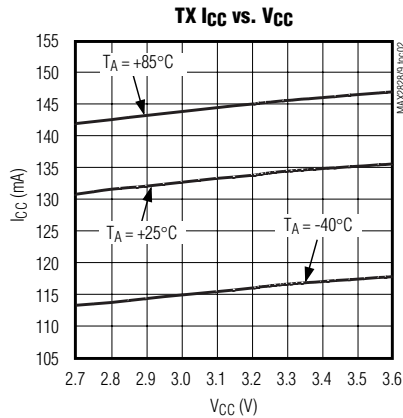
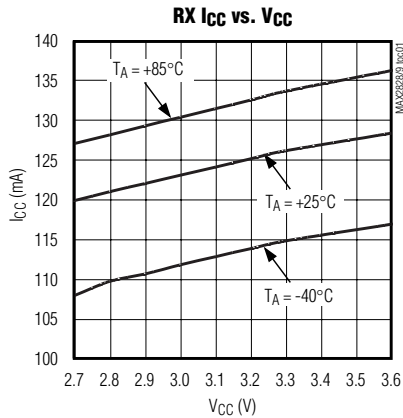


Figure 2. 3-Wire Serial-Interface Timing Diagram

Typical Operating Characteristics

($V_{CC} = 2.7V$, $f_{RF} = 2.437GHz$ (802.11g) or $f_{RF} = 5.25GHz$ (802.11a), $f_{REFOSC} = 40MHz$, $\overline{SHDN} = \overline{CS} = \text{high}$, $RXHP = SCLK = DIN = \text{low}$, $R_{BIAS} = 11k\Omega$, $T_A = +25^\circ C$ using the MAX2828/MAX2829 evaluation kits.)

802.11g



MAX2828/MAX2829

Single-/Dual-Band 802.11a/b/g

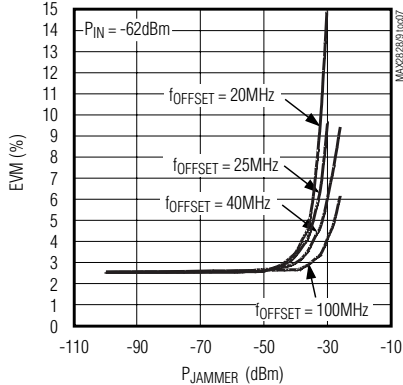
World-Band Transceiver ICs

Typical Operating Characteristics (continued)

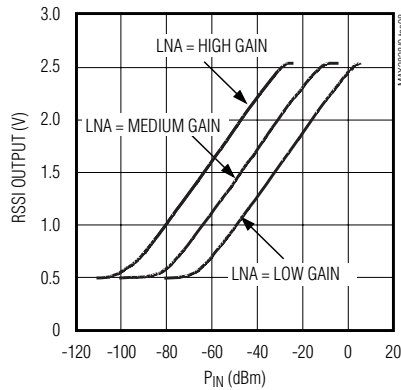
($V_{CC} = 2.7V$, $f_{RF} = 2.437GHz$ (802.11g) or $f_{RF} = 5.25GHz$ (802.11a), $f_{REFOSC} = 40MHz$, $\overline{SHDN} = \overline{CS} = \text{high}$, $RXHP = SCLK = DIN = \text{low}$, $R_{BIAS} = 11k\Omega$, $T_A = +25^\circ C$ using the MAX2828/MAX2829 evaluation kits.)

802.11g

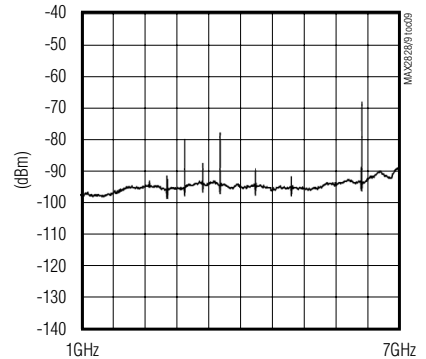
OFDM EVM WITH OFDM JAMMER vs. OFDM JAMMER LEVEL WITH JAMMER OFFSET FREQUENCY



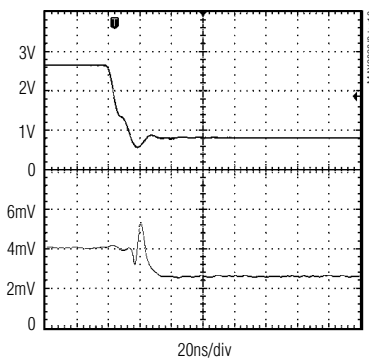
RX RSSI OUTPUT vs. INPUT POWER



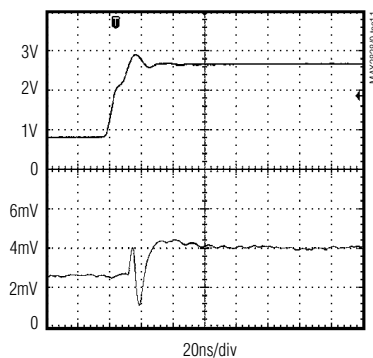
RX EMISSION SPECTRUM, LNA INPUT (TX OFF, LNA = LOW GAIN)



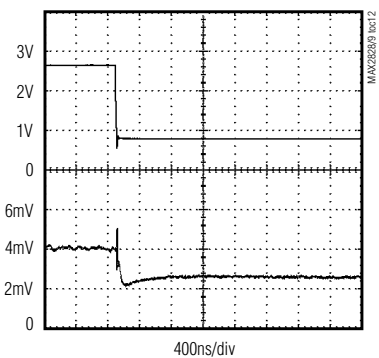
RX I/Q DC OFFSET SETTLING RESPONSE (-8dB BB VGA GAIN STEP)



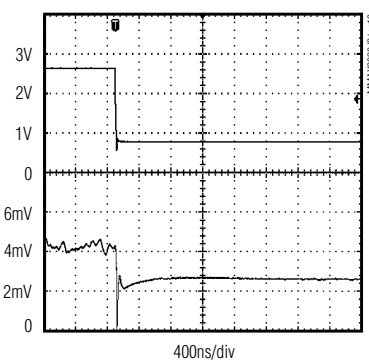
RX I/Q DC OFFSET SETTLING RESPONSE (+8dB BB VGA GAIN STEP)



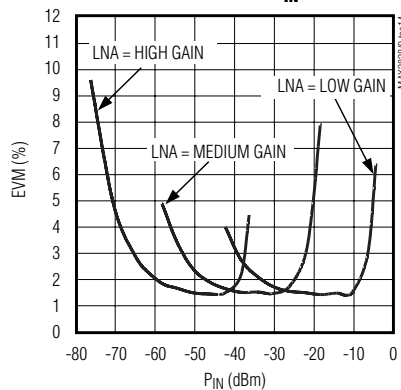
RX I/Q DC OFFSET SETTLING RESPONSE (-16dB BB VGA GAIN STEP)



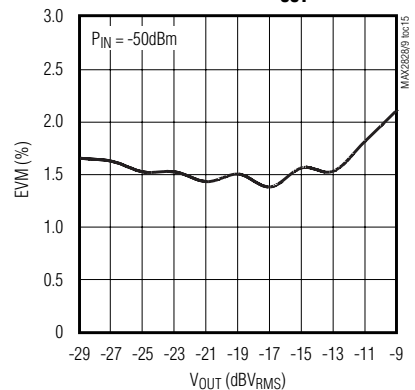
RX I/Q DC OFFSET SETTLING RESPONSE (-32dB BB VGA GAIN STEP)



RX EVM vs. P_IN



RX EVM vs. V_OUT



MAX2828/MAX2829

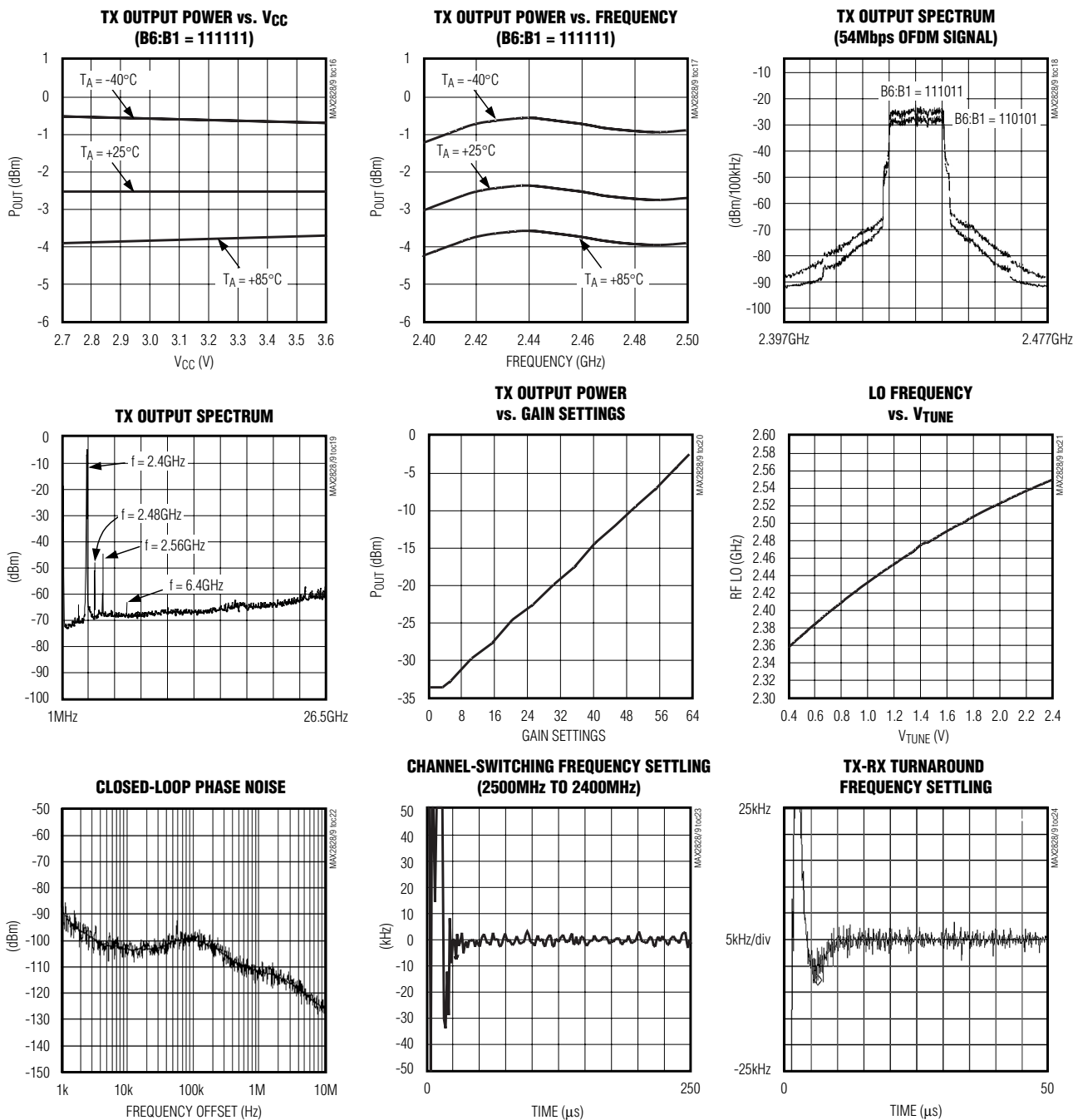
Single-/Dual-Band 802.11a/b/g

World-Band Transceiver ICs

Typical Operating Characteristics (continued)

($V_{CC} = 2.7V$, $f_{RF} = 2.437GHz$ (802.11g) or $f_{RF} = 5.25GHz$ (802.11a), $f_{REFOSC} = 40MHz$, $\overline{SHDN} = \overline{CS} = \text{high}$, $RXHP = SCLK = DIN = \text{low}$, $R_{BIAS} = 11k\Omega$, $T_A = +25^\circ C$ using the MAX2828/MAX2829 evaluation kits.)

802.11g



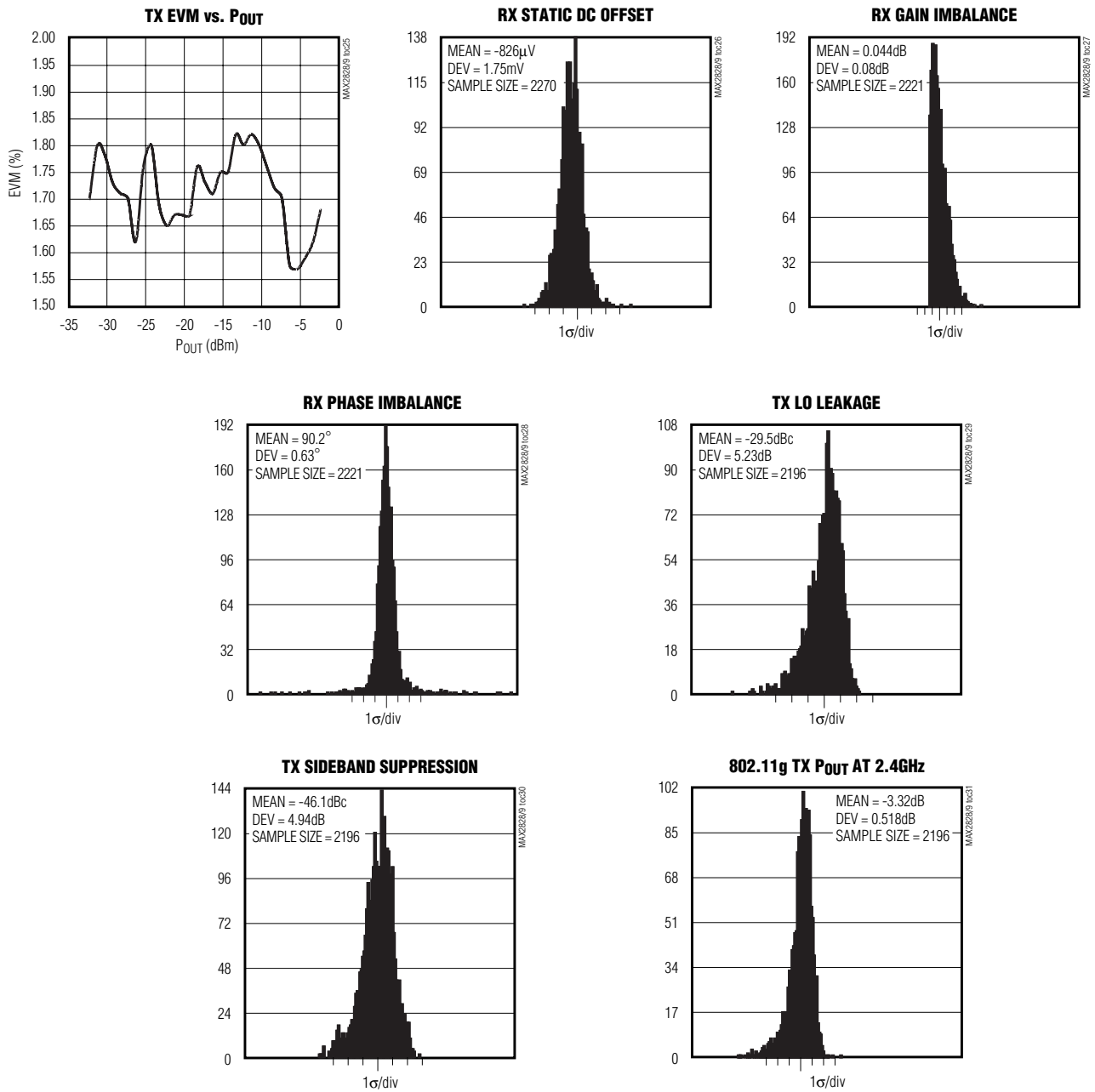
MAX2828/MAX2829

Single-/Dual-Band 802.11a/b/g World-Band Transceiver ICs

Typical Operating Characteristics (continued)

($V_{CC} = 2.7V$, $f_{RF} = 2.437GHz$ (802.11g) or $f_{RF} = 5.25GHz$ (802.11a), $f_{REFOSC} = 40MHz$, $\overline{SHDN} = \overline{CS} = \text{high}$, $RXHP = SCLK = DIN = \text{low}$, $R_{BIAS} = 11k\Omega$, $T_A = +25^\circ C$ using the MAX2828/MAX2829 evaluation kits.)

802.11g



MAX2828/MAX2829

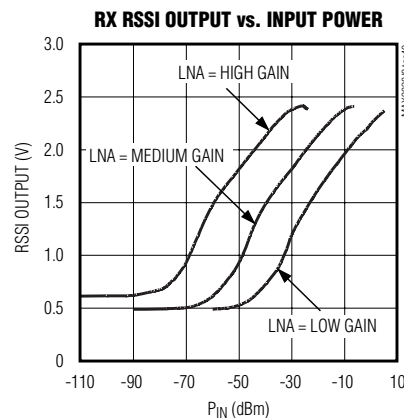
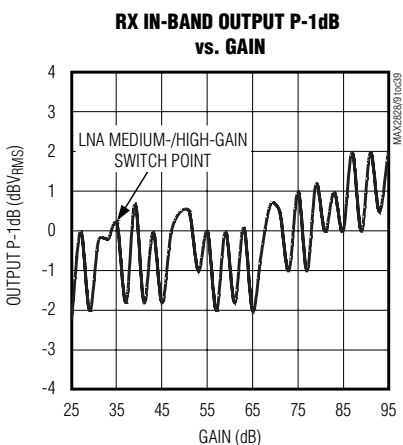
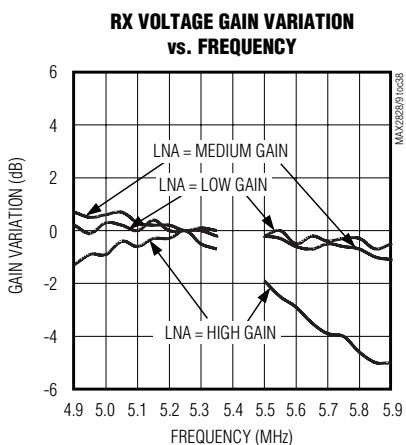
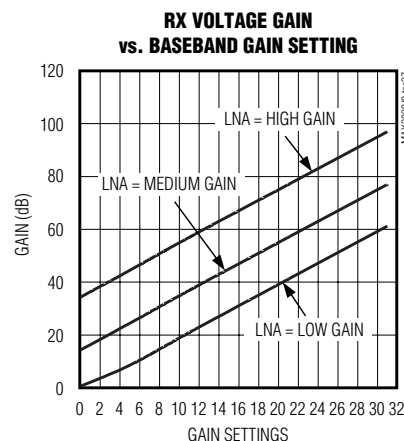
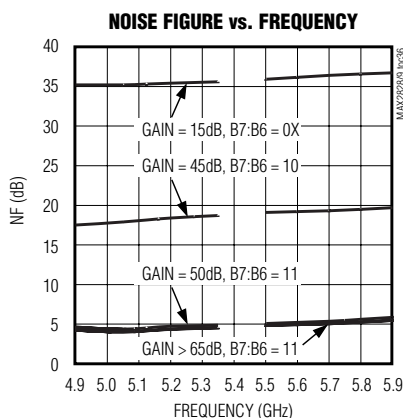
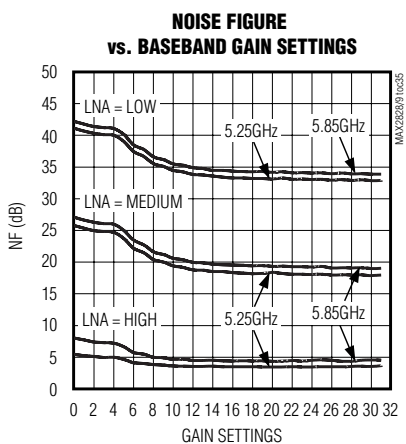
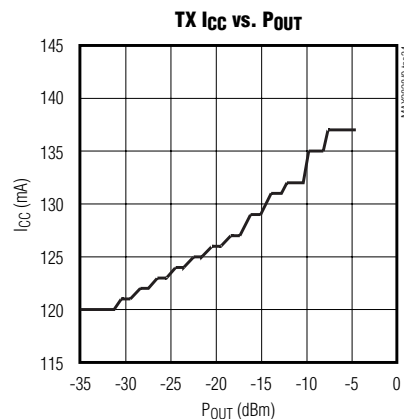
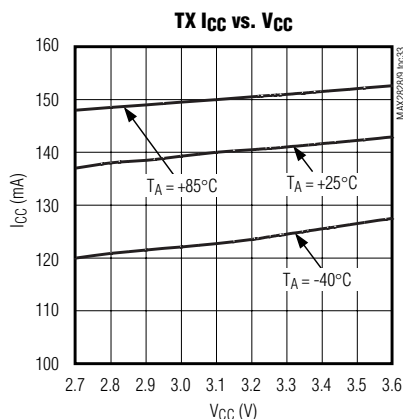
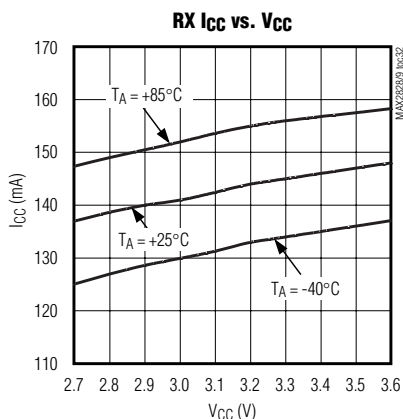
Single-/Dual-Band 802.11a/b/g

World-Band Transceiver ICs

Typical Operating Characteristics (continued)

($V_{CC} = 2.7V$, $f_{RF} = 2.437GHz$ (802.11g) or $f_{RF} = 5.25GHz$ (802.11a), $f_{REFOSC} = 40MHz$, $SHDN = \overline{CS} = high$, $RXHP = SCLK = DIN = low$, $R_{BIAS} = 11k\Omega$, $T_A = +25^\circ C$ using the MAX2828/MAX2829 evaluation kits.)

802.11a



MAX2828/MAX2829

Single-/Dual-Band 802.11a/b/g

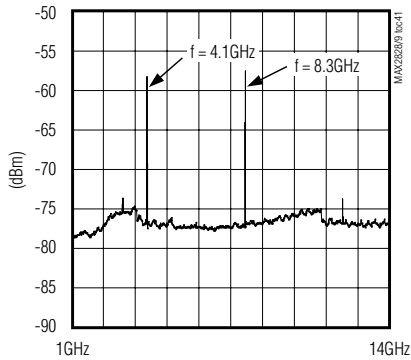
World-Band Transceiver ICs

Typical Operating Characteristics (continued)

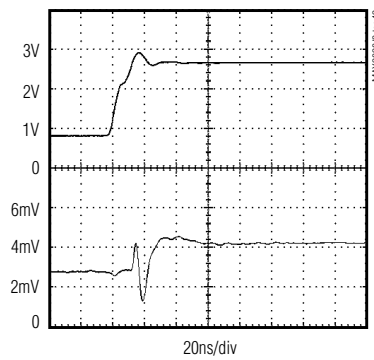
($V_{CC} = 2.7V$, $f_{RF} = 2.437GHz$ (802.11g) or $f_{RF} = 5.25GHz$ (802.11a), $f_{REFOSC} = 40MHz$, $\overline{SHDN} = \overline{CS} = \text{high}$, $RXHP = SCLK = DIN = \text{low}$, $R_{BIAS} = 11k\Omega$, $T_A = +25^\circ C$ using the MAX2828/MAX2829 evaluation kits.)

802.11a

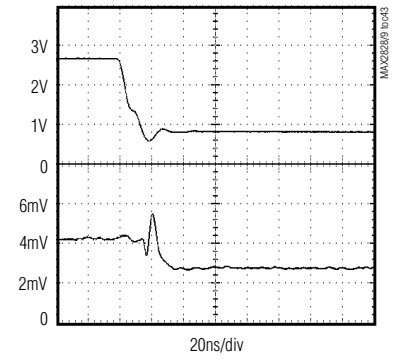
**RX EMISSION SPECTRUM, LNA INPUT
(TX OFF, LNA = LOW GAIN)**



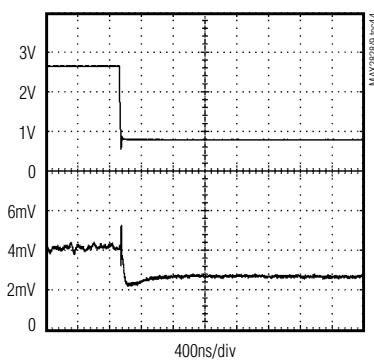
**RX I/Q DC OFFSET SETTLING RESPONSE
(+8dB BB VGA GAIN STEP)**



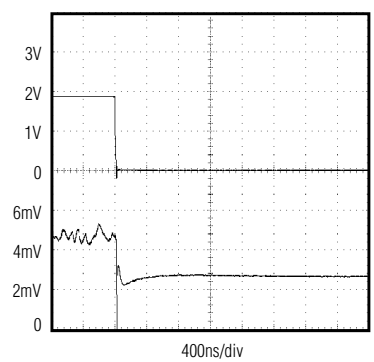
**RX I/Q DC OFFSET SETTLING RESPONSE
(-8dB BB VGA GAIN STEP)**



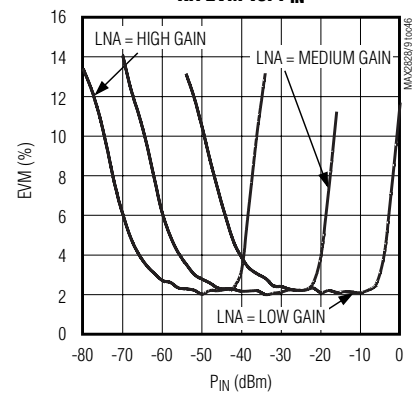
**RX I/Q DC OFFSET SETTLING RESPONSE
(-16dB BB VGA GAIN STEP)**



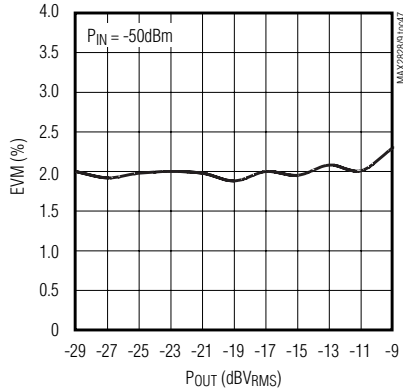
**RX I/Q DC OFFSET SETTLING RESPONSE
(-32dB BB VGA GAIN STEP)**



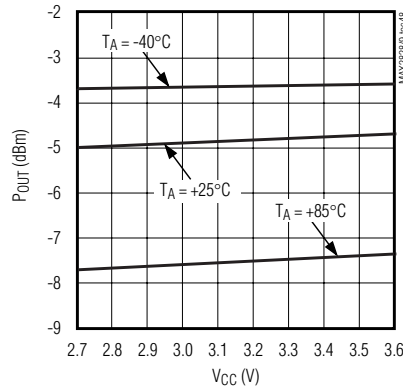
RX EVM vs. P_{IN}



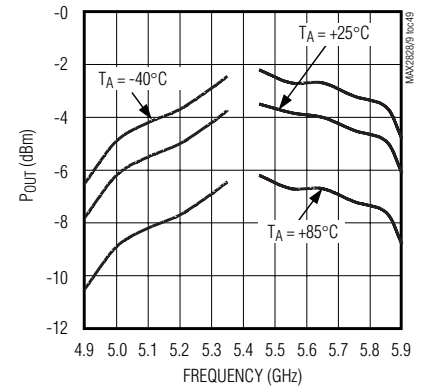
RX EVM vs. V_{OUT}



**TX OUTPUT POWER vs. V_{CC}
(B6:B1 = 111111)**



**TX OUTPUT POWER vs. FREQUENCY
(B6:B1 = 111111)**



MAX2828/MAX2829

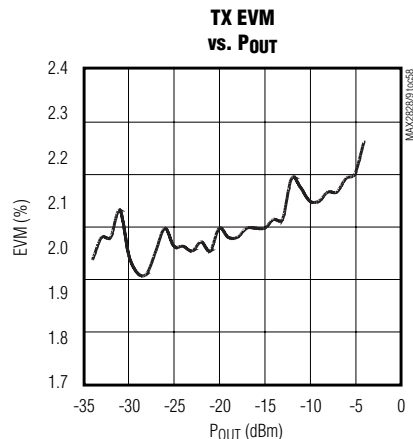
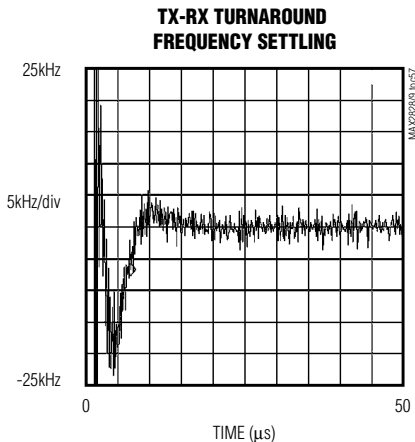
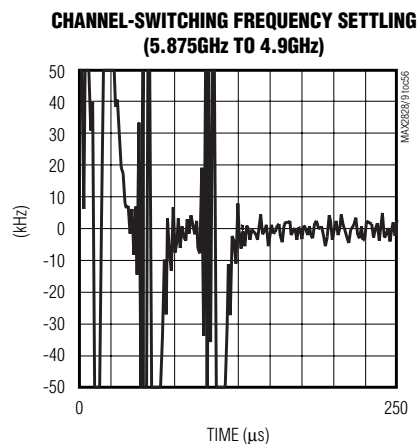
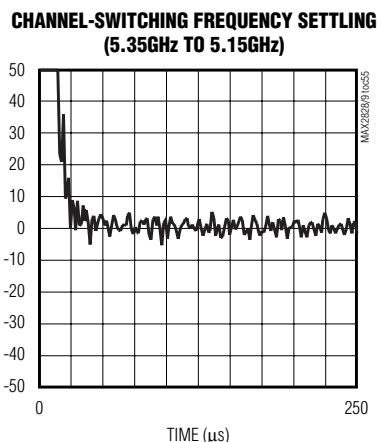
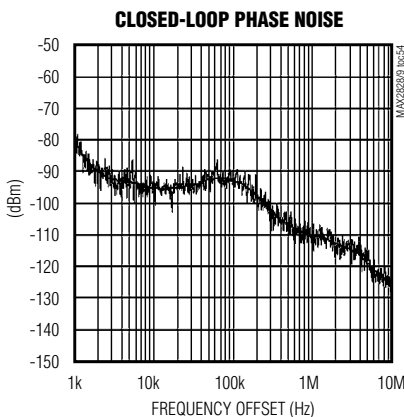
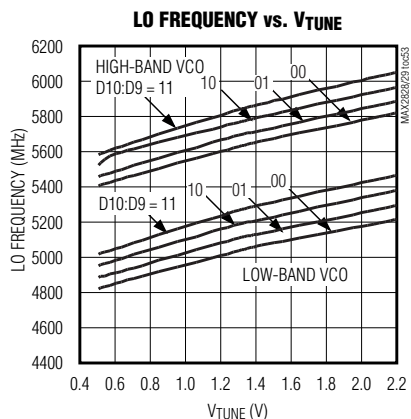
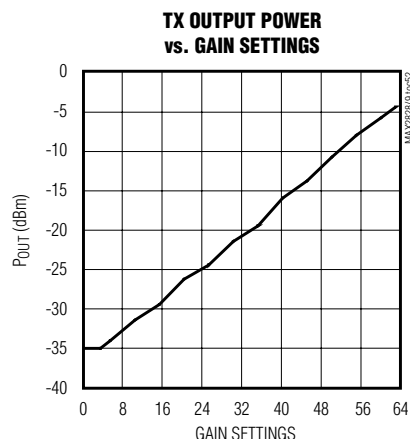
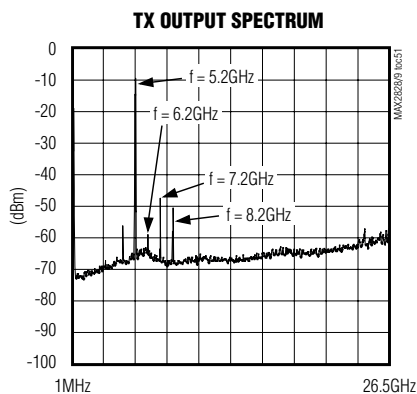
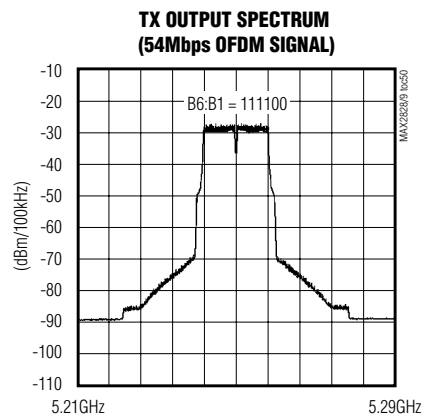
Single-/Dual-Band 802.11a/b/g

World-Band Transceiver ICs

Typical Operating Characteristics (continued)

($V_{CC} = 2.7V$, $f_{RF} = 2.437GHz$ (802.11g) or $f_{RF} = 5.25GHz$ (802.11a), $f_{REFOSC} = 40MHz$, $\overline{SHDN} = \overline{CS} = \text{high}$, $RXHP = SCLK = DIN = \text{low}$, $R_{BIAS} = 11k\Omega$, $T_A = +25^\circ C$ using the MAX2828/MAX2829 evaluation kits.)

802.11a



MAX2828/MAX2829

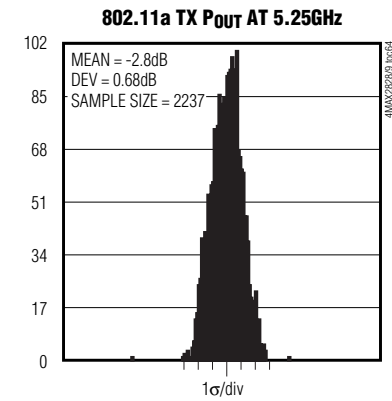
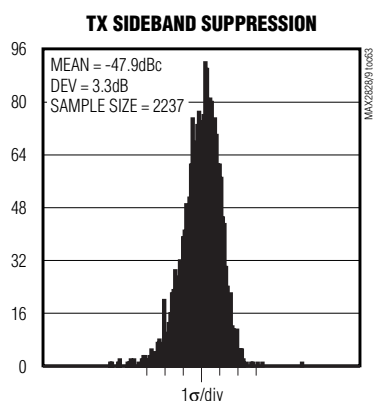
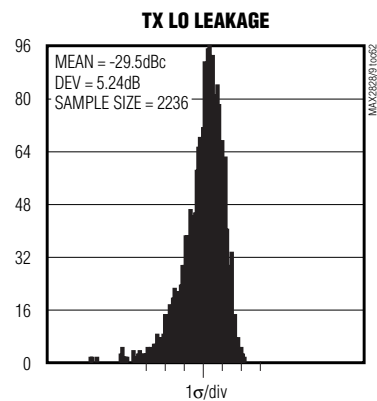
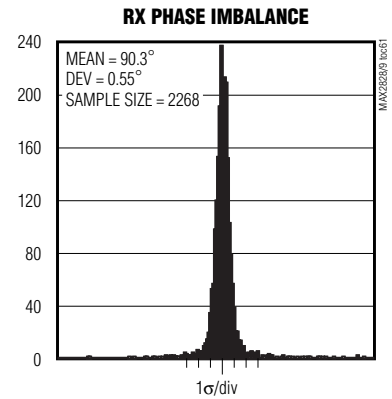
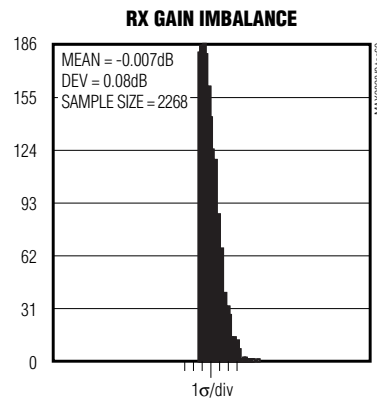
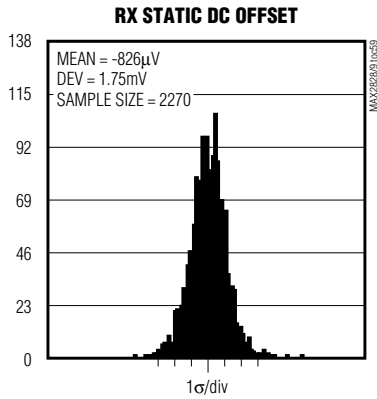
Single-/Dual-Band 802.11a/b/g

World-Band Transceiver ICs

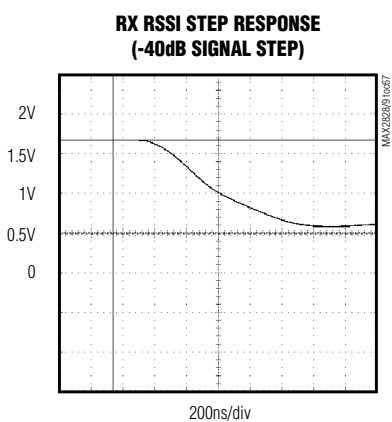
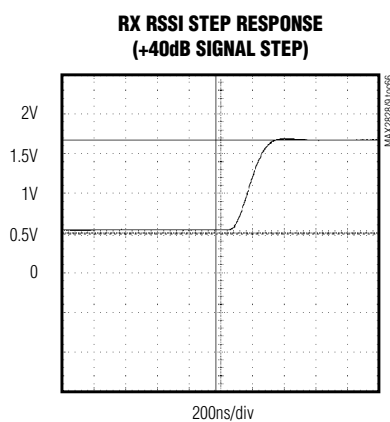
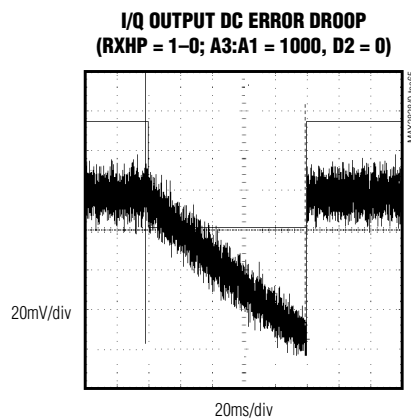
Typical Operating Characteristics (continued)

(VCC = 2.7V, fRF = 2.437GHz (802.11g) or fRF = 5.25GHz (802.11a), fREFOSC = 40MHz, SHDN = CS = high, RXHP = SCLK = DIN = low, RBIAS = 11kΩ, TA = +25°C using the MAX2828/MAX2829 evaluation kits.)

802.11a



802.11g/802.11a



MAX2828/MAX2829

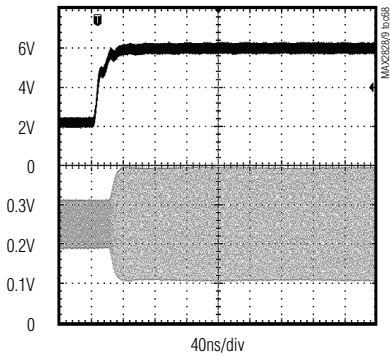
Single-/Dual-Band 802.11a/b/g World-Band Transceiver ICs

Typical Operating Characteristics (continued)

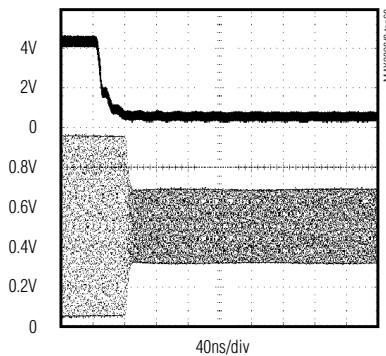
($V_{CC} = 2.7V$, $f_{RF} = 2.437GHz$ (802.11g) or $f_{RF} = 5.25GHz$ (802.11a), $f_{REFOSC} = 40MHz$, $\overline{SHDN} = \overline{CS} = high$, $RXHP = SCLK = DIN = low$, $R_{BIAS} = 11k\Omega$, $T_A = +25^\circ C$ using the MAX2828/MAX2829 evaluation kits.)

802.11g/802.11a

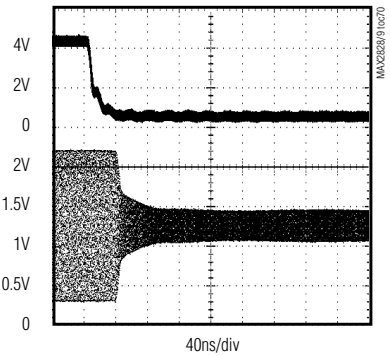
**RX BB VGA SETTLING RESPONSE
(+8dB GAIN STEP)**



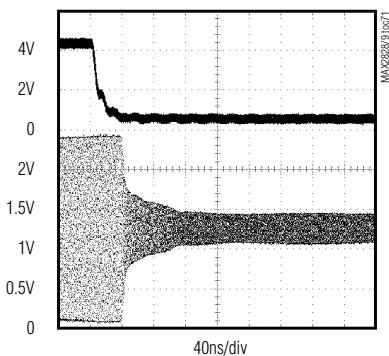
**RX BB VGA SETTLING RESPONSE
(-8dB GAIN STEP)**



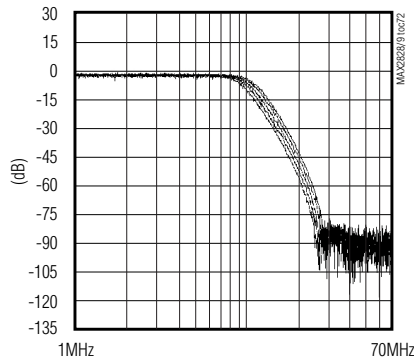
**RX BB VGA SETTLING RESPONSE
(-16dB GAIN STEP)**



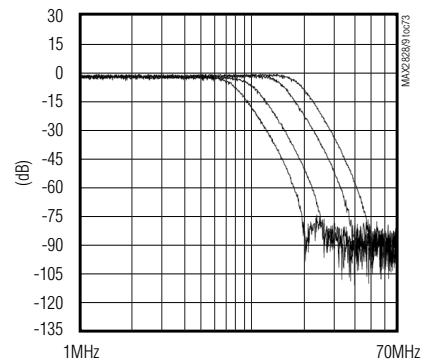
**RX BB VGA SETTLING RESPONSE
(-32dB GAIN STEP)**



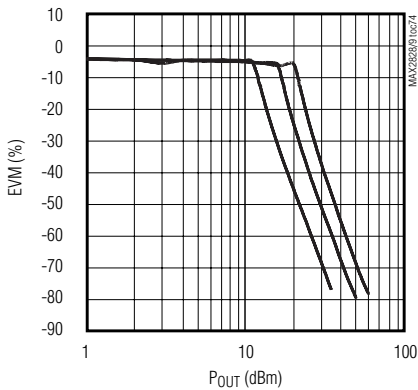
**RX BB FREQUENCY RESPONSE
vs. FINE SETTING (COARSE SETTING = 9.5MHz)**



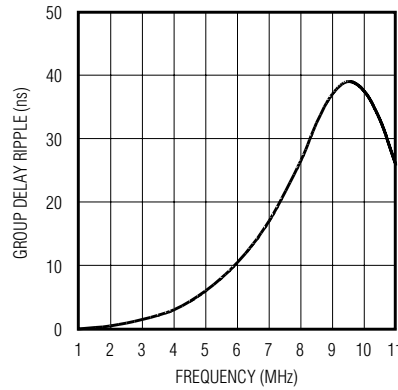
**RX BB FREQUENCY RESPONSE
vs. COARSE SETTING (FINE SETTING = 010)**



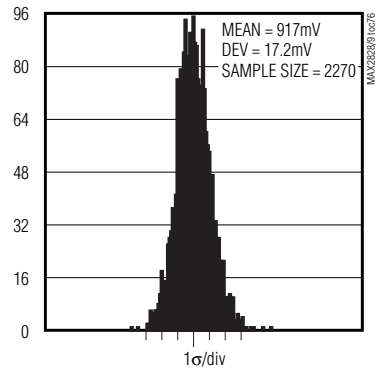
TX BASEBAND FREQUENCY RESPONSE



**GROUP DELAY RIPPLE
vs. FREQUENCY (COARSE SETTING = 9.5MHz)**



RX I/Q COMMON-MODE VOLTAGE SPREAD

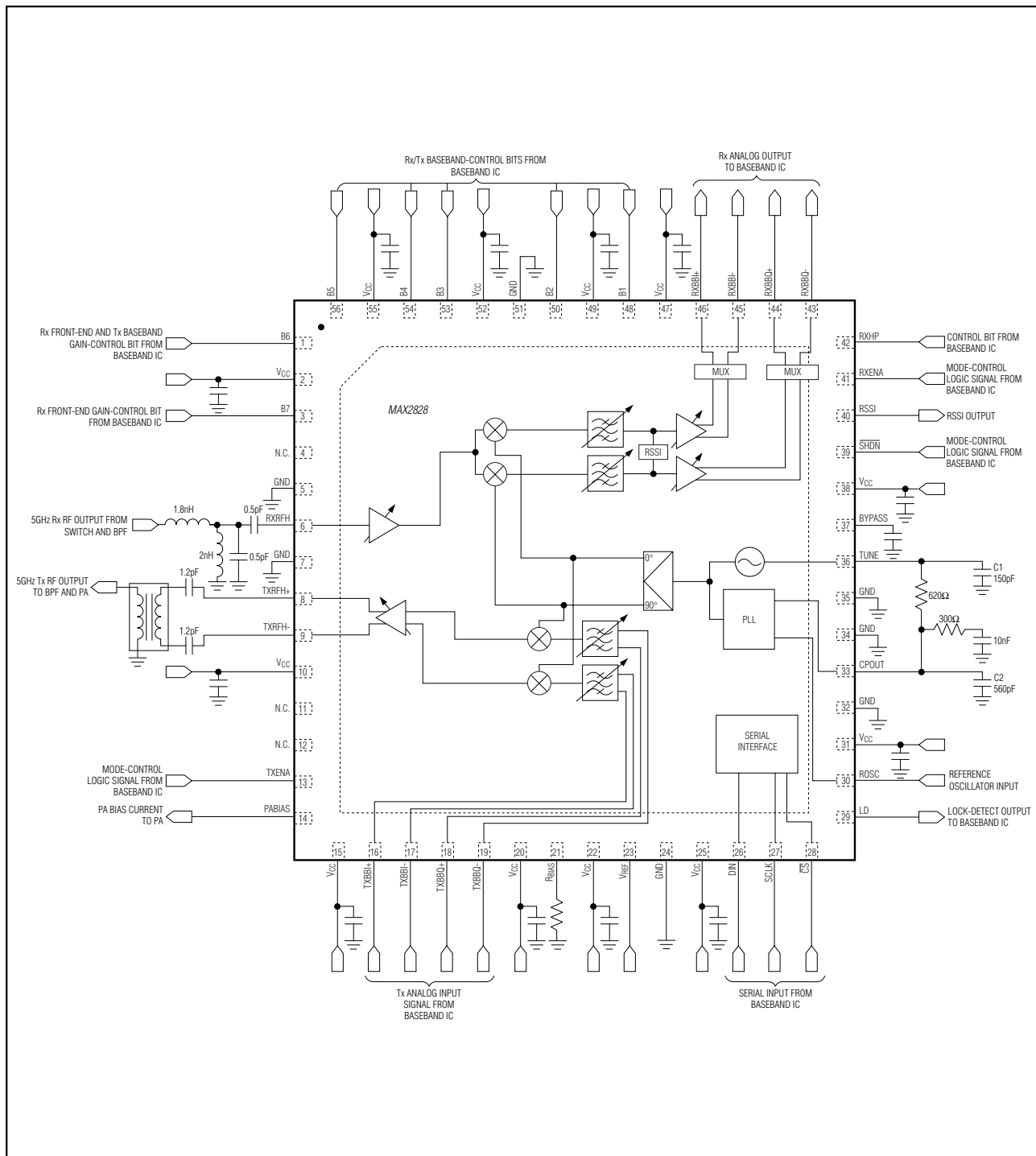


MAX2828/MAX2829

Single-/Dual-Band 802.11a/b/g

World-Band Transceiver ICs

Block Diagrams/Typical Operating Circuits

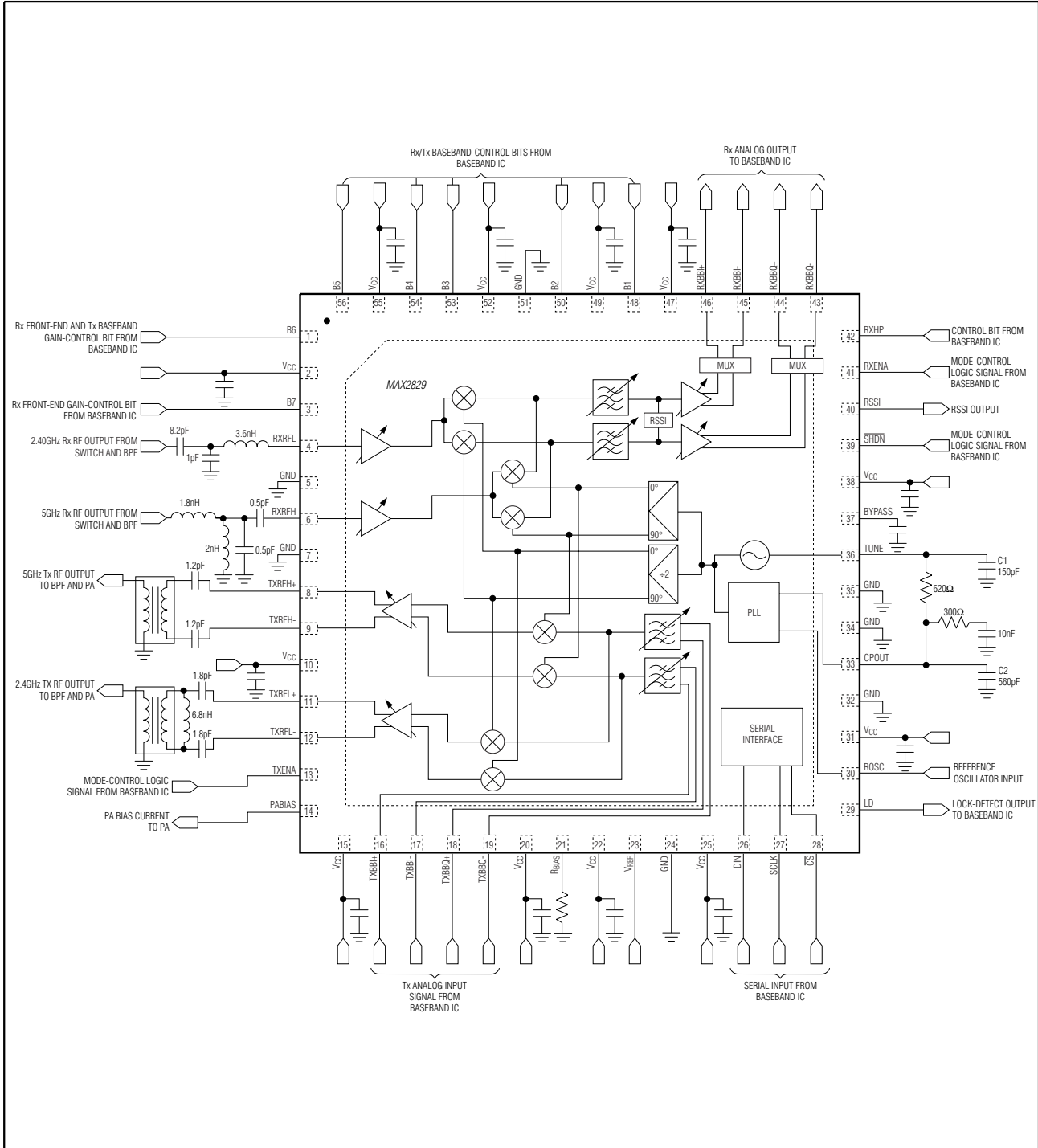


MAX2828/MAX2829

Single-/Dual-Band 802.11a/b/g

World-Band Transceiver ICs

Block Diagrams/Typical Operating Circuits (continued)



MAX2828/MAX2829

Single-/Dual-Band 802.11a/b/g

World-Band Transceiver ICs

Pin Description

PIN		NAME	FUNCTION
MAX2828	MAX2829		
1	1	B6	Rx Front-End and Tx Gain-Control Digital Input Bit 6
2	2	V _{CC}	2.4GHz/5GHz LNA Supply Voltage. Bypass with a capacitor as close to the pin as possible. Do not share the bypass-capacitor ground vias with any other branches.
3	3	B7	Rx Front-End Gain-Control Digital Input Bit 7
4, 11, 12	—	N.C.	No Connection. Leave unconnected.
5	5	GND	LNA Ground. Make connections to ground vias as short as possible. Do not share ground vias with any of the other branches.
6	6	RXRFH	5GHz Single-Ended LNA Input. Requires AC-coupling and external matching network.
7	7	GND	LNA Ground. Make connections to ground vias as short as possible. Do not share ground vias with any other branches.
8	8	TXRFH+	5GHz Tx PA Driver Differential Outputs. Requires AC-coupling and external matching network (and balun) to the external PA input.
9	9	TXRFH-	
10	10	V _{CC}	Tx RF Supply Voltage. Bypass with a capacitor as close to the pin as possible. Do not share the bypass-capacitor ground vias with any other branches.
13	13	TXENA	Tx Mode Enable Digital Input. Set high to enable Tx (see Figure 1).
14	14	PABIAS	DAC Current Output. Connect directly to the external PA bias pin.
15	15	V _{CC}	Tx Baseband Filter Supply Voltage. Bypass with a capacitor as close to the pin as possible. Do not share the bypass-capacitor ground vias with any other branches.
16	16	TXBBI+	Tx Baseband I-Channel Differential Inputs
17	17	TXBBI-	
18	18	TXBBQ+	Tx Baseband Q-Channel Differential Inputs
19	19	TXBBQ-	
20	20	V _{CC}	Tx Upconverter Supply Voltage. Bypass with a capacitor as close to the pin as possible. Do not share the bypass-capacitor ground vias with any other branches.
21	21	RBIAS	This Analog Voltage Input is Internally Biased to a Bandgap Voltage. Connect an external precision 11k Ω resistor or current source between this pin and ground to set the bias current for the device.
22	22	V _{CC}	Reference Circuit Supply Voltage. Bypass with a capacitor as close to the pin as possible. Do not share the bypass-capacitor ground vias with any other branches.
23	23	V _{REF}	Reference Voltage Output
24	24	GND	Digital Circuit Ground. Make connections to ground vias as short as possible. Do not share ground vias with any other branches.
25	25	V _{CC}	Digital Circuit Supply Voltage. Bypass with a capacitor as close to the pin as possible. Do not share the bypass-capacitor ground vias with any other branches.

MAX2828/MAX2829

Single-/Dual-Band 802.11a/b/g World-Band Transceiver ICs

Pin Description (continued)

PIN		NAME	FUNCTION
MAX2828	MAX2829		
26	26	DIN	Data Digital Input of 3-Wire Serial Interface (See Figure 2)
27	27	SCLK	Clock Digital Input of 3-Wire Serial Interface (See Figure 2)
28	28	\overline{CS}	Active-Low Enable Digital Input of 3-Wire Serial Interface (See Figure 2)
29	29	LD	Lock-Detect Digital Output of Frequency Synthesizer. Output high indicates that the frequency synthesizer is locked.
30	30	ROSC	Reference Oscillator Input. Connect an external reference oscillator to this analog input.
31	31	V _{CC}	PLL Charge-Pump Supply Voltage. Bypass with a capacitor as close to the pin as possible. Do not share the bypass-capacitor ground vias with any other branches.
32	32	GND	Charge-Pump Circuit Ground. Make connections to ground vias as short as possible. Do not share ground vias with any other branches.
33	33	CPOUT	Charge-Pump Output. Connect the frequency synthesizer's loop filter between CPOUT and TUNE. Keep the line from this pin to the tune input as short as possible to prevent spurious pickup. Connect C2 as close to CPOUT as possible. Do not share the capacitor ground vias with any other branches (see the <i>Typical Operating Circuit</i>).
34	34	GND	Ground. Make connections to ground vias as short as possible. Do not share ground vias with any other branches.
35	35	GND	VCO Ground. Make connections to ground vias as short as possible. Do not share ground vias with any other branches.
36	36	TUNE	VCO TUNE Input. Connect C1 as close to TUNE as possible. Connect the ground of C1 to VCO ground. Do not share the capacitor ground vias with any other branches (see the <i>Typical Operating Circuit</i>).
37	37	BYPASS	Bypass with a 0.1 μ F Capacitor to GND. The capacitor is used by the on-chip VCO voltage regulator.
38	38	V _{CC}	VCO Supply Voltage. Bypass to system ground as close as possible to the pin with capacitors. Do not share the ground vias for the bypass capacitors with any other branches.
39	39	\overline{SHDN}	Active-Low Shutdown Digital Input. Set high to enable the device.
40	40	RSSI	RSSI or Temperature-Sensor Multiplexed Output
41	41	RXENA	Rx Mode Enable Digital Input. Set high to enable Rx.
42	42	RXHP	Rx Baseband AC-Coupling Highpass Corner Frequency Control Digital Input Selection Bit
43	43	RXBBQ-	Rx Baseband Q-Channel Differential Outputs. In Tx calibration mode, these pins are the LO leakage and sideband-detector outputs.
44	44	RXBBQ+	
45	45	RXBBI-	Rx Baseband I-Channel Differential Outputs. In Tx calibration mode, these pins are the LO leakage and sideband-detector outputs.
46	46	RXBBI+	
47	47	V _{CC}	Rx Baseband Buffer Supply Voltage. Bypass with a capacitor as close to the pin as possible. Do not share the bypass-capacitor ground vias with any other branches.
48	48	B1	Rx/Tx Gain-Control Digital Input Bit 1
49	49	V _{CC}	Rx Baseband Filter Supply Voltage. Bypass with a capacitor as close to the pin as possible. Do not share the bypass-capacitor ground vias with any other branches.

MAX2828/MAX2829

Single-/Dual-Band 802.11a/b/g World-Band Transceiver ICs

Pin Description (continued)

PIN		NAME	FUNCTION
MAX2828	MAX2829		
50	50	B2	Rx/Tx Gain-Control Digital Input Bit 2
51	51	GND	Rx IF Ground. Make connections to ground vias as short as possible. Do not share ground vias with any other branches.
52	52	VCC	Rx IF Supply Voltage. Bypass with a capacitor as close to the pin as possible. Do not share the bypass-capacitor ground vias with any other branches.
53	53	B3	Rx/Tx Gain-Control Digital Input Bit 3
54	54	B4	Rx/Tx Gain-Control Digital Input Bit 4
55	55	VCC	Rx Downconverter Supply Voltage. Bypass with a capacitor as close to the pin as possible. Do not share the bypass-capacitor ground vias with any other branches.
56	56	B5	Rx/Tx Gain-Control Digital Input Bit 5
—	4	RXRFL	2.4GHz Single-Ended LNA Input. Requires AC-coupling and external matching network.
—	11	TXRFL+	2.4GHz Tx PA Driver Differential Outputs. Requires AC-coupling and external matching network (and balun) to the external PA input.
—	12	TXRFL-	
EP	EP	EXPOSED PADDLE	Exposed Paddle. Connect to the ground plane with multiple vias for proper operation and heat dissipation.

Table 5. Mode Table

MODE	LOGIC PINS			REGISTER SETTINGS
	SHDN	TXENA	RXENA	
SPI™ Reset	0	1	1	X
Shutdown	0	0	0	X
Standby	1	0	0	X
Rx	1	0	1	X
Tx	1	1	0	X
Tx Calibration	1	1	0	Calibration register D1 = 1
Rx Calibration	1	0	1	Calibration register D0 = 1

X = Don't care or do not apply.

Detailed Description

The MAX2828/MAX2829 single-chip, RF transceiver ICs are designed for WLAN applications. The MAX2828 is designed for 5GHz 802.11a (OFDM), and the MAX2829 is designed for dual-band 2.4GHz 802.11b/g and 5GHz 802.11a. The ICs include all circuitry required to implement the RF transceiver function, fully integrating the receive path, transmit path, VCO, frequency synthesizer, and baseband/control interface.

Modes of Operation

The MAX2828/MAX2829 have seven primary modes of operation: shutdown, SPI reset, standby, transmit, receive, transmitter calibration, and receiver calibration (see Table 5).

SPI is a trademark of Motorola, Inc.

MAX2828/MAX2829

Single-/Dual-Band 802.11a/b/g World-Band Transceiver ICs

Shutdown Mode

Shutdown mode is achieved by driving $\overline{\text{SHDN}}$ low. In shutdown mode, all circuit blocks are powered down, except for the serial interface. While the device is in shutdown, the values of the serial interface registers are maintained and can be changed as long as V_{CC} (pin 25) is applied.

SPI Reset

By driving RXENA and TXENA high while setting $\overline{\text{SHDN}}$ low, all circuit blocks are powered down, as in shutdown mode. However, in SPI reset mode, all registers are returned to their default states. It is recommended to reset the SPI and all registers at the start of power-up to ensure that the registers are set to the correct values (see Table 9).

Standby Mode

To place the device in standby mode, set $\overline{\text{SHDN}}$ high and RXENA and TXENA low. This mode is mainly used to enable the frequency synthesizer block while the rest of the device is powered down. In this mode, various blocks in the system can be selectively turned on or off according to the standby register table (Table 10).

Receive (Rx) Mode

To place the device in Rx mode, set RXENA high. All receiver blocks are enabled in this mode.

Transmit (Tx) Mode

To place the device in Tx mode, set TXENA high. All transmitter blocks are enabled in this mode.

Tx/Rx Calibration Mode

The MAX2828/MAX2829 feature Tx/Rx calibration modes to detect I/Q imbalances and transmit LO leakage. In the Tx calibration mode, the LO leakage calibration is done only for the LO leakage signal that is present at the center frequency of the channel (i.e., in the middle of the OFDM or QPSK spectrum). The LO leakage calibration includes the effect of all DC offsets in the entire baseband paths of the I/Q modulator, and also includes direct leakage of the LO to the I/Q modulator output.

The transmitter LO leakage and sideband-detector output is taken at the receiver I- or Q-channel output during this calibration phase.

During Tx LO leakage and I/Q imbalance calibration, a sine and cosine signal ($f = f_{\text{TONE}}$) is input to the baseband I/Q Tx pins from the baseband IC. At the LO leakage and sideband-detector output, the LO leakage corresponds to the signal at f_{TONE} and the sideband suppression corresponds to the signal at $2 \times f_{\text{TONE}}$. The output power of these signals vary 2dB for 1dB of variation in the LO leakage and unwanted sideband levels. To calibrate the Tx path, first set the power-detector gain to 8dB (Table 14). Adjust the DC offset of the baseband inputs to minimize the signal at f_{TONE} (LO leakage). Then, adjust the baseband input relative magnitude and phase offsets to reduce the signal at $2 \times f_{\text{TONE}}$. If required, calibration can be done with higher LO leakage and sideband-detector gain settings to decrease LO leakage and increase image suppression.

After calibrating the transmitter, receiver calibration can be done. In Rx calibration mode, the calibrated Tx RF signal is internally routed to the Rx downconverter inputs. In this loopback calibration mode, the voltage regulator must be able to source 350mA total since both Tx and Rx are turned on simultaneously.

RF Synthesizer Programming in 5GHz Mode

In the 5GHz mode, the RF frequency synthesizer covers a 4.9GHz to 5.9GHz range. To achieve this large tuning range while maintaining excellent noise performance, the 1GHz band is divided into sub-bands within which the VCO is tuned. The selection of the appropriate VCO sub-band is done automatically by a finite state machine (FSM). The PLL settling time is approximately 300 μ s for a change of 1GHz in the channel frequency. A faster PLL settling can be achieved by overriding the FSM and manually programming the VCO sub-band.

Automatic VCO Sub-Band Selection

By enabling this band-selection mode, only 1 bit needs to be programmed to start the frequency acquisition. The FSM will automatically stop after it selects the correct VCO sub-band, and after the PLL has locked.

MAX2828/MAX2829

Single-/Dual-Band 802.11a/b/g World-Band Transceiver ICs

Table 6. B1:B0 VCO Sub-Band Assignments (Read Back Through Lock-Detect Pin)

B1	B0	VCO FREQUENCY BAND
0	0	Band 0 (lowest frequency band)
0	1	Band 1
1	0	Band 2
1	1	Band 3 (highest frequency band)

The following steps should be followed:

- 1) Set D8 = 0 (A3:A0 = 0101) to enable the automatic VCO sub-band selection by the FSM.
- 2) Enable the PLL and VCO if required. If required, program the divider ratios corresponding to the desired channel frequency.
- 3) Set D7 = 1 (A3:A0 = 0101) to start the FSM. The FSM should only be started after PLL and VCO are enabled, or after channel frequency is changed.
- 4) The VCO sub-band selection and PLL settling time takes less than approximately 300 μ s. After the band switching is completed and the PLL has locked to the correct channel frequency, the FSM stops automatically.

Every time the channel frequency is programmed or the PLL+VCO is enabled, the FSM needs to be reset to be used again for the next time. This reset operation does not affect the PLL or VCO. To reset the FSM, set D7 = 0 (A3:A0 = 0101).

Every channel frequency maps to some VCO sub-band. Each VCO sub-band has a digital code, of which the 2 LSBs (B1:B0) are readable. The B1:B0 code can be read through pin LD by programming D3:D0 = 0111 (A3:A1 = 0000) for B1, or D3:D0 = 0110 (A3:A1 = 0000) for B0 (see Table 6).

Manual VCO Sub-Band Selection

For faster settling, the VCO sub-band (B1:B0) can be directly programmed through the SPI. First, the B1:B0 code for every channel frequency must be determined. Once this is known, the B1:B0 code is directly programmed along with the PLL divider values, for the given channel frequency. The PLL settling time in this case is approximately 50 μ s.

Large temperature changes (>+50°C) may cause the channel frequency to move into an adjacent sub-band. To determine the correct sub-band, two on-chip comparators monitor the VCO control voltage (VTUNE). These comparator logic outputs can be read through

Table 7. D10:D9 VCO Sub-Band Assignments (For Programming Through SPI)

D10	D9	PROGRAMMED VCO FREQUENCY BAND
0	0	Band 0
0	1	Band 1
1	0	Band 2
1	1	Band 3

Table 8. Comparator-Output Definition

A3:A1 = 0000; D3:D0 = 0101	A3:A1 = 0000; D3:D0 = 0100	RESPONSE
0	0	Program to a lower sub-band if VCO is not in Band 0.
0	1	No change.
1	0	Program to a higher sub-band if VCO is not in Band 3.
1	1	Invalid state, does not occur.

the LD pin to decide whether the frequency sub-band is correct or needs to be reprogrammed.

The following steps need to be followed to complete manual PLL frequency acquisition and VCO sub-band selection:

- 1) Set D8 = 1 (A3:A0 = 0101) to enable manual VCO sub-band selection.
- 2) Enable the PLL and VCO if required. If required, program the divider ratios corresponding to the desired channel frequency.
- 3) Set D10:D9 (A3:A0 = 0101) to program the VCO frequency sub-band according to Table 7. D10:D9 correspond to the same assignments as B1:B0. After D10:D9 are programmed, 50 μ s is required to allow the PLL to settle.
- 4) After 50 μ s of PLL settling time, the comparator outputs can be read through pin LD (see Table 8).
- 5) Based on the comparator outputs, the VCO frequency sub-band is programmed again according to Table 8 until the frequency acquisition is achieved.

Large Temperature Changes

If the PLL and VCO are continuously active (i.e., no reprogramming) and the die temperature changes by 50°C (as indicated by the on-chip temperature sensor), there is a possibility that the PLL may get unlocked due

MAX2828/MAX2829

Single-/Dual-Band 802.11a/b/g

World-Band Transceiver ICs

Table 9. Register Default/SPI Reset Settings

REGISTER	DEFAULT														ADDRESS	TABLE
	D13	D12	D11	D10	D9	D8	D7	D6	D5	D4	D3	D2	D1	D0	(A3:A0)	
Register 0	0	1	0	0	0	1	0	1	0	0	0	0	0	0	0000	—
Register 1	0	0	0	0	0	0	1	1	0	0	1	0	1	0	0001	—
Standby	0	1	0	0	0	0	0	0	0	0	0	1	1	1	0010	10
Integer-Divider Ratio	1	1	0	0	0	0	1	0	1	0	0	0	1	0	0011	11
Fractional-Divider Ratio	0	1	1	1	0	1	1	1	0	1	1	1	0	1	0100	12
Band Select and PLL	0	1	1	0	0	0	0	0	1	0	0	1	0	0	0101	13
Calibration	0	1	1	1	0	0	0	0	0	0	0	0	0	0	0110	14
Lowpass Filter	0	0	0	0	0	0	0	0	1	0	1	0	1	0	0111	15
Rx Control/RSSI	0	0	0	0	0	0	0	0	1	0	0	1	0	1	1000	16
Tx Linearity/Base-band Gain	0	0	0	0	1	0	0	0	0	0	0	0	0	0	1001	17
PA Bias DAC	0	0	0	0	1	1	1	1	0	0	0	0	0	0	1010	18
Rx Gain	0	0	0	0	0	0	0	1	1	1	1	1	1	1	1011	19
Tx VGA Gain	0	0	0	0	0	0	0	0	0	0	0	0	0	0	1100	20

Table 10. Standby Register (A3:A0 = 0010)

DATA BIT	DEFAULT	DESCRIPTION
D13	0	MIMO Select. Set to 0 for normal operation. Set to 1 for MIMO applications.
D12	1	Set to 1
D11	0	Voltage Reference (Pin 23)
D10	0	PA Bias DAC, in Tx Mode
D9	0	Set to 0
D8	0	
D7	0	
D6	0	
D5	0	
D4	0	
D3	0	
D2	1	Set to 1
D1	1	
D0	1	

to the VCO drifting to an adjacent sub-band. In this case, it is advisable to reprogram the PLL by either manual or automatic sub-band selection.

Programmable Registers

The MAX2828/MAX2829 include 13 programmable, 18-bit registers: 0, 1, standby, integer-divider ratio, fractional-divider ratio, band select and PLL, calibration, lowpass filter, Rx control/RSSI, Tx linearity/baseband gain, PA bias DAC, Rx gain, and Tx VGA gain. The 14 most significant bits (MSBs) are used for register data. The 4 least significant bits (LSBs) of each register contain the register address. Data is shifted in MSB first. The data sent to the devices, in 18-bit words, is framed by \overline{CS} . When \overline{CS} is low, the clock is active and data is shifted with the rising edge of the clock. When \overline{CS} transitions high, the shift register is latched into the register selected by the contents of the address bits. Only the last 18 bits shifted into the device are retained in the shift register. No check is made on the number of clock pulses. For programming data words less than 14 bits long, only the required data bits and the address bits are required to be shifted, resulting in faster Rx and Tx gain control where only the LSBs need to be pro-

MAX2828/MAX2829

Single-/Dual-Band 802.11a/b/g World-Band Transceiver ICs

Table 11. Integer-Divider Ratio Register (A3:A0 = 0011)

DATA BIT	DEFAULT	DESCRIPTION
D13	1	2 LSBs of the Fractional-Divider Ratio
D12	1	
D11	0	Set to 0
D10	0	
D9	0	
D8	0	
D7	1	Integer-Divider Ratio Word Programming Bits. Valid values are from 128 (D7:D0 = 10000000) to 255 (D7:D0 = 11111111).
D6	0	
D5	1	
D4	0	
D3	0	
D2	0	
D1	1	
D0	0	

grammed. The interface can be programmed through the 3-wire SPI/MICROWIRE™-compatible serial port.

On startup, it is recommended to reset all registers by placing the device in SPI reset mode (Table 5).

MICROWIRE is a trademark of National Semiconductor Corp.

Table 12a. IEEE 802.11g Frequency Plan and Divider Ratio Programming Words

f _{RF} (MHz)	(f _{RF} x 4/3) / 20MHz (DIVIDER RATIO)	INTEGER-DIVIDER RATIO	FRACTIONAL-DIVIDER RATIO	
		A3:A0 = 0011, D7:D0	A3:A0 = 0100, D13:D0 (hex)	A3:A0 = 0011, D13:D12 (hex)
2412	160.8000	1010 0000	3333	00
2417	161.1333	1010 0001	0888	10
2422	161.4667	1010 0001	1DDD	11
2427	161.8000	1010 0001	3333	00
2432	162.1333	1010 0010	0888	10
2437 (default)	162.4667	1010 0010	1DDD	11
2442	162.8000	1010 0010	3333	00
2447	163.1333	1010 0011	0888	10
2452	163.4667	1010 0011	1DDD	11
2457	163.8000	1010 0011	3333	00
2462	164.1333	1010 0100	0888	10
2467	164.4667	1010 0100	1DDD	11
2472	164.8000	1010 0100	3333	00
2484	165.6000	1010 0101	2666	01

Standby Register Definition (A3:A0 = 0010)

Various internal blocks can be turned on or off using the standby register (in standby mode, see Table 10). Setting a bit to 1 turns the block on, while setting a bit to 0 turns the block off.

Integer-Divider Ratio Register Definition (A3:A0 = 0011)

This register contains the integer portion of the divider ratio of the synthesizer. This register, in conjunction with the fractional-divider ratio register, permits selection of a precise frequency. The main synthesizer divide ratio is an 8-bit value for the integer portion (see Table 11). Valid values for this register are from 128 (D7–D0). The default value is 210. D13 and D12 are reserved for the 2 LSBs of the fractional-divider ratio.

Fractional-Divider Ratio Register Definition (A3:A0 = 0100)

This register (along with D13 and D12 of the integer-divider ratio register) controls the fractional-divider ratio with 16-bit resolution. D13 to D0 of this register combined with D13 and D12 of the integer-divider ratio register form the whole fractional-divider ratio (see Tables 12a and 12b).

MAX2828/MAX2829

Single-/Dual-Band 802.11a/b/g

World-Band Transceiver ICs

Table 12b. IEEE 802.11a Frequency Plan and Divider Ratio Programming Words

f _{RF} (MHz)	(f _{RF} X 4/5) / 20MHz (DIVIDER RATIO)	INTEGER-DIVIDER RATIO	FRACTIONAL-DIVIDER RATIO	
		A3:A0 = 0011, D7:D0	A3:A0 = 0100, D13:D0 (hex)	A3:A0 = 0011, D13:D12 (hex)
5180	207.2	1100 1111	0CCC	11
5200	208.0	1101 0000	0000	00
5220	208.8	1101 0000	3333	00
5240	209.6	1101 0001	2666	01
5260	210.4	1101 0010	1999	10
5280	211.2	1101 0011	0CCC	11
5300	212.0	1101 0100	0000	00
5320	212.8	1101 0100	3333	00
5500	220.0	1101 1100	0000	00
5520	220.8	1101 1100	3333	00
5540	221.6	1101 1101	2666	01
5560	222.4	1101 1110	1999	10
5580	223.2	1101 1111	0CCC	11
5600	224.0	1110 0000	0000	00
5620	224.8	1110 0000	3333	00
5640	225.6	1110 0001	2666	01
5660	226.4	1110 0010	1999	10
5680	227.2	1110 0011	0CCC	11
5700	228.0	1110 0100	0000	00
5745	229.8	1110 0101	3333	00
5765	230.6	1110 0110	2666	01
5785	231.4	1110 0111	1999	10
5805	232.2	1110 1000	0CCC	11

MAX2828/MAX2829

Single-/Dual-Band 802.11a/b/g World-Band Transceiver ICs

Table 13. Band-Select and PLL Register (A3:A0 = 0101)

DATA BIT	DEFAULT	DESCRIPTION
D13	0	Set to 0 for Normal Operation. Set to 1 for MIMO applications.
D12	1	Set D12:D11 = 11
D11	1	
D10	0	These Bits Set the VCO Sub-Band when Programmed Using the SPI (D8 = 1). D10:D9 = 00: lowest frequency band; 11: highest frequency band.
D9	0	
D8	0	VCO SPI Bandswitch Enable. 0: disable SPI control, bandswitch is done by FSM; 1: bandswitch is done by SPI programming.
D7	0	VCO Bandswitch Enable. 0: disable; 1: start automatic bandswitch.
D6	0	RF Frequency Band Select in 802.11a Mode (D0 = 1). 0: 4.9GHz to 5.35GHz Band; 1: 5.47GHz to 5.875GHz Band.
D5	1	PLL Charge-Pump-Current Select. 0: 2mA; 1: 4mA.
D4	0	Set to 0
D3	0	These Bits Set the Reference-Divider Ratio. D3:D1 = 001 corresponds to R = 1 and 111 corresponds to R = 7.
D2	1	
D1	0	
D0	0	RF Frequency Band Select. 0: 2.4GHz Band; 1: 5GHz band.

Band-Select and PLL Register Definition (A3:A0 = 0101)

This register configures the programmable-reference frequency dividers for the synthesizers, and sets the DC current for the charge pump. The programmable-reference frequency divider provides the reference frequencies to the phase detector by dividing the crystal oscillator frequency (see Table 13).

Calibration Register Definition (A3:A0 = 0110)

This register configures the Rx/Tx calibration modes (See Table 14).

Table 14. Calibration Register (A3:A0 = 0110)

DATA BIT	DEFAULT	DESCRIPTION
D13	0	Set to 0
D12	1	Transmitter I/Q Calibration LO Leakage and Sideband-Detector Gain-Control Bits. D12:D11 = 00: 8dB; 01: 18dB; 10: 24dB; 11: 34dB
D11	1	
D10	1	Set to 1
D9	0	Set to 0
D8	0	
D7	0	
D6	0	
D5	0	
D4	0	
D3	0	
D2	0	0: Tx Calibration Mode Disabled; 1: Tx Calibration Mode Enabled (Rx outputs provide the LO leakage and sideband-detector signal)
D1	0	
D0	0	0: RX Calibration Mode Disabled; 1: Rx Calibration Mode Enabled

MAX2828/MAX2829

Single-/Dual-Band 802.11a/b/g World-Band Transceiver ICs

Table 15. Lowpass-Filter Register (A3:A0 = 0111)

DATA BIT	DEFAULT	DESCRIPTION
D13	0	Set to 0
D12	0	
D11	0	RSSI High Bandwidth Enable. 0: 2MHz; 1: 6MHz
D10	0	Set to 0
D9	0	
D8	0	
D7	0	
D6	0	Tx LPF Corner Frequency Coarse Adjustment. D6:D5 = 00: undefined; 01: 12MHz (nominal mode); 10: 18MHz (turbo mode 1); 11: 24MHz (turbo mode 2).
D5	1	
D4	0	Rx LPF Corner Frequency Coarse Adjustment. D4:D3 = 00: 7.5MHz; 01: 9.5MHz (nominal mode); 10: 14MHz (turbo mode 1); 11: 18MHz (turbo mode 2).
D3	1	
D2	0	Rx LPF Corner Frequency Fine Adjustment (Relative to the Course Setting). D2:D0 = 000: 90%; 001: 95%; 010: 100%; 011: 105%; 100: 110%.
D1	1	
D0	0	

Lowpass Filter Register Definition (A3:A0 = 0111)

This register allows the adjustment of the Rx and Tx lowpass filter corner frequencies (see Table 15).

Rx Control/RSSI Register Definition (A3:A0 = 1000)

This register allows the adjustment of the Rx section and the RSSI output (see Tables 16a and 16b).

Table 16a. Rx Control/RSSI Register (A3:A0 = 1000)

DATA BIT	DEFAULT	DESCRIPTION
D13	0	Set to 0
D12	0	Enable Rx VGA Gain Programming Serially. 0: Rx VGA gain programmed with external digital inputs (B7:B1); 1: Rx VGA gain programmed with serial data bits in the Rx gain register (D6:D0).
D11	0	RSSI Output Range. 0: low range (0.5V to 2V); 1: high range (0.5V to 2.5V).
D10	0	RSSI Operating Mode. 0: RSSI disabled if RXHP = 0, and enabled if RXHP = 1; 1: RSSI enabled independent of RXHP (see Table 16c).
D9	0	Set to 0
D8	0	RSSI Pin Function. 0: outputs RSSI signal in Rx mode; 1: outputs temperature sensor voltage in Rx, Tx, and standby modes (see Table 16c).
D7	0	Set to 0
D6	0	
D5	1	Set to 1
D4	0	Set to 0
D3	0	
D2	1	Rx Highpass -3dB Corner Frequency when RXHP = 0. 0: 100Hz; 1: 30kHz
D1	0	Set D1:D0 = 01
D0	1	

MAX2828/MAX2829

Single-/Dual-Band 802.11a/b/g World-Band Transceiver ICs

Table 16b. Rx HP -3dB Corner Frequency Adjustment

RXHP	A3:A0 = 1000, D2	Rx HP -3dB CORNER FREQUENCY
1	X	600kHz
0	1	30kHz
0	0	100Hz

Table 16c. RSSI Pin Truth Table

INPUT CONDITIONS				RSSI OUTPUT
A3:A0 = 1000, D8	A3:A0 = 1000, D10	RXENA	RXHP	
0	0	0	X	No Signal
0	0	1	0	No Signal
0	0	1	1	RSSI
0	1	0	X	No Signal
0	1	1	X	RSSI
1	X	X	X	Temperature Sensor

Tx Linearity/Baseband Gain Register Definition **(A3:A0 = 1001)**

This register allows the adjustment of the Tx gain and linearity (see Table 17).

Table 17. Tx Linearity/Baseband Gain Register (A3:A0 = 1001)

DATA BIT	DEFAULT	DESCRIPTION
D13	0	Set to 0
D12	0	
D11	0	
D10	0	Enable Tx VGA Gain Programming Serially. 0: Tx VGA gain programmed with external digital inputs (B6:B1); 1: Tx VGA gain programmed with data bits in the Tx gain register (D5:D0).
D9	1	PA Driver Linearity. D9:D8 = 00: 50% current (minimum linearity); 01: 63% current; 10: 78% current; 11: 100% current (maximum linearity).
D8	0	
D7	0	Tx VGA Linearity. D7:D6 = 00: 50% current (minimum linearity); 01: 63% current; 10: 78% current; 11: 100% current (maximum linearity).
D6	0	
D5	0	Set to 0
D4	0	
D3	0	Tx Upconverter Linearity. D3:D2 = 00: 50% current (minimum linearity); 01: 63% current; 10: 78% current; 11: 100% current (maximum linearity).
D2	0	
D1	0	Tx Baseband Gain. D1:D0 = 00: max baseband gain - 5dB; 01: max baseband gain - 3dB; 10: max baseband gain - 1.5dB; 11: max baseband gain.
D0	0	

MAX2828/MAX2829

Single-/Dual-Band 802.11a/b/g World-Band Transceiver ICs

**Table 18. PA Bias DAC Register
(A3:A0 = 1010)**

DATA BIT	DEFAULT	DESCRIPTION
D13	0	Set to 0
D12	0	
D11	0	
D10	0	
D9	1	Sets PA bias DAC turn-on delay after TXENA is set high and A3:A0 = 0010, D10 = 1, in steps of 0.5μs. D9:D6 = 0001 corresponds to 0μs and 1111 corresponds to 7μs.
D8	1	
D7	1	
D6	1	
D5	0	Sets PA bias DAC output current in steps of 5μA. D5:D0 = 000000 corresponds to 0μA and 111111 corresponds to 315μA.
D4	0	
D3	0	
D2	0	
D1	0	
D0	0	

**Table 19. Rx Gain Register
(A3:A0 = 1011)**

DATA BIT	DEFAULT	DESCRIPTION	
D13	0	Not Used. For faster Rx gain setting, only D6:D0 need to be programmed.	
D12	0		
D11	0		
D10	0		
D9	0		
D8	0		
D7	0		
D6	1	Rx LNA Gain Control	Rx baseband and RF gain-control bits. D6 maps to digital input pin B7 and D0 maps to digital input pin B1. D6:D0 = 0000000 corresponds to minimum gain.
D5	1	Rx VGA Gain Control	
D4	1		
D3	1		
D2	1		
D1	1		
D0	1		

**Table 20. Tx VGA Gain Register
(A3:A0 = 1100)**

DATA BIT	DEFAULT	DESCRIPTION
D13	0	Not Used. For faster Tx VGA gain setting, only D5:D0 need to be programmed.
D12	0	
D11	0	
D10	0	
D9	0	
D8	0	
D7	0	
D6	0	
D5	0	Tx VGA Gain Control. D5 maps to digital input pin B6 and D0 maps to digital input pin B1. D5:D0 = 000000 corresponds to minimum gain.
D4	0	
D3	0	
D2	0	
D1	0	
D0	0	

PA Bias DAC Register Definition (A3:A0 = 1010)

This register controls the output current of the DAC, which biases the external PA (see Table 18).

Rx Gain Register Definition (A3:A0 = 1011)

This register sets the Rx baseband and RF gain when A3:A0 = 1000, D12 = 1 (see Table 19).

Tx VGA Gain Register Definition (A3:A0 = 1100)

This register sets the Tx VGA gain when A3:A0 = 1001, D10 = 1 (see Table 20).

Applications Information

MIMO Applications

The MAX2828/MAX2829 support multiple input multiple output (MIMO) applications where multiple transceivers are used in parallel. A special requirement for this application is that all receivers must maintain a constant relative local oscillator phase, and that they continue to do so after any receive-transmit-receive mode switching. The same requirement holds for the transmitters—they should all maintain a constant relative phase, and continue to do so after any transmit-receive-transmit mode switching. This feature is enabled in the MAX2828/MAX2829 by programming A3:A0 = 0010, D13 = 1 and A3:A0 = 0101, D13 = 1. The constant relative phases of the multiple transceivers are maintained in the transmit, receive, and standby modes of operation, as long as they are all using a common external reference frequency source (crystal oscillator).

MAX2828/MAX2829

Single-/Dual-Band 802.11a/b/g World-Band Transceiver ICs

Rx Gain Control

The receiver gain can be set either by the digital input pins B1 through B7 or by the internal Rx gain register. The gain-control characteristic is shown in the *Typical Operating Characteristics*.

RSSI

The RSSI output can be configured for two output voltage ranges: 0.5V to 2V and 0.5V to 2.5V (see Table 16a). The RSSI output is unaffected by the Rx VGA gain setting. They are capable of driving loads up to 10kΩ || 5pF.

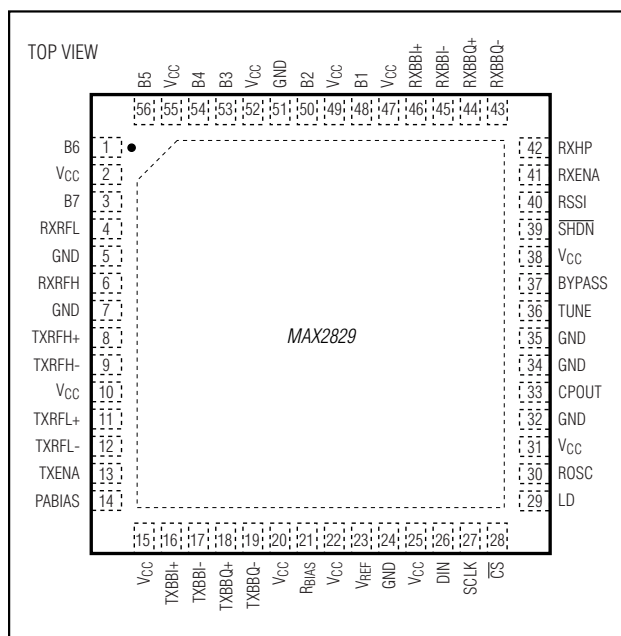
Tx VGA Gain Control

The Tx gain can be set either by digital input pins B1 through B6 or by the internal Tx VGA gain register. The linearity of the Tx blocks can also be adjusted (Table 17). The Tx VGA gain-control characteristic is shown in the *Typical Operating Characteristics*.

Loop Filter

The loop-filter topology and component values can be found in the MAX2828/MAX2829 evaluation kit data sheet. A 150kHz loop bandwidth is recommended to ensure that the loop settles fast enough during Tx/Rx turnaround times.

Pin Configurations (continued)



Chip Information

TRANSISTOR COUNT: 42,998

PROCESS: BiCMOS

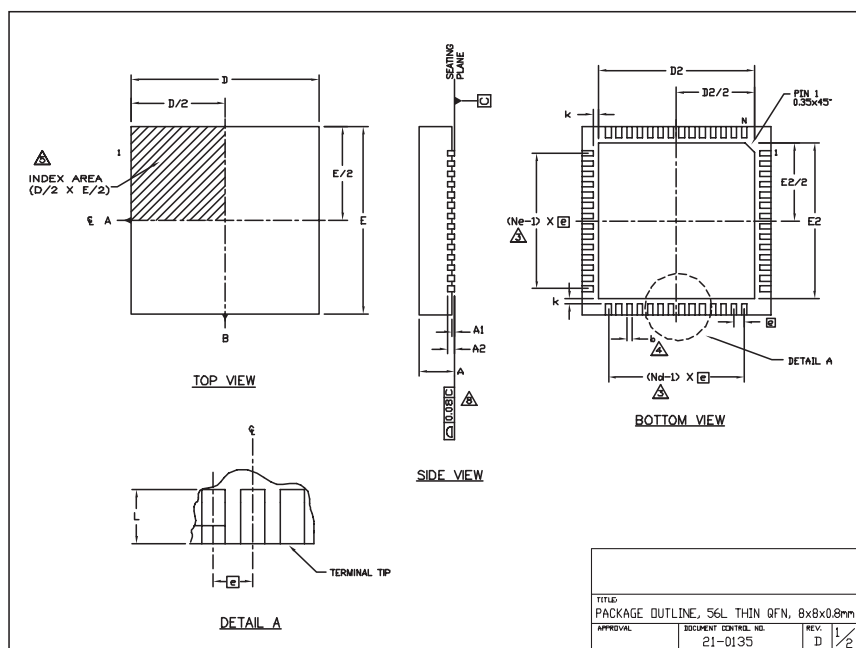
MAX2828/MAX2829

Single-/Dual-Band 802.11a/b/g

World-Band Transceiver ICs

Package Information

(The package drawing(s) in this data sheet may not reflect the most current specifications. For the latest package outline information go to www.maxim-ic.com/packages.)



NOTES:

1. DIE THICKNESS ALLOWABLE IS 0.225mm MAXIMUM (0.009 INCHES MAXIMUM).
2. DIMENSIONING & TOLERANCES CONFORM TO ASME Y14.5M. - 1994.
3. N IS THE NUMBER OF TERMINALS.
Nd IS THE NUMBER OF TERMINALS IN X-DIRECTION &
Ne IS THE NUMBER OF TERMINALS IN Y-DIRECTION.
4. DIMENSION b APPLIES TO PLATED TERMINAL AND IS MEASURED BETWEEN 0.20 AND 0.25mm FROM TERMINAL TIP.
5. THE PIN #1 IDENTIFIER MUST BE LOCATED ON THE TOP SURFACE OF THE PACKAGE WITHIN HATCHED AREA AS SHOWN. EITHER AN INDENTATION MARK OR INK/LASER MARK IS ACCEPTABLE.
6. ALL DIMENSIONS ARE IN MILLIMETERS.
7. PACKAGE WARPAGE MAX 0.01mm.
8. APPLIES TO EXPOSED PAD AND TERMINALS. EXCLUDES INTERNAL DIMENSION OF EXPOSED PAD.
9. MEETS JEDEC MO220.

Symbol	56L 8x8			Units
	MIN.	NOM.	MAX.	
A	0.70	0.75	0.80	
b	0.20	0.25	0.30	4
D	7.90	8.00	8.10	
E	7.90	8.00	8.10	
□	0.50 BSC			
N	56			3
Nd	14			3
Ne	14			3
L	0.30	0.40	0.50	
A1	0.00	0.02	0.05	
A2	0.20 REF			
k	0.25	---	---	

PKG. CODE	EXPOSED PAD VARIATION						JEDEC	BONDING ALLOWED
	D2			E2				
	MIN.	NOM.	MAX.	MIN.	NOM.	MAX.		
TS688-1	6.50	6.65	6.70	6.50	6.65	6.70	WLLD-5	NO
TS688-2	6.50	6.65	6.70	6.50	6.65	6.70	WLLD-5	YES
TS688-3	6.50	6.65	6.70	6.50	6.65	6.70	WLLD-5	NO



TITLE: PACKAGE OUTLINE, 56L THIN QFN, 8x8x0.8mm			
APPROVAL	DOCUMENT CONTROL NO.	REV.	
	21-0135	D	1/2

Maxim cannot assume responsibility for use of any circuitry other than circuitry entirely embodied in a Maxim product. No circuit patent licenses are implied. Maxim reserves the right to change the circuitry and specifications without notice at any time. The parametric values (min and max limits) shown in the Electrical Characteristics table are guaranteed. Other parametric values quoted in this data sheet are provided for guidance.

Maxim Integrated 160 Rio Robles, San Jose, CA 95134 USA 1-408-601-1000

39

Bibliography

- [1] S. Brandes, I. Cosovic, and M. Schnell. Reduction of out-of-band radiation in ofdm systems by insertion of cancellation carriers. *Communications Letters, IEEE*, 10(6): 420–422, 2006. ISSN 1089-7798.
- [2] A.G. Armada. Understanding the effects of phase noise in orthogonal frequency division multiplexing (OFDM). *Broadcasting, IEEE Transactions on*, 47(2):153–159, 2001. ISSN 0018-9316.
- [3] M. Windisch and G. Fettweis. On the impact of I/Q imbalance in multi-carrier systems for different channel scenarios. In *Circuits and Systems, 2007. ISCAS 2007. IEEE International Symposium on*, pages 33–36, 2007.
- [4] V.A. Bohara and S. O. Ting. Theoretical analysis of OFDM signals in nonlinear polynomial models. In *Information, Communications Signal Processing, 2007 6th International Conference on*, pages 1–5, 2007.
- [5] D. Brumbi. *Fundamentals of Radar Technology for Level Gauging*. Krohne, 2003.
- [6] J. Bergervoet, H. Kundur, D.M.W. Leenaerts, R.C.H. van de Beek, R. Roovers, G. Van Der Weide, H. Waite, and S. Aggarwal. A fully integrated 3-band OFDM UWB transceiver in 0.25/spl mu/m SiGe BiCMOS. In *Radio Frequency Integrated Circuits (RFIC) Symposium, 2006 IEEE*, 2006.
- [7] IEEE standard for information technology- telecommunications and information exchange between systems- local and metropolitan area networks- specific requirements- part 11: Wireless lan medium access control (MAC) and physical layer (PHY) specifications. *ANSI/IEEE Std 802.11, 1999 Edition (R2003)*, 2003.
- [8] M. Morelli, C.-C.J. Kuo, and Man-On Pun. Synchronization techniques for orthogonal frequency division multiple access (OFDMA): A tutorial review. *Proceedings of the IEEE*, 95(7):1394–1427, 2007. ISSN 0018-9219.
- [9] R. W. Chang. Synthesis of band-limited orthogonal signals for multichannel data transmission. *Bell System Technical Journal*, 45:1775–1796, 1966.
- [10] S. Weinstein and P. Ebert. Data transmission by frequency-division multiplexing using the discrete fourier transform. *Communication Technology, IEEE Transactions on*, 19(5):628–634, 1971. ISSN 0018-9332.

- [11] Z. Yuan. Sidelobe suppression and agile transmission techniques for multicarrier-based cognitive radio systems, May 2009.
- [12] F.J. Harris. On the use of windows for harmonic analysis with the discrete fourier transform. *Proceedings of the IEEE*, 66(1):51–83, 1978. ISSN 0018-9219.
- [13] I. Cosovic and V. Janardhanam. Sidelobe suppression in OFDM systems. In K. Fazel and S. Kaiser, editors, *Multi-Carrier Spread Spectrum: Proceedings from the 5th International Workshop, Oberpfaffenhofen, Germany*, pages 473–482. Springer, Sept. 2005.
- [14] I. Cosovic, S. Brandes, and M. Schnell. Subcarrier weighting: a method for sidelobe suppression in OFDM systems. *Communications Letters, IEEE*, 10(6):444–446, 2006. ISSN 1089-7798.
- [15] S. Pagadarai, R. Rajbanshi, A. M. Wyglinski, and G.J. Minden. Sidelobe suppression for ofdm-based cognitive radios using constellation expansion. In *Wireless Communications and Networking Conference, 2008. WCNC 2008. IEEE*, pages 888–893, 2008.
- [16] S. Brandes, I. Cosovic, and M. Schnell. Reduction of out-of-band radiation in ofdm based overlay systems. In *New Frontiers in Dynamic Spectrum Access Networks, 2005. DySPAN 2005. 2005 First IEEE International Symposium on*, pages 662–665, 2005.
- [17] R. B. F. Lopes and S. G. J. Panaro. OFDM sidelobe suppression combining active and null cancellation carriers in the guard bands. *International Microwave and Optoelectronics Conference, Rio de Janeiro, Brazil*, Aug. 2013.
- [18] Pagadarai S. and A. M. Wyglinski. Novel sidelobe suppression technique for OFDM-based cognitive radio transmission. *Proceedings of the IEEE Symposium on New Frontiers in Dynamic Spectrum Access Networks, Chicago, IL, USA., Oct. 2008*.
- [19] E. McCune. *Practical Digital Wireless Signals, The Cambridge RF and Microwave Engineering Series*. Cambridge University Press, 2010. ISBN 9781139484732.
- [20] J. H. Stott. The effects of frequency errors in OFDM. *BBC Research and Development Report*, 1995.
- [21] Paul H. Moose. A technique for orthogonal frequency division multiplexing frequency offset correction. *Communications, IEEE Transactions on*, 42(10):2908–2914, 1994. ISSN 0090-6778.
- [22] H. Nogami and T. Nagashima. A frequency and timing period acquisition technique for ofdm systems. In *Personal, Indoor and Mobile Radio Communications, 1995. PIMRC'95. Wireless: Merging onto the Information Superhighway., Sixth IEEE International Symposium on*, volume 3, 1995.
- [23] T.M. Schmidl and D.C. Cox. Robust frequency and timing synchronization for OFDM. *Communications, IEEE Transactions on*, 45(12):1613–1621, 1997. ISSN 0090-6778.
- [24] B. Park, H. Cheon, C. Kang, and D. Hong. A novel timing estimation method for ofdm systems. *Communications Letters, IEEE*, 7(5):239–241, 2003. ISSN 1089-7798.

- [25] C. Maoquan, M. Aidong, and Y. Bo. New timing synchronization methods for OFDM systems. In *Information Science and Engineering (ICISE), 2009 1st International Conference on*, pages 2662–2665, 2009.
- [26] A. Czylik. Synchronization for systems with antenna diversity. In *Vehicular Technology Conference, 1999. VTC 1999 - Fall. IEEE VTS 50th*, volume 2, pages 728–732, 1999.
- [27] G. Ren, Y. Chang, Hui Zhang, and Huining Zhang. Synchronization method based on a new constant envelop preamble for OFDM systems. *Broadcasting, IEEE Transactions on*, 51(1):139–143, 2005. ISSN 0018-9316.
- [28] Y. Kang, K. Kang, and D. Ahn. Preamble based OFDM timing synchronization method for WLAN and WMAN standard systems. In *Consumer Electronics, 2007. ICCE 2007. Digest of Technical Papers. International Conference on*, pages 1–2, 2007.
- [29] G. Wang, Y. Xiao, X. Lei, L. Yan, and Y. Luo. A simplified timing synchronization algorithm for OFDM systems. In *Communications and Mobile Computing (CMC), 2010 International Conference on*, volume 2, pages 413–416, 2010.
- [30] J. Wu, Q. Zhou, and K. K. M. Cheng. The adaptive algorithm of symbol timing and carrier phase estimation in OFDM systems. In *Communications, 2001. ICC 2001. IEEE International Conference on*, volume 1, pages 156–160, 2001.
- [31] C. R N Athaudage. BER sensitivity of OFDM systems to time synchronization error. In *Communication Systems, 2002. ICCS 2002. The 8th International Conference on*, volume 1, pages 42–46, 2002.
- [32] X. Wang, T.T. Tjhung, Y. Wu, and B. Caron. SER performance evaluation and optimization of OFDM systems with residual frequency and timing offsets from imperfect synchronization. *Broadcasting, IEEE Transactions on*, 49(2):170–177, 2003. ISSN 0018-9316.
- [33] G. Liu and W. Zhu. Compensation of phase noise in OFDM systems using an ICI reduction scheme. *Broadcasting, IEEE Transactions on*, 50(4):399–407, 2004. ISSN 0018-9316.
- [34] A.G. Armada and M. Calvo. Phase noise and sub-carrier spacing effects on the performance of an OFDM communication system. *Communications Letters, IEEE*, 2(1):11–13, 1998. ISSN 1089-7798.
- [35] M. Windisch. *Estimation and Compensation of I/Q Imbalance in Broadband Communication Receivers*. PhD thesis, Fakult at Elektrotechnik und Informationstechnik der Technischen Universit at Dresden, March 2007.
- [36] A. Tarighat, R. Bagheri, and A.H. Sayed. Compensation schemes and performance analysis of IQ imbalances in OFDM receivers. *Signal Processing, IEEE Transactions on*, 53(8):3257–3268, 2005. ISSN 1053-587X.
- [37] S. Merchan, A.G. Armada, and J.L. Garcia. OFDM performance in amplifier nonlinearity. *Broadcasting, IEEE Transactions on*, 44(1):106–114, 1998. ISSN 0018-9316.

- [38] N. H. Mistry. Implementation of a peak windowing algorithm for crest factor reduction in wcdma. Master's thesis, Simon Fraser University, Summer 2003.
- [39] Agilent Technologies. *Agilent N6030A Series Arbitrary Waveform Generators — User's Guide*. Agilent Technologies, Inc., Printed in USA, May 2006.
- [40] Agilent Technologies. *Agilent E8257D/67D & E8663D PSG Signal Generator — User's Guide*. Agilent Technologies, Inc., Printed in USA, February 2013.
- [41] National Instruments. *NI 5772R User Manual & Specifications*, July 2012.
- [42] H. T. Friis. Noise figures of radio receivers. *Proceedings of the I.R.E.*, pages 419–422, July 1944.
- [43] R. Frank, S. Zadoff, and R. Heimiller. Phase shift pulse codes with good periodic correlation properties (corresp.). *Information Theory, IRE Transactions on*, 8(6):381–382, 1962. ISSN 0096-1000.
- [44] R. C. Heimiller. Phase shift pulse codes with good periodic correlation properties. *Information Theory, IRE Transactions on*, 7(4):254–257, 1961. ISSN 0096-1000.
- [45] D. Chu. Polyphase codes with good periodic correlation properties (corresp.). *Information Theory, IEEE Transactions on*, 18(4):531–532, 1972. ISSN 0018-9448.
- [46] M. Skolnik. *Radar Handbook*. Electronic Engineering Series. McGraw-Hill, 1990. ISBN 9780070579132.
- [47] W. Kester. *Mastering the Mix in Signal Processing*. Analog Devices Inc., 1991.